PARAMETER ESTIMATION OF HYBRID MAGNETIC BEARINGS SYSTEM FOR AXIAL FLOW BLOOD PUMP APPLICATIONS WITH POSSIBLE SELF-SENSING CAPABILITY

CHENG SHANBAO

School of Mechanical and Aerospace Engineering

A thesis submitted to the Nanyang Technological University
in partial fulfillment of the requirement for the degree of
Doctor of Philosophy

2008

Acknowledgements

Firstly, I would like to thank my supervisor, Associate Professor Lim Tau Meng for his guidance, help and support in my research. Without him, my PhD dissertation could not have been completed.

Secondly, I would like to express my appreciation to the examiners of my PhD first year report: Associate Professor Lau Wai Shing, Michael, and Assistant Professor Phee Soo Jay, Louis, for their valuable help and comments on my PhD first year report, which lay a solid foundation for my future research.

Thirdly, special thanks are extended to Mr. Zhang Dongsheng for his help in the pump blades design, teaching me how to use Matlab and Pro/E for modelling the pump blades.

I also want to give many thanks to the graduate students in Mechanics of Machines Lab: Mr. Wong Yoke Rung, Mr. Chen Ping, Mrs. Lu Fangfang, and Mr.Yang Yongbo, for sharing a lot of good time with me; and the following technicians: Mr. Poon Weng Wai and Mrs. Lim Lang Hiang Christina in Mechanics of Machines Lab, Mrs. Lee Koon Fong and Mrs. Loh Jee Luan Pamela in Mechatronics and Control Lab, for lending me a lot of lab equipment; and Mr. Koh Wing Leong, Mr. Kong Seng Ann in CNC Lab, and Mr. Chu Chor Lee in the Machines Workshop, for helping me do a lot of manual and CNC machining.

Lastly, I would like to thank my wife, Bai Xue, for her continuous and unconditional encouragement and care.

Abstract

The active magnetic bearing (AMB) system has been widely employed in industrial applications, among which one of the most important applications is the magnetically levitated rotary blood pumps. It is because AMB can replace traditional ball bearings and realize the non-contact support of rotating impellers/rotors of the pumps. Current state-of-the art ventricular assist devices (VADs) are magnetically suspended rotary pumps, and it is due to the advantages of the magnetic bearings: no mechanical contact between the bearing and rotor, no lubrication needed, less heat generation and lower hemolytic risk.

In this research, a completely magnetically levitated axial flow blood pump incorporating a hybrid magnetic bearings (HMBs) system has been designed and developed. The impeller is enclosed in the rotor, which is controlled in five degrees-of-freedom (DOF), among which four radial directions are actively controlled and one axial direction is passively controlled. The HMBs system is composed of two hybrid magnetic bearings for suspending the rotor of the pump with PID controllers, and one brushless and sensorless three-phase permanent magnet (PM) motor for driving the rotor. The design target of the axial flow blood pump is to realize 100 mmHg differential pressure and 5 L/min flow rate. The HMBs system of the axial flow blood pump has been tested to be able to achieve good system performance in air: the pump rotor can rotate in stable suspension at speeds of up to 14,000 rpm.

The method of parameter estimation has been proposed to extract the stiffness and damping properties of the HMBs system employed by the axial flow blood pump. A special test rig has been designed such that the rotor of the pump can be perturbed in suspension both in the radial and axial directions, whether it is stationary or rotating. Schroeder Phased Harmonics Sequence (SPHS) is used as the multi-frequency test input signal of the parameter estimation. The dynamic model of the HMBs is validated by the high goodness of fit using statistical analysis. The actuator gain of the HMBs is determined to be linear within 20% of the static eccentricity ratio.

Self-sensing parameter estimator for AMB system has been developed and tested. The switching frequency component of the coil current contains the air gap length between the stator and the suspended target. Current demodulation technique is used to extract the air gap length from the coil current with demodulation filters, and the result is the function of the air gap length and the duty cycle of the PWM amplifiers. Self-sensing parameter estimation is composed of two identical demodulation filters, one coil inductance simulator and one PI convergence controller. The output of one demodulation filter is compared with the output of the other demodulation filter, which extracts the simulated coil currents with the input of actual switching voltages and the estimated air gap length. The error between the two demodulation filters is processed by the PI convergence controller to correct the estimated air gap. Benefiting from the close loop characteristics of the self-sensing parameter estimation, not only is the influence of the duty cycle removed, but the dynamic response of the self-sensing system is also greatly increased.

Contents

ABSTRACT II

CONTENTS III

LIST OF FIGURES VIII

LIST OF TABLES XV

LIST OF ABBREVIATIONS XVI

CHAPTER 1 INTRODUCTION 1

1.1 AMB system 1

1.1.1 Benefits and limitations of magnetic bearings 2

1.1.2 Attractive features of magnetic bearings 3

1.2 Stiffness and damping coefficients of AMB system 4

1.3 Self-sensing AMB 6

1.4 Maglev ventricular assist devices (VADs) 7

1.5 Hybrid magnetic bearings (HMBs) 8

1.6 Research objectives & summary 8

1.7 Dissertation outline 10

1.8 Original Contributions 11

CHAPTER 2 LITERATURE REVIEW 14

2.1 Design of AMB system and motors 14

2.1.1 Design of AMB system 14

2.1.2 Design of brushless PM DC motor 17

2.2 Ventricular assist devices 19

2.3 Some typical MagLev VADs 21

2.3.1 Berlin Heart INCOR® 21

2.3.2 Streamliner axial flow blood pump 22

2.3.3 TMDU/TIT disposable centrifugal blood pump 23

2.3.4 Thoratec HeartMate III 24

2.4 Parameter estimation on rotor-bearing system 25

2.5 Stiffness and damping properties of magnetic bearings 27

2.6 Approaches of self-sensing magnetic bearings 30

2.6.1 Current demodulation 31

2.6.2 State-space observer 32

CHAPTER 3 THE DEVELOPMENT OF HYBRID MAGNETIC BEARINGS SYSTEM FOR AXIAL FLOW BLOOD PUMP 33

3.1 Design of axial flow blood pump 33

3.1.1 Overall design of axial flow blood pump 33

3.1.2 Enclosed-impeller 37

3.1.3 Design of pump impeller, straightener and diffuser 37

3.2 Fabrication of the straightener, impeller and diffuser 46

3.2.1 The straightener 47

3.2.2 The impeller 47

3.2.3 The diffuser 48

3.2.4 5-axis machining and SolidCAM® 49

3.3 Development of the HMBs, the rotor and the Lorentz-typed motor 51

3.3.1 Design of the HMBs 51

3.3.2 Fabrication of the HMBs 58

3.3.3 The rotor 60

3.3.4 The Lorentz-typed three-phase brushless and sensorless PM motor 62

3.4 Control of the HMBs system 67

3.4.1 Finite element calculation of the electromagnetic forces 67

3.4.2 Control of HMBs 70

3.4.3 Control of the Lorentz-typed three phase PM motor 78

3.5 Performance of HMBs system 78

CHAPTER 4 PARAMETER ESTIMATION ON ONE DOF MAGNETICALLY LEVITATED SYSTEM WITH A DIGITAL PID CONTROLLERS 84

4.1 Principles 84

4.1.1 Effective stiffness and damping coefficients of electromagnetic suspension system 84

4.1.2 Actual stiffness and damping coefficients of electromagnetic suspension system 87

4.1.3 One DOF parameter estimation algorithm in frequency domain 88

4.1.4 Model validation and statistical information of estimated parameters 91

4.1.5 One DOF parameter estimation procedure 92

4.2 Design of test rig 93

4.3 Experimental results 94

4.3.1 Experimental setup 94

4.3.2 Comparisons of effective and actual stiffness and damping coefficients 97

4.4 Influences of controller parameters on system responses 100

4.4.1 Influences of varying proportional feedback 101

4.4.2 Influences of varying integral feedback 102

4.4.3 Influences of varying derivative feedback 104

CHAPTER 5 PARAMETER ESTIMATION AND ACTUATOR CHARACTERISTICS OF MAGNETIC BEARINGS FOR AXIAL FLOW BLOOD PUMP APPLICATIONS 106

5.1 System's dynamic model and parameter estimation procedure 106

5.1.1 One DOF dynamics model 107

5.1.2 Two DOF rotor-bearing model with direct- and cross-axes coefficients 109

5.1.3 Two DOF rotor-bearing model with only direct-axis coefficients 111

5.1.4 Two-DOF parameter estimation procedure 113

5.2 Preparatory experiments 114

5.2.1 Description of the test rig 114

5.2.2 Parameter estimation of pedestal structural support using one DOF model 118

5.2.3 Determination of HMBs' actuator characteristics 122

5.3 Parameter estimation experiments 128

5.3.1 Radial estimation of HMBs modelled with direct- and cross-axes coefficients 128

5.3.2 Radial estimation of HMBs modelled with only direct-axis coefficients 134

5.3.3 Radial estimation of HMBs model with only direct-axis coefficients and with varying k_p of PID controller 137

5.3.4 Radial estimation of HMBs model with only direct-axis coefficients and with rotating rotor 139

5.4 Axial parameter estimation of HMBs system using one DOF model 140

CHAPTER 6 SELF-SENSING AMB 146

6.1 Coil inductor model 147

6.2 Switching noise demodulation 150

6.2.1 Theoretical analysis 150

6.2.2 Digital implementation of the forward path filter 153

6.2.3 Simulation of switching noise demodulation 156

6.3 Digital simulation of self-sensing parameter estimation 161

6.3.1 Introduction 161

6.3.2 Simulation results 162

6.4 Analog circuits of self-sensing parameter estimator 164

6.4.1 Circuit implementations 165

6.4.2 Static and dynamic calibrations of self-sensing scheme 173

CHAPTER 7 CONCLUSIONS & FUTURE WORK 183

7.1 Conclusions 183

7.2 Future work 186

APPENDIX A 202

APPENDIX B 203

APPENDIX C 205

APPENDIX D 215

APPENDIX E 216

List of Figures

Figure 1.1: Control diagram of active magnetic bearings 1

Figure 2.1: Berlin Heart INCOR® 21

Figure 2.2: Streamliner axial flow blood pump 22

Figure 2.3: TMDU/TIT disposable centrifugal blood pump 23

Figure 2.4: Photograph of Thoratec HeartMate III 25

Figure 3.1: Cross section view of axial flow blood pump 34

Figure 3.2: Schematic view of the straightener, impeller, diffuser and the rotor 35

Figure 3.3: Scheme of the axial flow blood pump with main dimensions 36

Figure 3.4: Photograph of the fabricated pump casing 36

Figure 3.5: Straightener 38

Figure 3.6: Two-dimensional analysis of the impeller 38

Figure 3.7: Blade geometry of the impeller 39

Figure 3.8: Assembled velocity diagram of impeller 40

Figure 3.9: Final assembled diagram of impeller 41

Figure 3.10: Two-dimensional analysis of the diffuser 43

Figure 3.11: Blade geometry of the diffuser 44

Figure 3.12: Photograph of the fabricated impeller, diffuser and straightener 46

Figure 3.13: Exploded view of the straightener 47

Figure 3.14: Assembly of the impeller 47

Figure 3.15: Photograph of the dissembled impeller 48

Figure 3.16: Exploded view of the diffuser 49

Figure 3.17: 5-axis precision machining 50

Figure 3.18: SolidCAM® 50

Figure 3.19: Scheme of flux flow in HMB 52

Figure 3.20: 2D model of the axial flow blood pump in Maxwell 2D 53

Figure 3.21: Simulation result of magnetic flux of the HMB by Maxwell 2D 54

Figure 3.22: Enlarged part of flux loop of HMB in Maxwell 2D 54

Figure 3.23: Configuration of the HMB 55

Figure 3.24: HMB Stator with lamination holder for position probes 56

Figure 3.25: Photograph of the HMBs' stator 58

Figure 3.26: 3D model of the lamination fixture 59

Figure 3.27: Scheme of the rotor with part materials and dimensions 60

Figure 3.28: Explored view of inner sleeve of the rotor 61

Figure 3.29: Photograph of the rotor, assembly fixture and the outer sleeve 62

Figure 3.30: Schematic of the motor wiring connections 63

Figure 3.31: Three parts of the motor coil fixture 65

Figure 3.32: Photograph of the fabricated motor coil fixture 65

Figure 3.33: Photograph of the coil winding operation 66

Figure 3.34: Photograph of the fabricated motor stator 67

Figure 3.35: 3D model of the HMB in Maxwell 3D 68

Figure 3.36: Force in y direction changes with axial movement of rotor 69

Figure 3.37: Force in z direction changes with axial movement of rotor 69

Figure 3.38: Magnetic force in the vertical direction 70

Figure 3.39: Equivalent magnetic circuit of HMB 71

Figure 3.40: Block diagram of controlling the HMBs in one radial direction 75

Figure 3.41: Levitated rotor displacements in x, y, z directions at 0 rpm 79

Figure 3.42: Levitated rotor displacements in the x, y, z directions at 14,000 rpm 80

Figure 3.43: Levitated response of the HMBs system of axial flow blood pump in x, y and z directions ('displacement' shortened to 'dp' in graph) 81

Figure 3.44: Bearing coil current vs. rotor rotational speed.....82

Figure 4.1: Block diagram of AMB in one axis.....85

Figure 4.2: Parameter estimation procedure for one DOF rotor-bearing system....92

Figure 4.3: Photograph of the one DOF test rig.....93

Figure 4.4: Scheme of instrumental arrangement 95

Figure 4.5: Photograph of experimental setup 96

Figure 4.6: SPHS and the averaging effect of 5 periods of the force and displacement signals.....97

Figure 4.7: Comparisons between effective and actual stiffness and damping coefficients.....98

Figure 4.8: Statistical information on the estimated stiffness and damping coefficients.....100

Figure 4.9: Estimated stiffness and damping coefficients with varying proportional feedback.....101

Figure 4.10: Estimated stiffness and damping coefficients with varying integral feedback.....103

Figure 4.11: Expansion of Figure 4.10 in the neighbourhood of natural frequency 103

Figure 4.12: Estimated stiffness and damping coefficients with varying derivative feedback.....104

Figure 5.1: General model of the one DOF rotor-bearing system 108

Figure 5.2: Two DOF rotor-bearing system modeled with eight linearised direct- and cross-axes coefficients 109

Figure 5.3: Two DOF rotor-bearing model with only direct-axis coefficients 112

Figure 5.4: Parameter estimation procedure for two DOF rotor-bearing system..113

Figure 5.5: Test rig used for parameter estimation of the HMBs system 115

Figure 5.6: Schematic arrangement for parameter estimation test rig 116

Figure 5.7: Excitation force and displacement plots with 5 periods of signal averaging 119

Figure 5.8: Amplitude and phase transfer functions of the pedestal structure 121

Figure 5.9: Photograph of experimental setup for calibrating actuator gain.....123

Figure 5.10: Block diagram of open loop calibration of the HMBs' actuator gain 124

Figure 5.11: Amplitude and phase transfer functions of actuator gain 124

Figure 5.12: Flat amplitude transfer function of actuator gain from 1 to 50 Hz...125

Figure 5.13: Measured HMBs' actuator gain at rotor's zero static eccentricity ...126

Figure 5.14: Determination of HMBs' maximum displacement linear operating range 127

Figure 5.15: Experimental arrangement of x-y axes, excitation force and displacement probes for estimating eight direct- and cross-axes coefficients.....128

Figure 5.16: The measured transfer function in the x and y directions of HMBs system with goodness of fit (G.o.F). 'Transfer function' is shortened to 'TF' in graph.....131

Figure 5.17: Radial estimation of the HMBs system with direct- and cross-axes stiffness coefficients 132

Figure 5.18: Radial estimation of the HMBs system with direct- and cross-axes damping coefficients.....133

Figure 5.19: The decomposition of excitation force in x- and y- directions and HMBs system modelled with four direct-axis coefficients 134

Figure 5.20: Radial estimation of the HMBs system with only four direct-axis coefficients.....135

Figure 5.21: Comparison of estimated stiffness coefficients obtained with direct-axis, and direct-with cross-axes dynamic models 136

Figure 5.22: Radial estimation results of the HMBs system with different values of k_p 138

Figure 5.23: Comparisons of radial HMBs estimated results modelled with only direct-axis coefficients at 0 and at 8,000 rpm.....140

Figure 5.24: Experimental arrangement of the axial parameter estimation of the HMBs system 141

Figure 5.25: Schematic arrangement of axial parameter estimation of the HMBs system using one DOF model.....142

Figure 5.26: One DOF model of axial parameter estimation of HMBs system....143

Figure 5.27: The parameter estimation results of HMBs system in the axial direction.....144

Figure 5.28: Comparisons of estimation results between the axial and radial directions 145

Figure 6.1: Schematics of flux path of AMB 147

Figure 6.2: Block diagram of the inductor model implemented in Simulink 150

Figure 6.3: The switching voltage waveform in one period 151

Figure 6.4: Bode diagram of the digital second order high-pass filter.....154

Figure 6.5: The rectifier realized by Abs block in Simulink.....155

Figure 6.6: Bode diagram of the digital second order low-pass filter.....156

Figure 6.7: Flowchart of simulation model for switching noise demodulation 157

Figure 6.8: Simulink block model of switching noise demodulation 157

Figure 6.9: Forward path filter output compared with the actual displacement when the duty cycle is constant.....158

Figure 6.10: Comparison of simulated forward path filter output with the actual displacement with varying duty cycle 159

Figure 6.11: Enlarged part of Figure 6.10, showing the corruption caused by the changing duty cycle 160

Figure 6.12: Self-sensing parameter estimation scheme for determining air gap displacement 161

Figure 6.13: Parameter estimator output compared with the actual displacement and the forward path filter output.....163

Figure 6.14: Frequency response of self-sensing parameter estimator in simulation 164

Figure 6.15: The main structure of self-sensing circuit implemented in OrCAD.165

Figure 6.16: Honeywell current sensor CSNE151 166

Figure 6.17:The switching coil current represented by voltage waveform as sensed by CSNE151 167

Figure 6.18: The band pass filter used in forward path filter.....168

Figure 6.19: Waveform of measured coil current after the band pass filter.....169

Figure 6.20: AD637 with 2-Pole Sallen-Key Filter acts as a rms-to-dc converter 169

Figure 6.21: The circuit of PI controller 170

Figure 6.22: Switching voltage obtained by INA105KP 171

Figure 6.23: MPY634KP functions as a balance modulator with typical modulated output 171

Figure 6.24: Connection between self-sensing board and backplane 172

Figure 6.25: Four self-sensing boards mounted on one backplane board.....173

Figure 6.26: Photograph of the self-sensing test rig.....174

Figure 6.27: Photograph of the self-sensing static calibration test 175

Figure 6.28: Linearity of the self-sensing parameter estimator 177

Figure 6.29: Instrumentation arrangement for self-sensing dynamic calibration .178

Figure 6.30: Eddy current probe output compared with self-sensing parameter estimated output.....179

Figure 6.31: Frequency response of self-sensing parameter estimated output over eddy current probe output.....180

Figure 6.32: Frequency response of the self-sensing parameter estimator 182

List of Tables

Table 3.1: Design optimization results of impeller, straightener and diffuser 45

Table 3.2: Definition of variables 64

Table 3.3: Electromagnetic forces on rotor with the axial movement of the rotor .68

Table 3.4:Coefficients values of hybrid magnetic bearings 73

Table 3.5: Control parameters of hybrid magnetic bearings 77

Table 4.1: Basic dimensions of the electromagnetic actuator 93

Table 5.1: Parameter estimation of pedestal support spring stiffness with statistics 120

Table 5.2: Estimation results of pedestal support spring in different frequency ranges 120

Table 5.3: Radial parameter estimation of the HMBs system with 8 direct- and cross-axes coefficients 130

Table 5.4: Sample of parameter estimation results in the axial direction 144

Table 6.1: Static calibration result of self-sensing parameter estimator 176

List of Abbreviations

AMB	active magnetic bearing
DC	direct current
DOF	degree of freedom
DSP	digital signal processing
EMF	electro-motive-force
FEA	finite element analysis
FFT	Fast Fourier Transform
G.o.F	goodness of fit
HMBs	hybrid magnetic bearings
LVAD	left ventricular assist device
PCB	printed circuit board
PI	proportional-integral
PID	proportional-integral-derivative
PM	permanent magnet
PRBS	pseudo random binary sequences
PWM	pulse width modulation
SPHS	Schroeder phased harmonic sequences
VADs	ventricular assist devices

Chapter 1 Introduction

1.1 AMB system

Over the past few decades, great developments have been made in the field of improved bearings capable of supporting new high-speed flexible rotors to keep up with the significant improvements in rotating machinery, among which magnetic bearings are the most promising.

Magnetic bearings support and control rotors or other loads through contact-free electromagnetic forces. Magnetic bearings are unstable when operated in the open loop configuration, and therefore it requires control feedback to achieve system stability and required performance. A typical active magnetic bearing (AMB) system usually consists of an actuator, a position sensor, a controller and an amplifier, and its block diagram is shown in Figure 1.1.

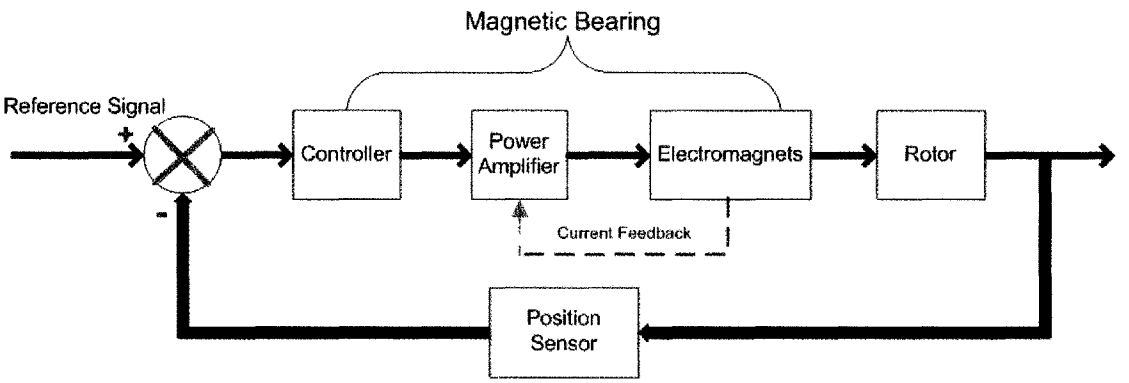

Figure 1.1: Control diagram of active magnetic bearings

The position sensor monitors the rotor position and delivers the position information into a comparator that compares the position signal with the reference

signal, and then sends the error between the two into the controller. Based on the defined control algorithm, the controller processes the input signal and then produces the resulting control output signal. Because the output signal of the controller is of low power and the magnetic actuator input (current) is of high power, a power amplifier is needed to convert the low power controller output to the high power actuator input (current). The magnetic bearing converts the current input into electromagnetic forces onto the rotor to adjust the rotor position, and therefore the AMB system is kept stable.

1.1.1 Benefits and limitations of magnetic bearings

Magnetic bearings have the following benefits over traditional bearings:

1. The air gap between the magnetic bearing and rotor prevents metal-to-metal contact, thus eliminating the problem of mechanical wear and ensuring silent operation.
2. Lubrication is not required, which is very desirable in a vacuum or non-contaminating environment.
3. Less frictional losses are created compared to regular bearings, and the maintenance costs can also be reduced.
4. Active control of bearing's dynamic characteristics can be achieved.
5. Very accurate positioning of the rotor can be ensured.
6. High-speed applications are possible. The fact that a rotor spins in a magnetic field without contact with the stator means that the drag on the rotor is minimal, which opens up new possibilities for extreme high-speed applications such as machine tool spindles and turbo compressors, where the only limitation becomes the yield strength of the rotor material.

However, the size of magnetic bearings is usually larger than other similarly specified bearings due to the fact that magnetic bearings have lower specific load capacity (maximum load per unit area of application) than most other bearing systems. Furthermore, magnetic bearings require power to drive the electromagnets, position sensors and control systems.

1.1.2 Attractive features of magnetic bearings

Benefiting from the above-mentioned unique advantages which usually outweigh their disadvantages, magnetic bearings have been widely applied in the rotating industry for the following purposes:

1. Non-contact support of rotating rotors. Non-contact support leads to little friction and absence of lubrication, which is the key reason for the application of magnetic bearings in artificial rotary blood pumps [1][19][20].
2. Better vibration control of rotors. Magnetic bearings require feedback and controller to maintain the stability of the system. Some control algorithms have been developed to better control the magnetic bearing-rotor system, such as LQG/LTR [2], H∞ [3], sliding mode [4], adaptive control [5], adaptive feed-forward [6], and PID [7], etc., among which PID control is the most popular one because of its simplicity and good performance. With the aid of these advanced controls of the AMB system, less vibration of the rotating rotor can be realized and therefore, the controlled rotor is able to rotate at higher speeds and operate through several critical speeds, which have been reported by the following: Sahinkaya *et al.* [8], Fujiwara *et al.* [9], Burrows *et al.* [10][11], Takami *et al.* [12], Shida *et al.* [13], Okada *et al.* [14], and Kasarda *et al.* [15], to highlight but a few.

3. System identification as an exciter [16][17]. The excitation force can be generated from the magnetic bearings and by means of the control algorithm of an AMB system, the amplitude and frequency of the excitation signals can be easily generated for system parameter identification purposes during operating conditions.
4. Force measurement device [17][18]. Due to the relationship between the magnetic force and the coil current, the generated force from the magnetic bearings can be estimated by measuring the corresponding coil currents or flux density. Otherwise, the magnetic force applied on the rotor will have to be measured by additional force transducers, which will raise the cost of the whole system and require additional space and parts for installation.
5. System fault diagnosis device [17]. The magnetic bearings are able to excite the rotating rotor without contact and at the same time to measure the force accurately. Hence, the system transfer function can be obtained on line with the measurement of displacements by position sensors, from which the physical or modal parameters can be identified. Those physical or modal parameters will be different when they are operated in normal and in fault conditions.

1.2 Stiffness and damping coefficients of AMB system

The magnetic bearing system can be considered as a typical second order mass-spring-damping system. A simple model of magnetic bearing suggests that in order to control the AMB system, at least two terms are needed, that is, proportional

control and derivative control. But with only a PD controller, the air gap length between the suspended object and the electromagnetic actuator is increased when external static force is applied due to steady-state error. So in practice, an integral controller is often employed in addition to a PD controller and PID controller is actually used to stabilize the system and eliminate the offset error [23], where the derivative controller is often used to provide desirable system damping. However, there is a disadvantage of PID controller for the AMB system, and that is it lacks systematic design tools and requires extensive manual tuning to achieve the desired performance for specific applications. This problem can be solved by using modern robust multivariable design methods, including H_∞ and μ-synthesis, where linear controllers can be developed for systems whose dominant dynamics can be captured using linear time-invariant (LTI) model [24][25].

The most important mechanical properties of a typical conventional bearing are its stiffness and damping support coefficients. Stiffness is the component of the bearing force applied in proportion to the displacement of the rotor, and damping is the component of the bearing force applied in proportion to the radial velocity of the rotor. Magnetic bearing is actually a special kind of bearing that supports and controls the rotor with electromagnetic forces. Like other conventional bearings, magnetic bearings also have similar characteristics of "stiffness" and "damping": the component of the electromagnetic forces generated proportional to rotor displacement, and the component of the electromagnetic forces generated proportional to rotor velocity. However, due to the frequency-dependent nature of the AMB system, the stiffness and damping coefficients of magnetic bearings are non-linear and frequency dependent [70]–[76], and can be easily adapted to various operating states; for example, when passing the rotor through critical

speeds. Therefore, in order to better understand the magnetic bearing system, stiffness and damping are two important dynamic characteristics of magnetic bearings to be investigated [73][80][81].

Traditional method of obtaining the dynamic behavior of AMB system is to sequentially model its components: eddy current probes, controller, amplifier, actuator, and rotor plant to construct the composite system, which may successfully capture the system essential behavior. In this dissertation, the method of parameter estimation is proposed to investigate the dynamic characteristics of AMB system, where the AMB system is treated as a black box and the stiffness and damping coefficients are two parameters of the system to be estimated.

1.3 Self-sensing AMB

In some cases, there is a need to eliminate the application of the position sensor in the AMB system because the number of wires across the actuator needs to be minimized. The artificial heart pump is a typical example where elimination of position sensors is very desirable, because it can reduce the number of wires across the chest to the minimum [19]. Also the self-sensing AMB will ease the work of coils layout and the system design (no need of fixation of the probes), especially when the axial position sensors are needed in the VAD [55][58]. The elimination of position sensors can also improve system reliability because previously, if one position sensor failed, the entire bearings system would fail as well, resulting in catastrophic consequences, while the chance of electronics system failing is much smaller than that of mechanical system failing. Furthermore, a rotor-bearing system can be designed to be shorter and stiffer without a discrete position sensor.

Lastly, if the method of self-sensing parameter estimation is used, the need for noise filtering circuits is eliminated because the Pulse Width Modulation (PWM) switching signal is used as position information rather than as noise.

Self-sensing magnetic bearings extract rotor position information from the electromagnetic signals of its coils. This is because the coil current signal contains the coil inductance information at the switching frequency, and the coil inductance is inversely proportional to the air gap distance. Consequently, the high-frequency component of the coil current signal contains the rotor position information. Demodulation filters are used to extract the position information from the coil currents, and this method can be called current demodulation. This direct current demodulation is open loop, and its output is a function of both air gap length and the duty cycle of PWM switching amplifier. The parameter estimation method [21][22] is a close loop current demodulation with a PI controller to remove the duty cycle information from the output of demodulation filters.

1.4 Maglev ventricular assist devices (VADs)

Studies have shown that failure of the cardiovascular system is one of the most common health disorders causing premature death in our society. Heart transplantation is the last option for those patients who suffer from heart diseases. Artificial heart pumps are good candidates for implantable ventricular assist devices (VADs) that can solve the problem of deficiency in the number of available organ donors. Nowadays, third-generation blood pumps, magnetically levitated artificial heart pumps, have been widely applied in rotary blood pumps [1][19][20], because of the advantages of magnetic bearings as mentioned above:

there is no mechanical contact that may otherwise result from ball or pivot bearings, and this non-mechanical contact eliminates the problem of material wear, red blood cell damage, heat generation, platelet aggregation, thrombus growth and even pump failure.

1.5 Hybrid magnetic bearings (HMBs)

Hybrid magnetic bearings are the magnetic bearings where permanent magnet rings are added to deliver the bias magnetic flux for the electromagnets. Due to the composition of the electromagnets and permanent magnets (PMs), this kind of magnetic bearings is known as hybrid magnetic bearings (HMBs).

HMBs depend on permanent magnets to provide the bias flux and several electromagnetic coils to supply the control flux, so the volume of its power amplifier is much smaller than active magnetic bearing, and this kind of bearings has a compact structure and lower power consumption, meanwhile, larger air gap can be realized due to the permanent magnet biased, and these advantages are especially very desirable to the VADs [20].

1.6 Research objectives & summary

The aim of this research is to develop a magnetically levitated axial flow blood pump with possible self-sensing capability and to perform parameter estimation on the HMBs system of the blood pump to investigate its dynamic properties.

A hybrid magnetic bearings (HMBs) system has been designed and developed for the maglev axial flow blood pump which has been designed with the feature of enclosed-impeller and target pump pressure of 100 mmHg and flow rate of 5

L/min. Hybrid magnetic bearings are used to suspend the rotor/impeller, and the 3-phase brushless and sensorless PM motor is used to drive the rotor. Experimental results have shown that the developed HMBs system of the axial flow blood pump can achieve good system performance: it can rotate with the speeds of up to 14,000 rpm in suspension with high stability both in radial and axial directions.

The stiffness and damping coefficients of one-DOF magnetically levitated system with a digital PID controller are estimated using the method of parameter estimation with statistical analysis. The influences of the PID controller's variables on system's dynamic properties are also investigated. Later, the method of parameter estimation is extended to the HMBs system of the axial flow blood pump. A special test rig has been designed, which makes it possible to apply the method of parameter estimation in frequency domain to investigate the stiffness and damping properties of the HMBs system in both the radial and axial axes in air, with a stationary or rotating rotor. The estimation results have been validated by statistics. The actuator gain and maximum linear operating range of the HMBs system have also been obtained experimentally.

Self-sensing parameter estimation for magnetic bearings has been digitally simulated. The self-sensing parameter estimator has also been experimentally tested: the static test has proven its good linearity, and the dynamic test has shown its good frequency response.

1.7 Dissertation outline

In Chapter 1, the background, previous and relevant work of the research are introduced, along with the research summary, the outline and the original contribution of this dissertation.

Chapter 2 reviews comprehensive literature on the contents of this research. Firstly, the literature of the design of AMB systems and motors is reviewed. Then different types of VADs are introduced, including some typical maglev VADs. After that, it discusses the different methods of parameter estimation of the rotor-bearing system, and it also reviews the literature on the investigation of the stiffness and damping properties of magnetic bearings, following which the investigation on the dynamic characteristics of VADs is introduced. Lastly, the self-sensing techniques used for AMB system are discussed.

Chapter 3 provides a description of the design, development of a HMBs system for the axial flow blood pump. The design of the axial flow blood pump with enclosed-impeller is introduced firstly. The design, fabrication and control of the HMBs and the 3-phase brushless and sensorless PM motor are described secondly. Lastly, the pump system performance in air is presented.

In Chapter 4, the effective and actual stiffness and damping properties of the AMB system are first introduced. The parameter estimation algorithm on a one-DOF AMB system is then presented. After the comparison of effective and actual stiffness and damping coefficients, the effects of PID controller parameters on the dynamic properties of one-DOF AMB system are illustrated with the experimentally obtained actual stiffness and damping coefficients.

In Chapter 5, parameter estimation algorithms on one-DOF and two-DOF rotor-bearing system model in frequency domain are first introduced, followed by the

description of the specially designed test rig for parameter estimation. Secondly, the experimentally obtained actuator gain and the maximum linear operating range of the HMBs system are presented. Lastly, the experimental results of parameter estimation of the dynamic characteristics of the HMBs system of the axial flow blood pump in both the radial and axial axes in air are reported and discussed.

In Chapter 6, current demodulation methods for self-sensing AMB system are first explained. Digital simulation of the current demodulation for the self-sensing AMB is then presented, after which the method of parameter estimation for self-sensing AMB system is described. The two digital simulation results of the current simulation and self-sensing parameter estimator are compared and the comparison results show the superiority of the self-sensing parameter estimator. Lastly, the design of a printed circuit board (PCB) implementing the self-sensing parameter estimator is introduced, and the results of the static and dynamic calibration of the PCB are reported.

In Chapter 7, conclusions of this dissertation are presented and some specific future work is outlined.

1.8 Original Contributions

In this dissertation, the author introduces the idea that the method of the parameter estimation with statistical analysis can be applied to HMBs of the axial flow blood pump to investigate its dynamic characteristics and demonstrates that this idea is valid by successfully and experimentally obtaining the stiffness and damping coefficients of HMBs of the axial flow blood pump both in radial and axial directions with statistics using the method of parameter estimation. Besides that,

some other original contributions have been achieved in the development of the magnetic levitated axial flow blood pump with possible self-sensing capabilities as shown below:

1. The design of the axial flow blood pump is innovative, compared with two current most typical maglev axial flow blood pumps, Berlin Heart INCOR® and Streamliner [55][58][59], in view of the impeller of the designed pump which is enclosed in the rotor that is driven by the motor and supported by two HMBs: this kind of enclosed impeller can lead to the benefits of better motor efficiency, larger pumping volume, higher structural strength of the blades and ease of manufacturing [26][56][57].
2. The axial flow blood pump with HMBs system is actively levitated in the radial directions, and passively levitated in the axial direction. This design is thus different from the Berlin Heart INCOR® and Streamliner which have active control in the axial direction and passive control in the radial directions. Although passively controlled in the axial direction, this new design has validated the high stability in that direction in the experiment in air. Also in this design, no position probes or controlling coils in the axial direction are required, and therefore no coils will have to be guided out from the impeller or rotor, which may lead to easier coils layout.
3. The stiffness and damping coefficients of HMBs have been obtained experimentally with the method of parameter estimation, which have been proved to be frequency dependent and different from the magnostatic analytical results.
4. In the parameter estimation of the HMBs of the axial flow blood pump, it is also proved experimentally that parameter estimation on the HMBs system

with non-rotating rotor can replace the estimation with rotating rotor, which can greatly facilitate the estimation procedure.

5. Digital simulation of the self-sensing parameter estimator for AMB has been done to establish the feasibility of digital implementation of the self-sensing AMB. From the digital simulation results, it is shown that the digital self-sensing parameter estimator for AMB can achieve even better self-sensing system performance than the analog system does.

Chapter 2 Literature review

In this chapter, the literature of the design of AMB system and motors is reviewed firstly, followed by the introduction of different types of magnetically levitated artificial heart pumps. Secondly, the parameter estimation of the rotor-bearing system is reviewed and the investigation on dynamic characteristics of magnetic bearings is also described. Thirdly, the efforts made to investigate the dynamic characteristics of VADs are reviewed. Lastly, the techniques of position self-sensing of magnetic bearings are introduced, among which the two most popular approaches – current demodulation and parameter estimation – are discussed in detail.

2.1 Design of AMB system and motors

2.1.1 Design of AMB system

Comprehensive descriptions of design of AMB system haven been given by Schweitzer [23] and Maslen [97]. Generally, the design procedure of an AMB system is composed of preliminary analysis, bearing actuator design, control system design, performance simulation and analysis [27].

In the preliminary analysis, it should be ensured that the rigid and flexible modal frequencies are assigned to lie outside the operating speed range or to be sufficiently well damped so that resonance at these speeds does not occur.

The design of the bearing actuator reflects a complex process, where all possible interdependencies of requirements and constrains should be considered. In the bearing stator design, given the estimated requirements for the actuator such as the

load capacity, suitable configurations of the actuator such as pole number, homo-polar or hetero-polar, are selected based on experience. With these parameters known, the rest unknown parameters can be determined through a set of rules [28] [32]. Also during the design process, in order to meet the load requirements and ensure at the same time the actuator dynamic and thermal performance is adequate, some parameters are needed to be determined, including the sizes of the yoke, the return rings, the permanent magnets, as well as the pole dimensions and ampere turns of the control coils. Furthermore, some special factors should be considered sufficiently in the design process, as listed below:

1. Power efficiency. Reducing the power consumption will reduce not only the operational costs, but also the acquisition cost. Reduction of power can not only lead to smaller and therefore cheaper amplifiers and power supplies, but also lessens winding cooling requirement. Parametric and systematic approaches have been developed to optimize the power to weight ratio of magnetic bearings [29] and to achieve minimum power [30]. Also there is a direct minimum power optimization method which can optimize the mathematic model of the electromagnetic actuator [31].
2. Load capacity. Because of the performance limitations of magnetic bearings, magnetic bearing actuators are often designed with large load capacities and slew rates, under the constraints of their geometrical sizes and available power amplifiers.
3. Biasing ratio and peak ratio. Lager biasing ratios increase the linear force range and slew rate of the bearing, but consume more power. The peak ratio is often set to one in the design, but sometimes the bearing can be more compact with a peak ratio less than one for the same load capacity.

In the control system design, position transducers, controller and power amplifiers should be selected or designed to meet the application requirement of the AMB system.

The position transducers should meet fairly stringent requirements of: reliability, high sensitivity, robustness and ease of application. Boehm *et al.* [33] compared three types of sensors and concluded that eddy current probe is the best choice for position sensing due to its wide bandwidth and smaller phase shift error.

Controller is the key point of the AMB system. Quite a few control schemes have been investigated till now such as LQG/LTR [2], H∞ [3], sliding mode [4], adaptive control [5], adaptive feed-forward [6], and PID [7], etc., among which PID control is the most popular one because of its simplicity and good performance. The implementation of controller can be divided into two types: analog and digital controllers. Digital controllers are more widely adopted in AMB systems [34][35], because they have two distinct advantages over analog controller: 1). tuning AMB system can be facilitated without hardware modifications; 2). realizing some control algorithms that are very difficult to be implemented in analog components. The only disadvantage of digital controller is the realization of fast sampling speed required by some high-speed rotating rotors. However, this can be lately realized by the advent of high-speed microprocessors and data acquisition system.

There are mainly two types of amplifiers used for AMB system: linear and PWM amplifiers. Linear amplifiers are easy to implement, and for space applications where small currents are required, linear amplifiers are preferred because of their low noise performances [83]. But the efficiency of linear amplifiers is much lower than that of PWM amplifiers due to the effect of i^2R

losses. For this reason, PWM amplifiers are preferred for high dynamic loads. However PWM amplifiers create more noise and large current ripple because of their switching characteristics. There are mainly two types of PWM amplifiers: 2-state and 3-state PWM amplifiers, which can also be called as half-bridge and full-bridge according to their implementation [84]. Half-bridge is easy to implement, but it has larger current ripple, while full-bridge has faster dynamics and smaller current ripple.

Lastly, with the assistance of some professional software such as Matlab®, Ansys®, or Maxwell®, and based on the modeling equations of the electromagnetic circuits, the simulation and analysis of the designed AMB is carried out and its results are compared with desired performance for the updated design values [36][37].

2.1.2 Design of brushless PM DC motor

The literature about motor design for different applications is quite extensive and because the brushless PM DC motor is most widely used in ventricular assist devices [1][20][55][58], the design of the brushless PM dc is hereby mainly introduced.

The brushless PM DC motor is essentially configured as a permanent magnet rotating past a set of current-carrying conductors. A step-by-step design procedure for a typical brushless PM DC motor as a rough guide can be generalized as follows [38]:

1. Determination of application requirements. The general requirements may include: peak power or torque requirement, maximum speed, supply voltage, etc.

2. Decide which kind of configuration: interior-rotor, exterior-rotor or axial gap.
3. Select number of poles, number of stator slots and phases.
4. Perform rough sizing estimate.
5. Select air gap length and determine magnetic loading.
6. Design rotor and determine flux/pole.
7. Lay out stator lamination dimensions
8. Solve for number of conductors and turns of coil
9. Calculate performance
10. Check temperature rise, current density, flux densities, demagnetization of magnet.
11. Modify design and reiterate until objects are met.

The following literature deals with the design of the brushless PM DC motors, their drive system, and their simulation and analysis.

[39] describes the design and analysis of a high-speed brushless PM DC motor for turbo-compressor. The optimization design criteria of the high-speed motor structure are described by 2-D analytical method with magnetic and mechanical constraints, and their results are validated by finite element analysis (FEA).

In [40], a computer-aided design (CAD) procedure for a radial-flux surface mounted permanent magnet brushless DC motor is presented, where the design variables such air gap flux density, winding factor, magnet fraction, etc., are assumed. The developed CAD program gives the design data and the calculated performances of the motor. But no detailed application example is given to validate the CAD program.

In [41] [42], a fully analytical procedure for the design of brushless PM DC motor combined with a genetic algorithms procedure is proposed, in order to optimize an objective function, such as the motor efficiency, the material costs, or some other motor figures. The proposed optimization technique is based on the completely analytical design procedure consisting of a system of non-linear equations which imposes PM characteristics, motor performance, magnetic stresses and thermal limits.

In [43], the performances of a PM brushless DC motor are calculated and tested using both the circuit method and finite element method provided by RMxprt and Maxwell of Ansoft. The good agreement of simulation results both from the circuit method and finite element method with the experimental results has indicated the validation of the commercial software RMxprt and Maxwell as the useful and convenient design and simulation tool for motor system.

In [44], the structure and design method of an electric drive system for multiphase brushless PM DC motor is proposed. The brushless PM DC motor is simulated by FEA, and the performance of power electronic converters is analyzed and simulated with Matlab/Simulink. From their simulation results, it is shown that the main circuit parameters have high influence on the motor system performance, and therefore they should be optimized by simulation, even by experiments.

2.2 Ventricular assist devices

VADs fall into two main categories: pulsatile and non-pulsatile. Non-pulsatile VADs are a new generation of pumps and mostly used nowadays because of their

advantages: smaller size, less components required and less hemolysis. Non-pulsatile VADs can also be further divided into two categories:

1) Centrifugal blood pumps
2) Axial flow blood pumps

The first pumps used in cardiopulmonary bypass are centrifugal blood pumps where the centrifugal force is produced from the impeller rotation to drag the blood from the inlet port on the top to the outlet on the bottom side. An electric motor is used to rotate the impeller; there are two ways of coupling between the motor and the impeller: the first is the magnetic coupling by means of permanent magnets that are fixed under the impeller or the rotor, and the second is the mechanical coupling by means of a shaft connecting the impeller and the motor. The centrifugal blood pumps have one disadvantage: they are too bulky to be implanted into human bodies and therefore cannot be used in the intra-ventricular implantation. To solve this problem, the axial flow blood pumps were developed accordingly.

In the axial flow blood pump, the impeller, blood inlet port and outlet port are all on the axial axis. The rotation of the impeller produces the axial force to absorb the blood in from the inlet port on one end of the pump and then pump it out from the outlet port on the other end of the pump. The motor drives the impeller with electromagnetic coupling by means of permanent magnets that are embedded on the impeller.

The development process of artificial blood pumps has gone through three generations: the first generation blood pumps belong to the type of pulsatile pumps which was started in the 1970s and have following representation products: CardioWest, Thoratec TCI HeartMate I VAD, the Novacor VAD, the HeartSaver

and the Pierce Lion Heart, to highlight but a few [45][46]. The second-generation blood pumps have the following typical products: the MicroMed DeBakey VAD [47], the Jarvik 2000 FlowMaker [48], and the Nimbus-TCI HeartMate II VAD [49], etc., whose development started in 1995 with the characteristics of blood immersed bearings. The third generation blood pumps, described as rotary pumps with non-contact bearings, include two types: the first one utilizing the magnetic bearings such as Terumo DuraHeart [50], the Berlin Heart INCOR [51], the Heartquest VAD [52]; and the HeartMate III [53], etc; the second one utilizing the hydrodynamic bearing mechanism such as CorAide and VentrAssist VADs [54].

2.3 Some typical MagLev VADs

2.3.1 Berlin Heart INCOR®

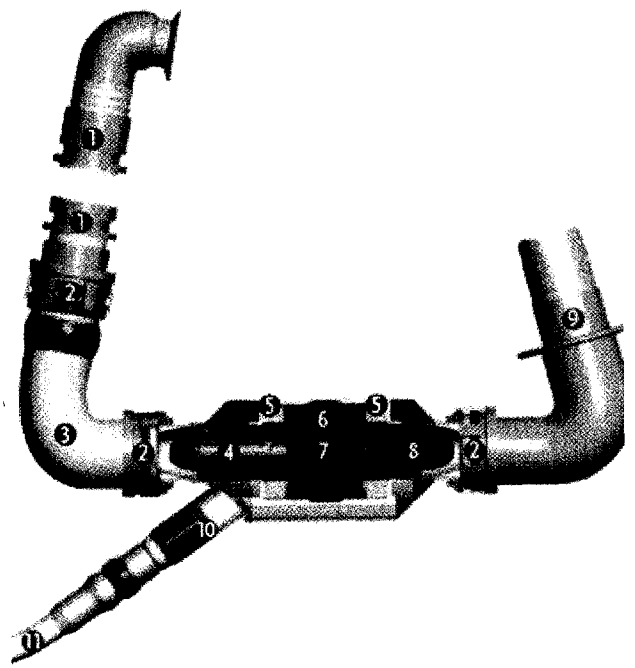

Figure 2.1: Berlin Heart INCOR®

The Berlin Heart INCOR® [55] is an axial flow blood pump whose impeller is completely free of contact with other parts. The scheme of the Berlin Heart INCOR® is shown above. The blood coming from the heart flows into the pump through its Inflow Cannula, and is then guided by the Inflow Guide Vane onto the impeller that has the actual pumping function when it rotates. After that, the Outflow Guide Vane, with some additional pressure, aligns the rotating blood flow which will then flow through the Outflow Cannula to the aorta.

The impeller of the Berlin Heart INCOR® is completely suspended by two magnetic bearings at the two ends of the rotor in the axial direction. Its axial movement is actively controlled with the help of an axial position sensor, and its radial and titling movements are passively controlled. The motor stator drives the impeller in which there is a permanent magnet embedded.

2.3.2 Streamliner axial flow blood pump

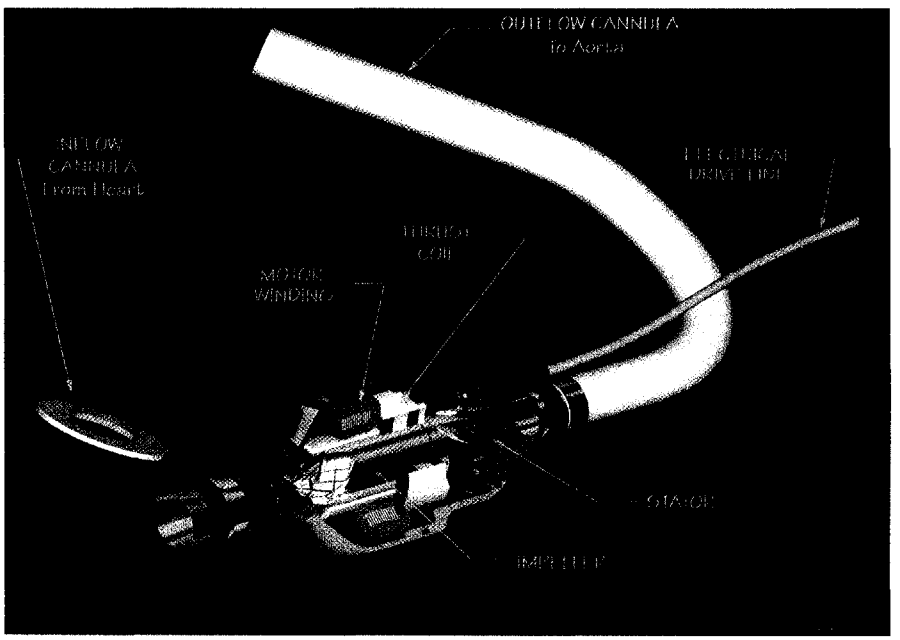

Figure 2.2: Streamliner axial flow blood pump

In the Streamliner axial flow blood pump [58][59], two permanent-magnet bearings provide passive radial support for the impeller which is not only the pumping component, but also serves as the permanent magnet rotor and contains the outer races of the PM bearing, and an active feedback-controlled voice-coil thrust bearings position the impeller in the axial direction.

The stator, the rotor and the pump housing of the Streamliner are all shaped to create streamlined or relatively smooth flow paths for the blood and to prevent relatively sharp surfaces or edges from contacting the blood, which is why it is named "Streamliner".

2.3.3 TMDU/TIT disposable centrifugal blood pump

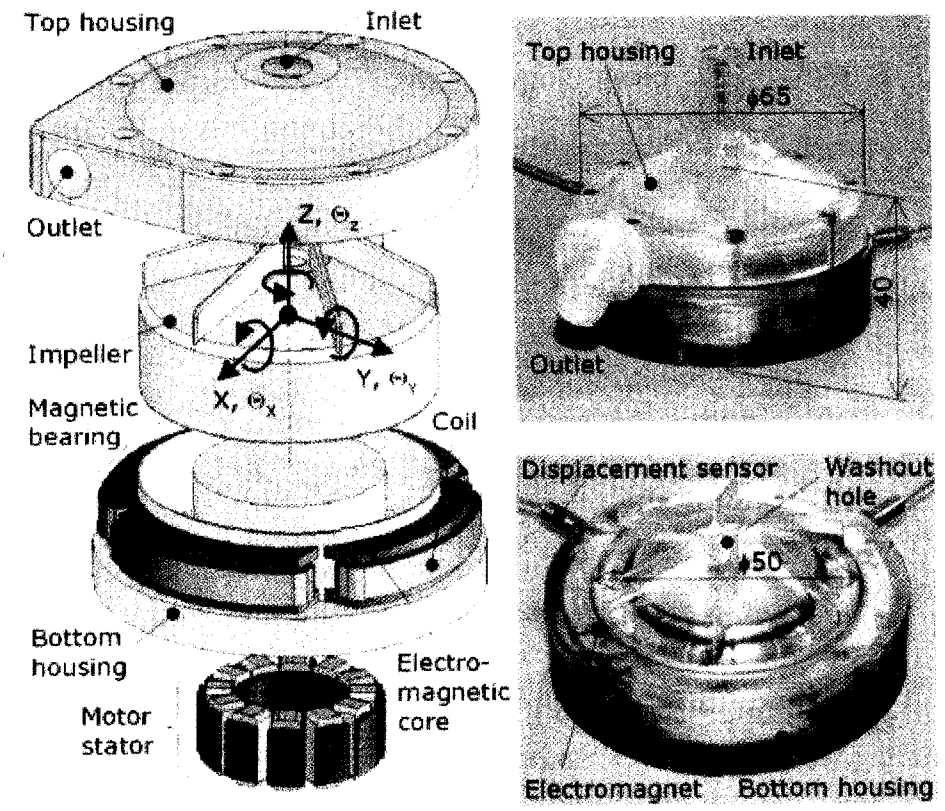

Figure 2.3: TMDU/TIT disposable centrifugal blood pump

The disposable magnetically levitated centrifugal blood pump is developed by the Tokyo Medical and Dental University and the Tokyo Institute of Technology [60][61]. The impeller of the pump is suspended by the radial magnetic bearings with two displacement sensors. The radial motions of the impeller are actively controlled and its axial and titling motions are passively controlled. The impeller is directly driven by an internal brushless direct current motor. The photograph and its explored view of the TMDU/TIT centrifugal blood pump are shown in Figure 2.3.

2.3.4 Thoratec HeartMate III

The Thoratec HeartMate III is a compact implantable centrifugal left ventricular assist device (LVAD) [53]. The magnetically levitated impeller is realized by the radial self-bearing motor that combines the function of magnetic bearings and motor, which makes the pump more compact. The self-bearing motor actively controls the radial axes of the impeller with displacement sensors, and the axial axis is stabilized by the passive magnetic forces. The photograph of the HeartMate® III is shown in Figure 2.4.

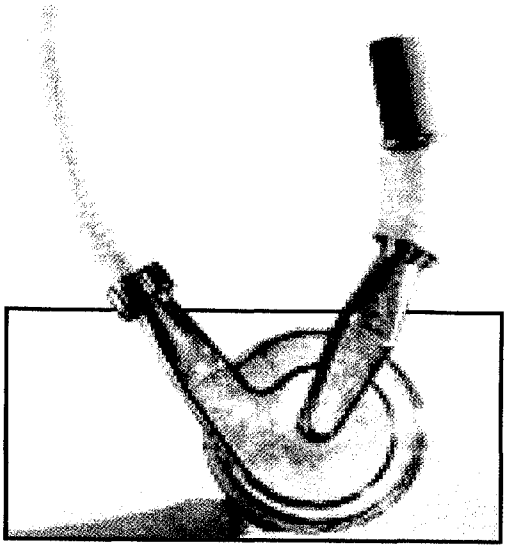

Figure 2.4: Photograph of Thoratec HeartMate III

2.4 Parameter estimation on rotor-bearing system

Firstly, it must be mentioned that if the model structure of a system is known and some of its parameter values are unknown, the problem of system identification is reduced to that of parameter estimation. Many different approaches to the estimation of the dynamic characteristics of rotor-bearing systems have been proposed [62]–[68]. Any technique for estimating bearing characteristics must satisfy certain criteria [62]: firstly, the techniques must be able to be applied in normal operating conditions of the equipment, which implies that the data acquisition time must be very short and secondly, the identification results must have unbiased, minimum variance and consistent estimates.

Morton [63] first thought of a method of applying external excitation force to the rotating shaft for parameter identification of bearings. Later, he modified his device to apply an effective periodic multi-frequency signal directly onto the shaft.

The use of the discrete harmonic excitation to estimating bearing characteristics has been well established [64]. However, it is rather difficult to obtain good

estimates using this method, because the sensitivity of the experimental data with respect to each parameter differs with the excitation frequency. An impact force technique to the frequency response function has been proposed by Nordmann [65] to improve the previous method. Although the impact method can bring better results, it suffers from the problem of a rapidly decaying response in a well-damped system and the difficulty of exactly reproducing the same input disturbance in the following successive test.

Burrows *et al.* [66][67] developed a frequency-domain algorithm for estimating oil-film coefficients by using pseudo random binary sequence (PRBS) multi-frequency test signal and the least-square estimator, which could produce good estimates from noisy data and also filter any unwanted harmonic components in the system measurement. Later, the shaft flexibility was taken into account and a full model was used, and good estimation results were produced, but at the cost of a large measurement task.

Lim *et al.* [68] proposed a modified frequency-domain approach using Schroeder Phased Harmonic Sequences (SPHS) test signal [69]. They reported more accurate estimated bearings coefficients with less computation task by measuring the relative displacement of the rotor and bearing pedestal. The mathematical formulation of SPHS is attached in Appendix A. The advantages of SPHS over other multi-frequency test signals i.e. step, impulse, white noise, Pseudo Random Binary Sequence, etc, can be summarized as follows [8][64][65][76]:

(a). It is a low peak-factor signal and persistently excites all of the system modes without violating the linear operating conditions.

(b). It is periodic and signal averaging is possible to reduce the effect of noise.

(c). It can be synthesized to give arbitrary defined spectrum, including flat spectrum with sharp cut off.

(d). By setting the amplitude of any particular harmonic as zero, that harmonic can be suppressed to prevent exciting certain modes in a given structure.

2.5 Stiffness and damping properties of magnetic bearings

The most important characteristics of a typical conventional bearing are its stiffness and damping properties. Magnetic bearings are actually a special type of bearing with electrical feedback control. To better understand and control magnetic bearings, it is necessary for the stiffness and damping properties of magnetic bearings to be investigated.

Williams *et al.* [73] and Humphris *et al.* [72] proposed the effective stiffness and damping properties of the magnetic bearing system, which is based on the theoretically derived frequency-dependent feedback controller transfer function. The relationship between the stiffness and damping and the control parameters were also presented. Matsumura *et al.* [70] and Aoyama *et al.* [71] also used this theoretical frequency-dependent controller's transfer function to obtain the stiffness and damping coefficients of magnetic bearings in simulation. However, their method of estimating both the stiffness and damping coefficients of magnetic bearings raised a fundamental question of possible time lags in the digital processing, amplifiers, feedback sensors, cross coupling capability and

electromagnet's eddy current and hysteresis losses, etc. in the system [23], which can actually greatly change the dynamic properties of magnetic bearings [77].

Xie *et al.* [74] reported experimental results on the influences of control parameters on the stiffness and damping of magnetic bearings, but only rotor displacements with different controller parameters at different rotating speeds were reported. The actual stiffness and damping coefficients of magnetic bearings, which were important to predict the response of the rotor-bearing system at the design stage [68], were not obtained.

In order to solve the problems above, the method of frequency domain parameter estimation on magnetic bearings with SPHS has been proposed by Lim *et al.* [75][76], to obtain the actual stiffness and damping coefficients of magnetic bearings. The whole AMB system is treated as a black box where all the system elements such as eddy current and hysteresis losses are included, and on-line parameter estimation on the system stiffness and damping coefficients can be realized experimentally.

The rotor stability is the key issue to the performance of VADs, while the rotor stability is relevant to its stiffness and damping: in [78][79], it was found the hemolysis or damage to red blood cells is related to both the clearance size and the rotor stability. Hence, the margin of stability can be calculated by the known stiffness and the damping coefficients of the support bearings. The HMBs system of the axial flow blood pump can be modelled as a typical mass-spring-damper system [81][82], the stiffness and damping of HMBs are two important parameters of the system transfer function and are critical to the rotor stability and therefore their investigation is necessary. The proportional control of PID controller provides the stiffness to the HMBs system, and its derivative control provides the

damping to the system. Integral control is dominant at very low frequencies to offset the system static error. Furthermore, the system stiffness and damping are also affected by system lags due to digital signal processing, amplifiers, feedback sensors, etc., and cross-coupling capabilities and actuator losses.

Baloh *et al.* [80] used the method of transfer function estimation based on modal decomposition to identify the actuator stiffness and fluid damping of CFVAD3, a centrifugal pump with its impeller entirely supported by magnetic bearings. Their system modal decomposition was tested to be working, and therefore the system with 5-DOF could be considered to be 5 separately parallel plants of identical forms. By means of measuring transfer functions experimentally and then fitting those data into the corresponding differential equations that describe the measured system, the unknown parameters in the transfer function can be obtained. Their method is dependent on the quality of system modal decomposition, and also on the accuracy of the differential equations that describe the corresponding system. The actuator gain's parameter in their plant model could not be determined satisfactorily. Except for the initial estimates of the actuator stiffness and damping, no further detailed experimental results were reported using this method, and there were no statistics provided to validate the experimental results.

Asama *et al.* [81] used a sinusoidal excitation method to investigate system dynamic characteristics in the axial and tilt direction of the Maglev centrifugal blood pump. The system in the axial direction is modelled as a one-DOF spring-mass-damper system. By measuring the frequency response to the excitation of the pump housing and then comparing the measured results with numerically simulated values, the dynamic characteristics of the Maglev impeller in the axial and tilt directions were analysed both in air and in water. However, although the

system frequency responses in the axial and tilt directions were reported, the detailed values of the system stiffness and damping coefficients were not obtained, and statistics were not provided to support their results. Furthermore, with their methods the system dynamic characteristics in radial axes could not be estimated.

Chung *et al.* [82] used the logarithmic decrement method to determine the dynamic characteristics of the VentrAssist implantable rotary blood pump, which is a centrifugal VAD whose impeller is completely suspended purely by hydrodynamic bearings. The pump was mounted on a suspension system with some additional springs. By applying a vertical impulsive force to the pump via the impact frame mounted on top of the pump, the corresponding axial displacement was measured. From the measured input and output data, the logarithmic method was utilized to obtain the system stiffness and damping coefficients. No statistics were provided for the experimental results and the system stiffness and damping coefficients in the radial directions could not be obtained with their method.

2.6 Approaches of self-sensing magnetic bearings

The efforts in investigating the self-sensing magnetic bearings can be divided into two categories: the modulation type and the observer type. For the modulation type, the coil current signal contains the air gap information, which modulates the switching waveform created by the PWM amplifier, and therefore the modulation type is also known as current demodulation. The air gap between the suspended object and the stator can be estimated by processing the modulated coil current. In the modulation type, the bearing air gap is treated as a time-varying parameter of the combination of the magnetic bearing and amplifier that is isolated from the

supported object. In the observer type, the magnetic bearing and the supported object are treated as a whole where the state-space equations are used to describe the system and the air gap is one of those states.

2.6.1 Current demodulation

Okada *et al.* [85] and Ueno *et al.* [86] utilized a demodulation technique to extract air gap information from the switching current waveform. Since the air gap length modulates the amplitude of the current switching waveform driven by the PWM amplifier, the switching frequency component of the current is the direct information of air gap length. The bearing coils are driven by bi-state switching voltages that are switched between +Vs and –Vs according to PWM signals. A signal conditioning circuit, including a high pass filter, a rectifier, and a low pass filter connected in this manner respectively, is used to obtain the amplitude of the switching frequency component of the current signal. The output of the demodulation filter is the function of the air gap length and the duty cycle of the PWM amplifier. The method is also known as switching noise demodulation because of the switching noise containing the position information.

Researchers [83][84][87][88][89] also successfully employed the current demodulation method with the demodulation filter to obtain the air gap length information. Particularly, [83][84][89] used the high frequency signal injection method to create the high-frequency coil current. In [83], linear amplifiers are used to drive the magnetic bearings, but the efficiency of linear amplifier can be very low [97]. In [84][89], the PWM amplifiers are used, but the problem of force feed-through still exists in their approaches.

Based on the current demodulation method described above, Maslen, Noh, and Montie [21][22] creatively proposed a parameter estimation technique for self-

sensing AMB. On one hand, the demodulation filter is used to obtain the amplitude of the switching component of the current signal; on the other hand, the magnetic bearing inductance is simulated real time with the inputs of the actual amplifier output voltage and the estimated air gap length. The amplitude of simulated current is compared with that of the actual current and the error between the two is processed by a PI convergence controller to update the estimated air gap. Using the method of parameter estimation, the influence of the duty cycle of the PWM amplifier on the self-sensing results can be greatly reduced. Their research parameter estimation technique is implemented using analog circuits, and experimental results show that self-sensing parameter estimator can achieve better system performance and wider system bandwidth.

2.6.2 State-space observer

Other research works by [90]–[95] used linear state-space observers to estimate the gap displacement. The magnetic bearings are treated as a two-port system with the coil voltage of the magnetic bearings as system input and the coil current as system output, and the linearised state-space equation describing the system is shown to be observable and controllable in the sense of control theory, allowing a magnetic bearing to be stabilized with a simple linear controller using current measurement alone. However, like what Morse *et al.* [96] has pointed out, the linear observer approach has the drawbacks of poor robustness and poor disturbance rejection. Small parameter variations in the physical system may produce system instability. If switching amplifiers are used in this system, high frequency switching noise will deteriorate the estimator performance. Due to these drawbacks, approaches like linear observer are useful only for designing simple and low-performance self-sensing systems [21].

Chapter 3 The development of hybrid magnetic bearings system for axial flow blood pump

In this chapter, the design and development of hybrid magnetic bearings (HMBs) system for axial flow blood pump are introduced. Firstly, the design of the axial blood pump is introduced. Secondly, the design and development of the HMBs and the Lorentz-typed three-phase brushless and sensorless PM motor are presented, following which the control methods of the HMBs and the Lorentz-typed three-phase PM motor are described. Lastly, the performance of the HMBs system is presented, and the small displacements of the levitated rotor in the x-, y- and z-directions both at stationary and at the maximum rotational speed of 14,000 rpm prove the stability and reliability of the HMBs system of the axial flow blood pump.

3.1 Design of axial flow blood pump

3.1.1 Overall design of axial flow blood pump

The cross sectional view of the axial flow blood pump is shown in Figure 3.1. The key feature of the pump design is that the impeller is enclosed in the rotor which is driven by the motor and supported by two HMBs without mechanical contact. This kind of enclosed impeller can lead to the benefits of better motor efficiency, larger pumping volume, higher structural strength of the blades and ease of manufacturing. The blood flow is in the axial direction with respect to the inlet and the outlet cannulae, that is, passing through the straightener that guides the blood

flow, the impeller that pumps the blood when it rotates and the diffuser that aligns the rotating blood flow to the outlet.

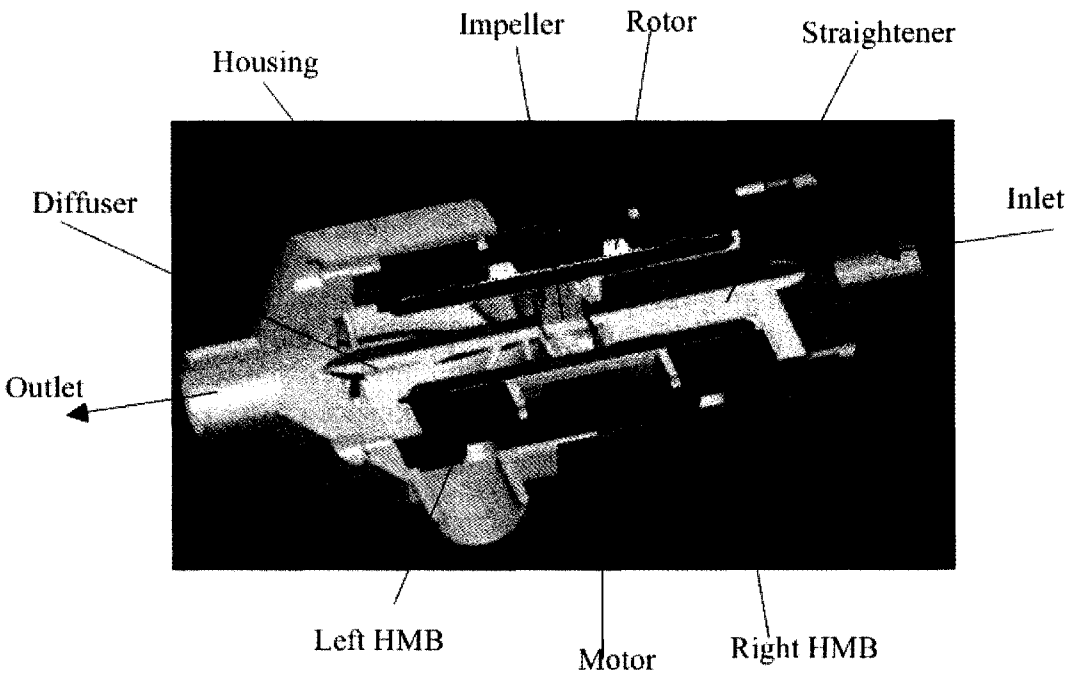

Figure 3.1: Cross section view of axial flow blood pump

To facilitate the understanding on the physical connection between the straightener, impeller, diffuser, rotor and the pump casing assembly, the schematic view of the parts is shown in Figure 3.2, from which it can be seen that the straightener and the diffuser, which are fixed to the pump housing, protrude into the rotor without physical contact with the rotor and the impeller, whilst the impeller is shrunk-fit into the bore of the rotor at its middle position. Therefore the rotor is rotating with the impeller as one entity, while the straightener and the diffuser are at static with the pump casing assembly.

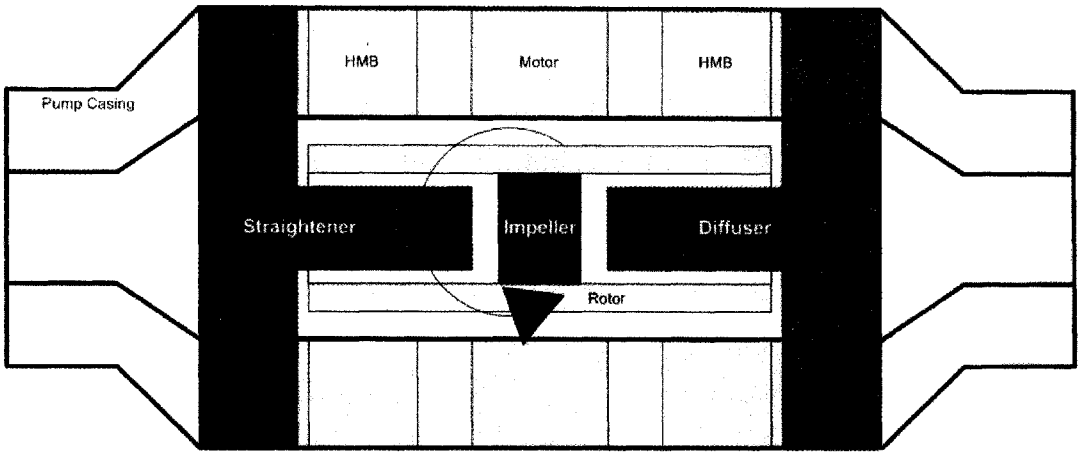

Figure 3.2: Schematic view of the straightener, impeller, diffuser and the rotor

The axial flow blood pump is compact and its main dimensions are shown in Figure 3.3, from which it can be seen that the pump is intra-ventricular implantable. The scheme of the HMBs system is also shown in Figure 3.3. The left and right HMBs support the two ends of the rotor and the motor drives the rotor in the middle. Figure 3.3 also shows the x, y, z directions with relations to the pump: z is the axial direction; the direction of the fluid flow; x and y are the radial directions, the directions that are perpendicular to the fluid flow direction.

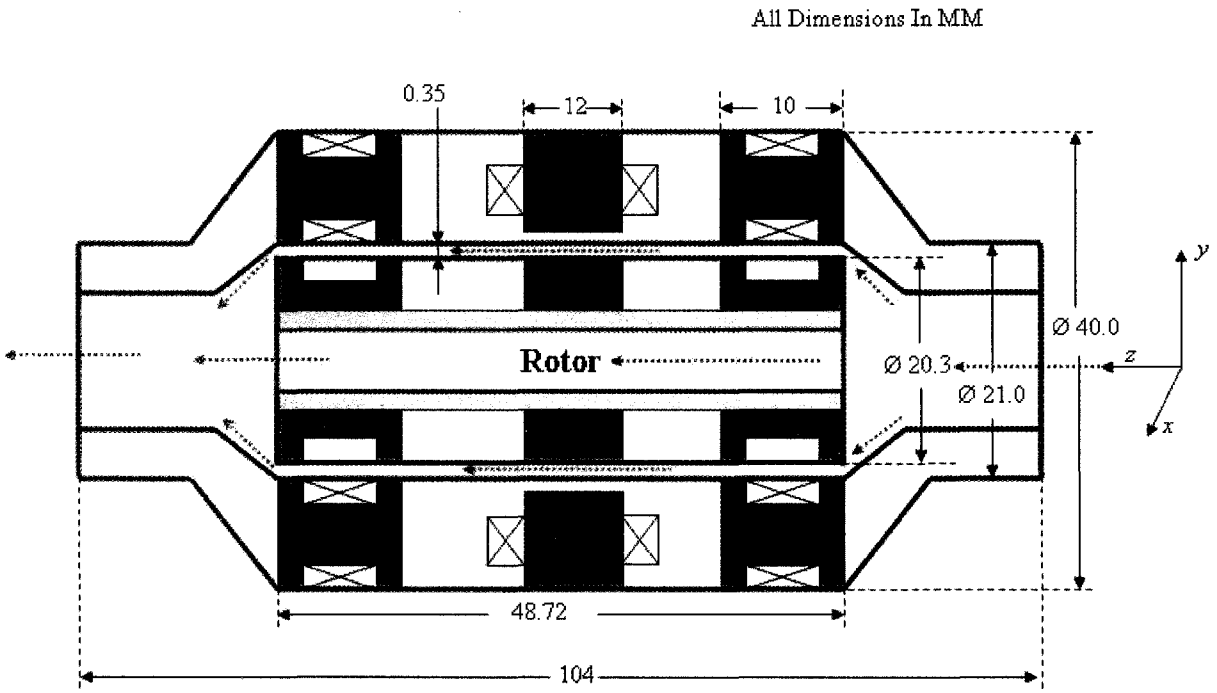

Figure 3.3: Scheme of the axial flow blood pump with main dimensions

Figure 3.4 below shows the photograph of the fabricated pump casing with nipples for connections to both the inlet and outlet cannulae.

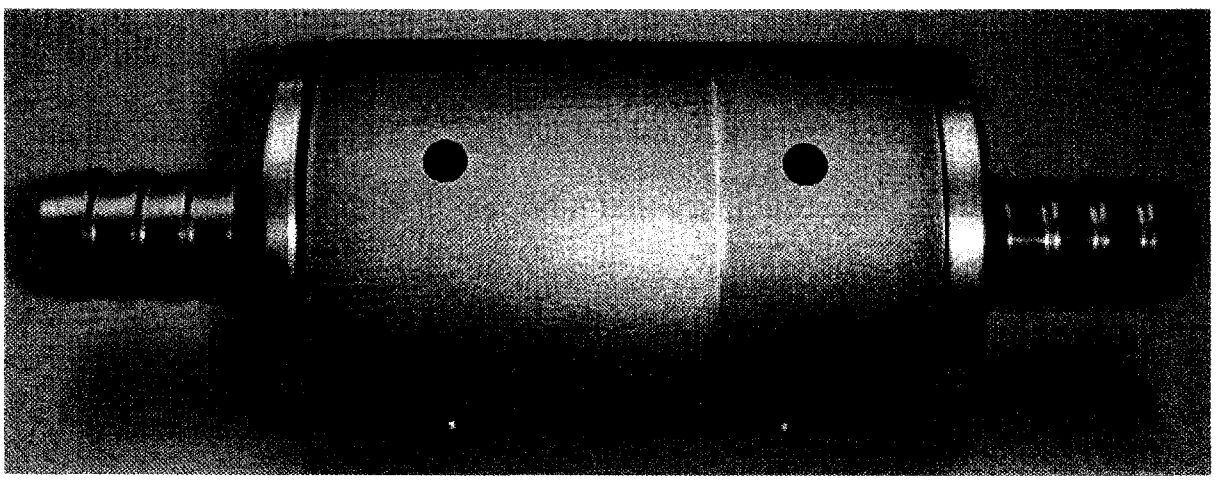

Figure 3.4: Photograph of the fabricated pump casing

3.1.2 Enclosed-impeller

Current axial flow blood pumps use permanent magnets inserted either in the central hub or in the impeller blades. However both methods require compromised considerations. Insertion of the permanent magnets (PMs) in the central hub requires a larger hub to locate the permanent magnets close to the motor windings for obvious electromagnetic coupling reasons; but a small hub is preferred as it can increase the volume of pumped blood. Insertion of the permanent magnets in the impeller blades also yields a compromise since the geometry of the blades must be curved for pumping efficiency. As a consequence, some of the embedded magnets move further away from the winding as the blade is curving.

In the proposed design, an enclosed-impeller is developed to eliminate the above drawbacks. The impeller comprises a set of blades enclosed in a casing. Elongated permanent magnets are inserted axially in the casing. Therefore, the blades of impeller can be fully designed according to pump optimal requirement and the permanent magnets are closer to the winding coils. Therefore, the blood pump can provide both a better electromagnetic coupling between the winding and the permanent magnets and larger pumping volume. The other advantage is that it is easy to manufacture.

3.1.3 Design of pump impeller, straightener and diffuser

3.1.3.1 Straightener

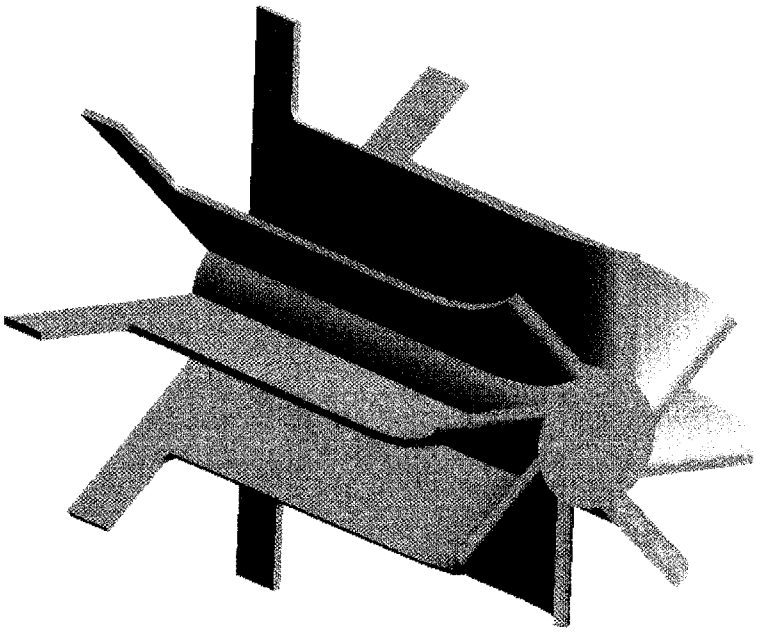

Figure 3.5: Straightener

As shown in Figure 3.5, the straightener is used to straighten the blood flow before it is pumped back into the aorta.

3.1.3.2 Impeller

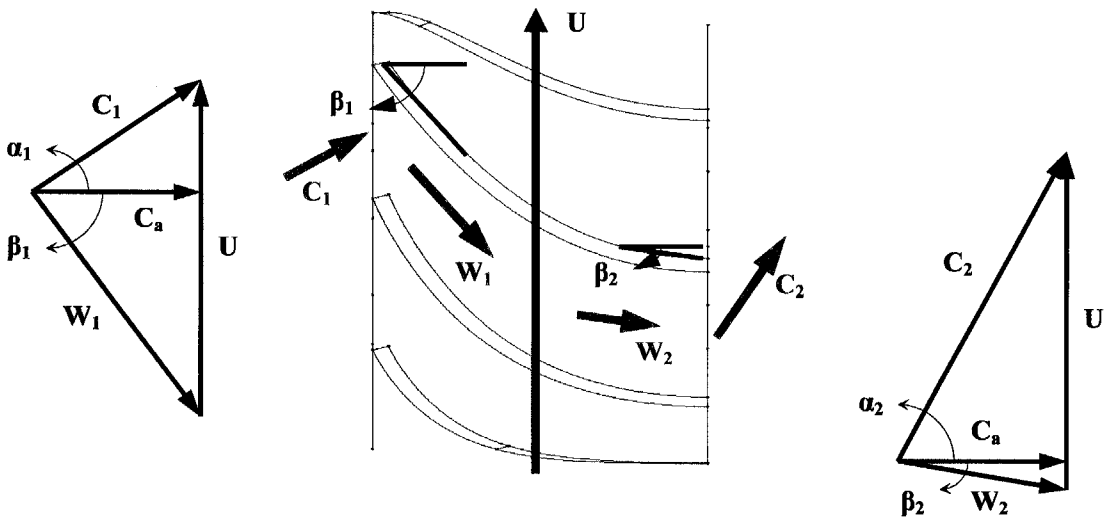

Figure 3.6: Two-dimensional analysis of the impeller

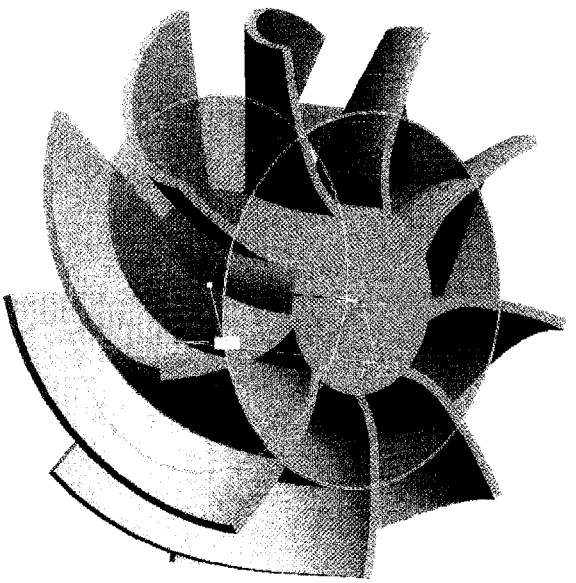

Figure 3.7: Blade geometry of the impeller

The performance of the axial blood pump lies with the design of the impeller. The simplest approach to the study of the axial flow pump is to assume that the flow conditions prevailing at the mean radius fully represent the flow at all other radii. Another assumption is that the fluid will flow along the blade. The two-dimension analysis of the impeller is shown in Figure 3.6, and the blade geometry of the impeller is shown in Figure 3.7. The assembled velocity diagram is shown in Figure 3.8.

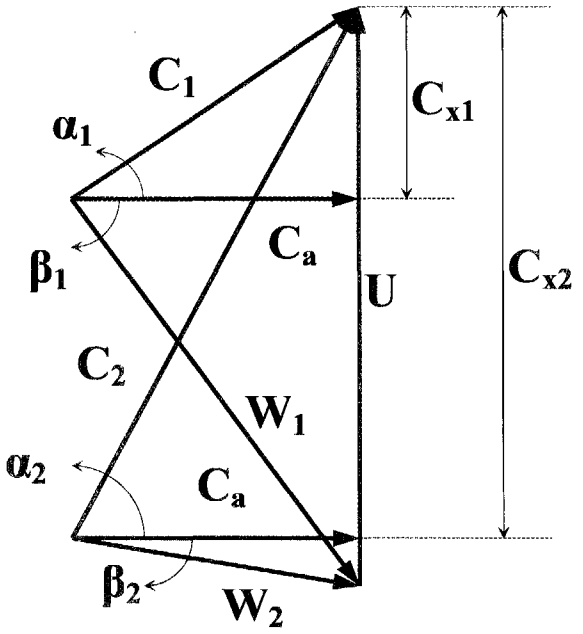

Figure 3.8: Assembled velocity diagram of impeller

Performance Requirement

Pressure P = 100mmHg = 133.32Pa

Flow rate Q = 5L/min

Dimension Constraints

Outlet blade angle β_2 = 0°

Length L_r = 6 mm

Radius of blade hub r_h = 2.5mm

Radius of blade tip r_t = 7.4mm

The flow rate Q is

$Q = 5L/\min$

$= 8.333 \times 10^{-3} m^3/s$

Therefore, the axial flow velocity C_a is

$$C_a = 1.2 \times \frac{Q}{\pi\left(r_t^2 - r_h^2\right)}$$

$$= 1.2 \times \frac{8.333 \times 10^{-5}}{\pi\left(7.4^2 - 2.5^2\right) \times 10^{-6}}$$

$$= 0.656 m/s$$

where, considering the thickness of the blades, a value factor of 1.2 has been taken into account.

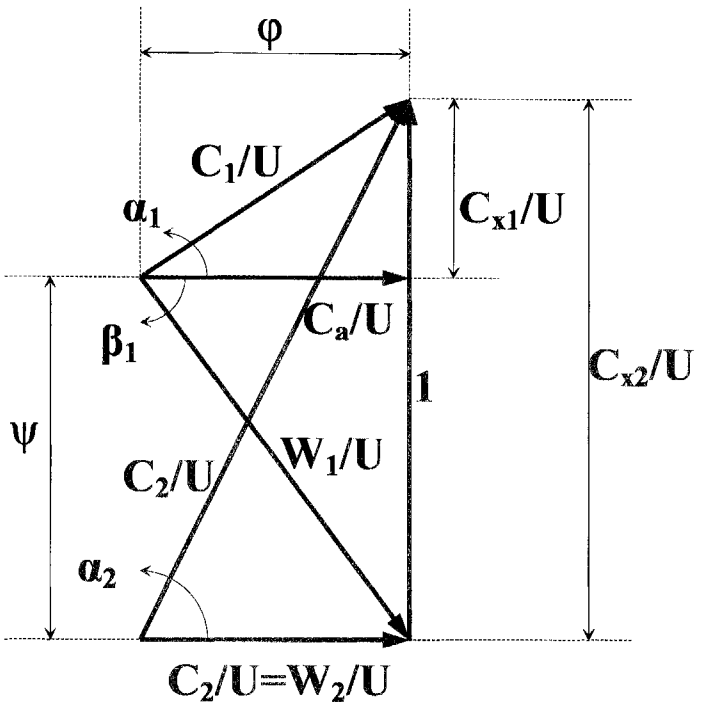

Figure 3.9: Final assembled diagram of impeller

The final assembled diagram of impeller is shown in Figure 3.9, where we define two dimensionless coefficients, the flow coefficient ϕ and the blade loading coefficient ψ

$$\phi = \frac{C_a}{U}$$

$$\psi = \frac{\Delta P}{\rho U^2}$$

From the Figure 3.9, using simple trigonometry, we can obtain:

$$\tan\alpha_1 = \frac{1-\psi}{\phi}$$

$$\tan\beta_1 = \frac{\psi}{\phi}$$

$$\tan\alpha_2 = \frac{1}{\phi}$$

If the height of the blade h is measured from the hub to the tip of the blade, then

$$2h = D_t - d_h$$

$$h = \frac{D_t - d_h}{2}$$

$$= \frac{14.8-5}{2}$$

$$= 4.9mm$$

where D_t is the diameter of the blade tips circumference and d_h is the hub diameter.

If the thickness of the blade t is assumed to be 0.5mm, then the number of blades n_r:

$$(h+t)n_r = \pi D_t$$

$$n_r = \frac{\pi D_t}{(h+t)}$$

$$= \frac{\pi(14.8)}{(4.9+0.5)}$$

$$\approx 9blades$$

3.1.3.3 Diffuser

In order to improve pumping efficiency, a diffuser is required to restore the flow at outlet to the axial direction. The function of the diffuser is to convert the dynamic pressure into static pressure.

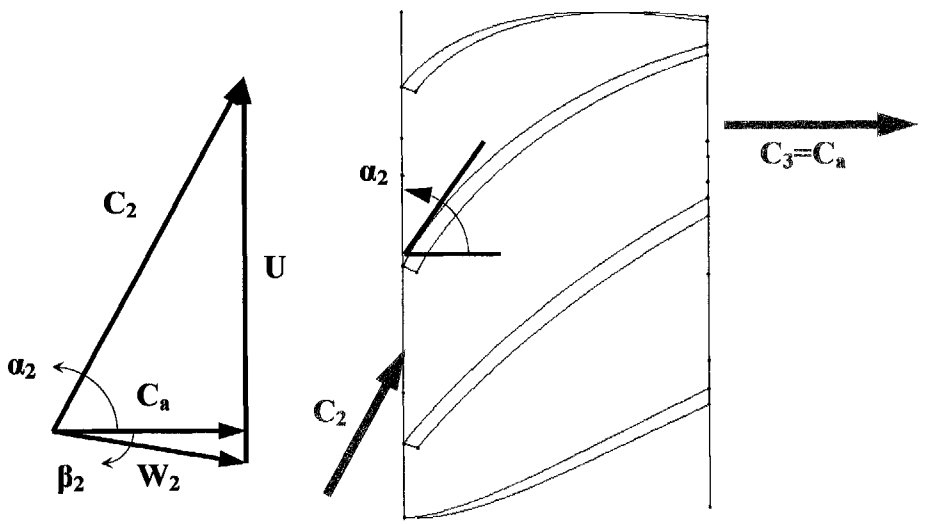

Figure 3.10: Two-dimensional analysis of the diffuser

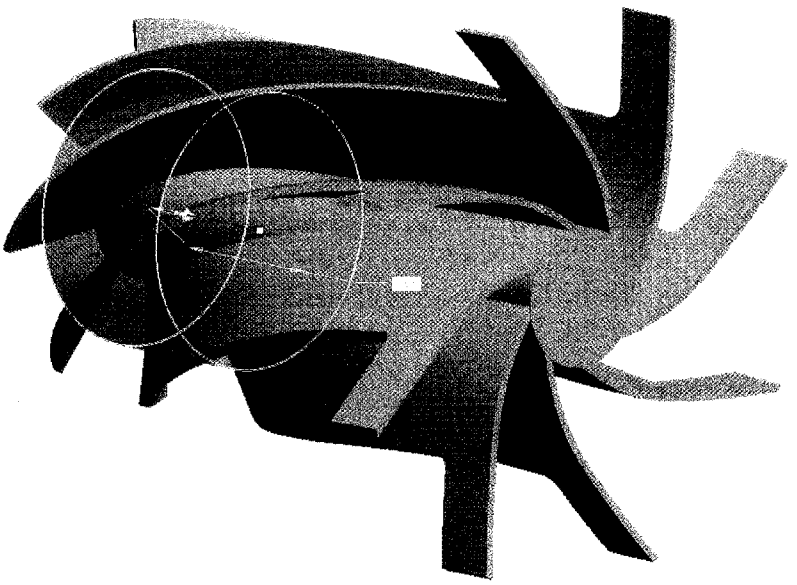

Figure 3.11: Blade geometry of the diffuser

Dimension Constraints

Outlet blade angle $\alpha_3 = 0°$

Length $L_s = 21.5\text{mm}$

Radius of blade hub $r_h = 2.5$ mm

Radius of blade tip $r_t = 6.86$ mm

Number of Blades

$$n_s = n_r - 1$$

$$= 9 - 1$$

$$= 8$$

3.1.3.4 Optimization

Using the Excel's Solver, the optimum blades angles can be found.

Table 3.1: Design optimization results of impeller, straightener and diffuser

CONSTANTS

DENSITY OF BLOOD	ρ	1003.00	kg/m^3
ROTOR RADIUS TIP	r_t	0.00740 7.40	m mm
FLOW RATE	Q	5.0 0.0000833	L/min m^3/s
THICKNESS OF BLADE	t	0.00050 0.50	m mm
IMPELLER RADIUS HUB	r_h	0.00250 2.50	m mm

PRIMARY VARIABLES

ROTOR INLET BLADE ANGLE	β_1	77.0	
STATOR INLET BLADE ANGLE	α_2	82.0	
NUMBER OF IMPELLER BLADES	n_r	9	blades
NUMBER OF STRAIGHTENER BLADES	n_s	8	blades
NUMBER OF DIFFUSER BLADES	n_s	8	blades

SECONDARY VARIABLES

STRAIGHTENER OUTLET BLADE ANGLE	α_1	70.24	
AXIAL VELOCITY	C_a	0.656	m/s
BLADE VELOCITY	U	4.669	m/s
ROTATION	ω	943.22 9007.05	rad/s RPM

COEFFICIENTS

FLOW COEFFICIENT	ϕ	0.141	
BLADE LOADING COEFFICIENT	ψ	0.61	

OBJECTIVE

OUTLET PRESSURE	ΔP	13309.8 99.82	Pa mmHg

3.2 Fabrication of the straightener, impeller and diffuser

The impeller, diffuser and straightener are made of stainless steel 316L, and machined by EDM (electrical discharge machining) and 5-axis CNC machine. Figure 3.12 shows the photograph of the fabricated impeller, diffuser and straightener of the axial blood pump.

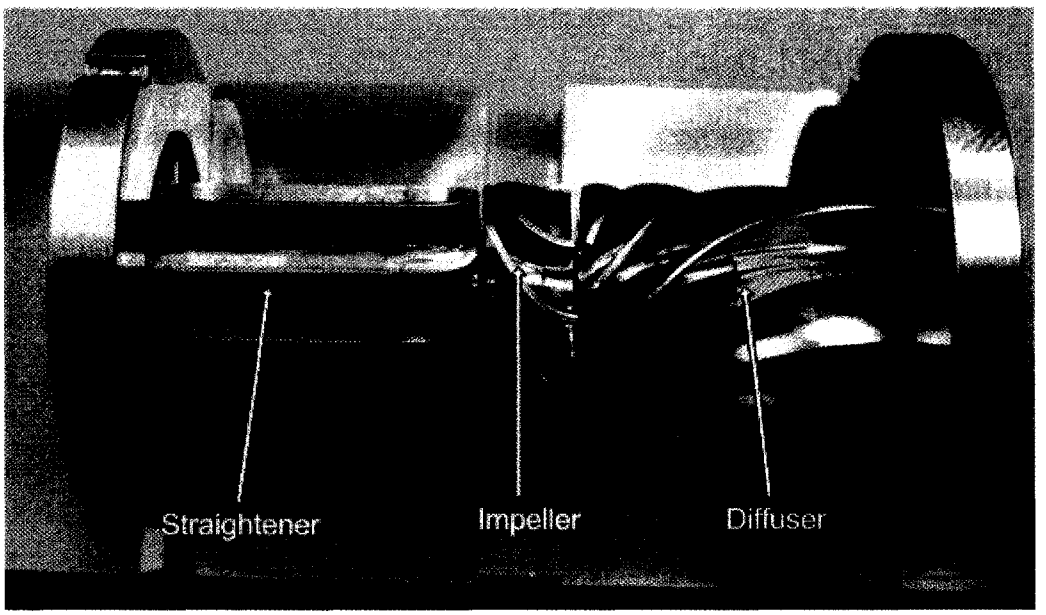

Figure 3.12: Photograph of the fabricated impeller, diffuser and straightener

To reduce possible fluid impulses acting on the impeller in the axial direction, the straightener, impeller and diffuser are constructed with 8 blades, 9 blades, and 8 blades respectively. The Pro/E drawings of the straightener, impeller and diffuser are attached in the Appendix B.

3.2.1 The straightener

For ease of machining, the two parts of the straightener are machined separately before being assembled together with a counter bore screw at the hub. The coned head is used to prevent a dramatic change flow speed in the blood pump. The explored view of the straightener is shown below.

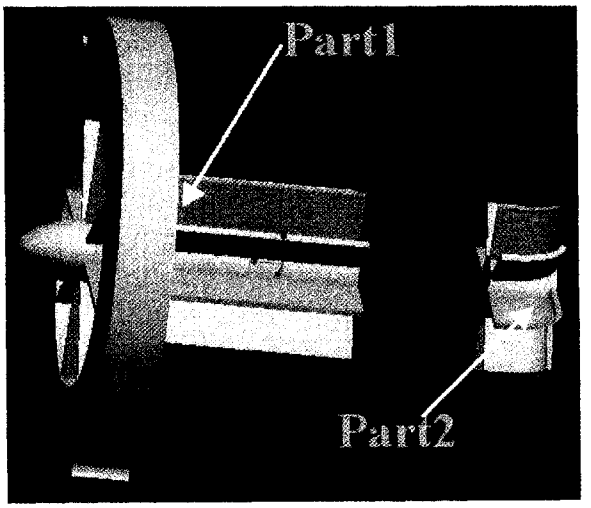

Figure 3.13: Exploded view of the straightener

3.2.2 The impeller

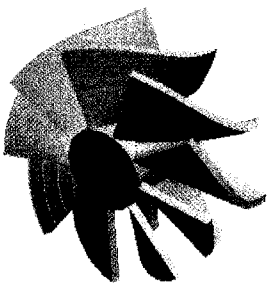

Figure 3.14: Assembly of the impeller

Because the blade angle of the impeller is too large to machine, the impeller is also dissembled into three parts for machining, and the three parts are then assembled together with a countersunk screw at the hub. Figure 3.14 shows the assembly model of the impeller. The photograph of the fabricated three parts of the impeller is shown in Figure 3.15.

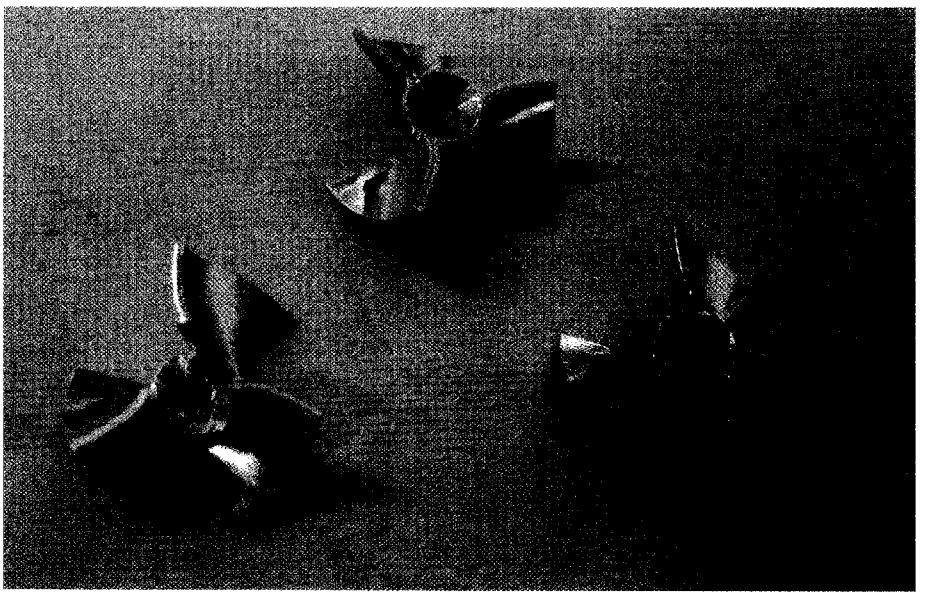

Figure 3.15: Photograph of the dissembled impeller

The impeller is fabricated with a slightly bigger blade tip radius than designed. It will be contracted later with the use of dry ice before being fit in the bore of the rotor. Once expanded in room temperature, it will be firmly stuck inside the rotor.

3.2.3 The diffuser

Similar to the straightener, the two parts of the diffuser are machined separately before being assembled together with a counter bore screw at the hub. The exploded view of the diffuser is shown in Figure 3.16.

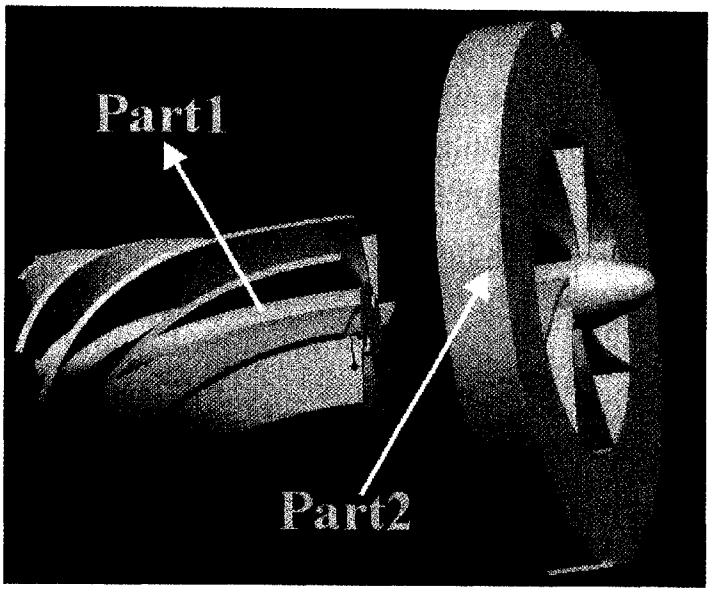

Figure 3.16: Exploded view of the diffuser

As screws are used to assemble the parts of the straightener, impeller and diffuser, it is inevitable that there will be some small gaps between the assembled parts and the screws. Araldite adhesive is used to fill in those gaps, which can also make the assembly stronger.

3.2.4 5-axis machining and SolidCAM®

As shown in Figure 3.17, 5-axis machining means '3+2' machining, that is, using a 5-axis machining to orientate the component into a particular angle in order to make the subsequent 3-axis machining operation more efficient. Simultaneous 5-axis machining is different altogether and brings to the right application; a host of benefits including reduced cycle times, better surface finish, lower consumable cost, as well as facilitating the machining of jobs that is sometimes quite impossible by other means.

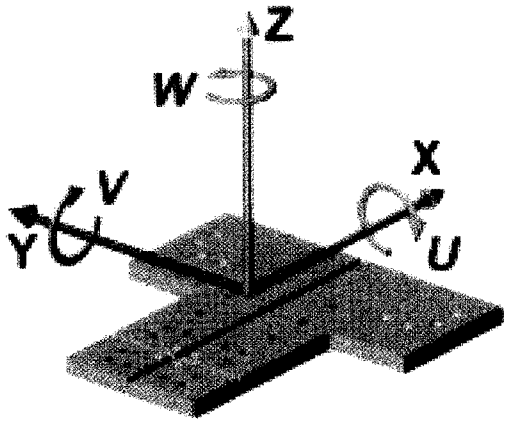

Figure 3.17: 5-axis precision machining

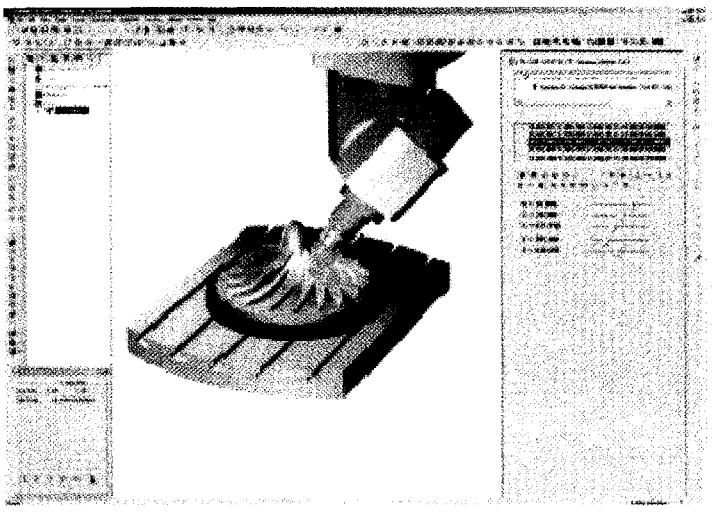

Figure 3.18: SolidCAM®

SolidCAM® is an efficient and profitable CNC-Programming inside SolidWorks®. It provides seamless single-window integration and full associability with the SolidWorks® design model. It utilizes all the advantages of simultaneous 5-axis machining and together with collision control and machine simulation, provides a solid base for the 5-axis solution. Intelligent and powerful 5-axis machining strategies, including swirling and trimming, enable the use of SolidCAM® for the machining of complex geometry parts including the blades of a

pump. All of the axial blood pump blades are machined using 5-axis machining with the aid of SolidCAM®. Figure 3.18 shows the user interface of SolidCAM®.

3.3 Development of the HMBs, the rotor and the Lorentz-typed motor

3.3.1 Design of the HMBs

In order to avoid the use of thrust bearings and make the axial flow blood pump more compact, while at the same time providing strong enough control force in the axial direction, the homopolar HMBs are utilized: an axially polarized permanent magnet is sandwiched in the rotor between the two set of lamination rings to provide the bias flux for the magnetic bearings; meanwhile the radial directions of the HMBs will be actively controlled and the axial direction will be passively controlled.

The scheme of flux flow in HMB is shown in Figure 3.19. The cross section view of the stator is like "H" shape, so that the coils can be wound around the L2 as shown in Figure 3.19. The PM provides the bias magnetic flux which starts from its north pole, passes the left lamination ring on the rotor, then passes the air gap, then flows along the lamination rings: L1, L2 and L3, after that it returns back from the air gap to the right lamination ring on the rotor, and at last it returns to the south pole to close the flux loop. Besides the primary magnetic field in the working air gap provided by the PM, the electromagnetic coils will also generate magnetic field that add to or subtract from the PM field. The net result of this approach to designing magnetic bearings is lower power consumption for the same load capacity or the same stiffness.

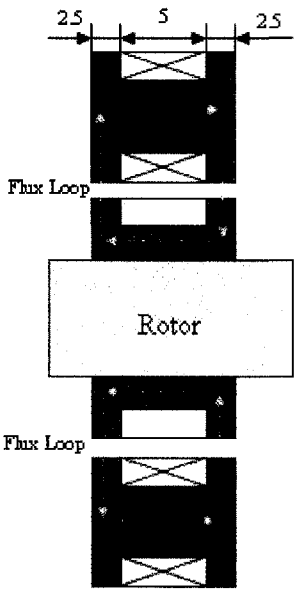

Figure 3.19: Scheme of flux flow in HMB

3.3.1.1 Flux flow of the HMBs

FEA simulation of the designed HMBs using the software of Maxwell 2D has been done to visualize and confirm the magnetic flux of the designed HMBs as drawin in Figure 3.19.

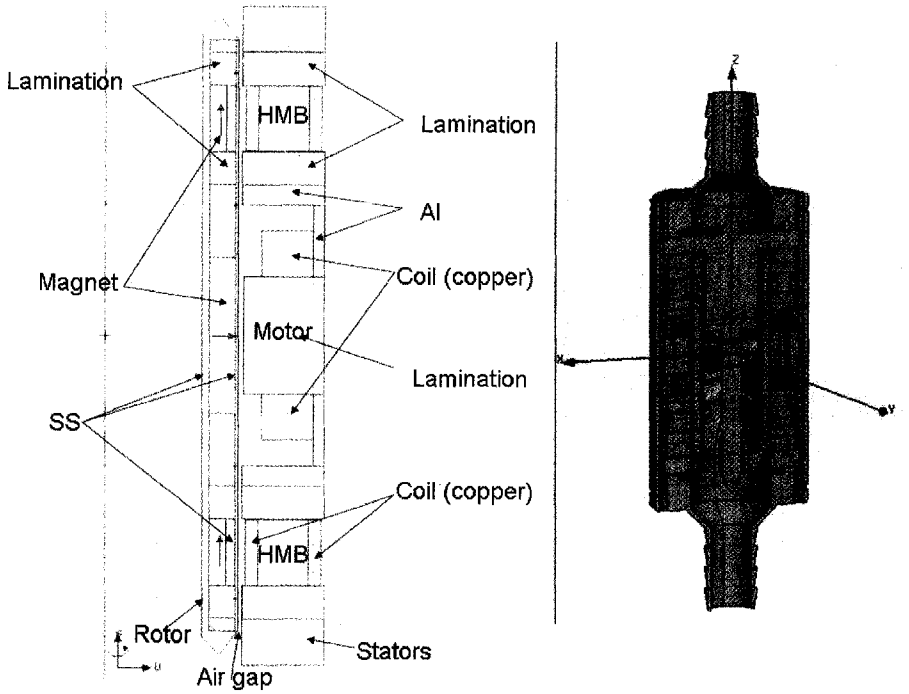

Figure 3.20: 2D model of the axial flow blood pump in Maxwell 2D

Figure 3.20 shows the 2D model of the axial flow blood pump with the HMBs in Maxwell 2D, where all the components of the pump including: rotor, impeller, diffuser, straightener, motor, HMBs, spacers and the pump housing, pump nipples, etc., are all modelled with part materials labelled. Figure 3.21 shows the simulation results of the magnetic flux around the components of the axial flow blood pump, and the enlarged view of flux loop of the HMB is shown in Figure 3.22, where it can be seen that the magnetic flux loop is exactly what we expects during the design.

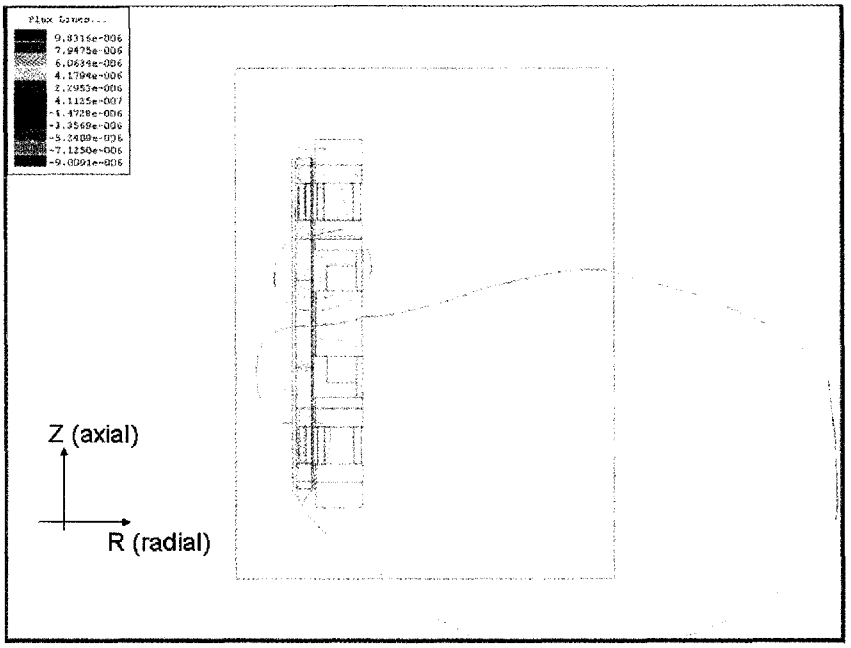

Figure 3.21: Simulation result of magnetic flux of the HMB by Maxwell 2D

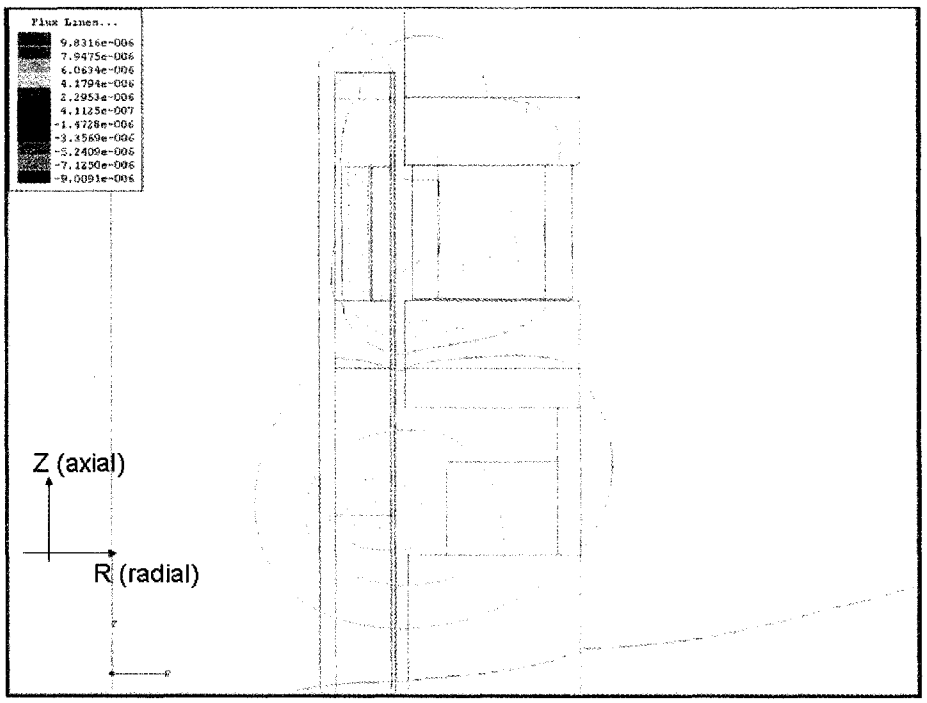

Figure 3.22: Enlarged part of flux loop of HMB in Maxwell 2D

3.3.1.2 Dimensions of the HMBs

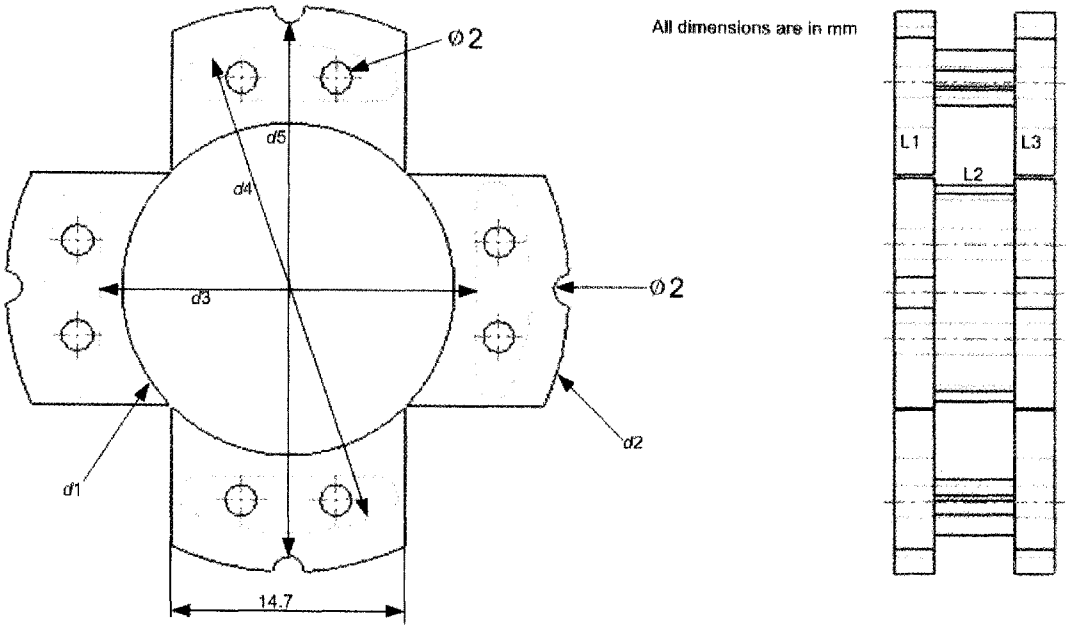

Figure 3.23: Configuration of the HMB

The configuration of the HMB is shown in Figure 3.23, where it can be seen that the HMB is not a round one, but composed of four stacks of lamination stators in four positions: up, down, left and right, in order to make room for the lamination fixture where eddy current probes are fixed. Here we set the width of the lamination stack as 14.7 mm, by which in Pro/E modeling environment, we can make sure that there is enough room for the eddy current probes to be fixed in the lamination holder, whose model is shown in Figure 3.24.

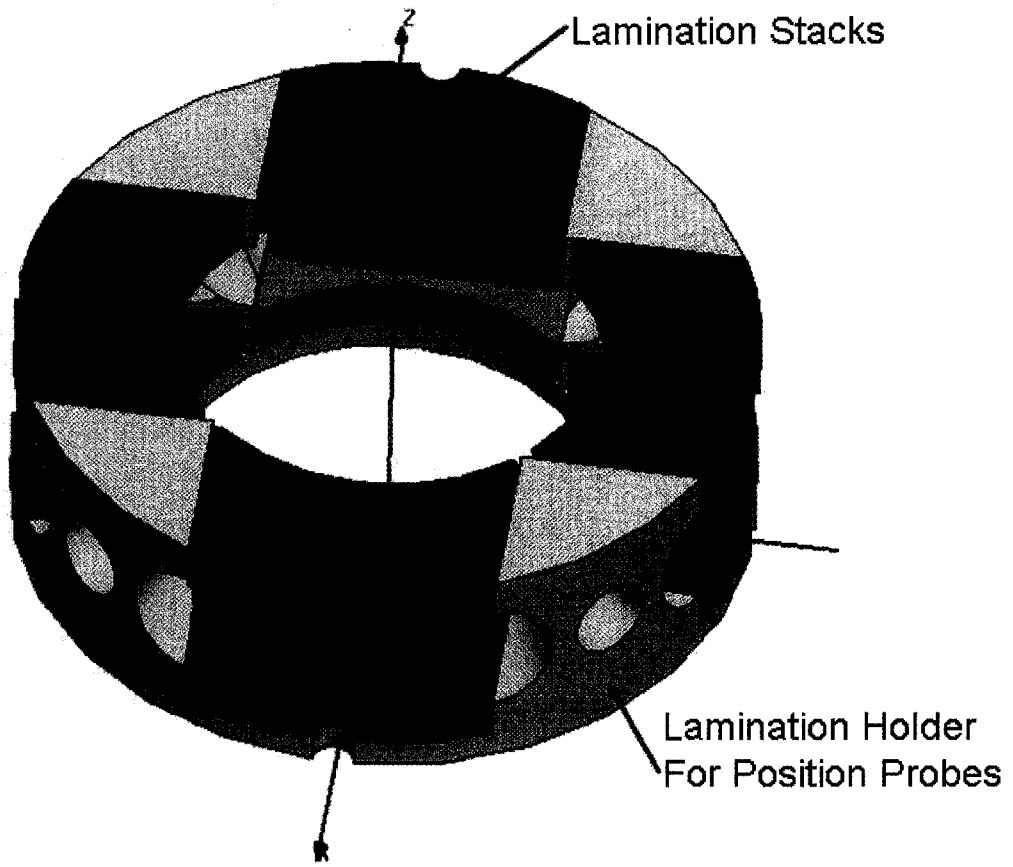

Figure 3.24: HMB Stator with lamination holder for position probes

As shown in Figure 3.23, the middle lamination set L2 is at the center of the L1 or L3. There is a design compromise: the area of the L2 should be as large as possible so that it has minimum magnetic reluctance, while at the same time there should be enough room for the coils wound around the L2 to generate enough electromagnetic forces. There are Ø2 mm holes on the outer circumferences and the center of the laminations for tightening purpose. Based on the configuration shown in Figure 3.23, where $d1$ is the inner diameter of L1 and L3, $d2$ is its outer diameter, $d3$ is the distance between the two undersides of the middle lamination set L2, while the $d4$ is the outer diameter of L2; $d5$ is the distance between the lowest points of the two opposite diameter 2mm holes on the outer circumference

of L1 and L3. We define the height of the vertically thickest part of L2 as $t_{l2} = \frac{d4 - d3}{2}$, and then we can get the following constraints:

$$\begin{aligned} & d5 = d2 - 2 \\ & \frac{d5 - d1}{2} > t_{l2} > 2 \\ & d3 = \frac{d5 - d1}{2} + d1 - t_{l2} \\ & d4 = \frac{d5 - d1}{2} + d1 + t_{l2} \end{aligned} \tag{3.1}$$

As it is shown in Figure 3.3, the outer diameter of the rotor is 20.3 mm. We design the air gap length as 0.35mm, so the inner diameter of the HMBs stator should be $d1 = 20.3 + 0.35 \times 2 = 21$ mm. Based on other developed VADs introduced in Chapter 2, we design the outer diameter $d2$ as 35.6 mm, and therefore with the housing thickness of 2.2 mm, we have the outer diameter of our pump as 40 mm. Based on equation (3.1), we set the thickness t_{l2} as 3.5 mm, so we can get

$d3 = 23.8mm$
$d4 = 30.8mm$

The height for the winding coils wrapped around L2 is only $\frac{d3 - d1}{2} = \frac{23.8 - 21}{2} = 1.4$ mm.

The diameter of the coils we used is 0.15mm, so we can have $1.4/0.15 = 9.33 \approx 9$ turns of coils each layer, while we have $5/0.15 = 33.3 \approx 33$ layers of coils, therefore we can have $9 \times 33 = 297$ turns of coils in all in one stack of lamination stator. If the PMs are not included in the magnetic bearings, for the control force f generated by the coils alone in the vertical direction, we have

$$f = \frac{\mu_0 N^2 A_g I^2}{4 g_0^{\ 2}} \tag{3.2}$$

where μ_0 is the permeability of free air, g_0 is the nominal air gap, N is the number of coils turns, A_g is the cross section area of the flux. For the HMBs developed, if the control current I is 0.2 A, then the electromagnetic force f which is provided by the coils of two HMBs alone in the vertical direction is 0.52 N, which is larger than the weight of the developed rotor whose mass is about 52 mg (the weight is $52 \times 10^{-3} \times 9.8 = 0.51\,\text{N}$). Since the PMs in the HMBs can provide bias magnetic flux, which will generate more electromagnetic force compared with normal magnetic bearings under the same conditions, the designed HMBs should be able to levitate the rotor with suitable control.

3.3.2 Fabrication of the HMBs

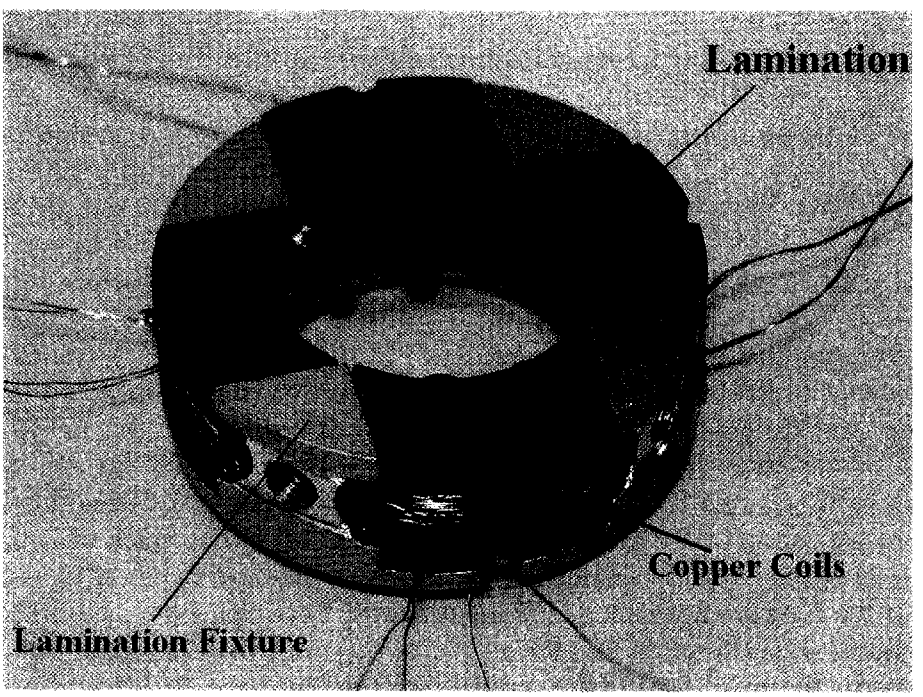

Figure 3.25: Photograph of the HMBs' stator

The photograph of the HMB stator is shown in Figure 3.25. The HMB stator is composed of three parts: four sets of lamination stacks, the lamination fixture and the coils.

The four sets of lamination stacks are made from 0.23 mm thick silicon steel laminations that are placed in the orthogonal directions. 90 turns of double-layer copper wires with a diameter of 0.15 mm are wound around the core of each set of silicon steel lamination, and the generated flux loop circulates through the corresponding two rings on the rotor, which are also made from silicon steel laminations to reduce the eddy current and hysteresis losses. The inductance of one quadrant of the coils in one HMB is 0.57 mH, and its resistance is 2 Ω. There is a permanent magnet (PM) ring between the two rings on the rotor that is made of Nd-Fe-B to produce the bias magnetic flux for the electromagnets.

On the lamination fixture, which is shown in Figure 3.26, there are threaded holes for eddy current probes to be placed in the orthogonal directions on each side to measure the radial positions of the rotor.

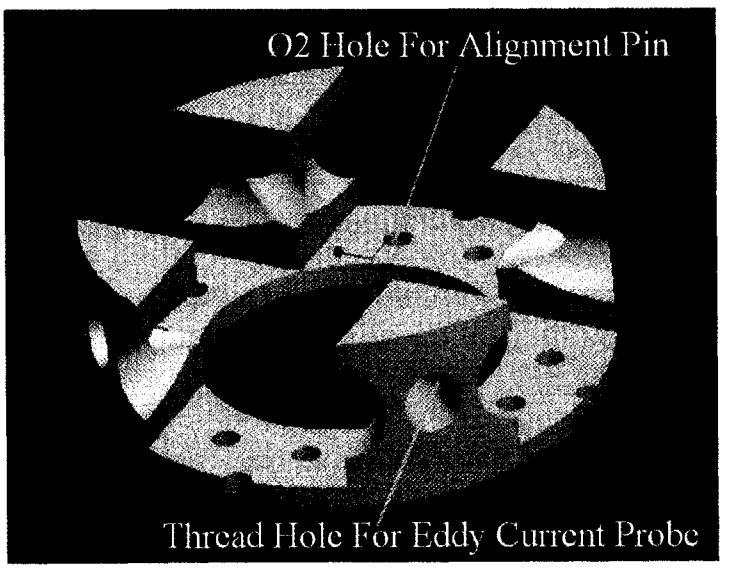

Figure 3.26: 3D model of the lamination fixture

In order to align the lamination stacks, Ø2 mm holes are made on the lamination fixture and the lamination stacks where Ø2 mm iron pins are inserted. The whole set of the HMB stator, with the coils and the alignment pins are all dipped in xylene to make the assembly stronger and also to protect the coils.

3.3.3 The rotor

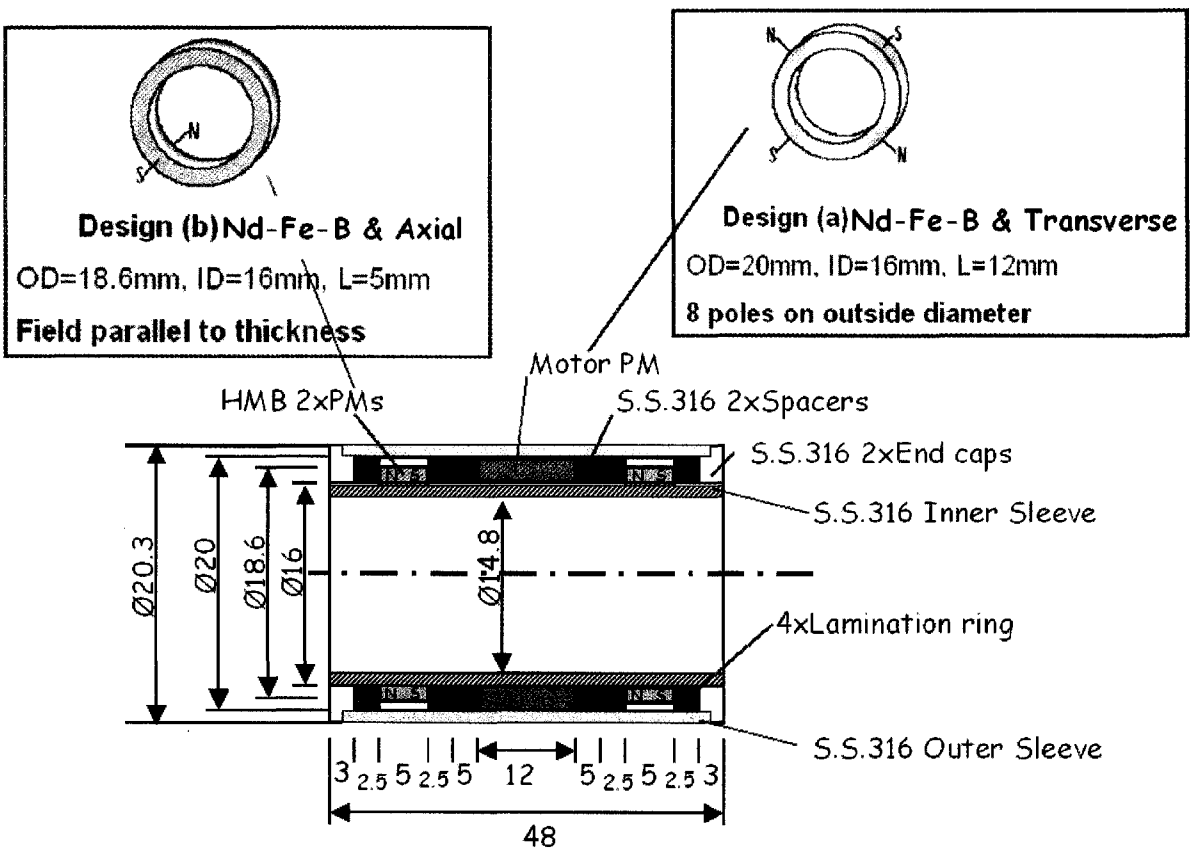

Figure 3.27: Scheme of the rotor with part materials and dimensions

The rotor is composed of an inner sleeve, an outer sleeve, rings of silicon steel laminations for HMBs, the HMBs' PMs, the motor's PM and the spacers. The scheme of the rotor with the part materials and the dimensions is shown in Figure 3.27.

In order to ease assembly and manufacture, the inner sleeve is composed of two parts whose models are shown in Figure 3.28.

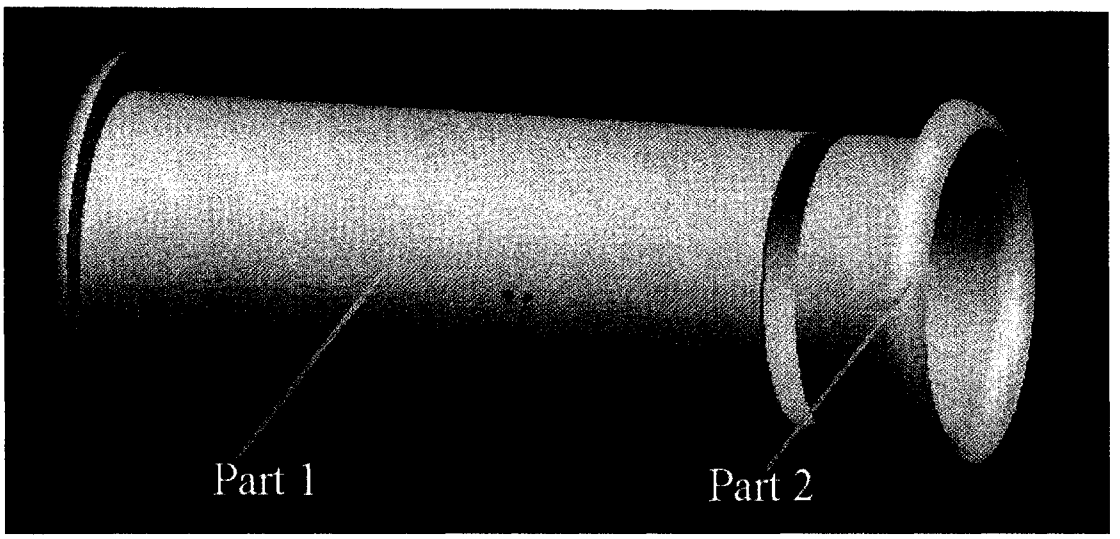

Figure 3.28: Explored view of inner sleeve of the rotor

To facilitate the fluid flow, the herringbone groves are machined on the outer sleeve.

To help to assemble the rotor, a special fixture is designed and fabricated. The assembly procedure is as follows:

Firstly, Part 1 of the inner sleeve is laid on the assembly fixture platform through the fixture shaft, and then the epoxy is spread on the outer side surface of Part 1. Secondly, the lamination rings, the HMBs' PMs, the motor's PM and the spacers are pulled through the inner sleeve in order, and the epoxy is then applied on their outer surfaces. Thirdly, the rotor outer sleeve is slipped on. Fourthly, Part 2 of the inner sleeve is inserted, and the fixture cap is put on Part 2. Lastly, a M10 screw is screwed down to tighten the rotor assembly. After the epoxy dries, the fixture can be taken out and the rotor assembly procedure is completed. The

photograph of the assembly fixture, the rotor, the outer sleeve with the herringbone groves, and without herringbone groves is shown in Figure 3.29.

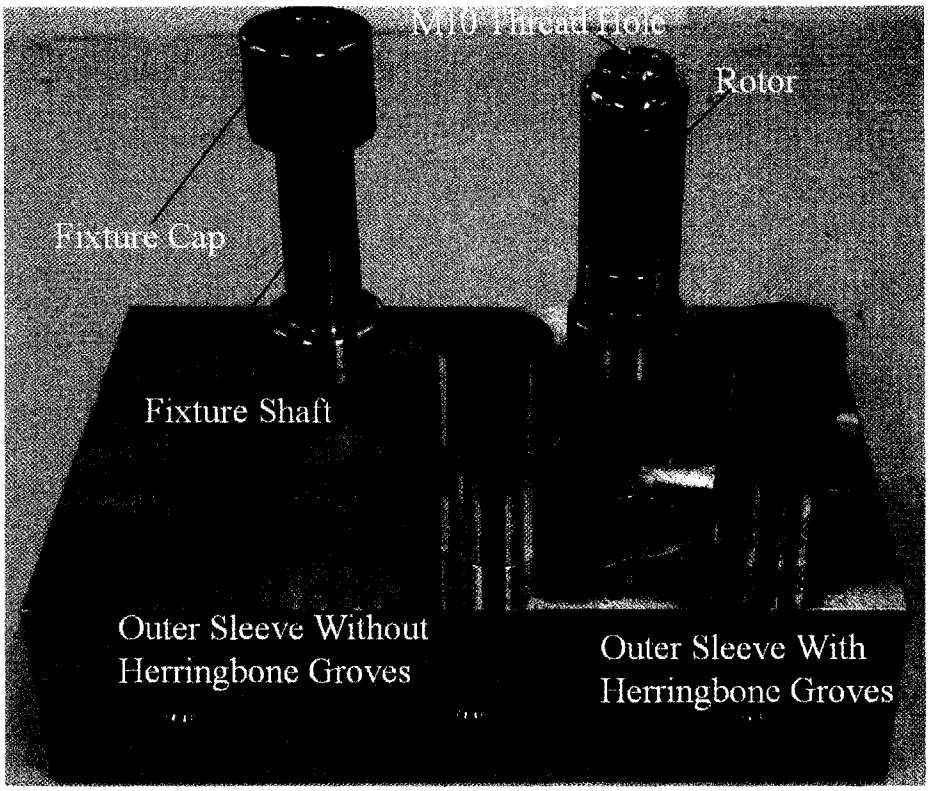

Figure 3.29: Photograph of the rotor, assembly fixture and the outer sleeve

3.3.4 The Lorentz-typed three-phase brushless and sensorless PM motor

The scheme of the motor is shown in Figure 3.30. Also made from silicon steel laminations, the motor stator has six teeth and each tooth is wound by 21 turns of motoring coils with a diameter of 0.54 mm. In the middle of the rotor, there is an 8- pole permanent magnet (PM) secured on it. The stator of the motor with the coils wound around has also been dipped in varnish, in order to protect these electrical windings.

The arrangement of the motor coils is U_m, W_m, and V_m respectively.

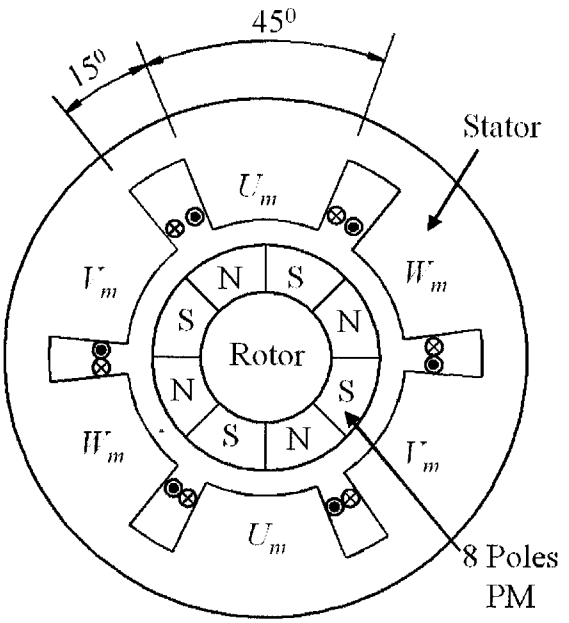

Figure 3.30: Schematic of the motor wiring connections

The PM on the rotor is assumed to produce the following sinusoidal waveform of flux density around the air gap for the motor stator [1]:

$$B_g = -B\sin(\omega t - 4\theta) \tag{3.3}$$

The motoring coils are driven by the following three-phase current:

$$\left\{\begin{array}{c} I_{U_m} = A\cos(\omega t + \varphi) \\ I_{W_m} = A\cos(\omega t + \frac{2}{3}\pi + \varphi) \\ I_{V_m} = A\cos(\omega t + \frac{4}{3}\pi + \varphi) \end{array}\right\} \tag{3.4}$$

Based on the equation (3.4), the current distribution in the circumferential direction can be expressed by Dirac's delta function as:

$$\begin{aligned} i_m = I_{U_m}[\delta(\theta-(-\frac{1}{8}\pi))-\delta(\theta-\frac{1}{8}\pi)+\delta(\theta-\frac{7}{8}\pi)-\delta(\theta-\frac{9}{8}\pi)] \\ +I_{W_m}[\delta(\theta-\frac{5}{24}\pi)-\delta(\theta-\frac{11}{24}\pi)+\delta(\theta-\frac{29}{24}\pi)-\delta(\theta-\frac{35}{24}\pi)] \\ +I_{V_m}[\delta(\theta-\frac{13}{24}\pi)-\delta(\theta-\frac{19}{24}\pi)+\delta(\theta-\frac{37}{24}\pi)-\delta(\theta-\frac{43}{24}\pi)] \end{aligned} \quad (3.5)$$

According to the Lorentz force principle, the torque produced by the currents is:

$$T = 2Nrl\int_{-\frac{\pi}{8}}^{\frac{7}{8}\pi} B_g i_m d\theta = 6NrlAB\cos\varphi \quad (3.6)$$

Equation (3.6) shows that the torque can be controlled by the current magnitude A and phase φ, and it is independent of rotor position and time. The corresponding variables above are defined in Table 3.2.

Table 3.2: Definition of variables

A	Magnitude of motoring current
B	Magnitude of flux density
θ	Mechanical angle
ω	Electric frequency
φ	Phase of motoring current
B_g	Flux density in the air gap
l	Length of stator
r	Radius of rotor
N	Number of turns

To make a cylinder-shaped motor coil, a special coil fixture is designed and it is composed of three parts: Part 1, Part 2 and Part 3, as shown in the Figure 3.31.

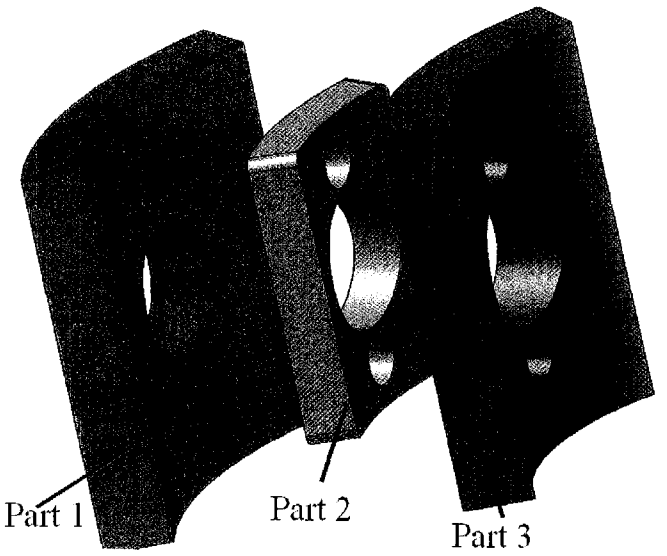

Figure 3.31: Three parts of the motor coil fixture

To ease machining, the left-side surface of Part 1 and the right-side surface of Part 3 are changed to be flat. The photograph of the fabricated motor coil fixture is shown in Figure 3.32.

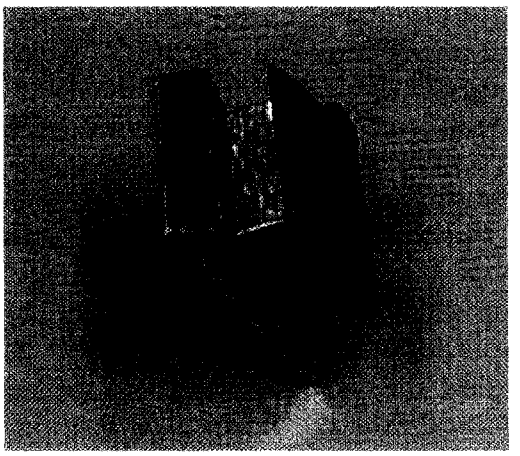

Figure 3.32: Photograph of the fabricated motor coil fixture

Part 2 is sandwiched between Part 1 and Part 3 and tightened by two M2 screws and nuts. The coils are wrapped around the outer surface of the Part 2 and meanwhile compressed by Part 1 and Part 2. A winding machine is used for coil winding. The winding machine with the coil fixture is shown in Figure 3.33.

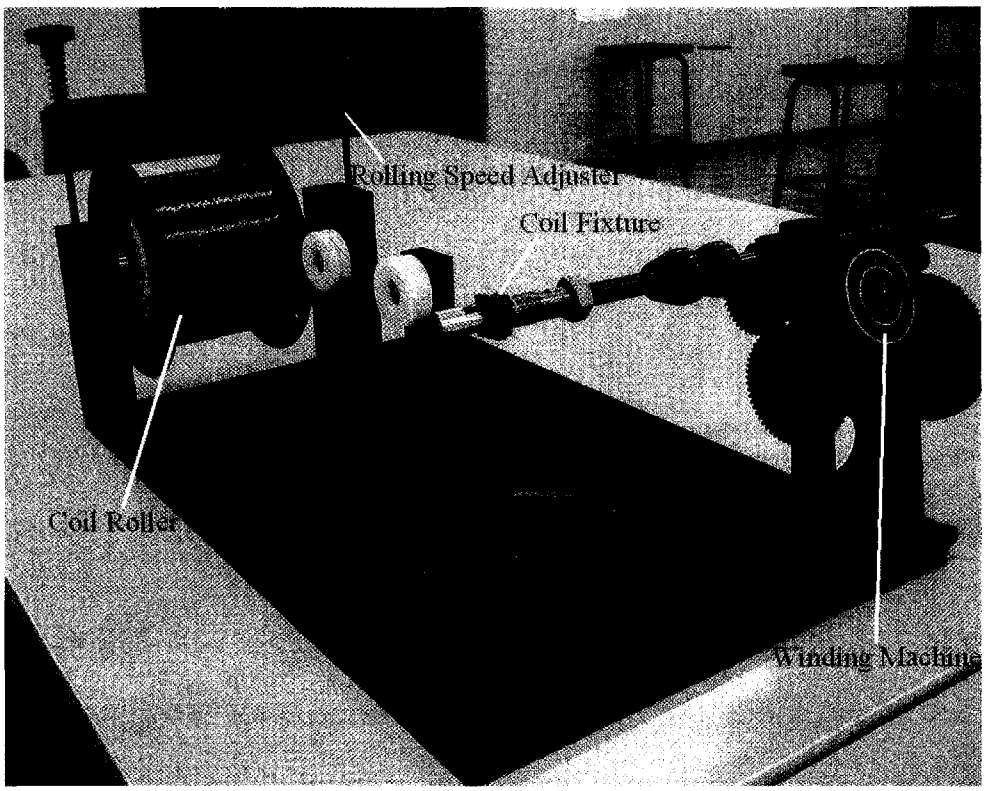

Figure 3.33: Photograph of the coil winding operation

A special self-bonding coil (NEMA, MW35-C, Bondable Magnet Wire) is used for the motor. Acetone is sprayed around the coils before coil winding to soften the bonding epoxy on the coils. After coil winding, the cylinder-shaped coils are put into the oven for baking at the temperature of 150°C for about 20 minutes. When the motor coils are finished, they are inserted through the teeth of the motor stator. Then, the motor stator with the coils is dipped in varnish so that the coils could

bond the stator teeth firmly. The photograph of the fabricated motor stator is shown in Figure 3.34.

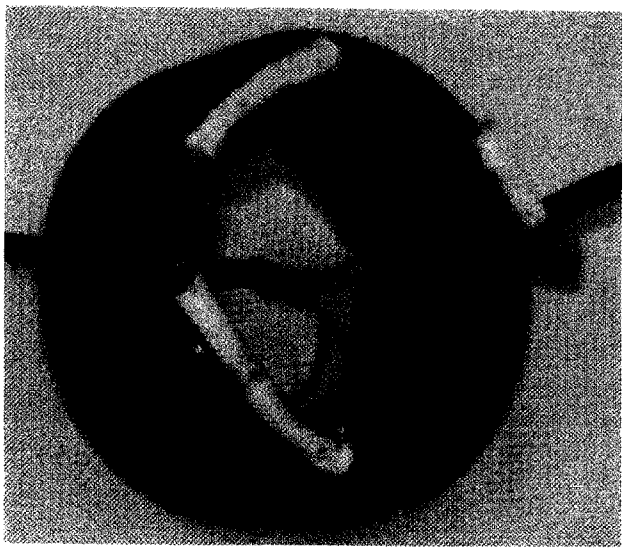

Figure 3.34: Photograph of the fabricated motor stator

3.4 Control of the HMBs system

3.4.1 Finite element calculation of the electromagnetic forces

From the experience of TMDU/IIT disposable centrifugal blood pump [60] [61] and Thoratec HeartMate III [53] where the rotor/impeller is actively controlled in radial directions and it is passively controlled in axial direction, the passive axial magnetic force is strong enough to keep the rotor stability in the axial direction. In the HMBs system of the axial flow blood pump, the four radial directions are actively controlled with the PID controllers. The axial movement of the rotor is constrained by the radial electromagnetic forces, and therefore passively controlled by the HMBs. As shown in Figure 3.35, the 3D model of the HMB is build in Maxwell 3D to calculate the magnetic forces with the method of FEA.

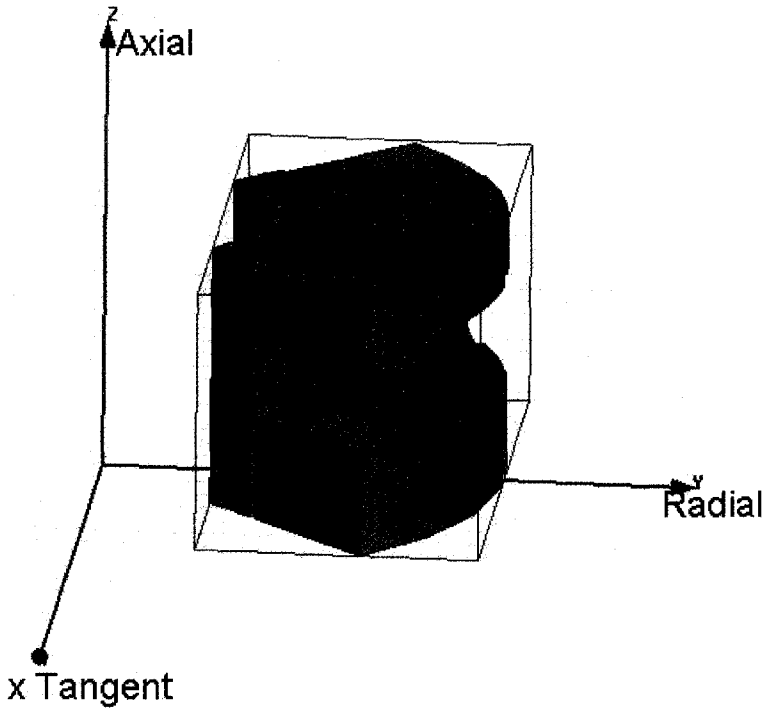

Figure 3.35: 3D model of the HMB in Maxwell 3D

By moving the rotor in the axial direction, we can obtain the corresponding radial and axial forces from the Maxwell 3D FEA results, as listed in Table 3.3 below, where the dz is the displacement of the rotor in the axial direction.

Table 3.3: Electromagnetic forces on rotor with the axial movement of the rotor

dz (mm)	F(x)_tangent (N)	F(y)_radial (N)	F(z)-axial (N)
0	6.10E-04	4.1207	-0.12949
0.0045	-0.00191	4.132	-0.14897
0.0135	-0.00347	4.1469	-0.16297
0.021	-0.05891	4.1523	-0.19112
0.027	-0.00272	4.1227	-0.2401

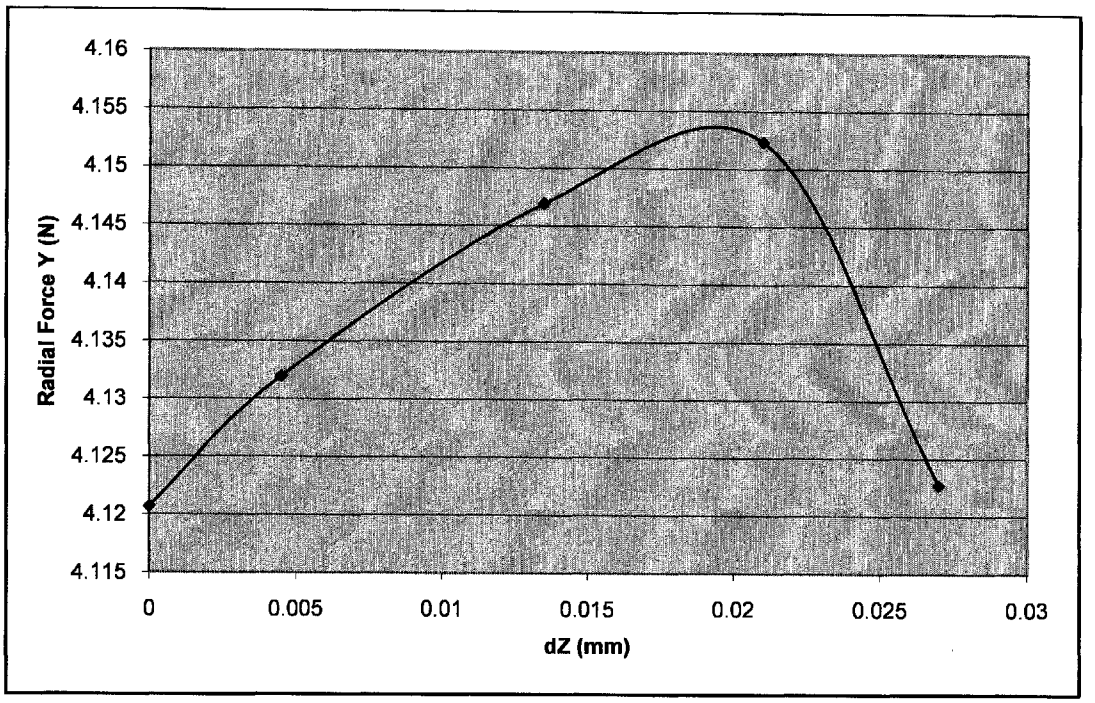

Figure 3.36: Force in y direction changes with axial movement of rotor

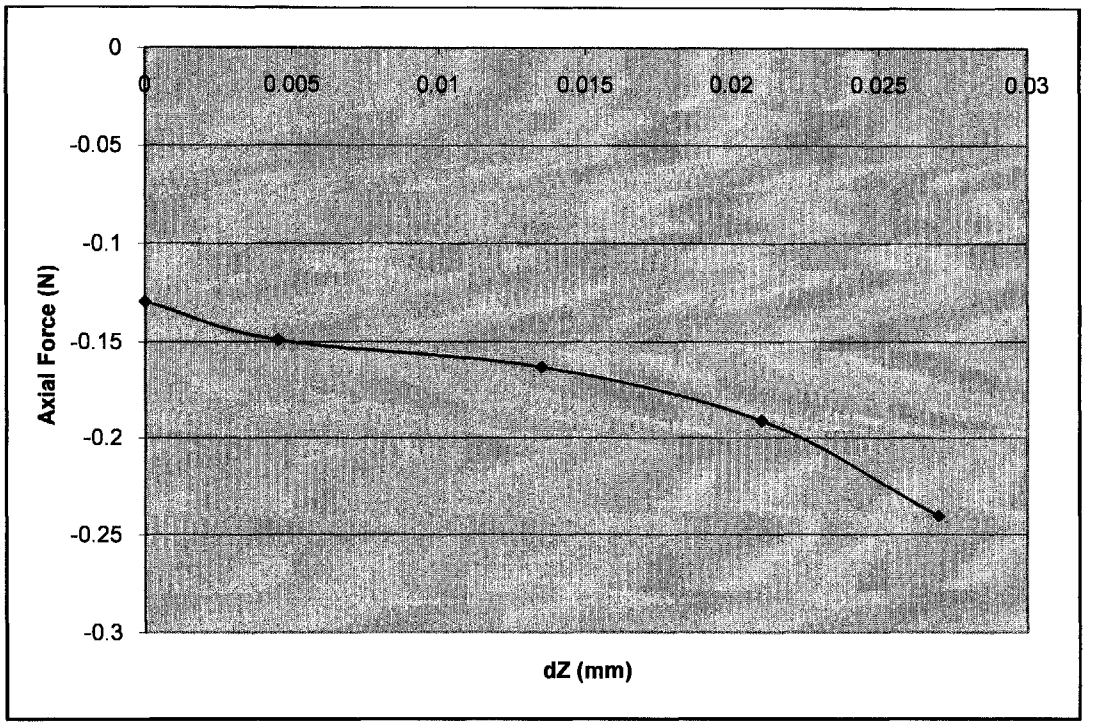

Figure 3.37: Force in z direction changes with axial movement of rotor

It can be seen from Table 3.3, that with the increase of the rotor axial displacement, the axial force is increased and the radial force in y direction varies little. The very small forces in the x direction are due to symmetry scheme of the model in x direction which caused the cancellation of electromagnetic forces in x direction. The force change trends in y and z directions are plotted in Figure 3.36 and Figure 3.37 respectively. The fore in y direction remains around 4.1 N as shown in Figure 3.36, while the axial force is increasing with the increase of the rotor axial displacement.

The obtained negative axial force indicates the axial force is trying to pull back the moving rotor in the axial direction, which can prove that the axial load of the HMBs can be carried by action of the actively controlled radial electromagnets which will produce the passive control force in the axial direction.

3.4.2 Control of HMBs

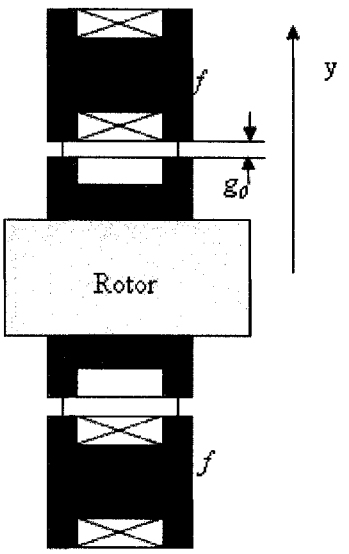

Figure 3.38: Magnetic force in the vertical direction

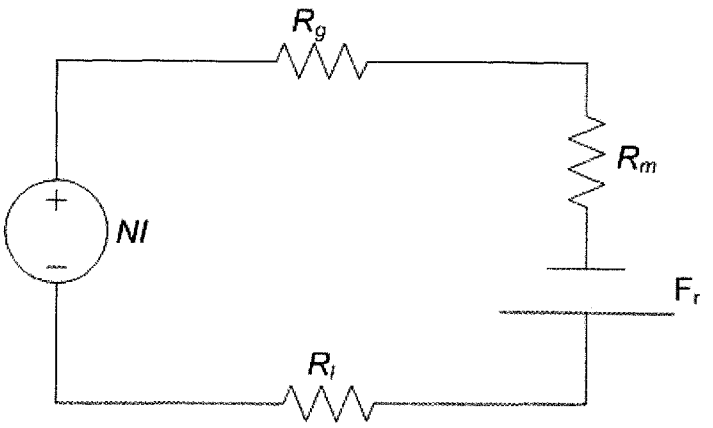

Figure 3.39: Equivalent magnetic circuit of HMB

The scheme of HMBs and its electromagnetic force on the rotor in the y direction is shown in Figure 3.38, whose equivalent magnetic circuit is shown in Figure 3.39 where N is number of turns of the coils, I is the coil current, R_g is the air gap reluctance, R_l is the reluctance of the lamination loop, R_m is the reluctance of the permanent magnet, F_r is the magnetomotive force of the permanent magnet. The corresponding circuit equation can be written as:

$$NI + F_r = (R_g + R_l)B_g A_g \tag{3.7}$$

where B_g is the magnetic flux density of the air gap, A_g is the cross section area of the air gap; Also because of the following:

$$\begin{aligned} F_r &= \frac{B_r l_m}{\mu_m} \\ R_g &= \frac{l_g}{\mu_0 A_g} \\ R_l &= \frac{l_l}{\mu_r A_g} \\ R_m &= \frac{l_m}{\mu_m A_m} \\ f &= \frac{B_g^2 A_g}{2\mu_0} \end{aligned} \tag{3.8}$$

where B_r is the residual flux density of the permanent magnet, l_m is the distance of the permanent magnet from north pole to the south pole, μ_m is incremental permeability of the permanent magnet; l_g is the air gap length in the flux loop, l_l is the length of the flux loop passing the laminations, μ_0 is the permeability of free air, μ_r is the relative permeability of the lamination compared to the free air; f is the electromagnetic force in the air gap on the rotor; substituting the equation (3.8) into equation (3.7), and when $\frac{l_l}{\mu_r} << \frac{l_g}{\mu_0}$, we can obtain the following:

$$f = \frac{(NI + \frac{B_r l_m}{\mu_m})^2 A_g}{2\mu_0 \left(\frac{2l_g}{\mu_0} + \frac{l_m A_g}{\mu_m A_m} \right)^2} \tag{3.9}$$

When there is a small disturbance of the rotor in the y direction, the corresponding electromagnetic force can be expressed by equation (3.10)

$$f = \frac{A_g}{2\mu_0} \left(\frac{(NI_1 + \frac{B_r l_m}{\mu_m})^2}{\left(\frac{2(g_0 + y)}{\mu_0} + \frac{l_m A_g}{\mu_m A_m} \right)^2} - \frac{(NI_2 + \frac{B_r l_m}{\mu_m})^2}{\left(\frac{2(g_0 - y)}{\mu_0} + \frac{l_m A_g}{\mu_m A_m} \right)^2} \right) \tag{3.10}$$

where I_1 is the coil current in the upper magnet, I_2 is the coil current in the lower magnet, g_0 is the nominal air gap, and y is the displacement of the rotor in the vertical direction.

The Taylor series expansion of equation (3.10) results in the system dynamic force equation that can be expressed as follows:

$$\Delta f = f - f_0 = k_{yy} y + k_{yi} i_y \tag{3.11}$$

where k_{yy} is defined as the restoring mechanical stiffness (displacement stiffness) coefficient of magnetic bearings, k_{yi} is defined as the current stiffness coefficient.

When I_0 – coil bias current is far larger than its static control current, we can obtain the following:

$$k_{yy} = \frac{-8A_g}{\mu_0{}^2} \frac{(NI_0 + \frac{B_r l_m}{\mu_m})^2}{(\frac{2g_0}{\mu_0} + \frac{l_m A_g}{\mu_m A_m})^3} \tag{3.12}$$

$$k_{yi} = \frac{4A_g}{\mu_0} \frac{(N^2 I_0 + N\frac{B_r l_m}{\mu_m})}{(\frac{2g_0}{\mu_0} + \frac{l_m A_g}{\mu_m A_m})^2} \tag{3.13}$$

As it can be seen from the equation (3.12), the displacement stiffness coefficient, k_{yy}, is negative, which means that if the system is to be kept stable, it is necessary to adjust the controlling current i_y.

For the HMBs developed, the values of relevant coefficients are listed below:

Table 3.4:Coefficients values of hybrid magnetic bearings

B_r	0.7 T	A_m	34.715 mm^2
l_m	5 mm	A_g	39.27 mm^2
μ_m	$1.05\mu_0$	I_0	0.20 A
μ_0	4Л × 10^{-7} T.m/A	N	90

Based on the equations (3.12) and (3.13), and the values provided in Table 3.4, we can obtain the theoretical mechanical stiffness and current stiffness:

$$\begin{aligned} k_{yy} &= -12.5 \ N/mm \\ k_{yi} &= 1.28 \ N/A \end{aligned} \tag{3.14}$$

The typical differential equation of mass-spring-damping system is as follows:

$$m\ddot{y} + ky + c\dot{y} = f_y \tag{3.15}$$

where k is the stiffness coefficient, and c is the damping coefficient, while the differential equation for electromagnetic bearing & rotor system is:

$$m\ddot{y} + k_{yy}y + k_{yi}i_y = f \tag{3.16}$$

Assuming the two systems have the same dynamic effect, we obtain:

$$ky + c\dot{y} = k_{yy}y + k_{yi}i_y$$

and therefore

$$i_y = \frac{(k - k_{yy})y + c\dot{y}}{k_{yi}} = k_p y + k_d \dot{y} \tag{3.17}$$

From equation (3.17) it can be seen that in order to adjust the controlling current i_y, we need at least two control parameters:

1. Proportional control, and the proportional gain is:

$$k_p = \frac{(k - k_{yy})}{k_{yi}} \tag{3.18}$$

2. Differential control, and the differential gain is:

$$k_d = \frac{c}{k_{yi}} \tag{3.19}$$

However, in practice, simply a PD controller (proportional and differential control) is insufficient, due to the fact that static error is always inherent in the system. Accordingly, integral control needs to be added and therefore, a PID controller is actually used to stabilize the magnetic bearing system.

Figure 3.40 shows the block diagram of controlling the HMBs system in one radial direction with PID controller.

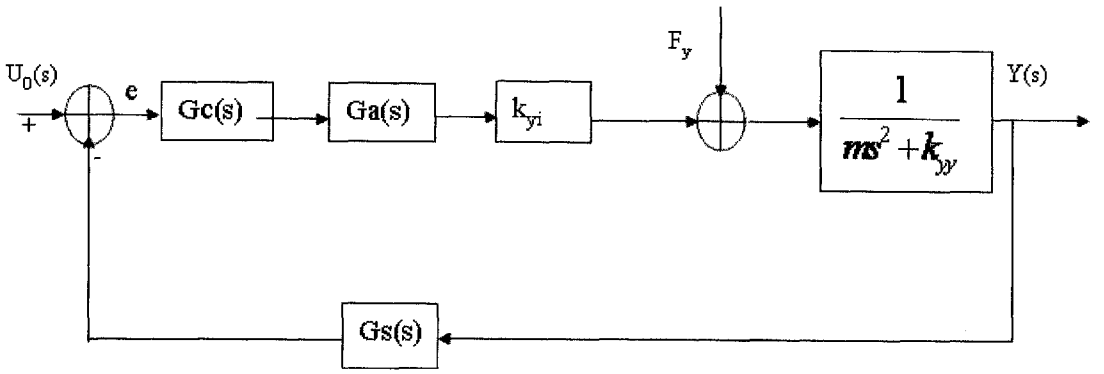

Figure 3.40: Block diagram of controlling the HMBs in one radial direction

where the transfer function of displacement sensor is:

$$G_s(s) = \frac{A_s}{1 + T_s s} \tag{3.20}$$

where $A_s = 0.5$.

The transfer function of the PID controller is as follows:

$$G_c(s) = k_p + \frac{k_d s}{1 + sT_d} + \frac{k_i}{s} \tag{3.21}$$

where, k_p is the proportional coefficient, k_d is the differential coefficient, k_i is the integration coefficient, and T_d is time constant of differentiator. The transfer function of the amplifier is:

$$G_a(s) = \frac{\alpha_a}{1 + sT_a} \tag{3.22}$$

where, α_a is the amplifier gain, and T_a is the decay time constant of the amplifier, and we have α_a=1 and T_a=1/10000. The close-loop transfer function of the whole system as depicted in Figure 3.40 is:

$$G_{cl}^i = \frac{Y(s)}{U_0(s)} = \frac{k_{yi} G_c(s) G_a(s)}{ms^2 + k_{yy} + k_{yi} G_s(s) G_c(s) G_a(s)} \tag{3.23}$$

The characteristic polynomial of the system is:

$$ms^2 + k_{yy} + k_{yi} G_s(s) G_c(s) G_a(s) = 0 \tag{3.24}$$

Each coefficient of the polynomial should be greater than 0 if the system is to be stable, so we can obtain the following conditions:

$$\left.\begin{aligned} T_a T_d &< -\frac{m}{k_{yy}} \\ k_d + k_p T_d &> \frac{I_0 (T_a + T_d)}{g_0 A_s \alpha_a} \\ k_p + T_d k_i &> \frac{I_0}{g_0 A_s \alpha_a} \end{aligned}\right\} \tag{3.25}$$

Based on (3.25), we can obtain:

$$\left.\begin{aligned} k_d + k_p{*}0.008 &> 3.13\text{e-}4 \\ k_p + k_i {*}0.008 &> 0.04 \end{aligned}\right\} \tag{3.26}$$

The gain of the eddy current probes is 8 V/mm, and the gain of the PWM amplifiers is adjusted to be 1 A/V. Based on (3.26) and through experiment, we obtain the gains of PID control parameters of the HMBs, which are tabulated in Table 3.5. Due to the almost infinite integral force when there is system static error, we add in a time constant T_i in the integrator to decrease the integral force at very low frequency range when system starts up and the new PID control algorithm is shown in equation (3.27).

$$G_c(s) = k_p + \frac{k_d s}{1 + s T_d} + \frac{k_i}{T_i s + 1} \tag{3.27}$$

Table 3.5: Control parameters of hybrid magnetic bearings

k_p	8 A/mm	k_i	2 A/(sec.mm)
k_d	0.0052 A·sec/mm	T_d	0. 1 ms
T_i	31.8 ms	I_0	0. 2 A

In Table 3.5, K_p.is the parameters of the PID controller with the unit of 8 A/mm; with the obtained actuator gain of 5.7 N/A on section 5.2.3.2 of the thesis, the system K_p.should be $8 \times 5.7 = 45.6$ N/mm, which is much larger than the absolute value of the theoretical open loop negative stiffness of $k_{yy} = -12.5$ N/mm.

The dSPACE ds1103 in conjunction with the MATLAB® 6.1 and Simulink software are used as the rapid prototyping tools for the development of the digital PID controller of the HMBs. The model of the digital controller is designed and simulated in Simulink. After building the Simulink model into the digital signal processing (DSP) model of dSPACE ds1103, the control algorithms are successfully implemented digitally in the DSP and the digital controller can operate real-time via the dSPACE ds1103's hardware in the loop interface. The voltage range of the interface for dSPACE ds1103 is set from -10V to +10V, sampling frequency of the controller is 20 kHz, 16-bit A/D and 14-bit D/A converters are chosen as the settings for this experiment. The rotor displacements are measured by the Applied Electronics Corporation's eddy current probes (AEC-5503A) which has a resolution of 0.5 μm and gain of 8 V/mm. The coils of the HMBs are driven by the Advanced Motion Controls (AMC) PWM (25A series) servo amplifiers. The port connection scheme of AMC 3-state PWM amplifiers is attached in Appendix E.

3.4.3 Control of the Lorentz-typed three phase PM motor

The STMicroelectronics' ST7FMC micro-controller is used to control the three-phase PM brushless motor. The ST7FMC micro controller is an integrated system designed to provide the users with a complete, ready-to-use motor application. Sensorless Control Mode is chosen to drive the motor using a back electromotive force zero-crossing detector as a part of the ST7 motor controller peripheral, and therefore the requirement of a flux sensor in the HMBs system is eliminated, which makes the overall system compact.

3.5 Performance of HMBs system

The mass of the rotor is 80.12 g. The nominal air gap of the rotor is 0.35 mm. The radial (x- and y-) directions are actively controlled, and the axial (z-) direction is passively controlled. The rotor can rotate in stable suspension at speeds of up to 14,000 rpm. Figure 3.41 and Figure 3.42 show the displacements of the rotor in the x, y and z directions when the rotor is at stationary and at the rotational speed of 14,000 rpm.

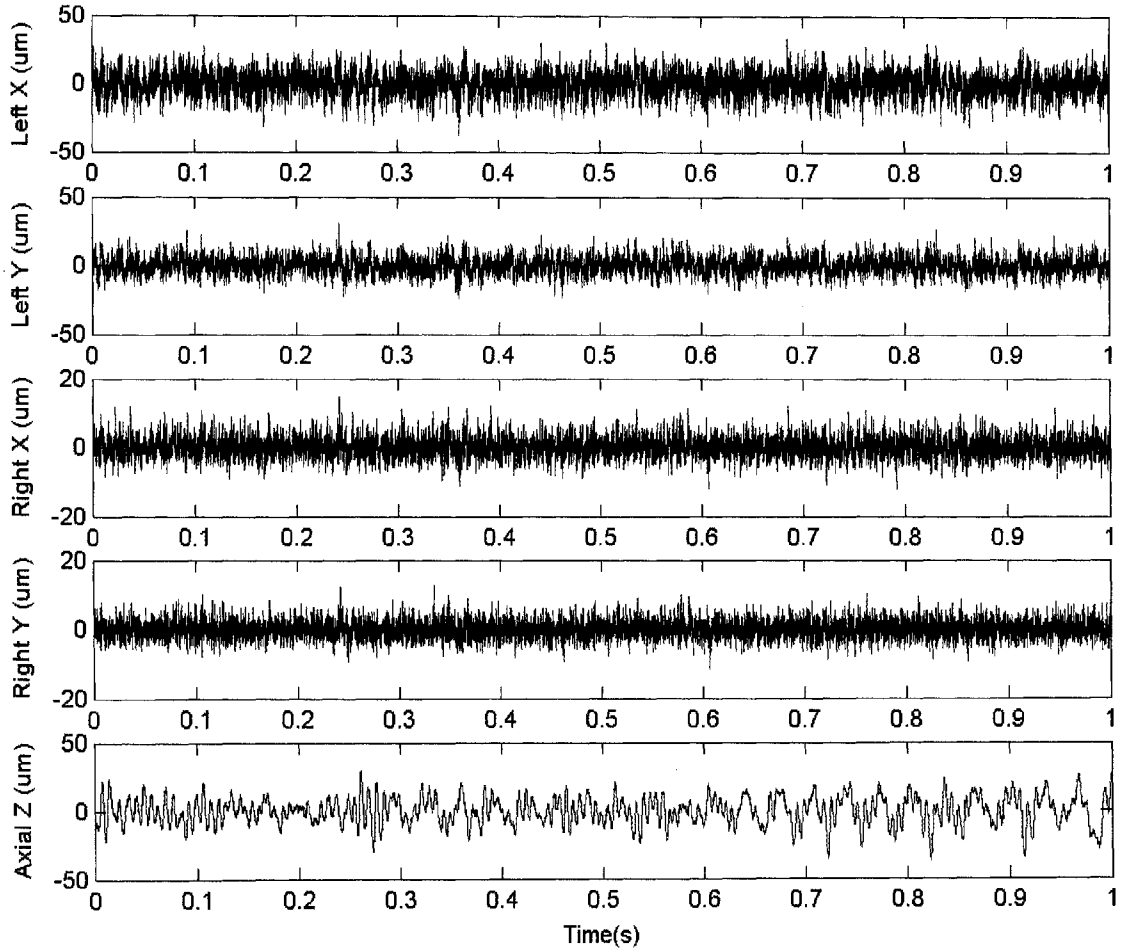

Figure 3.41: Levitated rotor displacements in x, y, z directions at 0 rpm

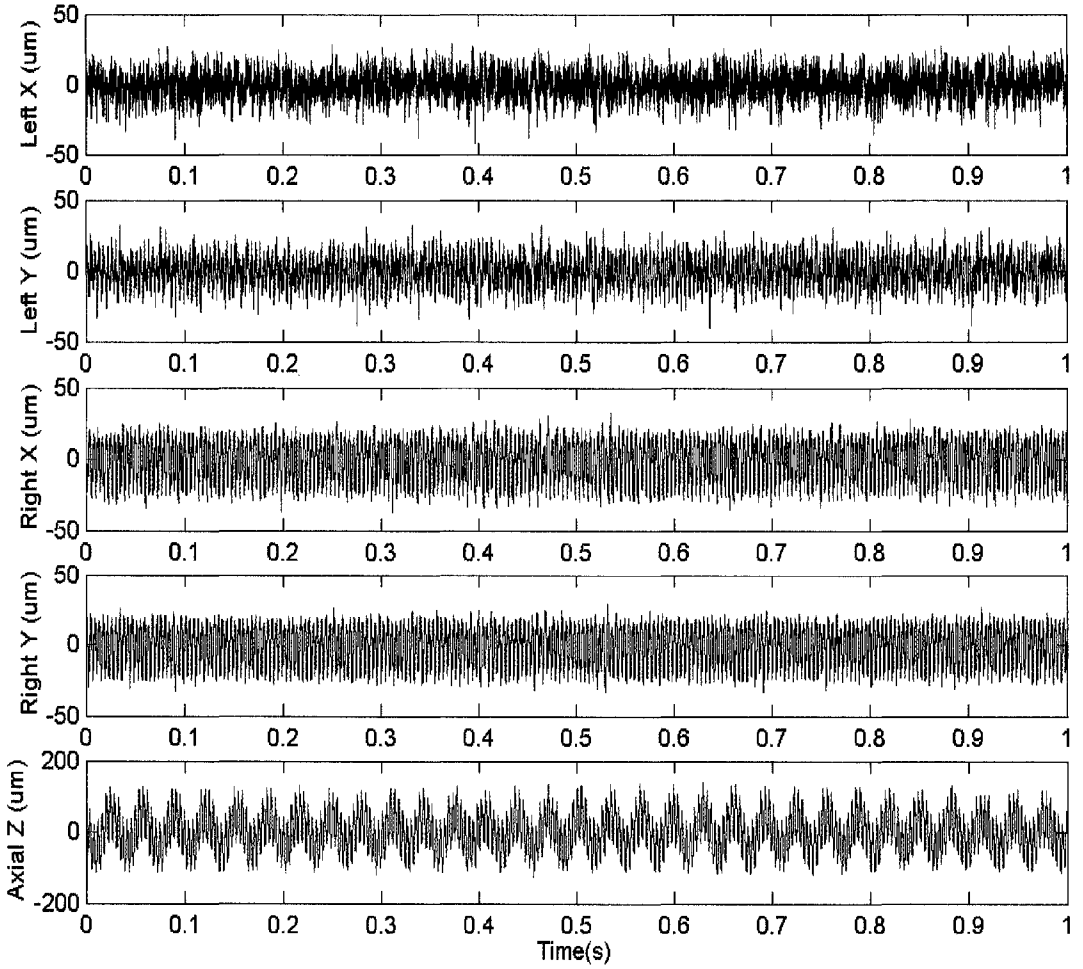

Figure 3.42: Levitated rotor displacements in the x, y, z directions at 14,000 rpm

The displacement contents in the x, y and z directions are noisy due to the switching noise and harmonics, and therefore, it is difficult to see the actual displacements in the three directions directly from the time domain signals. The FFT (Fast Fourier Transform) is utilized to transform the time domain signal into frequency domain, and the FFT amplitude at the rotor rotation frequency is then measured as the displacement of the rotor at the corresponding speed.

In order to obtain the frequency response of the HMBs system, the rotor displacement is recorded in the x, y and z directions when the rotor rotation speed is increased from 0 rpm to 14,000 rpm with an interval of 500 rpm. Using FFT, their corresponding frequency responses can be obtained as shown in Figure 3.43,

from which it can be seen that the rotor rotation in suspension in air is very stable and no collision with the stator and pump housing is observed. When it is not rotating, the hovering displacement of the rotor is only about 1 μm in the x, y and z directions. The maximum rotor displacements occurred at 10,000 rpm in the radial and axial directions are about 30 μm and 70 μm respectively. At the maximum speed of 14,000 rpm, the displacements in the x, y and z directions are about 8 μm and 35 μm respectively.

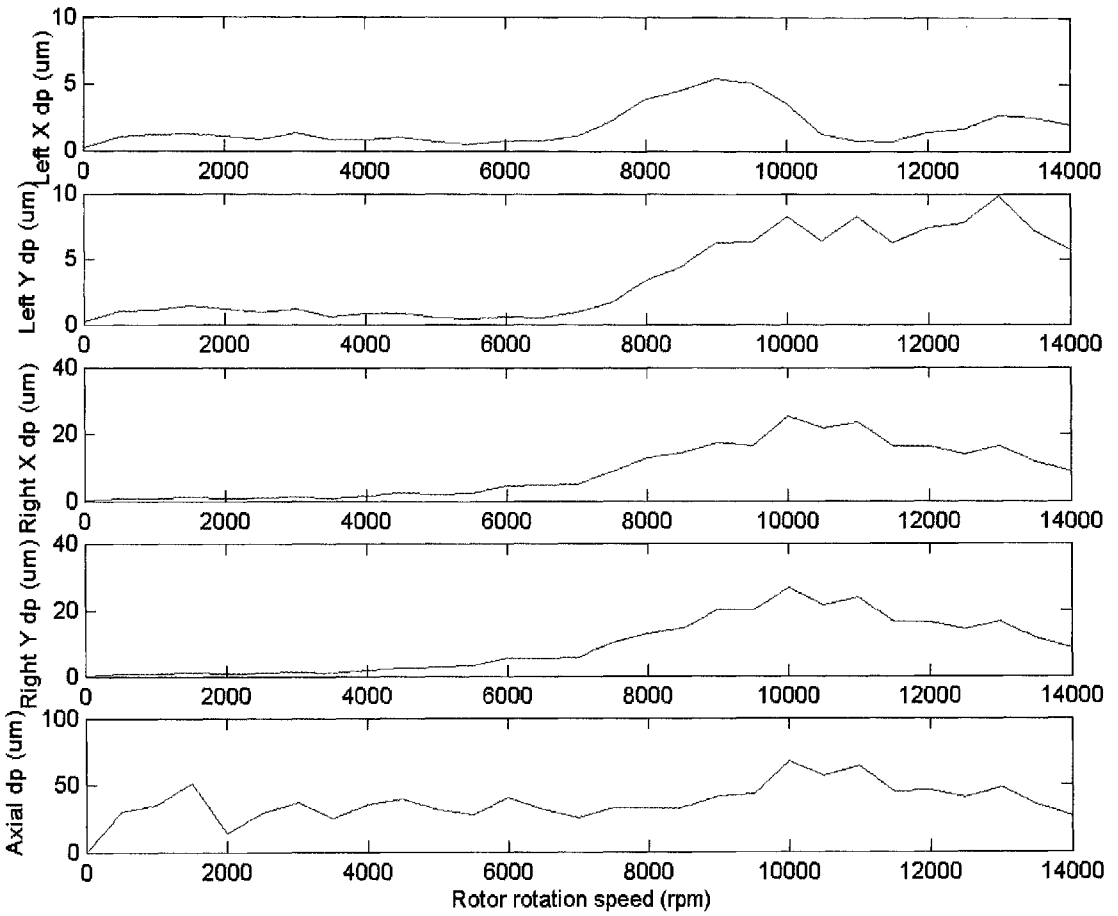

Figure 3.43: Levitated response of the HMBs system of axial flow blood pump in x, y and z directions ('displacement' shortened to 'dp' in graph)

The bearing coil versus the rotor rotational speed is shown Figure 3.44.

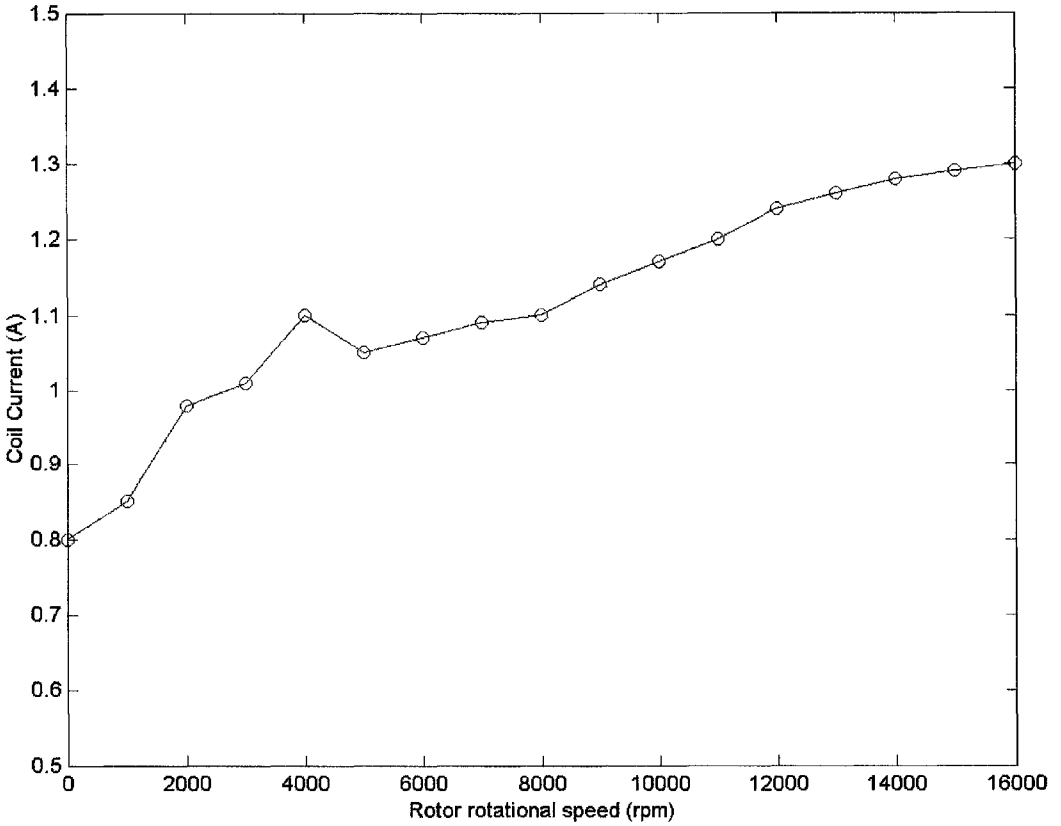

Figure 3.44: Bearing coil current vs. rotor rotational speed

The power consumption for the pump system under normal operation conditions when the rotor is rotating at the speed of 10,000 rpm is as follows:

	Voltage (V)	Current (A)	Power (W)
Motor	23.5	0.22	5.2
HMBs	23.5	1.17	27.3
		Total Power(W):	32.5

The total VAD power consumption under normal operation conditions is very large, being about 32.5 W, which strengthens the necessity of using the low rate power amplifiers in the near future for the axial flow blood pump with zero bias current.

In order to test the temperature of the HMBs system when the pump is operating in air, the rotor is kept to rotate at the speed of 14,000 in stable suspension for two hours. It is found out that the temperature of the pump housing is increased from 22°C to 40°C during the two testing hours. The temperature of the pump system is a little high, but will be lowered if the pump is tested in water or blood. Within the system stability, the operation of zero bias current can be adopted and therefore the temperature will also be decreased further.

Chapter 4 Parameter estimation on one DOF magnetically levitated system with a digital PID controllers

In this chapter, one DOF electromagnetic suspension system is realized with a digital PID controller. Effective and actual stiffness, and damping coefficients of the electromagnetic actuator are introduced and compared. The one DOF parameter estimation algorithm and procedure are also described. A multi-frequency SPHS test signal [69] is used to persistently excite the mode of the suspended platform. The system excitation force/displacement transfer function is then obtained experimentally. It is in this manner that the actual stiffness and damping coefficients of the electromagnetic actuator are obtained. Statistical information is also provided to validate the system model and verify the estimated coefficients. Comprehensive relationships between digital PID controller gains versus stiffness and damping coefficients and system responses are also studied.

4.1 Principles

4.1.1 Effective stiffness and damping coefficients of electromagnetic suspension system

The actuation force for a single DOF active magnetic bearing system can be expressed by its mechanical restoring stiffness (K_{yy}) and current related stiffness

(K_{iy}) respectively, as shown in Figure 4.1, which is the simplified block diagram of the suspension system in the control loop for the uncoupled one DOF motion.

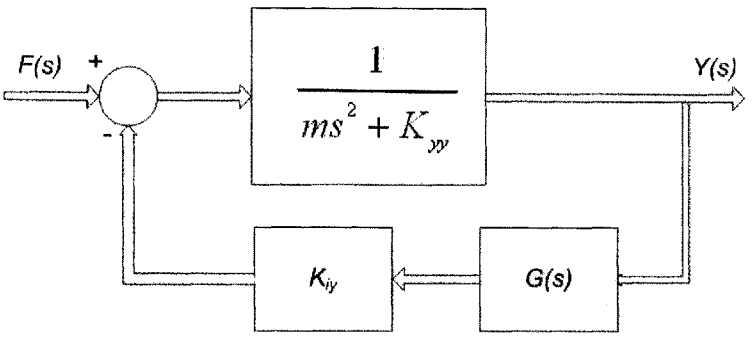

Figure 4.1: Block diagram of AMB in one axis

The transfer function of the close-loop system shown above can be expressed as:

$$\frac{Y(s)}{F(s)} = \frac{1}{ms^2 + K_{yy} + K_{iy}G(s)} \tag{4.1}$$

The transfer function of equation (4.1) in the frequency domain can be expressed as:

$$\frac{Y(j\omega)}{F(j\omega)} = \frac{1}{-m\omega^2 + K_{yy} + K_{iy}G(j\omega)} \tag{4.2}$$

where $Y(j\omega)$ is the Fourier transform of the displacement $Y(s)$, and $F(j\omega)$ is the Fourier transform of excitation force $F(s)$. With small rotor gap perturbation, the magnetic bearing system can be modelled as a typical linear second order mass-spring-damping system, that is the bearing dynamics could be modelled as stiffness and damping, and the system equation of motion can be written as:

$$m\ddot{y} + ky + c\dot{y} = f \tag{4.3}$$

where m, k and c represent the rotor mass, stiffness and damping coefficients respectively. Equation (4.3) can be written in the frequency domain as shown below:

$$\frac{Y(j\omega)}{F(j\omega)} = \frac{1}{-m\omega^2 + k + cj\omega} \tag{4.4}$$

Combining frequency domain equations (4.2) and (4.4), we can obtain the effective stiffness and damping coefficients of the magnetically suspended system, i.e. by separating the real and imaginary parts of equation (4.5):

$$\begin{aligned} k &= K_{yy} + K_{iy}\,\mathrm{Re}(G(j\omega)) \\ c &= K_{iy}\frac{\mathrm{Im}(G(j\omega))}{\omega} \end{aligned} \tag{4.5}$$

If the transfer function of PID controller $G(s)$ is expressed as follows:

$$G(s) = K_p + \frac{K_i}{s} + \frac{K_d s}{1+\tau_d s} \tag{4.6}$$

The effective stiffness and damping coefficient can be expressed by:

$$\begin{cases} k = K_{iy}\left(K_p + \dfrac{K_d\tau_d\omega^2}{1+\tau_d{}^2\omega^2}\right) + K_{yy} \\ c = K_{iy}\left(\dfrac{K_d}{1+\tau_d{}^2\omega^2} - \dfrac{K_i}{\omega^2}\right) \end{cases} \tag{4.7}$$

They are called "effective" or "equivalent" stiffness and damping coefficients because they are not the actual coefficients associated with equation (4.3), and they are obtained using the theoretical frequency dependent controller's transfer

function, $G(j\omega)$. This $G(j\omega)$ may exclude system lags due to digital signal processing, amplifiers, feedback sensor, cross-coupling capability and actuator losses, etc.

In order to obtain the actual stiffness and damping coefficients, the system will be treated as a black box, and the stiffness and damping coefficients are the unknown parameters of the box to be estimated. A multi-frequency Schroeder Harmonic Sequences (SPHS) test signal will be used to persistently excite the suspended object, and the system input (shaking force) and the system output (corresponding suspended object displacements) will be measured online, from which the actual stiffness and damping coefficients will be obtained experimentally in the frequency domain with the method of parameter estimation, which will be introduced next.

4.1.2 Actual stiffness and damping coefficients of electromagnetic suspension system

In the frequency domain, equation (4.3) can be expressed as:

$$F(j\omega) = -m\omega^2 Y(j\omega) + kY(j\omega) + cj\omega Y(j\omega) \tag{4.8}$$

The real and imaginary parts of the Fast Fourier Transform of equation (4.8) are expressed as:

$$\left.\begin{aligned} \mathrm{Re}\left(\frac{F(j\omega)}{Y(j\omega)}\right) &= -m\omega^2 + k \\ \mathrm{Im}\left(\frac{F(j\omega)}{Y(j\omega)}\right) &= \omega c \end{aligned}\right\} \tag{4.9}$$

Therefore, the actual stiffness coefficient k and damping coefficient c of the electromagnetic actuator can be rewritten as:

$$\left.\begin{aligned} k &= m\omega^2 + \mathrm{Re}\left(\frac{F(j\omega)}{Y(j\omega)}\right) \\ c &= \frac{\mathrm{Im}\left(\frac{F(j\omega)}{Y(j\omega)}\right)}{\omega} \end{aligned}\right\} \tag{4.10}$$

These coefficients in equation (4.10) are called "actual" coefficients of the single-axis suspension system of equation (4.3). This is because they take the known system mass m into account and are calculated directly from the measured transfer function in the frequency domain. The measurements include all possible system time lags and losses, and therefore they truly represent the "actual" stiffness and damping properties of the electromagnets.

4.1.3 One DOF parameter estimation algorithm in frequency domain

As can be seen from equation (4.8) there are two parameters in this system to be estimated, and they are the stiffness and damping coefficients of the electromagnetic actuators; namely k and c. Defining the displacement/force transfer function as:

$$G(j\omega) = \frac{Y(j\omega)}{F(j\omega)} \tag{4.11}$$

This complex transfer function can be separated into real and imaginary parts of the Fourier coefficients:

$$G(j\omega) = \begin{bmatrix} (G)^r \\ (G)^i \end{bmatrix} \tag{4.12}$$

Then equation (4.8) can be written as:

$$\begin{bmatrix} (G)^r & -\omega(G)^i \\ (G)^i & \omega(G)^i \\ " & " \\ " & " \end{bmatrix} \begin{bmatrix} k \\ c \end{bmatrix} = \begin{bmatrix} m\omega^2(G)^r + 1 \\ m\omega^2(G)^i \\ " \\ " \end{bmatrix} \tag{4.13}$$

Replacing ω in equation (4.13) with $n\omega_0$ to indicate the discrete frequencies where n is an integer in the range of 1 to N, and ω_0 is the fundamental excitation frequency of the applied force, then we can obtain equation as shown below:

$$\begin{bmatrix} (G)_n^r & -n\omega_0(G)_n^i \\ (G)_n^i & n\omega_0(G)_n^r \\ " & " \\ " & " \end{bmatrix} \begin{bmatrix} k \\ c \end{bmatrix} = \begin{bmatrix} mn^2\omega_0^2(G)_n^r + 1 \\ mn^2\omega_0^2(G)_n^i \\ " \\ " \end{bmatrix} \tag{4.14}$$

The equation (4.14) can be written in standard form as:

$$[W_F]_{2N\times 2}\{\Phi_F\}_{2\times 1} = [C_F]_{2N\times 1} \tag{4.15}$$

where W_F is a $2N \times 2$ matrix containing Fourier coefficients of the transfer function of the displacement and applied force, Φ_F is a $2N \times 1$ matrix containing the parameters to be estimated, and C_F is a $2N \times 1$ matrix containing the Fourier

coefficients of the transfer function of the displacement, applied force and mass. From the theory of least-square estimator, the estimation coefficients matrix $\hat{\Phi}_F$ is proposed to satisfy all $2N$ equations. Define an error vector $\vec{E} = (E_1, E_2, ..., E_{2N})^T$ as follows:

$$\vec{E} = C_F - W_F \hat{\Phi}_F \tag{4.16}$$

The $\hat{\Phi}_F$ is determined in such a way that the criterion J:

$$J = \sum_{i=1}^{2N} E_i^2 = \vec{E}^T \vec{E} \tag{4.17}$$

is minimum. To minimize J, differentiate J with respect to Φ_F and equate the result to zero, which is as shown below:

$$\left. \frac{\partial J}{\partial \Phi_F} \right|_{\Phi_F = \hat{\Phi}_F} = -2W_F^T C_F + 2W_F^T W_F \hat{\Phi}_F = 0 \tag{4.18}$$

From equation (4.18), the least-square identifier $\hat{\Phi}_F$ for the coefficient matrix can be solved as:

$$\hat{\Phi}_F = (W_F^T W_F)^{-1} W_F^T C_F \tag{4.19}$$

It is in this manner that the stiffness and damping coefficients of electromagnetic actuators can be estimated by measuring the excitation force and the corresponding displacement.

4.1.4 Model validation and statistical information of estimated parameters

The validation of the system model by the simple comparison of theoretical and experimental results is not a satisfactory measure of its validity. A reasonable solution to the problem is by driving the system with the coefficients estimated under various operating conditions, thereby comparing the magnitude of the difference or errors to that measured during the course of the experiment. In this aspect, the goodness of fit, R^2, calculation in the estimation program provides a quantitative measure of the model validity, when interpreted in conjunction with the confidence bounds associated with each parameter [98]. R^2 can be corrected for the degrees of freedom by:

$$\overline{R}^2 = 1-(1-R^2)\frac{n-1}{n-k} \tag{4.20}$$

where $\overline{R}^2$ is a measure of goodness of fit of the whole experimental data, and k is the number of coefficients to be estimated. However, in many cases, a well-fitted regression may still contain some insignificant coefficients. The significance test for the estimated coefficients is established by introducing a scalar, w, representing the sum of squares of the residual error. w_i^2 can be estimated as:

$$w_i^2 = \frac{(1-R^2)(\Sigma s_i^2)}{n-3} \tag{4.21}$$

where subscript i represents the corresponding coefficient to be estimated. Σs_i^2 determines the total sum of square error from the regression estimate. The standard error of the estimated coefficient can be described as:

$$s.e._i = w_i \sqrt{j\text{th diagonal element of } (W_F^T W_F)^{-1}} \tag{4.22}$$

The standard *t*-ratios are obtained by dividing the estimated coefficients by the corresponding standard errors. Coefficients estimated will be considered to be significant, i.e. non-zero, if the *t*-value is greater than the value obtained from standard *t*-distribution tables for a 95 percent confidence interval.

4.1.5 One DOF parameter estimation procedure

The one DOF parameter estimation procedure is shown in Figure 4.2. The force signal $f(t)$ and the corresponding displacement $y(t)$ is sampled and digitized. A discrete-time, Fast Fourier Transform (FFT) is applied to the acquired signals $f(t)$and $y(t)$, and then based on the equation (4.11), $G(j\omega)$ can be constructed, which provides the data to form the arrays of W_F and C_F in the equation (4.14). The least-square identifier $\hat{\Phi}_F$ is then determined using the equation (4.19). Lastly, based on the equations (4.20), (4.21), and (4.22), statistical tests are performed to validate the system model and evaluate results.

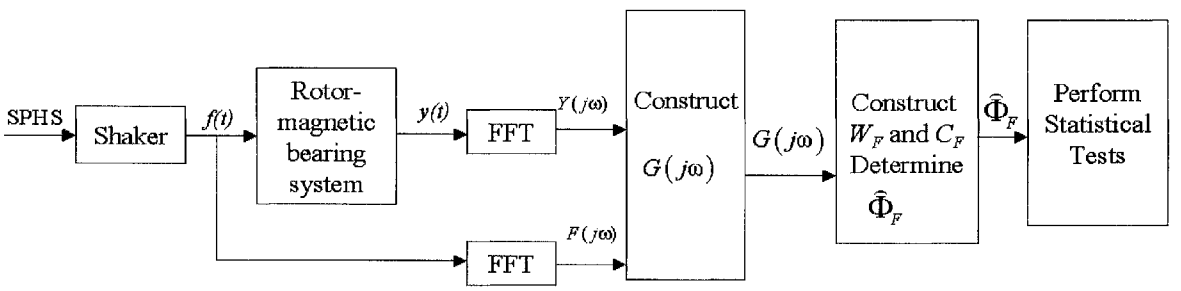

Figure 4.2: Parameter estimation procedure for one DOF rotor-bearing system

4.2 Design of test rig

The test rig is mainly composed of top cover, base, middle platform with lamination target, upper E-frame and lower E-frame. The E-frame is made of laminated silicon steel, with copper coils wrapped around. There is an air gap between the E-frames and the middle platform. The E-frames can generate magnetic force on the platform to suspend it in the magnetic field. The platform can move only in one degree of freedom along the 4 vertical sliding shafts. The eddy current probe is used to measure the displacement of the middle platform.

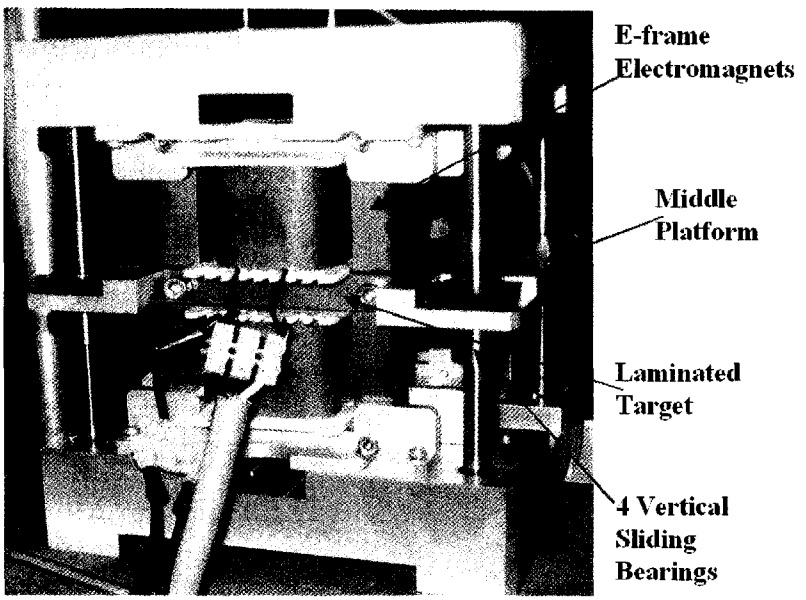

Figure 4.3: Photograph of the one DOF test rig

The parameters' values of the E-frame actuator are as follows:

Table 4.1: Basic dimensions of the electromagnetic actuator

The width of the left arm	13 mm
Nominal air gap length	1 mm

The thickness of the structure (into the plane)	20 mm
The number of coil turns	200
The mass of the middle platform	1.06 kg
The cross section area of left arm	260×10^{-6} m^2
Resistance of coil	1 ohm
Thickness of lamination	0.23 mm

4.3 Experimental results

4.3.1 Experimental setup

The instrumental arrangement for the frequency domain parameter estimation of the stiffness and damping coefficients of the electromagnetic suspension system is as shown in the schematic of Figure 4.4. The H-shaped rigid middle platform is suspended by the magnetic forces generated by a pair of E-frame electromagnetic actuators. Its coil currents are actively controlled by a digital PID controller via a PC using the dSPACE ds1103 controller board.

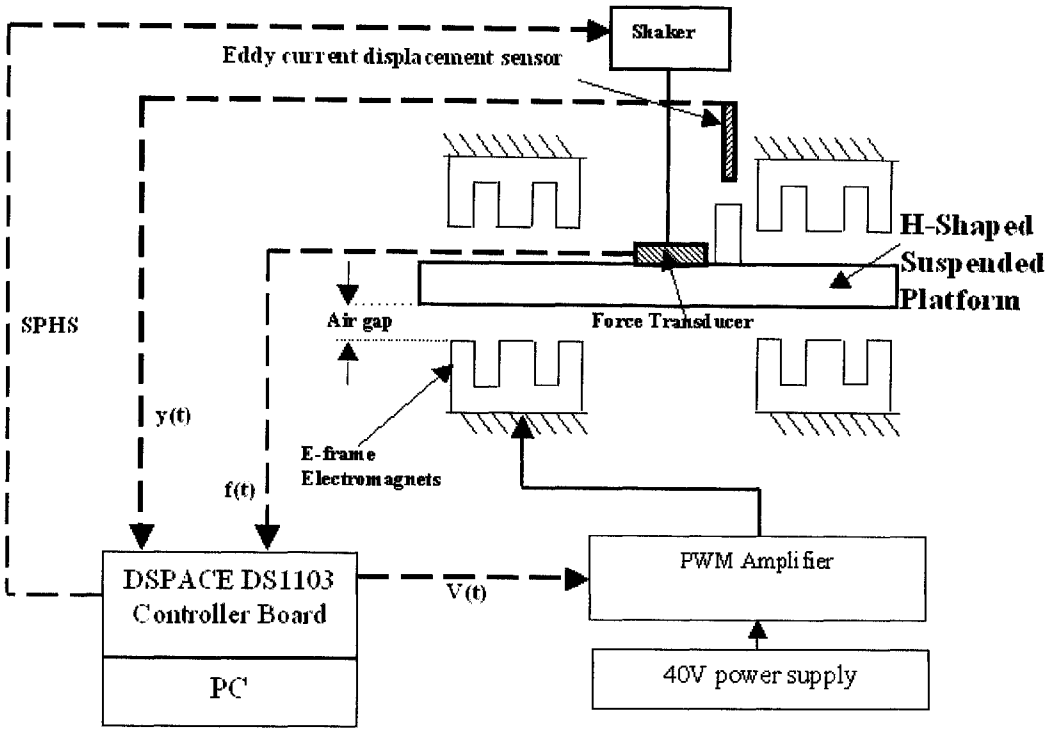

Figure 4.4: Scheme of instrumental arrangement

An eddy current probe and force transducer are used to measure the displacements of the platform and its excitation forces respectively. The displacement and force signals are connected to the PC via the ds1103 ADCs, where they are transformed into frequency-domain signals by FFT software. The photograph for the experimental setup in Figure 4.5 shows the $160 \times 160 \times 12$ mm^3 and 1.06 kg H-shaped platform being constrained to move only in the vertical direction by means of 4 sliding bearing with negligible friction. The air gap between the electromagnets and the middle platform is set as 1 mm. The DC bias premagnetization current for the electromagnets is 0.3A. The sampling rate of the digital PID close loop control system is set at 5 kHz to avoid signal aliasing and provide adequate control bandwidth.

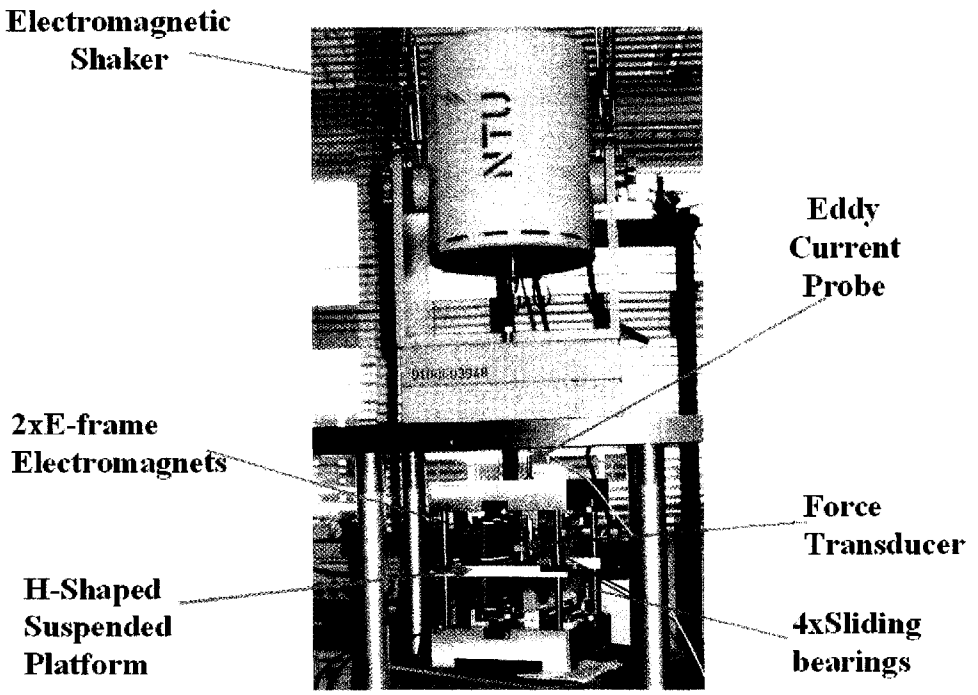

Figure 4.5: Photograph of experimental setup

A broadband SPHS multi-frequency test signal with bandwidth of 1 to 200Hz and fundamental frequency of 1 Hz is used to persistently excite all modes in the suspended system. The mathematical formulation of SPHS is attached in Appendix A. If this is done with the sweep method, i.e. by applying a test signal at each frequency in turn, it may require a long time and the system response may be unacceptable. This digital signal is constructed in MATLAB's software and fed to a shaker via the ds1103 DAC.

The suitable estimation bandwidth selected is 10 Hz, i.e. if the discrete excitation frequency concerned is 25 Hz, then the chosen lower and upper frequency limits of the transfer function in equation (4.14) are 20 Hz and 30 Hz respectively. In addition, Figure 4.6 shows that signal averaging of 5 periods is adequate to reduce the effect of noise on the displacement and force signals.

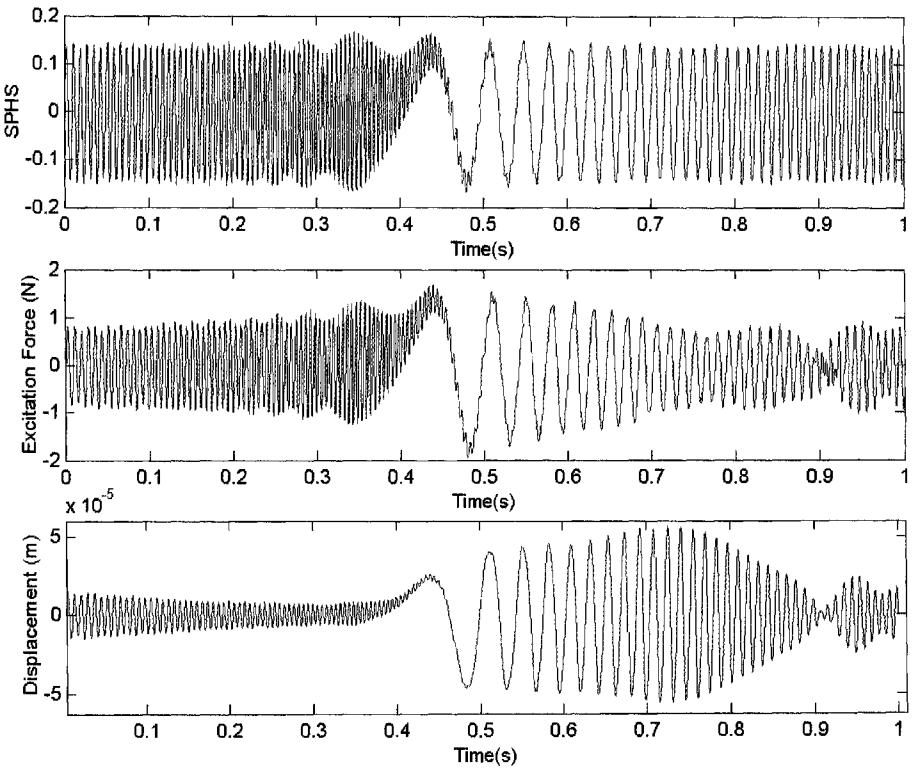

Figure 4.6: SPHS and the averaging effect of 5 periods of the force and displacement signals

4.3.2 Comparisons of effective and actual stiffness and damping coefficients

Effective stiffness and damping coefficients, and actual ones are compared and shown in Figure 4.7. Based on equation (4.5), the effective stiffness and damping coefficients of the electromagnetic actuator in this experiment can be obtained. It can be seen from Figure 4.7 that the effective stiffness and damping coefficients of the electromagnetic actuator are frequency dependent and smooth in nature. The actual stiffness and damping coefficients are obtained at discrete excitation

frequencies with the method of one DOF frequency domain parameter estimation introduced above.

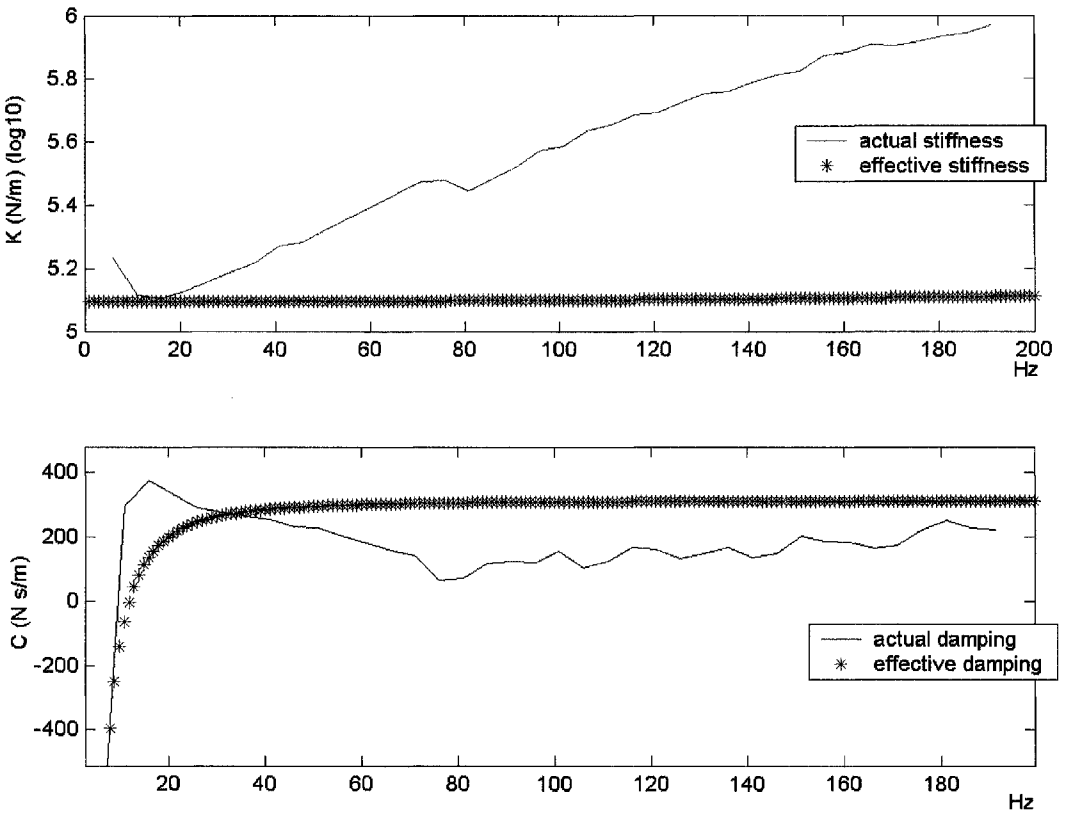

Figure 4.7: Comparisons between effective and actual stiffness and damping coefficients

Figure 4.7 also shows that the effective stiffness obtained is rather flat, but the actual stiffness increases with frequency. The effective damping is quite flat above 60 Hz, while the actual damping fluctuates throughout the frequency range. Also, the values of actual stiffness and damping coefficients differ from the effective ones. This is because the effective characteristics of electromagnetic actuator are calculated in ideal conditions, i.e. only requiring the theoretical input and output of the digital controller. However, in practice, because of non-linearity in electromagnets, magnetic flux losses such as leakage, hysteresis, fringing effects,

time-delay effects by eddy-currents and limited amplifier bandwidth, the actual coefficients will differ greatly from the effective ones. Therefore, the effective characteristics of the electromagnetic actuator cannot accurately represent its actual properties.

The actual stiffness and damping coefficients estimated are verified with the accompanying statistical information as shown in Figure 4.8. It is observed that the goodness of fit obtained is very high through out the frequency domain, maximum and minimum values are 0.996 and 0.988 respectively. On the other hand, a poor goodness of fit on the system model could be due to modelling, linearization and lumping errors.

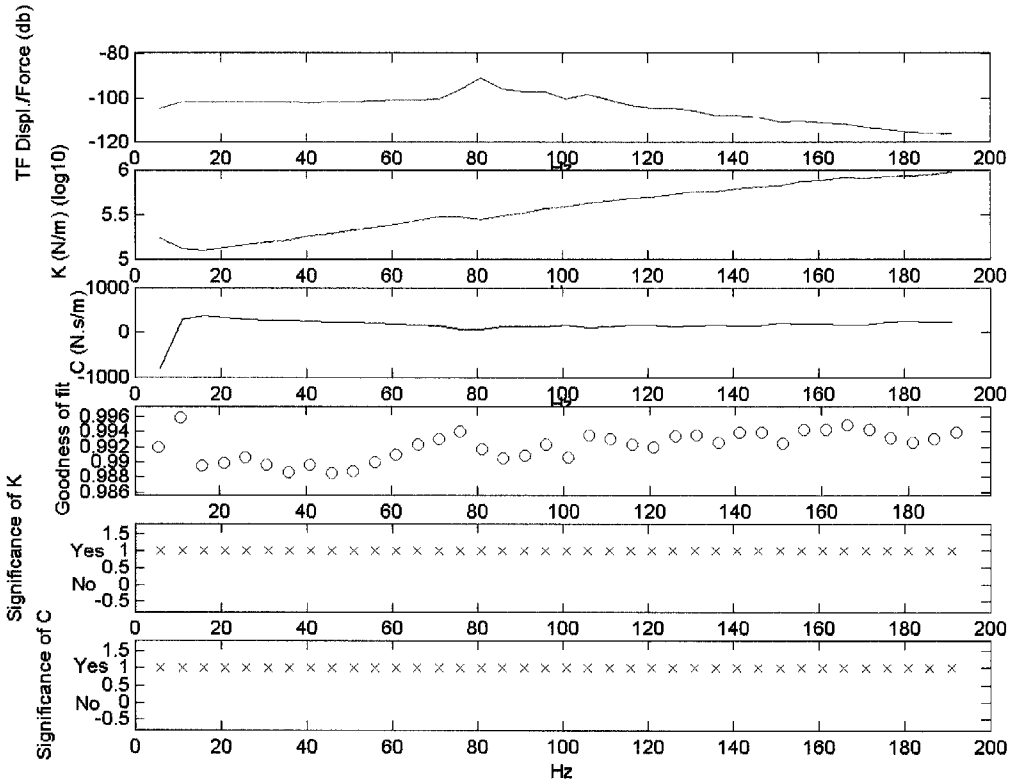

Figure 4.8: Statistical information on the estimated stiffness and damping coefficients

4.4 Influences of controller parameters on system responses

By digitally varying the gain constants of the PID controller, the system's dynamic characteristics – stiffness and damping of electromagnetic actuator – can also be changed. The influences of controller parameters on system dynamic characteristics can be observed by calculating the actual stiffness and damping coefficients, while these influences cannot be fully known by obtaining effective stiffness and damping coefficients. The system response that is represented as the amplitude of close loop system transfer function can be used to illustrate the changes of system dynamic characteristics.

4.4.1 Influences of varying proportional feedback

Figure 4.9 shows that varying the proportional feedback gain has the expected effect of increasing system stiffness coefficients, and therefore the resonant frequency of system is increased. It needs to be mentioned that with the increase of proportional gain, the system damping is increased in the low frequency range, but is decreased beyond the low frequency range. Therefore, the system response around the resonant frequency is increased with the increase of K_p, as is shown in the system response graph of Figure 4.9. However, based on equation (4.7) of obtaining effective stiffness and damping, the proportional gain K_p should not affect system damping at all.

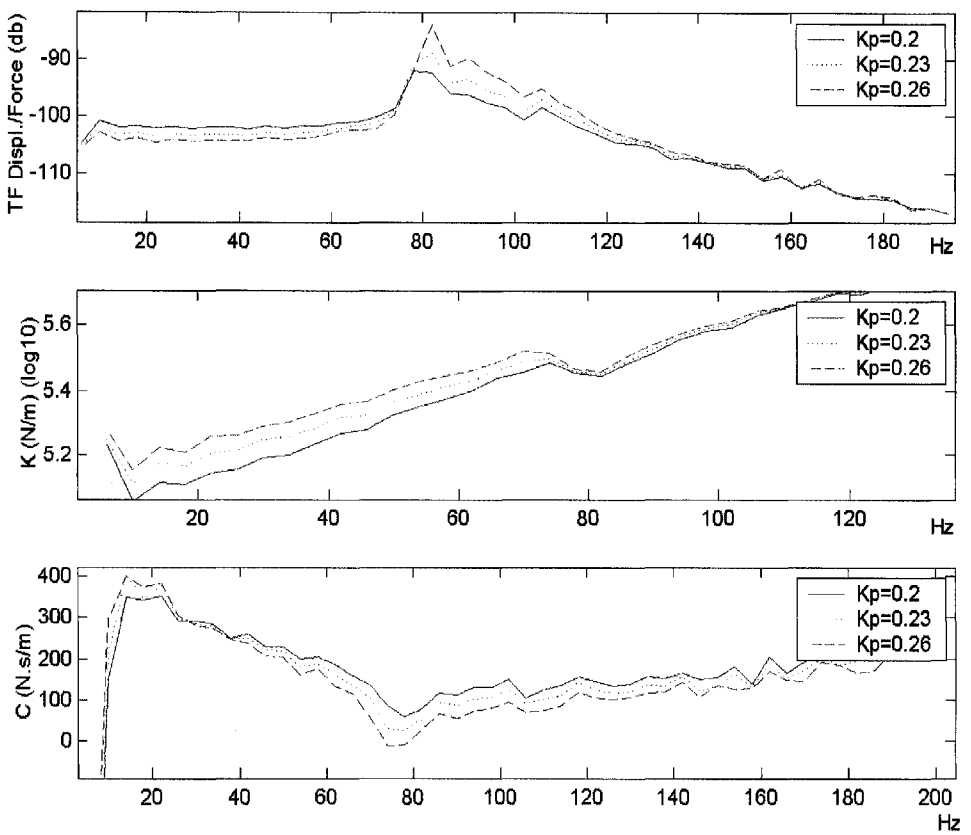

Figure 4.9: Estimated stiffness and damping coefficients with varying proportional feedback

4.4.2 Influences of varying integral feedback

Figure 4.10 and Figure 4.11 show the effects of varying integral feedback on the system response. From Figure 4.11 it can be seen from the system transfer function that by increasing the integrator gain, the amplitude response of system at natural frequency will also be increased. It is also observed that integral feedback has dominant influences on low-frequency response but has negligible effect on the high-frequency response. This is consistent to integral feedback being well known to eliminate position error in the presence of static loads. Damping coefficients of electromagnetic actuator are decreased significantly with the increase in integrator gain K_i in low frequency range.

It needs to be mentioned that the integrator gain has influences not only on the damping of electromagnetic actuator, but also on its stiffness. Figure 4.10 shows that stiffness of electromagnetic actuator in low-frequency range is increased with the increase of K_i. On the contrary, using the theoretical obtained $G(j\omega)$, it was reported that integral term had little effect on the stiffness coefficients. This may be due to the effective stiffness coefficients calculations based on the ideal conditions of equation (4.5). It is noted in Figure 4.10 that an increase in K_i decreases the damping coefficient at low frequencies, as this is due to the integrator providing the low pass filter action.

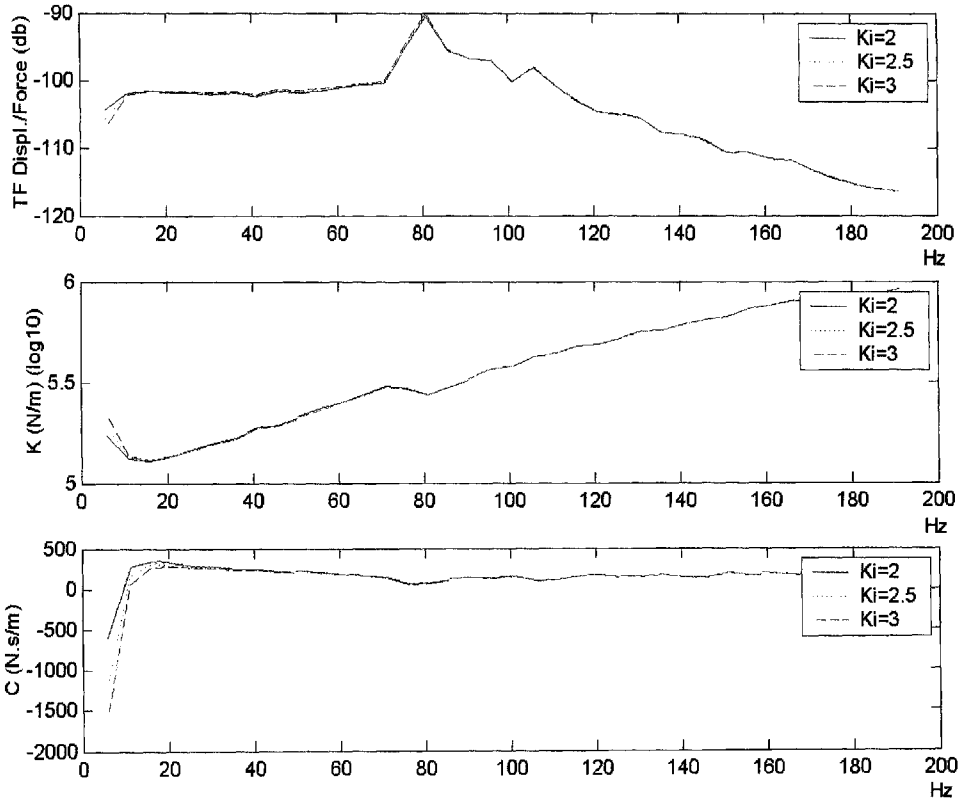

Figure 4.10: Estimated stiffness and damping coefficients with varying integral feedback

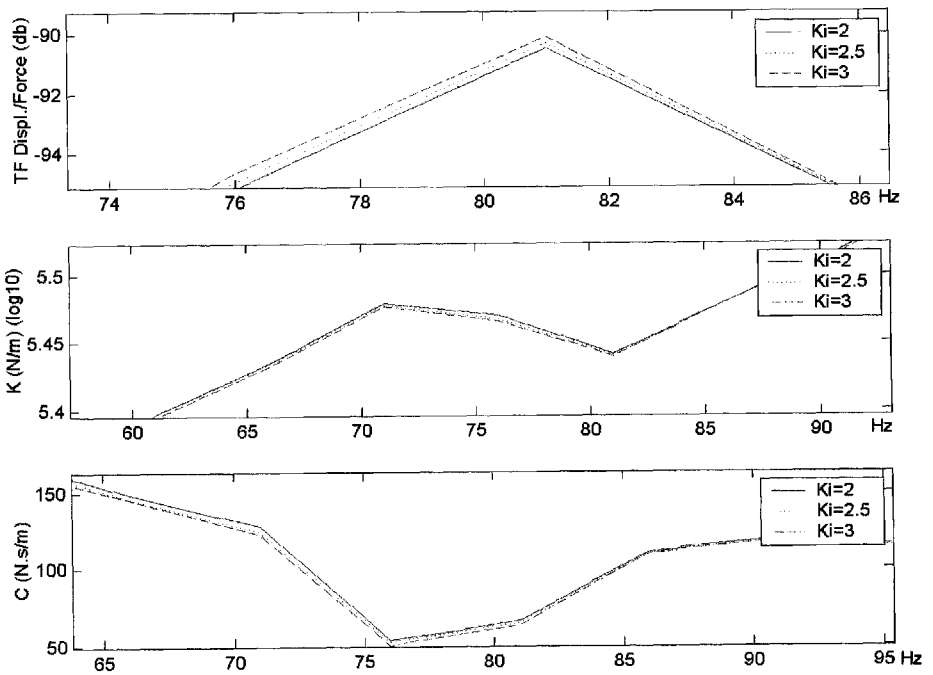

Figure 4.11: Expansion of Figure 4.10 in the neighbourhood of natural frequency

4.4.3 Influences of varying derivative feedback

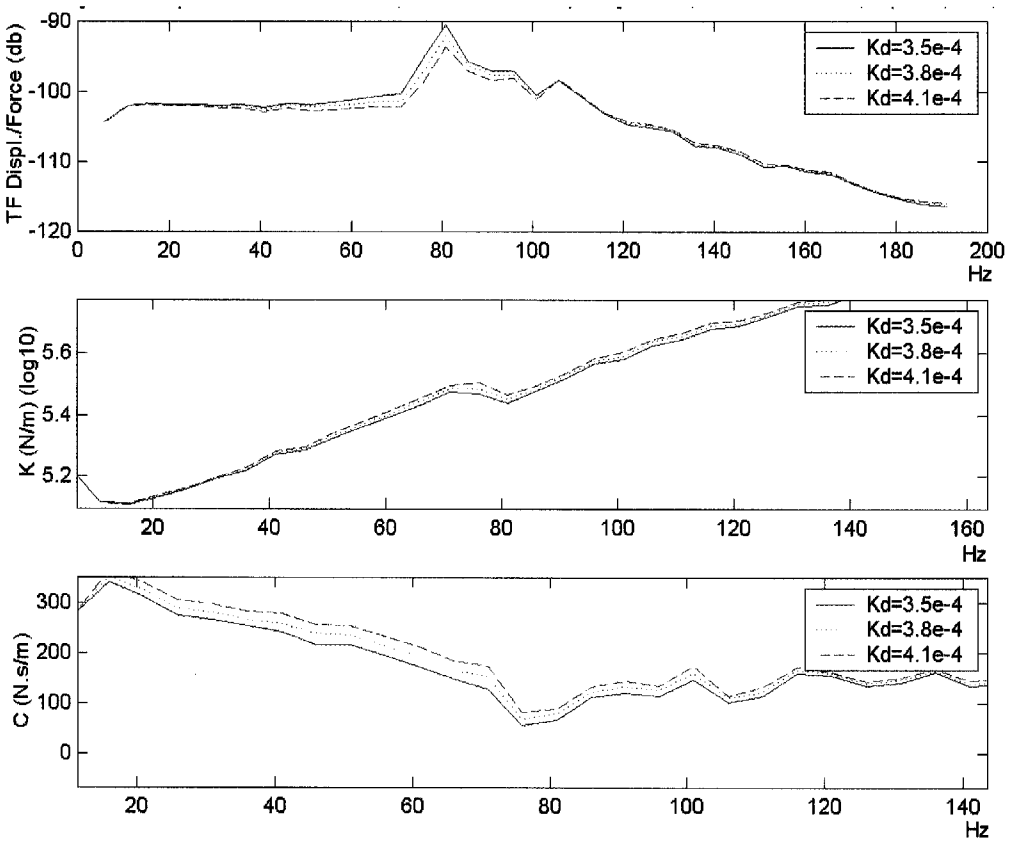

Figure 4.12: Estimated stiffness and damping coefficients with varying derivative feedback

From Figure 4.12, it can be seen that increasing derivative gain can increase the damping coefficients, and therefore the amplitude of system response at the resonant frequency is reduced significantly. It is also shown in Figure 4.12 that stiffness coefficients in low-frequency range are affected a little by the derivative gain, but beyond the low frequency range, they are increased with the increase of the derivative gain, which cannot be realized by obtaining the effective stiffness and damping coefficients from equation (4.7).

In general, the noise in the responses from Figure 4.9 to Figure 4.12 is attributed to the switching frequency of 25 kHz from the PWM amplifiers that we use in the

experiments to drive the pair of electromagnets. Although we have implemented several noise reduction techniques, such as twisted and shielded cables, to reduce the PWM switching noises, the noise signals are still present with a magnitude level of around 100 mV. In addition, there are also other factors such as eddy current and hysteresis losses in electromagnets. There is also a possibility of the switching noise inducing electromagnetic interference with the eddy current displacement probe. However, in spite of this noise problem, the system stability in levitating the platform is still robust, which is confirmed by applying impulse on the levitated platform with a mallet.

Chapter 5 Parameter estimation and actuator characteristics of magnetic bearings for axial flow blood pump applications

This chapter introduces the principles of the frequency domain parameter estimation technique with statistical analysis, which is adopted to estimate the stiffness and damping coefficients of the HMBs system. A specially designed test rig facilitates the estimation of the bearing's coefficients in air - in both the radial and axial directions. Experimental estimation results show that the dynamic characteristics of the HMBs system are dominated by the frequency dependent stiffness coefficients. By injecting a wideband signal onto the rotor through the HMBs, experimental results show that the actuator gain can be determined to extend the technique here to the identification and monitoring of the pump's dynamic properties under normal operating conditions.

5.1 System's dynamic model and parameter estimation procedure

The experiment design for parameter estimation is usually tackled by the following procedure:

a). formulating a mathematical equation for the model based on physical assumptions describing the system's dynamics,

b). selection of a suitable excitation force signal,

c). selection of a suitable method and location to inject this excitation force signal into the dynamic model,

d). selection of a data analysis package that provides good sampling rate,

e). method of validating the dynamics model and evaluating the estimated results using statistical methods.

These five factors are significant contributions towards achieving the estimated system's dynamics support coefficients with minimum variance. A multi-frequency signal, such as the SPHS which has been successfully employed by Lim *et al.* [75][76] to persistently excite a simple second-order model test rig, will be adopted as the excitation force signal in the following parameter estimation procedures.

5.1.1 One DOF dynamics model

The one DOF dynamics model formulated here will be used to estimate the structural dynamics support parameters of the experimental test rig, as well as the HMBs in the radial and axial directions.

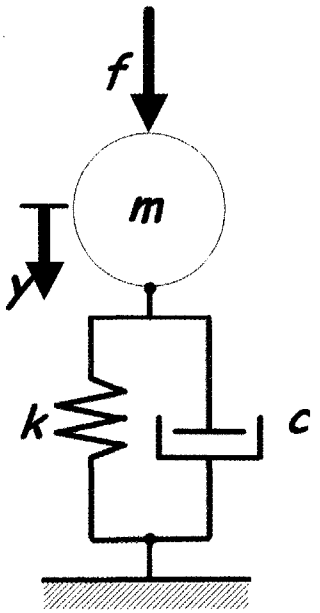

Figure 5.1: General model of the one DOF rotor-bearing system

Referring to Figure 5.1, consider a mass m supported by two linearised spring and damping coefficients. The equation of motion with a wide band excitation force f applied in the y-direction is:

$$m\ddot{y} + ky + c\dot{y} = f \tag{5.1}$$

Equation (5.1) can be expressed in the form of frequency domain:

$$F(j\omega) = -m\omega^2 Y(j\omega) + kY(j\omega) + cj\omega Y(j\omega) \tag{5.2}$$

Following the same algorithm of one DOF parameter estimation described in Chapter 4 from equation (4.11) to equation (4.15), the same standard form of equation (4.15) can be obtained, which is repeated below:

$$[W_F]_{2N\times 2}\{\Phi_F\}_{2\times 1} = [C_F]_{2N\times 1} \tag{5.3}$$

Similarly, following the equations (4.16) to (4.19), the same least-square identifier $\hat{\Phi}_F$ shown in equation (4.19) can be obtained:

$$\hat{\Phi}_F = (W_F^T W_F)^{-1} W_F^T C_F \tag{5.4}$$

5.1.2 Two DOF rotor-bearing model with direct- and cross-axes coefficients

The following 2 DOF model will be used to estimate the dynamics support parameters of the HMBs in the radial directions. Like squeeze film dampers [100], the HMBs' dynamics support parameters can be modelled by eight linearised direct- and cross-axes coefficients. Referring to Figure 5.2, consider a rotor of mass *m* supported by the direct- and cross-axes springs and dampers modelled by eight linearised coefficients of the HMBs.

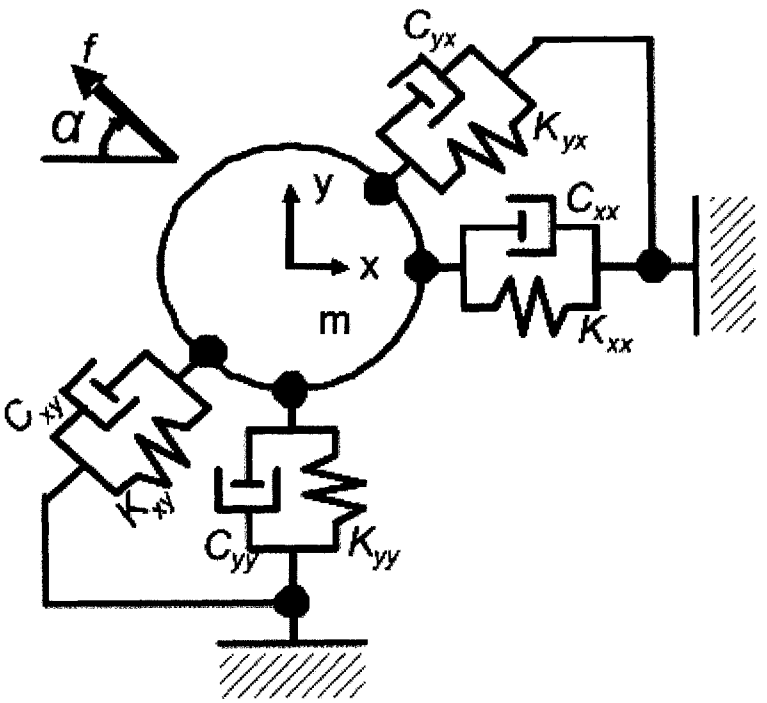

Figure 5.2: Two DOF rotor-bearing system modeled with eight linearised direct- and cross-axes coefficients

$$m\ddot{x} + C_{xx}\dot{x} + C_{xy}\dot{y} + K_{xx}x + K_{xy}y = \beta_x f \tag{5.5}$$

$$m\ddot{y} + C_{yy}\dot{y} + C_{yx}\dot{x} + K_{yy}y + K_{yx}x = \beta_y f$$

Equation (5.5) can be expressed in the form of frequency domain:

$$(-m\omega^2 + C_{xx}j\omega + K_{xx})X(j\omega) + (C_{xy}j\omega + K_{xy})Y(j\omega) = \beta_x F(j\omega)$$

$$(-m\omega^2 + C_{yy}j\omega + K_{yy})Y(j\omega) + (C_{yx}j\omega + K_{yx})X(j\omega) = \beta_y F(j\omega) \tag{5.6}$$

where f is the excitation force signal applied to the rotor, $\beta_x = b\cos\alpha$, $\beta_y = b\sin\alpha$, $\alpha = \tan^{-1}\left(\beta_y / \beta_x\right)$ is the forcing angle and b is the input transducer coefficient. Defining $G_x(j\omega)$ and $G_y(j\omega)$ as the Fourier coefficients of the transfer function,

$$G_x(j\omega) = \frac{X(j\omega)}{F(j\omega)}$$

$$G_y(j\omega) = \frac{Y(j\omega)}{F(j\omega)} \tag{5.7}$$

The complex transfer function $G_x(j\omega)$ and $G_y(j\omega)$ can be separated into real and imaginary parts as:

$$G_x(j\omega) = (G_x)^r + j(G_x)^i$$

$$G_y(j\omega) = (G_y)^r + j(G_y)^i \tag{5.8}$$

Again, by replacing ω in equation (5.6) with $n\omega_0$ to indicate the use of discrete frequencies where n is an integer in the range of 1 to N, and ω_0 is the fundamental excitation frequency of the applied force, and then expressing equations (5.6), (5.7) and (5.8) in matrix form, equation (5.9) can be obtained:

$$\begin{bmatrix} (G_x)_n^r & (G_y)_n^r & -n\omega_0(G_x)_n^i & -n\omega_0(G_y)_n^i & -1 \\ (G_x)_n^i & (G_y)_n^i & n\omega_0(G_x)_n^r & n\omega_0(G_y)_n^r & 0 \\ " & " & " & " & " \\ " & " & " & " & " \\ " & " & " & " & " \end{bmatrix} \begin{bmatrix} K_{xx} & K_{yx} \\ K_{xy} & K_{yy} \\ C_{xx} & C_{yx} \\ C_{xy} & C_{yy} \\ \beta_x & \beta_y \end{bmatrix} = m(n\omega_0)^2 \begin{bmatrix} (G_x)_n^r & (G_y)_n^r \\ (G_x)_n^i & (G_y)_n^i \\ " & " \\ " & " \\ " & " \end{bmatrix}_{n=1,..,N} \tag{5.9}$$

Similarly, equation (5.9) can be generalized as equation (5.3) and solved by equation (5.4).

5.1.3 Two DOF rotor-bearing model with only direct-axis coefficients

As demonstrated by Burrows *et al.* [100], the cross-axis coefficients in a squeeze film damper can cause the parameters of the bearing in the direct-axis to be incorrectly estimated. For this reason and also as the radial HMBs here are symmetrically designed, this section will introduce the two DOF rotor-bearing model with only direct-axis coefficients. As shown in Figure 5.3, if the forcing angle α is designed at $45°$, the applied force in the vertical direction can be decomposed equally into two components: f_x and f_y in the x and y directions, respectively. The rotor of mass m is supported by only direct symmetric stiffness, $K_{xx} = K_{yy}$, and damping, $C_{xx} = C_{yy}$, coefficients in the x- and y-direction respectively.

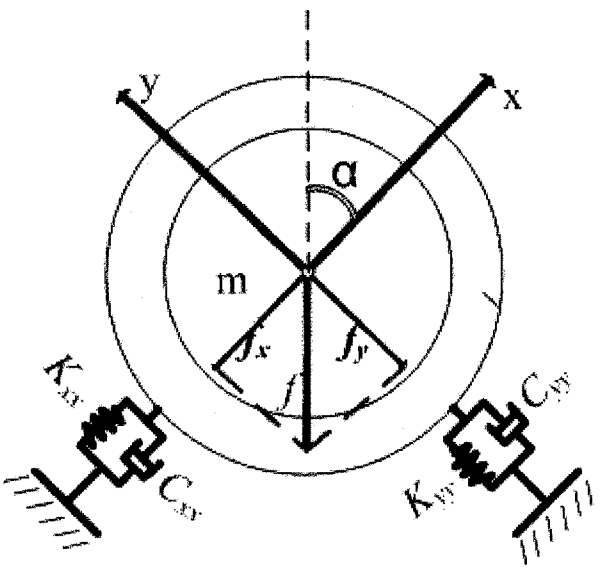

Figure 5.3: Two DOF rotor-bearing model with only direct-axis coefficients

The equation of motion for the rotor-bearing system in the y-direction can be expressed as:

$$m\ddot{y} + K_{yy}y + C_{yy}\dot{y} = f_y = f\sin\alpha \tag{5.10}$$

The parameter estimation algorithm is simplified, as the two-DOF rotor-bearing model is reduced to one as in equation (5.10). Therefore, based on the same one DOF parameter estimation algorithm, we can formulate the following W_F, Φ_F and C_F matrices:

$$W_F = \begin{bmatrix} (G)_n^r & -n\omega_0(G)_n^i \\ (G)_n^i & n\omega_0(G)_n^r \\ " & " \\ " & " \end{bmatrix}$$

$$\Phi_F = \begin{bmatrix} K_{yy} \\ C_{yy} \end{bmatrix} \tag{5.11}$$

$$C_F = \begin{bmatrix} mn^2\omega_0^2(G)_n^r + 1 \\ mn^2\omega_0^2(G)_n^i \\ " \\ " \end{bmatrix}$$

where

$$G(j\omega) = \frac{Y(j\omega)}{F\sin\alpha(j\omega)} = \begin{bmatrix} (G)^r \\ (G)^i \end{bmatrix} \tag{5.12}$$

Similarly, equation (5.11) can be generalized as equation (5.3) and solved by equation (5.4).

5.1.4 Two-DOF parameter estimation procedure

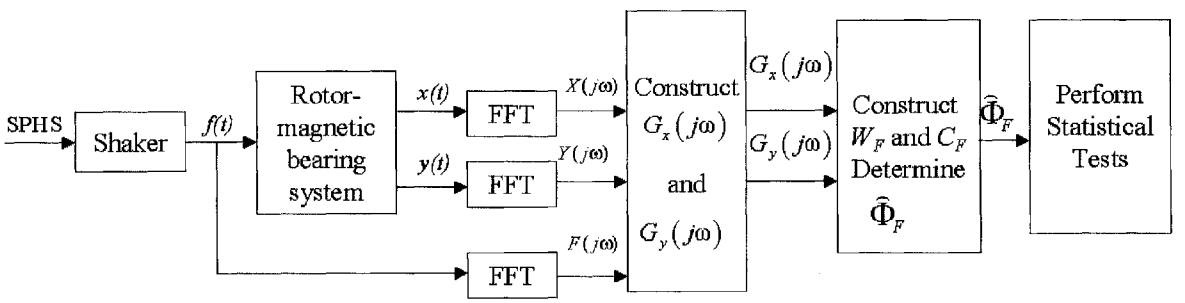

Figure 5.4: Parameter estimation procedure for two DOF rotor-bearing system

As illustrated in Figure 5.4, the parameter estimation procedure for the two-DOF rotor-bearing system is similar to that of one DOF parameter estimation described

in Chapter 4. The force signal $f(t)$ and the corresponding displacements $x(t)$ and $y(t)$ are sampled and digitized. A discrete-time Fast Fourier Transform (FFT) is applied to the acquired signals $f(t)$, $x(t)$ and $y(t)$, and then based on the equation (5.7), $G_x(j\omega)$ and $G_y(j\omega)$ could be constructed, to provide the data to form the arrays of W_F and C_F in the equation (5.11). The least-square identifier $\hat{\Phi}_F$ is then determined using the equation (5.4). Lastly, based on the evaluation methods introduced in Chapter 4 from equations (4.20) to (4.22), statistical tests are performed to validate the system model and evaluate results.

5.2 Preparatory experiments

5.2.1 Description of the test rig

It is clear from the modelling of the one and two DOF dynamics systems earlier, that the important measurement to be undertaken in the radial and axial parameter estimation of the HMBs would be the force and displacement variables. Figure 5.5 shows a photograph of the multi-purpose test rig that has been designed to achieve the following:

a). measurement and injection of the excitation force into the dynamics model,

b). restraint of the angular deflexion of the rotor in the orthogonal directions,

c). adjustment of the air gap between rotor and stator of the HMBs, and

d). measurement of the x- and y- direction displacements using eddy current probes.

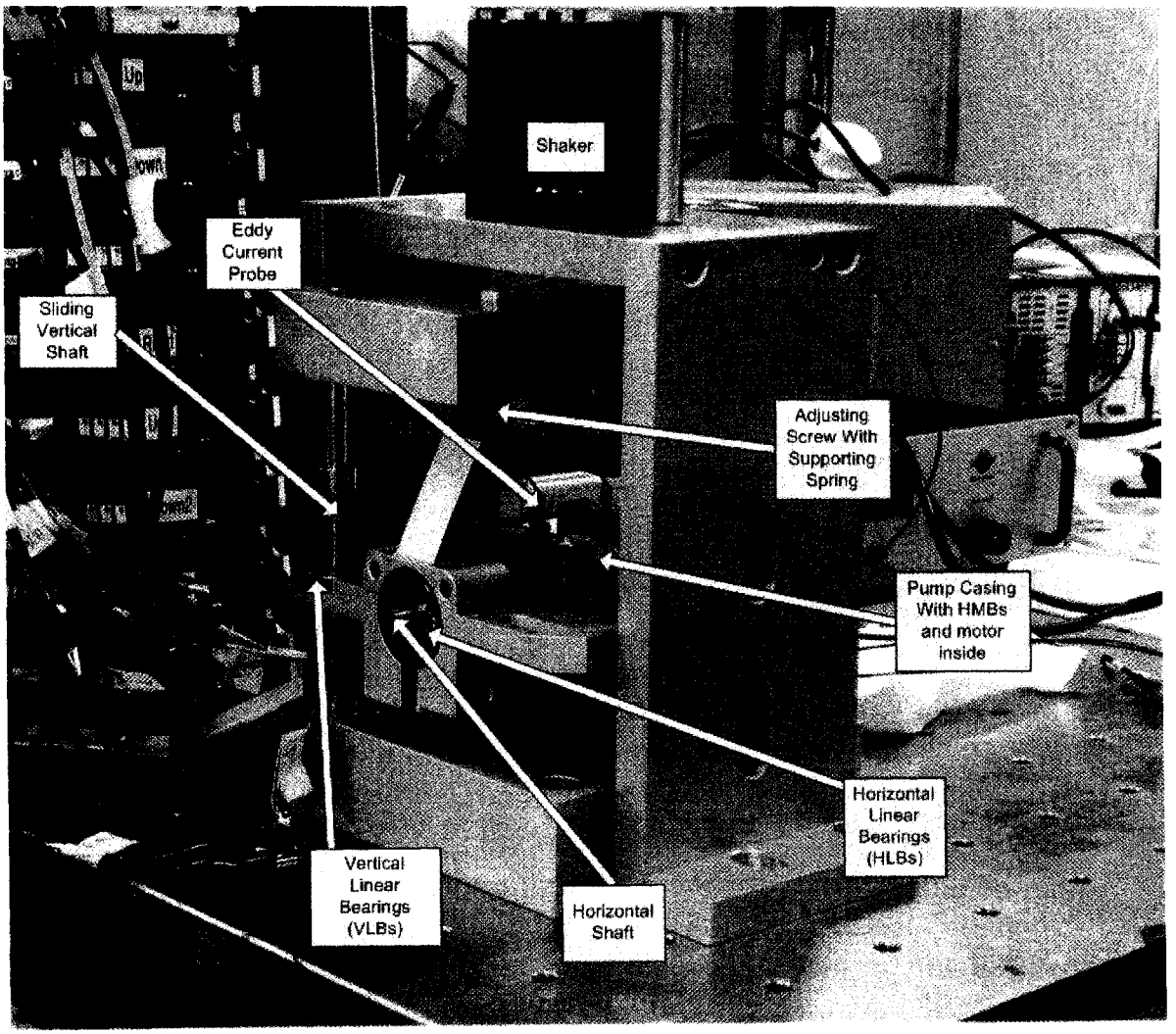

Figure 5.5: Test rig used for parameter estimation of the HMBs system

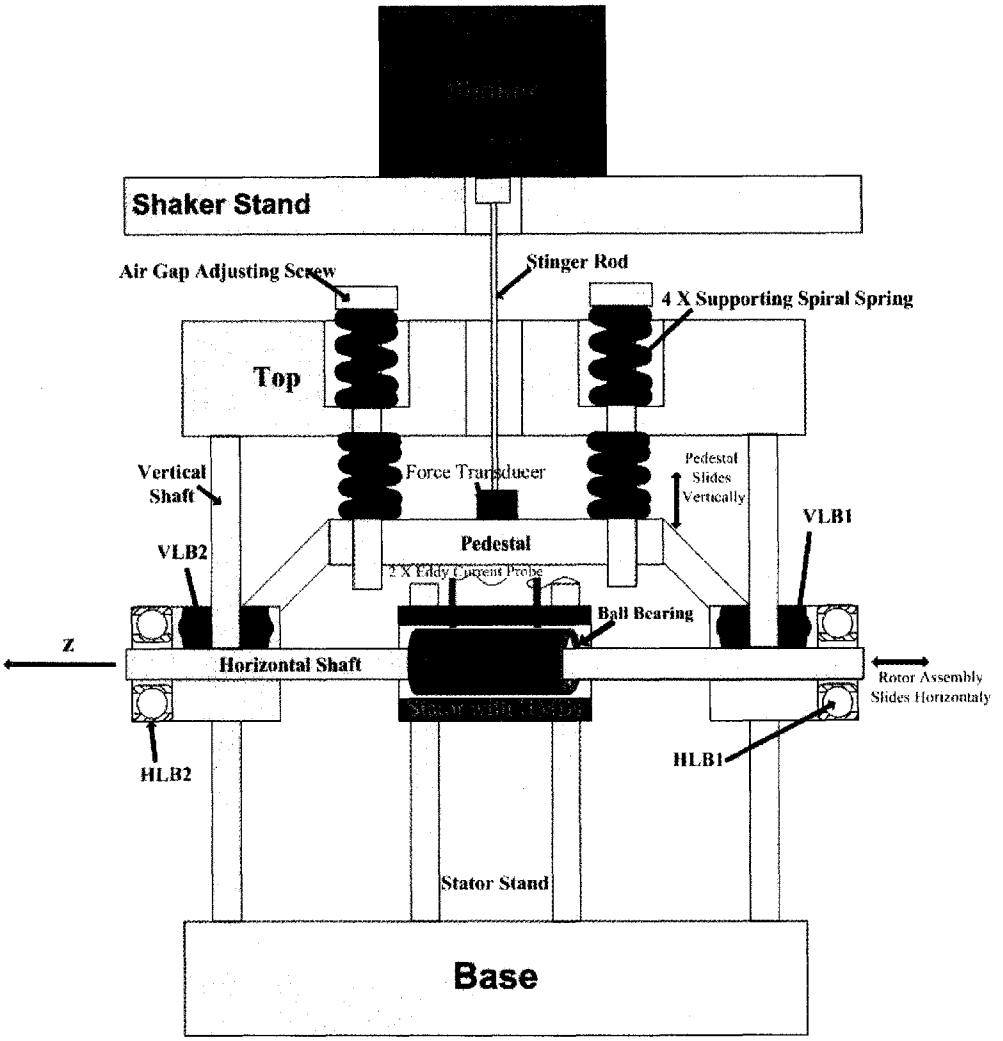

Figure 5.6: Schematic arrangement for parameter estimation test rig

The schematic arrangement in Figure 5.6 shows an 8 mm diameter horizontal steel shaft is assembled to the rotor by means of two rolling element bearings. This design allows the rotor to rotate freely on the two bearings, however, the rotor axial movement relative to the shaft is fixed by two end collars. The horizontal shaft is able to slide freely on the two horizontal linear bearings (HLBs) which are mounted onto the pedestal. The pedestal assembly consisting of the horizontal shaft, rotor, and pedestal, is able to slide vertically along the two 8 mm diameter vertical steel shafts located diagonally across the pedestal. The two ends of the

vertical shafts are fixed to the top and base plates respectively. The stator housing of the pump is held by two stator stands rigidly fixed onto the base plate. During the start of the experiment, the concentric adjustment of the rotor and stator bore is facilitated by the two vertical adjusting screws that are inserted through the four supporting spiral springs. This is due to adjustment of the pedestal height, which is connected to the rotor, directly affecting the air gap thickness between the rotor and HMBs' stator. Besides realizing the application of excitation force onto the rotor, the spring supported pedestal also assists in the partial levitation of the rotor assembly, which otherwise would be slightly too heavy for the HMBs' actuator forces to manage. The design also ensures that only rotor translational movement is allowed in the HMBs' stator bore and that axial movement is restrained.

A force transducer (B&K) is connected to a shaker and mounted on top of the pedestal to measure the excitation force. The SPHS test signal is fed to the shaker, which is mounted on a stand, to perturb the pedestal and the eddy current probes are used to measure the rotor displacement in x- and y- directions. During the experiment, the SPHS is digitally generated in the dSPACE ds1103 with MATLAB Simulink and then pre-recorded onto the TEAC RD-145T DAT DATA Recorder for playback purposes. It is in this manner, that the pedestal is persistently excited by the shaker (B&K 4810) with the SPHS test signal via the tape recorder. The DSPACE ds1103 acquires the force and the resulting displacements signals real-time for the successful implementation of the online parameter estimation procedure. In order to minimize the variance of the estimated coefficients, five periods of measured signals are averaged throughout the experiments.

5.2.2 Parameter estimation of pedestal structural support using one DOF model

Successful experimental determination of the estimated coefficients for the HMBs requires a good prior knowledge of the supporting structural parameters. Otherwise, the estimated coefficients will be a composite of both HMBs and supporting structure. Awareness of this consequence has led to the performance of structural identification tests on the pedestal support spring stiffness.

For this test, the horizontal shaft with rotor assembly is removed but the pedestal is adjusted to the desired height where the rotor would be concentric with the HMBs' stator bore. The pedestal supported by the four spiral springs could only move in the vertical direction. Hence, the one DOF parameter estimation algorithm is used to estimate the total stiffness coefficient of the spiral springs. The mass of the pedestal is 0.79 kg. The SPHS bandwidth is chosen to be 1 to 100 Hz with a fundamental frequency of 0.5 Hz. Sampling frequency is set at 20 kHz. Based on the procedure of parameter estimation of a one DOF system, the acquired excitation force and displacement signal data are read into the MATLAB program of the one DOF parameter estimation algorithm, from which the estimated results of spring stiffness are then obtained. Figure 5.7 below shows the time domain plots of the excitation force and the corresponding pedestal displacement.

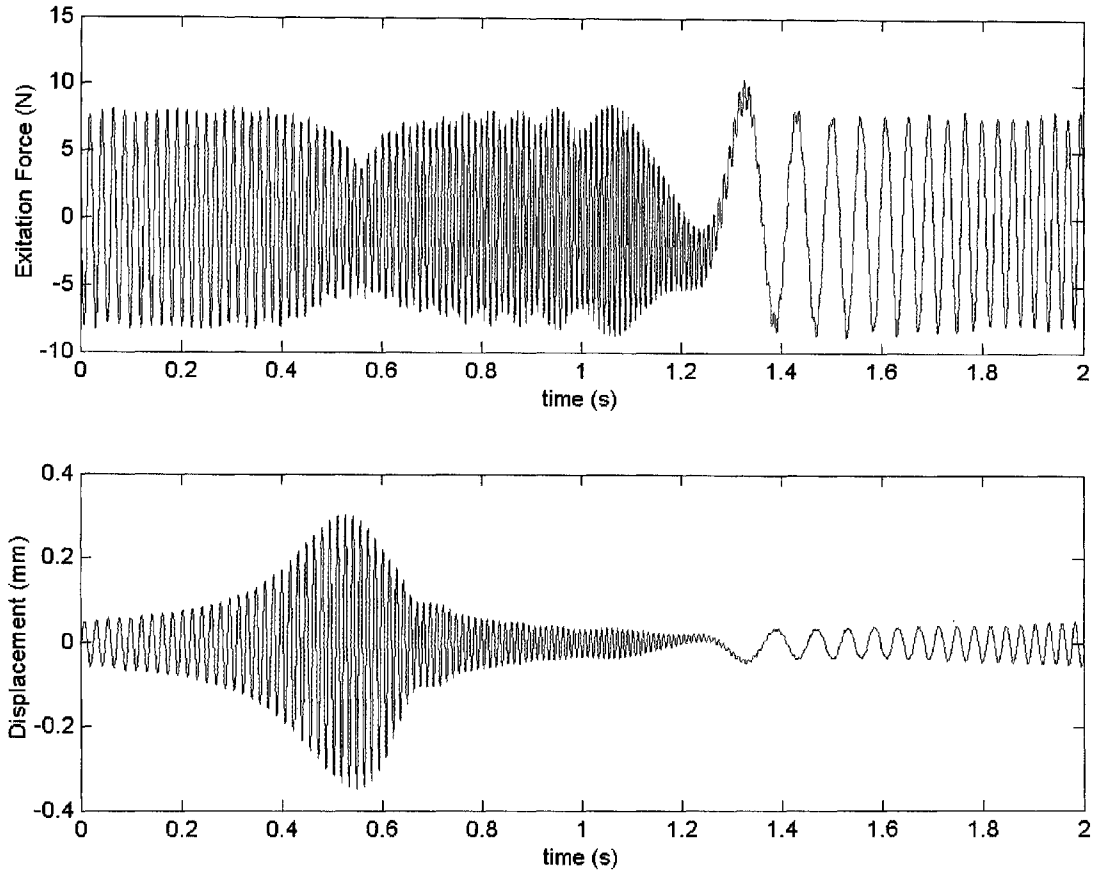

Figure 5.7: Excitation force and displacement plots with 5 periods of signal averaging

In Table 5.1, the estimated stiffness coefficient of 134.5 kN/m indicates that the best goodness of fit of 0.9952 is obtained from using the frequency band of 60 to 70 Hz, i.e. in the neighbourhood of the rig natural frequency. The goodness of fit of almost unity indicates that a perfect mathematical model structure is adopted in the estimation procedure. On the other hand, the damping coefficient as statistically interpreted to be insignificant; that means it could be treated as zero value.

Table 5.1: Parameter estimation of pedestal support spring stiffness with statistics

Frequency Band Used:	60 to 70 Hz
The Goodness of Fit:	0.9952
Stiffness $(kN/m)^{-1}$:	134.5
Damping $(N \cdot s/m)^{-1}$:	-3.682*

Note: * denotes insignificant coefficient(s)

In other wider frequency ranges, we can obtain similar estimation of stiffness and damping, and the goodness of fit are decreased, as shown in Table 5.2, but they are still sufficiently high in the upper range of 0.90 higher. This proves that the model is valid [10][11][100].

Table 5.2: Estimation results of pedestal support spring in different frequency ranges

Frequency Range (Hz)	Goodness of fit	Stiffness $(KN/m)^{-1}$	Damping $(N.s/m)^{-1}$
60-70	0.99	134.5	-3.68
50-80	0.96	134.1	-3.47
40-90	0.94	133.2	-3.42
30-100	0.91	131.8	-3.57

The measured amplitude and phase transfer functions of the pedestal structural system are as shown in Figure 5.8.

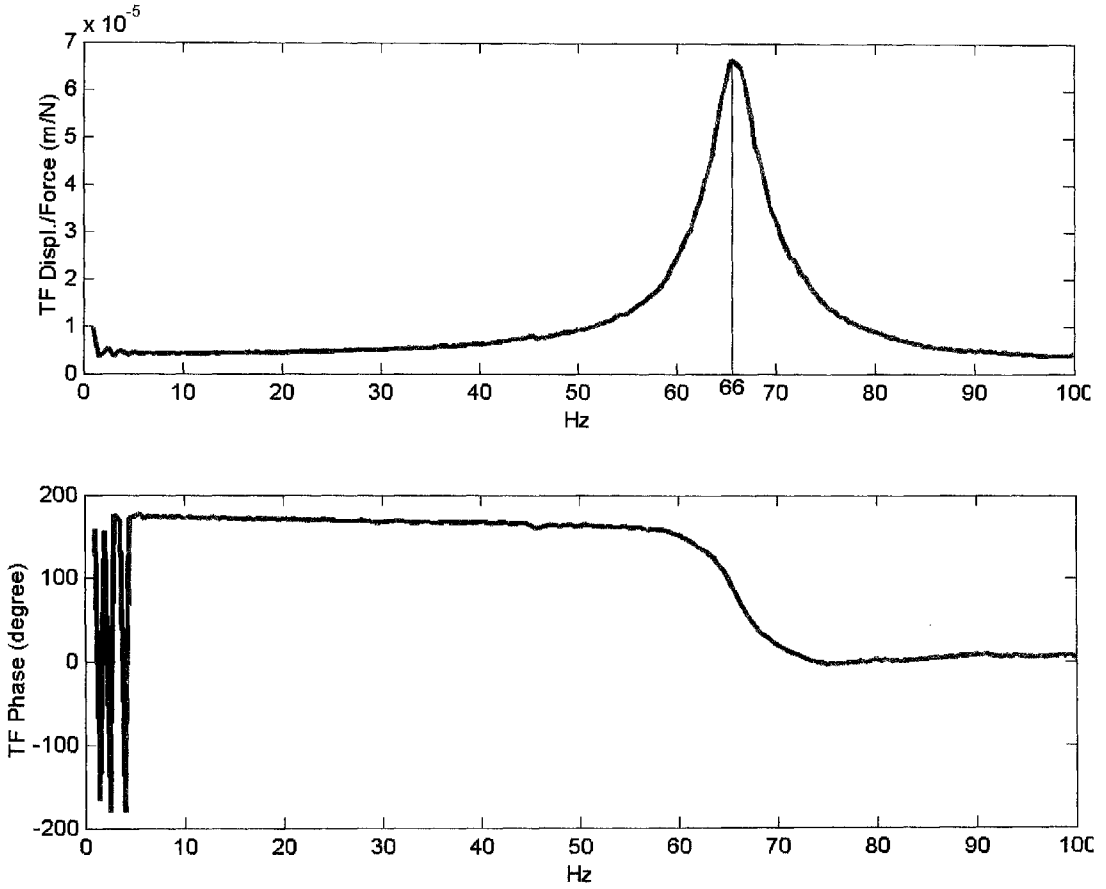

Figure 5.8: Amplitude and phase transfer functions of the pedestal structure

The natural frequency of the pedestal is determined at 66 Hz as shown in Figure 5.8. With the stiffness coefficient estimated at 134.5 kN/m , and based on the equation of system's undamped natural frequency (5.13),

$$\omega_n = \sqrt{\frac{k}{m}} = \sqrt{\frac{134.5 \times 10^3}{0.79}} = 412.6 \text{ rad/s or } 65.6 \text{ Hz} \tag{5.13}$$

we could obtain the theoretical fundamental response frequency of 65.6 Hz, which is in excellent agreement with the experimentally obtained natural frequency of 66

Hz. Hence, in the following radial parameter estimation procedures, the HMBs' stiffness coefficient can be determined by subtracting the pedestal support stiffness from the total estimated stiffness coefficient.

5.2.3 Determination of HMBs' actuator characteristics

The HMBs' actuator gain is one of the important properties of the magnetic bearing system. With the knowledge of actuator gain, the parameter estimation technique introduced here can be potentially extended to in-situ identification of the pump dynamics properties during operating conditions. Furthermore, before the embarkation of the HMBs' parameter estimation procedure, this section investigates the maximum displacement linear operating range of the rotor perturbation limits; the rotor movement range where the HMBs' actuator gain does not change significantly. This is to ensure that the linearised stiffness and damping coefficients adopted in the dynamics model are not violated throughout the experimental investigations. Any violation, however, will be detected and reflected in the goodness of fit calculation in the parameter estimation algorithm, which is the distinct benefit of employing the statistical method.

In order to obtain the HMBs' actuator gain, some minor setup changes have been made to the test rig shown in Figure 5.5. The photograph of the setup, as shown in Figure 5.9, has the shaker removed, and the bottom surface of the force transducer connected directly onto the pedestal, while its top surface is connected to a height adjusting screw. There are two nuts going through the height adjusting screw. By fastening the two lock-nuts on both sides of the top plate, the pedestal with the rotor/shaft assembly is supported by the force transducer alone. Therefore, in this manner, any force applied on the rotor will be transmitted to the force transducer.

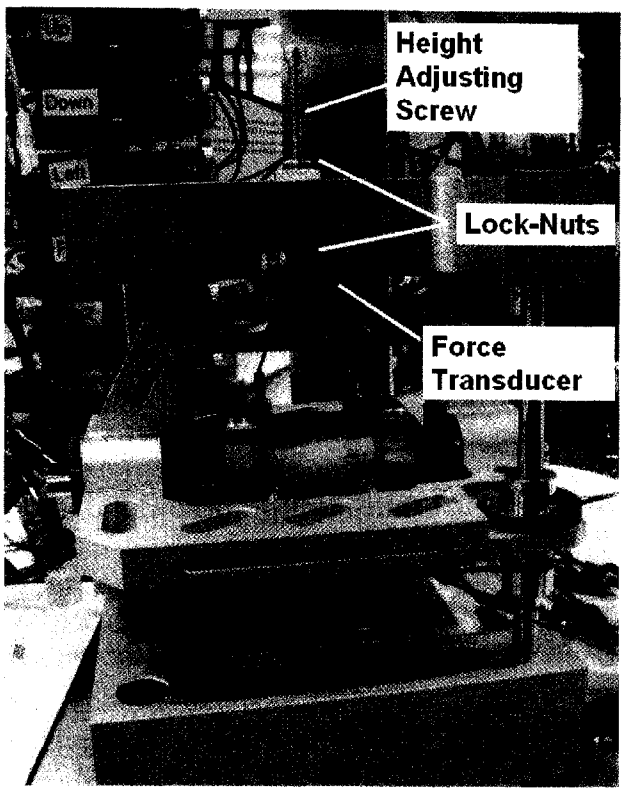

Figure 5.9: Photograph of experimental setup for calibrating actuator gain

5.2.3.1 Frequency response of test rig for calibrating actuator gain

A SPHS (V) test signal is injected into the HMBs' summing block, while the force transducer measures the corresponding force (N), from which the transfer function of the HMBs' actuator gain force/voltage (N/V) can be obtained. The block diagram of the open loop transfer function test of the HMBs' actuator gain is shown in Figure 5.10:

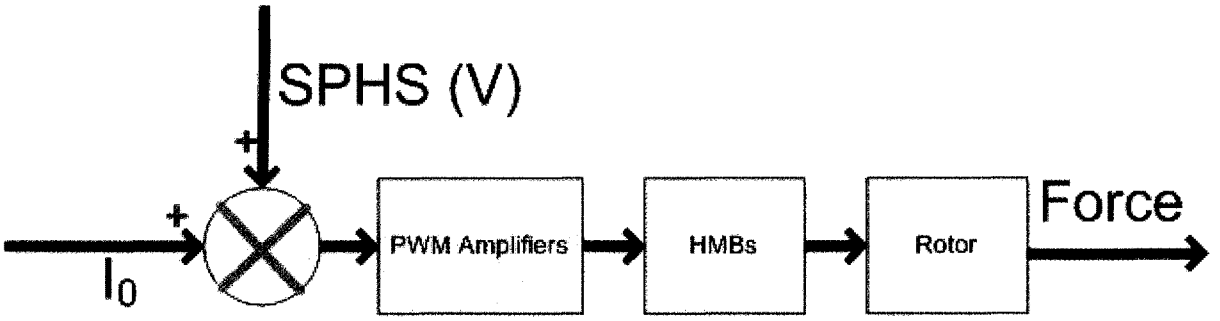

Figure 5.10: Block diagram of open loop calibration of the HMBs' actuator gain

In order to ensure that the dynamic magnification factor of the test rig does not affect the test, the test rig is excited with a bandwidth of 1 to 500 Hz and a fundamental frequency of 1 Hz. The bias current is 0.2A. The sampling frequency is 20 kHz. The measured transfer function of the HMBs' actuator gain (force/voltage) is shown in Figure 5.11.

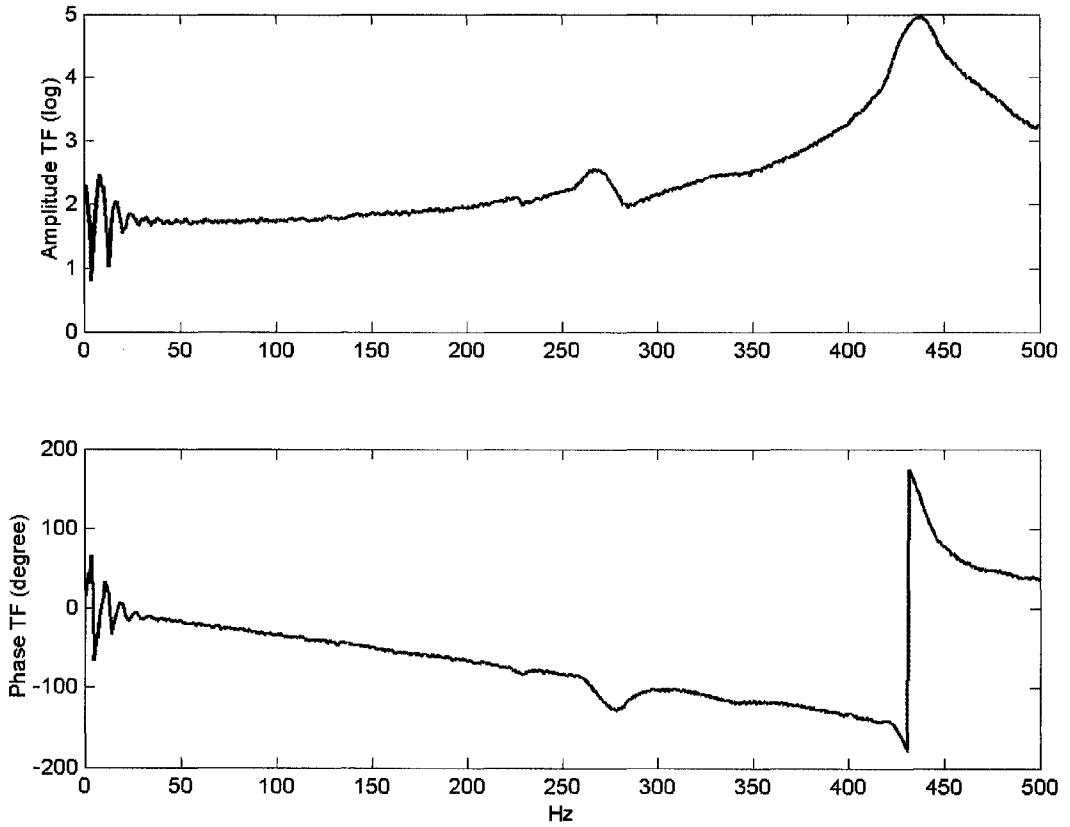

Figure 5.11: Amplitude and phase transfer functions of actuator gain

As can be seen from Figure 5.11, the system is adequately stiff: the natural frequency is above 270 Hz; except for the small fluctuation in the very low frequency range (1 – 20 Hz) is caused by the sampling, the actuator gain varies little in the low frequency range (1 – 100 Hz) and therefore can be approximated as constant. In order to overcome the fluctuation in the beginning frequency range (1 – 20 Hz), the bandwidth of SPHS is decreased to the range of 1 – 50 Hz with a fundamental frequency of 1 Hz. The corresponding frequency domain actuator gain in the range of 1 – 50 Hz is shown in Figure 5.12.

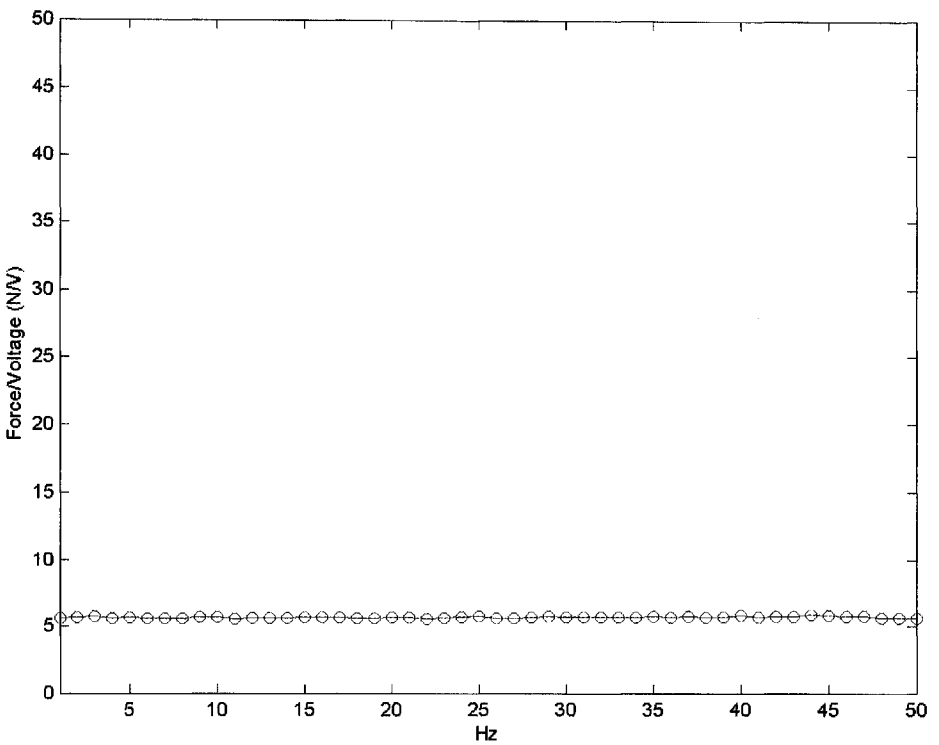

Figure 5.12: Flat amplitude transfer function of actuator gain from 1 to 50 Hz

It is clearly shown in Figure 5.12 that the actuator gain (force/voltage) is almost constant, being about 5.7 (N/V), in the low frequency range of 1 to 50 Hz.

Therefore, it can be concluded that the amplitude transfer function of the actuator gain can be accurately calibrated within this frequency range.

5.2.3.2 Calibration of HMBs' actuator gain

In order to show the linearity of HMBs' actuator gain (force/voltage), the rotor is fixed at the centre position of the stator bore, which means the rotor eccentricity ε_0 = 0%. The SPHS amplitude is then increased, and the corresponding maximum force is measured. The seven sets of SPHS (V) and force (N) are plotted in Figure 5.13, from which it can be clearly seen that the HMBs' actuator gain at ε_0 = 0% is almost linear, with a sensitivity of around 5.8 (N/V). Determination of the HMBs' saturation force is not possible during the experiment as the HMBs are found to heat up after 3.5 N of force output.

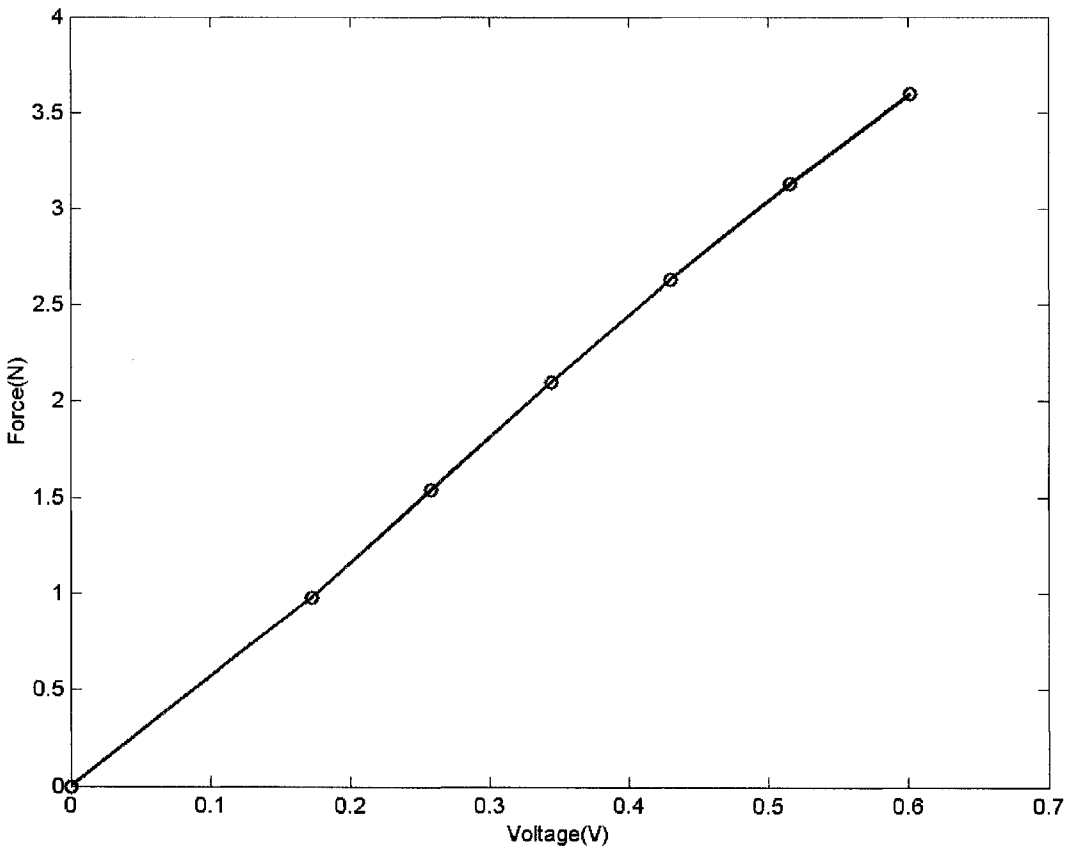

Figure 5.13: Measured HMBs' actuator gain at rotor's zero static eccentricity

In order to find out the maximum linear operating range of the HMBs' actuator when the rotor is at different orbit positions, the rotor position is adjusted such that ε_0 is gradually increased from 10%, 15%, 20%, 30%, 40% to 50%, respectively. Figure 5.14 below shows the maximum linear operating range of the HMBs' actuator gain, from which it can be seen that when ε_0 is within 20%, the HMBs have good linearity, and their actuator gain varies little in the range of 5.7 – 6.0 (N/V); when ε_0 is beyond 20%, their linearity deteriorates and the actuator gain will be decreased from 5.7 to 4.1 (N/V) with an increase of ε_0 from 20% to 50%.

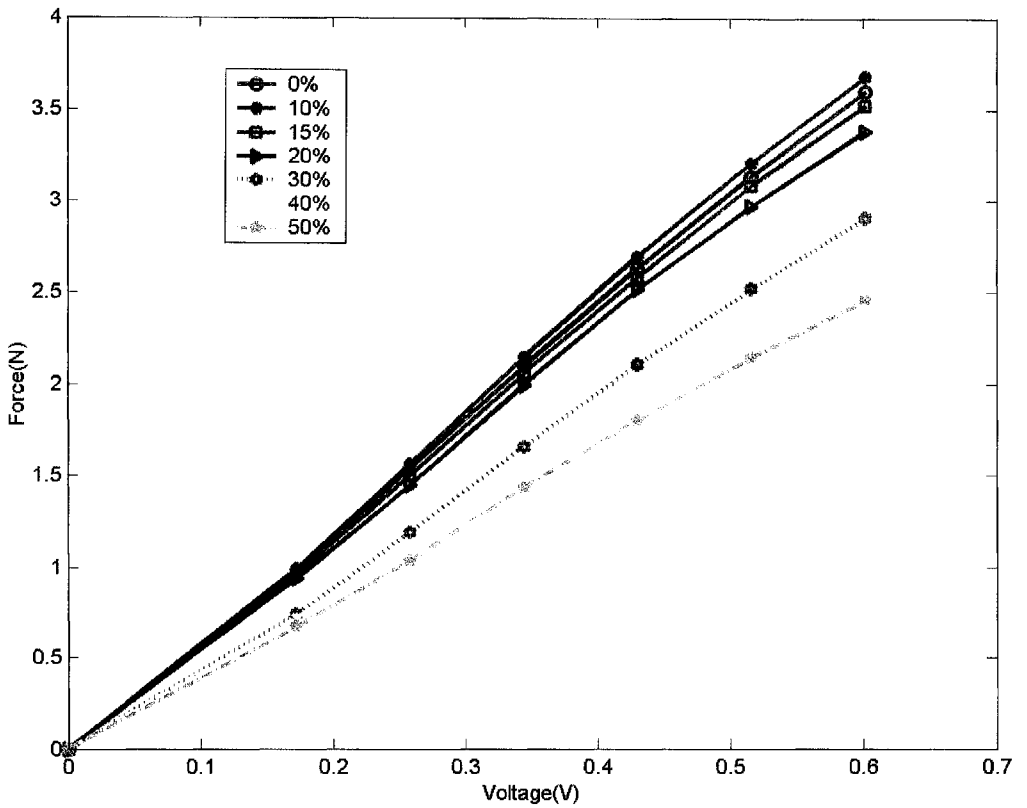

Figure 5.14: Determination of HMBs' maximum displacement linear operating range

5.3 Parameter estimation experiments

5.3.1 Radial estimation of HMBs modelled with direct- and cross-axes coefficients

The x-y axes orientation of the HMBs system and perturbation force with respect to the eddy current probes in radial parameter estimation exercises are as shown in Figure 5.15:

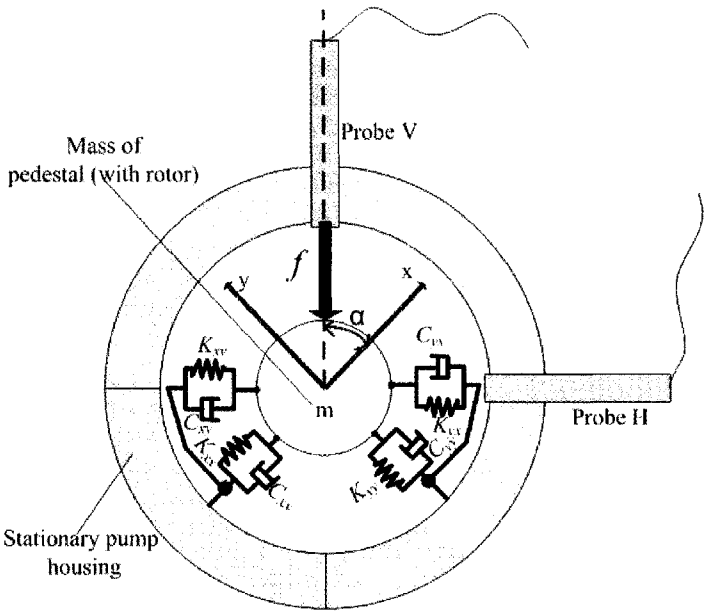

Figure 5.15: Experimental arrangement of x-y axes, excitation force and displacement probes for estimating eight direct- and cross-axes coefficients

The shaker force, f, is used to excite the pedestal, and the eddy current probes measure the corresponding rotor displacements which are transformed into the displacements in the x- and y-directions, for the radial parameter estimation of the HMBs system that is represented by eight linearised stiffness and damping coefficients as shown in Figure 5.15. The forcing angle between f and the x direction is α. The equation of rotor motion in the x- and y- directions is already

described in the equation (5.5). Therefore, following the same algorithm of 2-DOF parameter estimation and the estimation procedure introduced above, the eight stiffness and damping coefficients of the HMBs system in the radial directions could be obtained in the frequency domain. The corresponding MATLAB program of 2-DOF parameter estimation algorithm is attached in Appendix C.

The SPHS bandwidth is set at 1 to 250 Hz with a fundamental frequency of 1 Hz. The sampling frequency is 20 kHz for acquiring the force signal f and the corresponding displacement signals in the x- and y- directions. The mass of the pedestal with the rotor assembly is 0.92 kg. The estimation bandwidth is 15 Hz with a fundamental frequency of 1 Hz, and therefore 15 points are obtained for estimation. The estimation result around the natural frequency is shown in Table 5.3, where the discrete frequency range is 65 to 80 Hz, and the stiffness and damping coefficients are estimated for the mean frequency of 72.5 Hz. The maximum measured displacement is 40 μm, which is within the linear operating range of HMBs system.

Table 5.3: Radial parameter estimation of the HMBs system with 8 direct- and cross-axes coefficients

Frequency Band Used:	65 to 80 Hz
Goodness of Fit in x-direction:	0.9999
Goodness of Fit in y- direction:	0.9999
K_{xx} $(kN/m)^{-1}$	111.7
K_{xy} $(kN/m)^{-1}$	-46.65
K_{yx} $(kN/m)^{-1}$	43.87
K_{yy} $(kN/m)^{-1}$	22.37
C_{xx} $(N \cdot s/m)^{-1}$	66.50
C_{xy} $(N \cdot s/m)^{-1}$	-28.00
C_{yx} $(N \cdot s/m)^{-1}$	26.39
C_{yy} $(N \cdot s/m)^{-1}$	13.19*
Forcing angle, α	44.7°

Note: * denotes insignificant coefficient(s)

The measured transfer functions in the x- and y- directions with goodness of fit in the frequency domain are as shown in Figure 5.16.

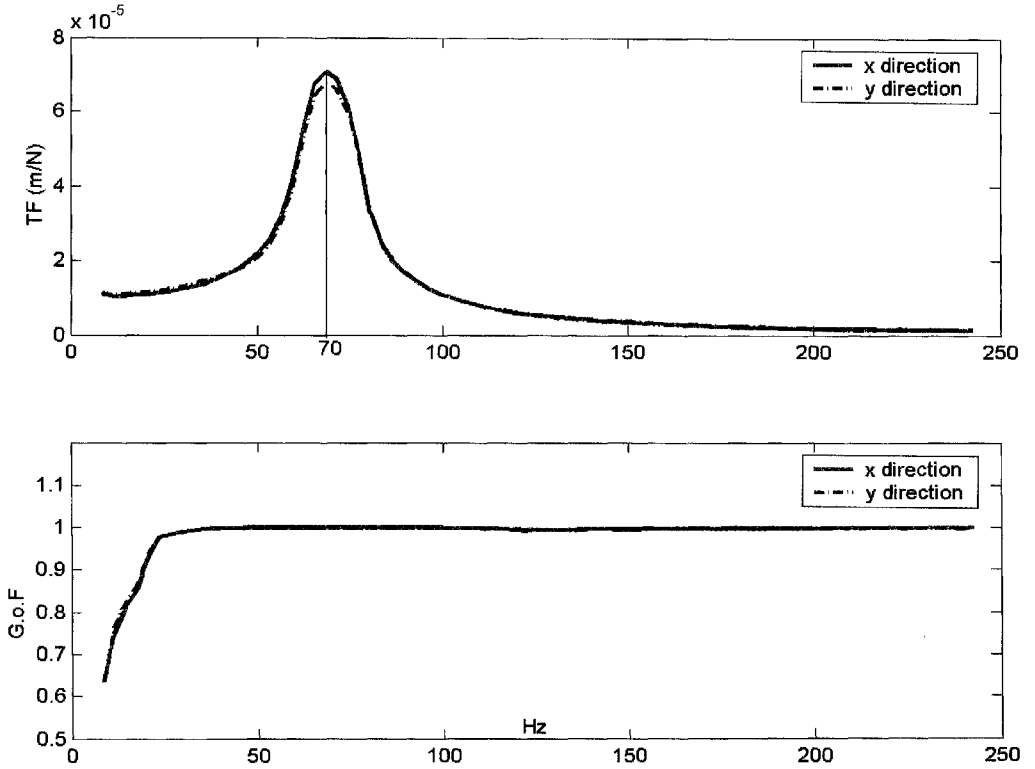

Figure 5.16: The measured transfer function in the x and y directions of HMBs system with goodness of fit (G.o.F). 'Transfer function' is shortened to 'TF' in graph

As can be seen from Figure 5.16, because of the symmetry of the HMBs system, the transfer functions in the x- and y- directions are expected to be similar in magnitude. With the introduction of the HMBs' stiffness control force, the natural frequency of the system is naturally increased from 66 to 70 Hz. The goodness of fit in the x- and y- directions is observed to be almost perfect from 40 to 250 Hz. The goodness of fit of 0.65 to 0.95 in the 0 to 40 Hz range is due to the integral feedback constant. This is because integral feedback is well known to eliminate low frequency position offset error, thus acting as a low pass filter in the control loop.

Figure 5.17 shows the four estimated stiffness coefficients of the HMBs system throughout the whole estimation frequency range. The maximum estimated

stiffness is about 1470 kN/m. The stiffness coefficients are statistically tested by equation (4.22) to be significant in the whole estimation frequency range. The direct-axis stiffness coefficients K_{xx} and K_{yy}, ranging from –90 to 1500 kN/m, are observed to be frequency dependent as their magnitudes increase with frequency, which has also been proven theoretically by Matsumura *et al.* [70], Aoyama *et al.* [71], and experimentally by Williams *et al.* [[73].

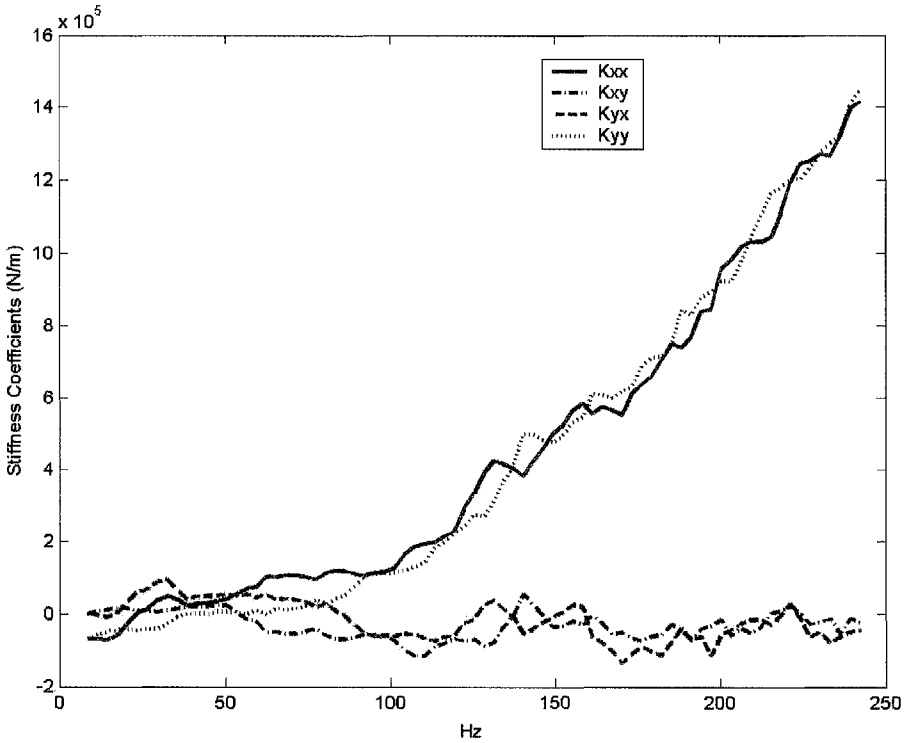

Figure 5.17: Radial estimation of the HMBs system with direct- and cross-axes stiffness coefficients

On the other hand, the four estimated damping coefficients as shown in Figure 5.18 are observed to be small and irregular with respect to frequency, and range from –50 to 200 N·s/m. They are statistically tested by equation (4.22) to be insignificant or can be considered as zero values.

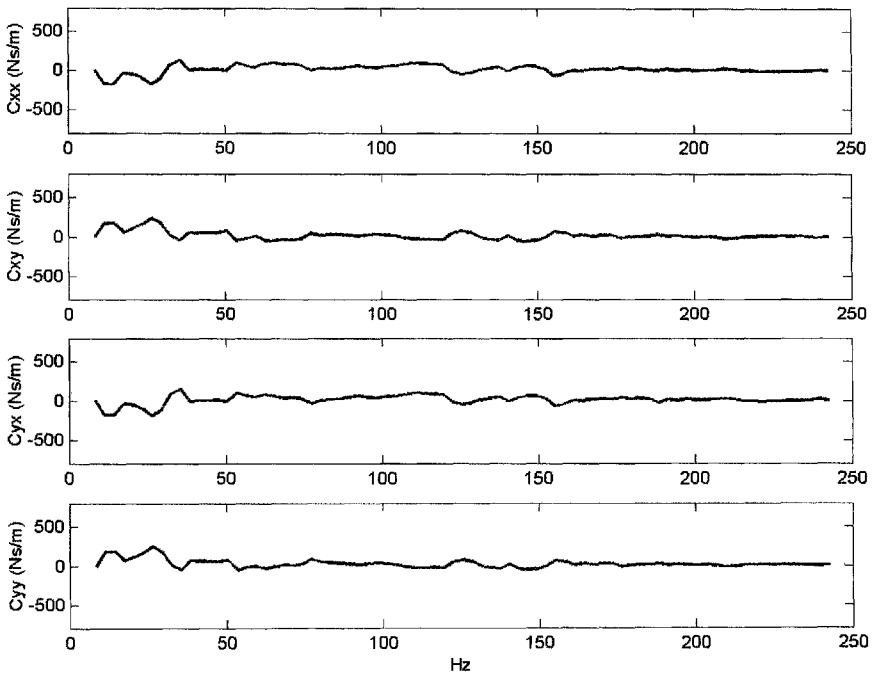

Figure 5.18: Radial estimation of the HMBs system with direct- and cross-axes damping coefficients

In spite of the perfect goodness of fit in the 40-250 Hz range, it can be seen that the direct-axis stiffness coefficients in the initial frequency range of 0 to 80 Hz are sometimes smaller in magnitude as compared to their cross-axis terms. This result contradicts the original intended design of the HMBs, that is, the concentration of the actuator forces should be in the middle of the pole faces or on the direct-axes. Further investigation found that this is due to the experimental approach being unable to distinguish between the effects of the complex quantities involving the direct- and cross-axes stiffness and damping forces in the x- and y-directions of equation (5.5). These phenomena and shortcomings of the method are consistent to observations made by Burrows *et al.* [100]. Hence, to solve this problem, only the direct-axis support coefficients of the HMBs system will be estimated in the following sections. However, it is clear from the estimated results that the stiffness

coefficient is very dominant and frequency dependent in the dynamics characteristics of the HMBs system.

5.3.2 Radial estimation of HMBs modelled with only direct-axis coefficients

In the earlier section, the distinguishing difficulties associated with the HMBs cross-axis capabilities are identified. This can be overcome by adopting in the experiment a reduced order dynamics model as shown in Figure 5.19, which is the equivalent of Figure 5.3, in the following parameter estimation procedure. Moreover, since the mechanical design of the HMBs is symmetrical about the x- and y-axes with a concentric rotor, it is reasonable to assume that its direct-axis stiffness and damping coefficients will be identical in the orthogonal directions, that is, $K_{xx} = K_{yy}$ and $C_{xx} = C_{yy}$.

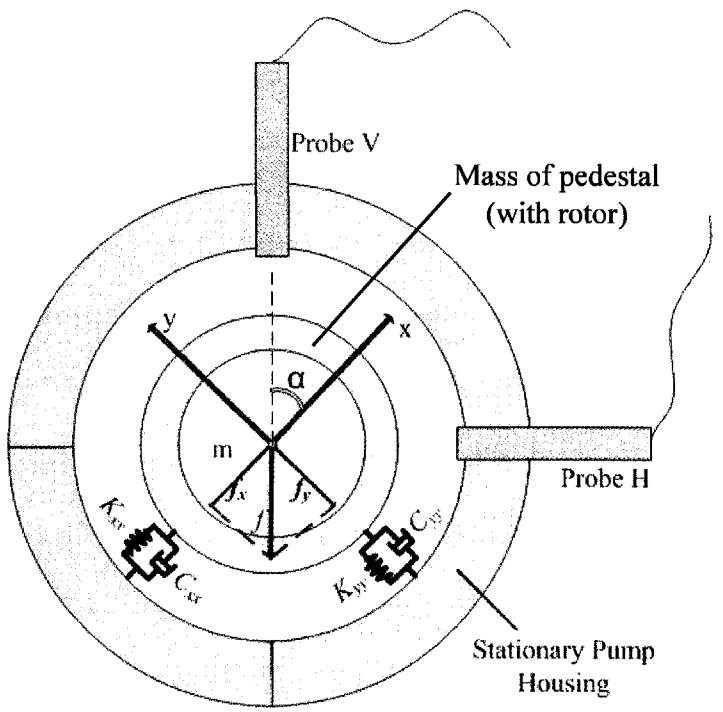

Figure 5.19: The decomposition of excitation force in x- and y- directions and HMBs system modelled with four direct-axis coefficients

It is in this manner, by using the system equation of motion (5.10) in the estimation algorithm, that the stiffness and damping coefficients are successfully estimated as shown in Figure 5.20. The estimated coefficients in Figure 5.20 must be halved for each set of HMBs. However, it has to be emphasized that the estimated stiffness coefficients are accurately represented as the pedestal spring stiffness $K_s/\sqrt{2}$ (equivalent of vertical pedestal stiffness in the x- and y-directions) subtracted from the total estimated stiffness coefficient. Likewise, the stiffness coefficients here are statistically tested to be significant with a maximum value of around 1400 kN/m. This maximum value is similar to those obtained with HMBs modelled with eight possible coefficients. The slightly low goodness of fit in the 160 to 250 Hz range is attributed to hysteresis and eddy current losses of the HMBs.

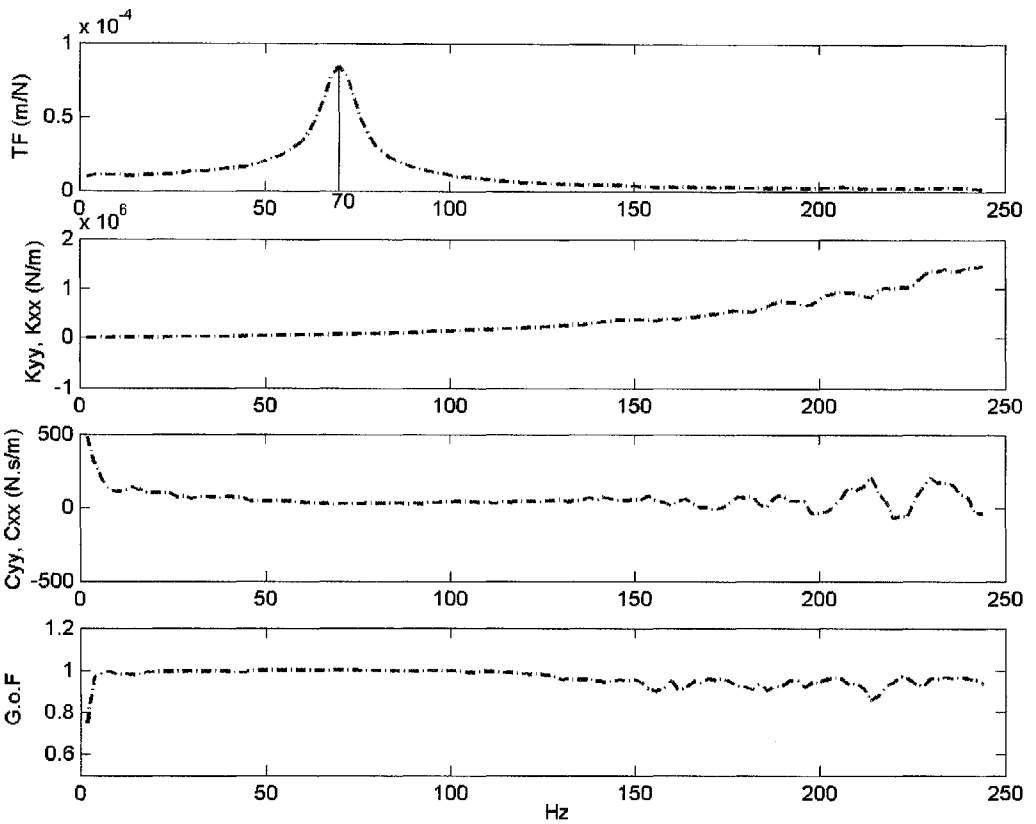

Figure 5.20: Radial estimation of the HMBs system with only four direct-axis coefficients

A graph is plotted in Figure 5.21 to study the differences in the estimated stiffness coefficients obtained between the direct-axis and direct- with cross-axes dynamics models. It can be observed that the direct-axis stiffness coefficients estimated with both models are in good agreement throughout the frequency range. In addition, it is also encouraging to note that the direct-axis model displays a smoother curve at the lower frequency range of 0 to 80 Hz, which is quite indistinguishable in the earlier section with the direct- and cross-axes model. In conjunction with the goodness of fit calculations and intended HMBs mechanical design, we can therefore conclude that there is no deficiency in HMBs modelled with only the direct-axis coefficients.

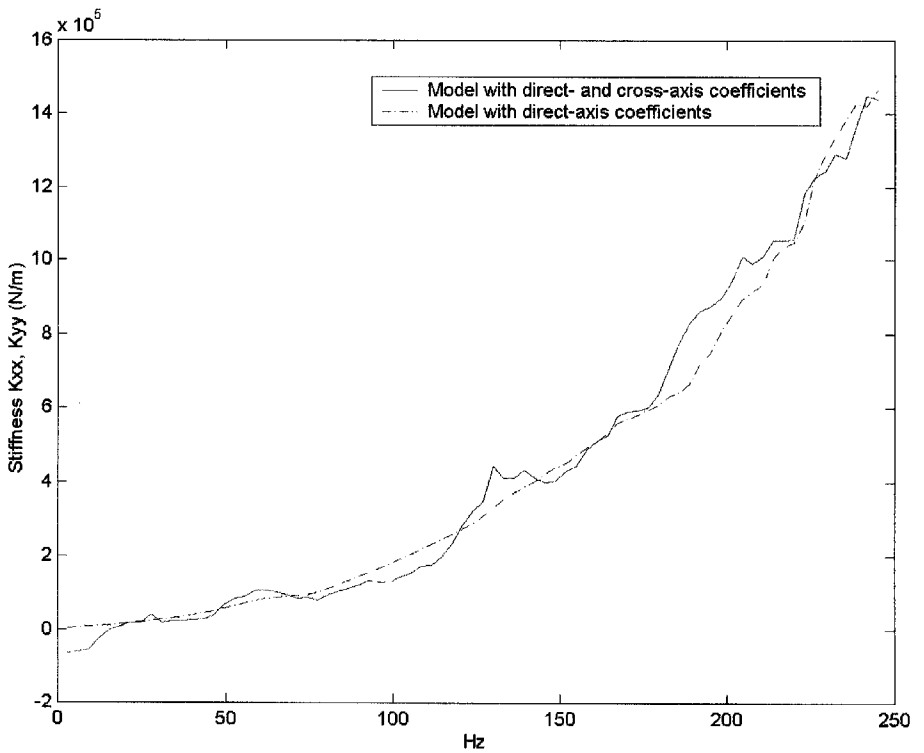

Figure 5.21: Comparison of estimated stiffness coefficients obtained with direct-axis, and direct-with cross-axes dynamic models

5.3.3 Radial estimation of HMBs model with only direct-axis coefficients and with varying k_p of PID controller

In order to show the influences of k_p of PID controller, the proportional gain of the PID controller, on the stiffness coefficient of the HMBs system, the force signal f_y and the resulting displacement signals in the y direction are acquired three times, each time with a different value of k_p. Figure 5.22 shows the estimation results of the HMBs system with direct-axis coefficients in the y direction with three different values of k_p.

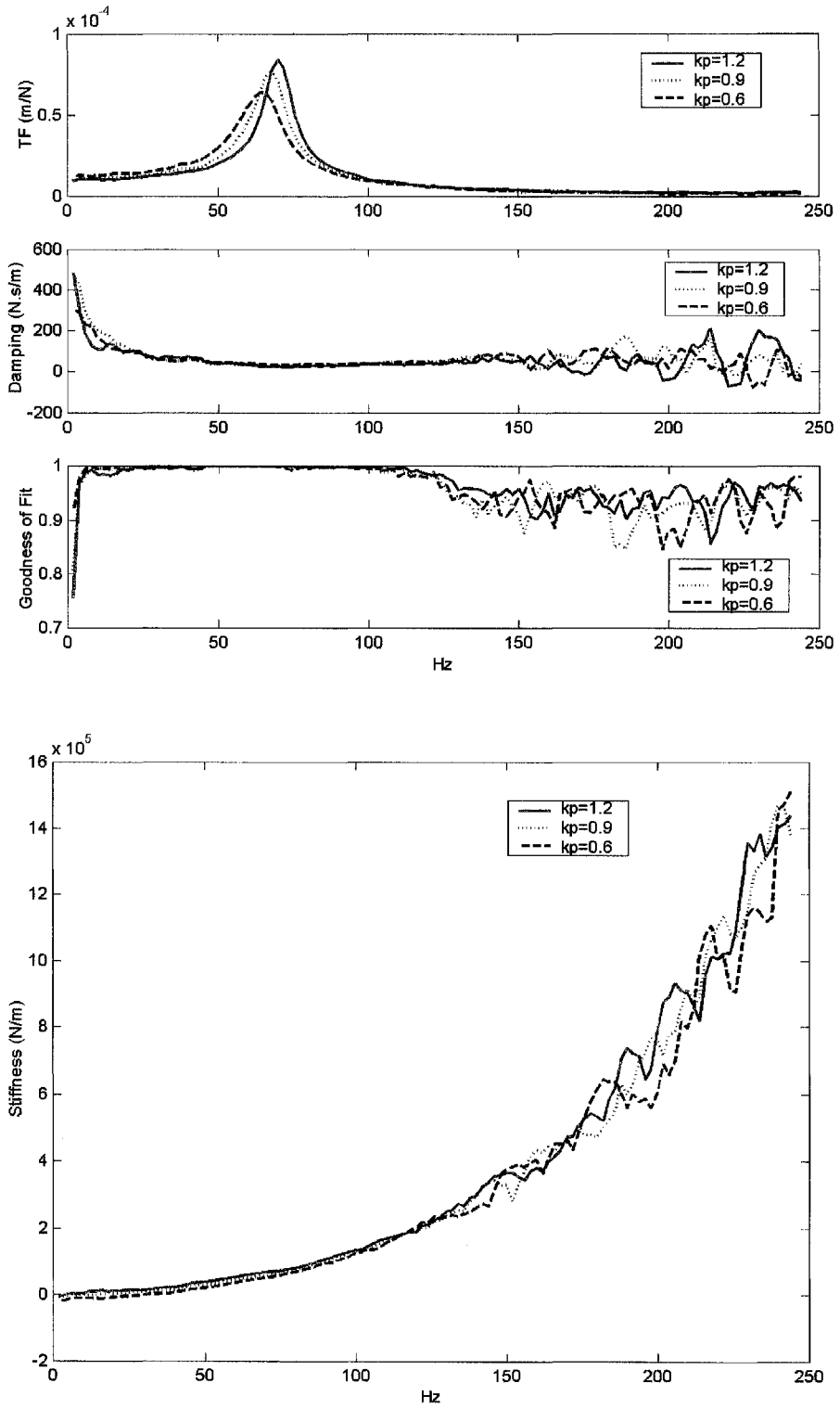

Figure 5.22: Radial estimation results of the HMBs system with different values of k_p

Figure 5.22 shows the influence of k_p on the stiffness coefficient of the HMBs system. The stiffness coefficient can be increased with the increase of k_p in the

frequency range of 1 to 130 Hz. In the high frequency range of 130 to 250 Hz, due to the eddy current and hysteresis loss, the effect of k_p on the stiffness coefficient cannot be distinguished. Moreover, due to the increase in stiffness, the system natural frequency is also increased, which is also clearly shown in Figure 5.22.

It is also noted that the estimated static bearing stiffness when $k_p = 0.9$ is $k = -6.6\,N/mm$, and because the gain of the eddy current probes is 8 V/mm, and the gain of the PWM amplifiers is 1 A/V, the system K_p shown in equation (4.7) should be 8 *A/mm*, from which we can obtain the corresponding measured open-loop bearing stiffness $k_{yy} = -13.6\,N/mm$, which is quite similar to the theoretical open loop bearing stiffness of HMBs calculated in equation (3.12) in Chapter 3 where $k_{yy} = -12.5\ N/mm$.

5.3.4 Radial estimation of HMBs model with only direct-axis coefficients and with rotating rotor

By adopting the same setup as in Figure 5.6, this section investigates and compares the estimated coefficients between stationary and rotating rotor at a speed of 8,000 rpm (133 Hz), by using HMBs modelled with only direct-axis coefficients. The two estimation results are compared in Figure 5.23, where it can be seen that their transfer function, stiffness, damping, and even the goodness of fit are almost identical in magnitude. This implies that there is negligible skin effect in the thickness of the rotor. A conclusion can therefore be drawn here, that parameter estimation procedure on the rotor-bearing system at stationary position may replace the estimation procedure in rotation. This can greatly facilitate the estimation procedure because the rotor does not need to be rotated, and therefore,

the possibility of coinciding excitation test signal with rotor rotational speed can be avoided.

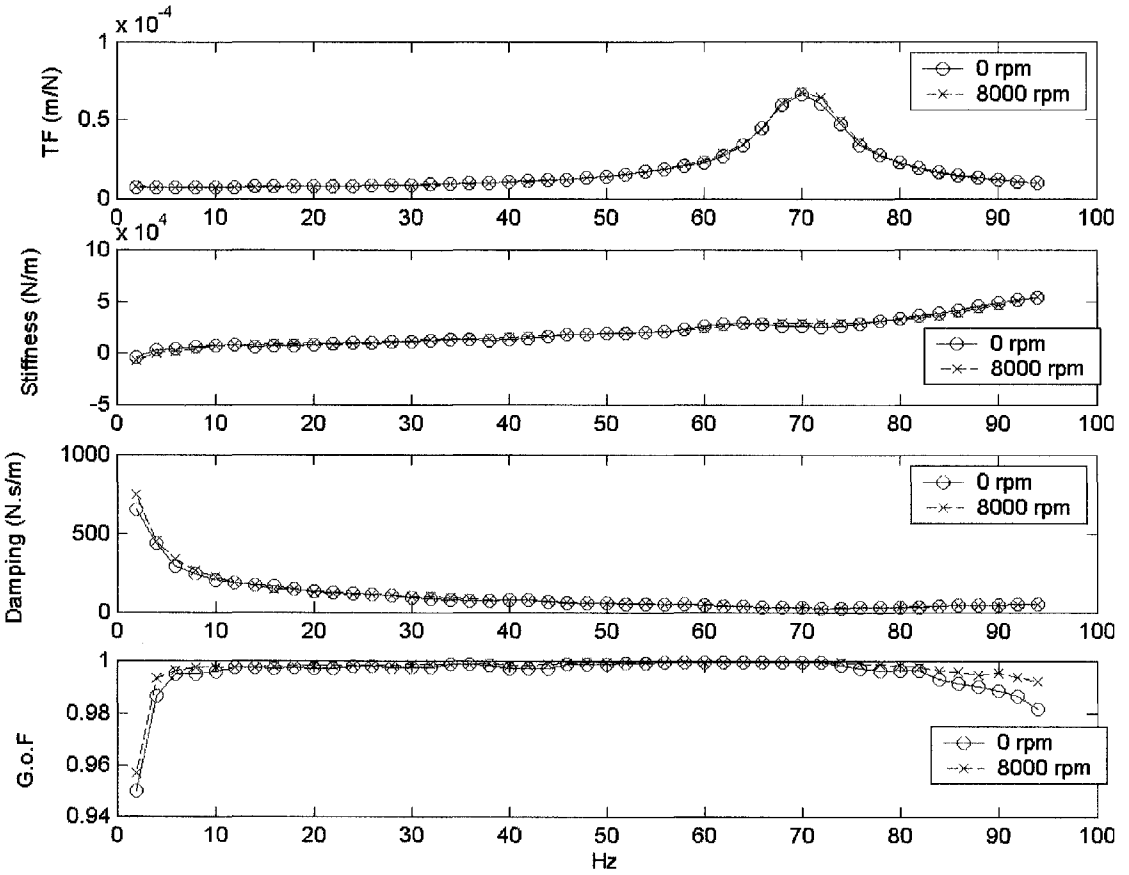

Figure 5.23: Comparisons of radial HMBs estimated results modelled with only direct-axis coefficients at 0 and at 8,000 rpm

5.4 Axial parameter estimation of HMBs system using one DOF model

The arrangement for parameter estimation in the axial direction is similar to that of the radial parameter estimation, except that the shaker and the eddy current probe are placed axially; sharing the center axis of the horizontal shaft, and the pedestal is fixed at the desired vertical position by four mechanical clamping rings secured

onto the vertical shafts. The horizontal shaft, with the rotor as a whole, could slide freely along the horizontal linear bearings in the axial direction. The photograph of the test rig for axial parameter estimation of the HMBs system is shown in Figure 5.24 and its scheme is shown in Figure 5.25.

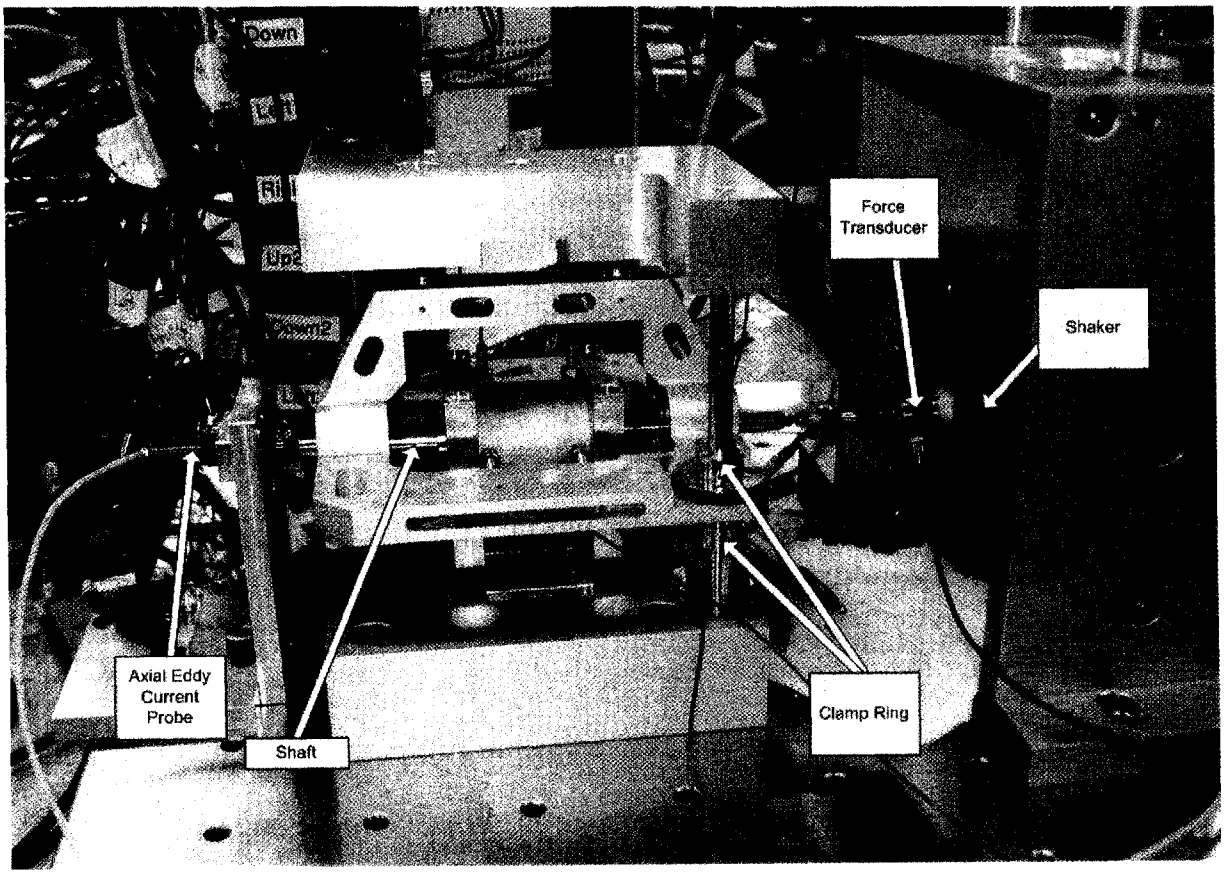

Figure 5.24: Experimental arrangement of the axial parameter estimation of the HMBs system

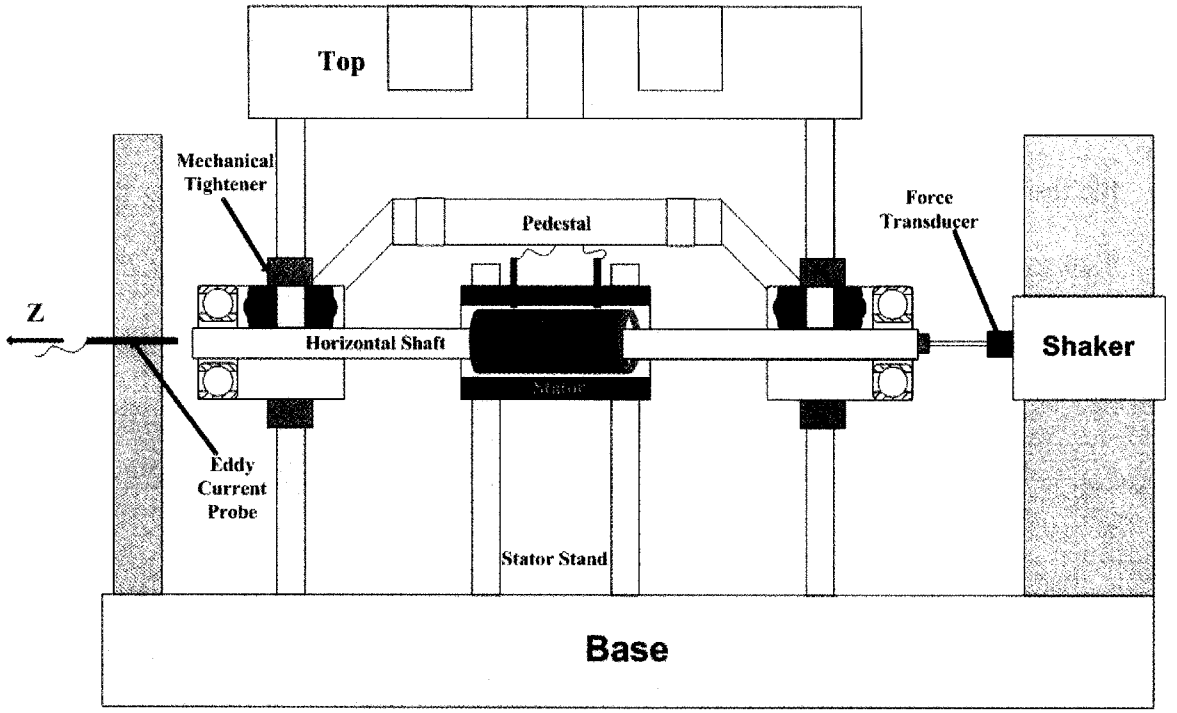

Figure 5.25: Schematic arrangement of axial parameter estimation of the HMBs system using one DOF model

Due to reaction forces caused by moving fluid during operation in an axial flow blood pump, the stiffness and damping properties in the axial direction of the HMBs system are of fundamental importance to the performance and stability of the axial flow blood pump. The rotor assembly in the HMBs with the horizontal shaft is passively controlled in the axial direction. The shaker perturbs the horizontal shaft with the rotor in the axial direction, and an eddy current probe is used to measure the corresponding displacement of the shaft. The system model of axial parameter estimation of the HMBs system is shown in Figure 5.26.

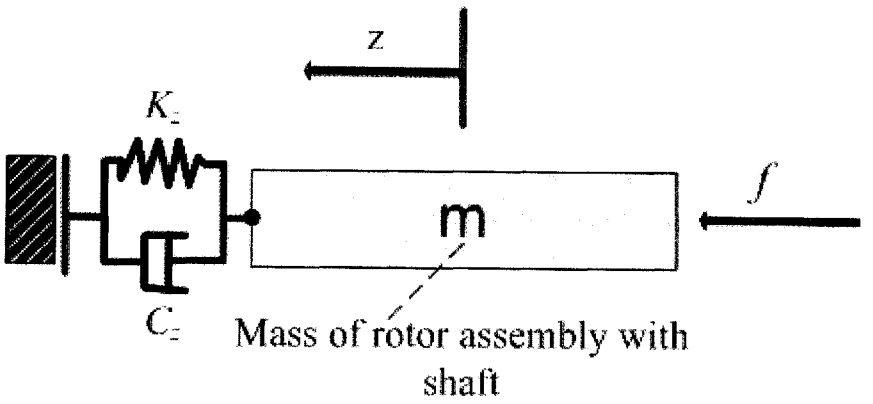

Figure 5.26: One DOF model of axial parameter estimation of HMBs system

The rotor motion equation in the z direction can be expressed as:

$$m\ddot{z} + K_z z + C_z \dot{z} = f \tag{5.14}$$

As this is a one DOF system, the earlier parameter estimation algorithm in equation (5.1) and estimation procedure can be utilized to obtain the stiffness and damping coefficients K_z and C_z.

The force and the displacement signals are measured on line with a sampling frequency of 20 kHz, and the acquired data is then read into the program for one DOF parameter estimation for computational purposes. The mass of the rotor and shaft assembly is 0.13 kg. The bandwidth of the SPHS test signal is 1-250 Hz with a fundamental frequency of 1 Hz. The estimation bandwidth is set at 10 Hz with an overlapping range of 8 Hz. One set of the estimation results around natural frequency is shown in Table 5.4 and the whole range of estimation results in the frequency domain are shown in Figure 5.27, from which it can be seen that the stiffness coefficient also increases with the increase in frequency. The maximum estimated stiffness coefficient is 270 kN/m. The damping coefficient is observed to be very small, being from 1 $\mathrm{N \cdot s/m}$ to 6 $\mathrm{N \cdot s/m}$. The structural natural frequency

of the test rig is tested to be about 38 Hz, which causes the poor goodness of fit in its neighbourhood (30 Hz – 44 Hz) as shown in Figure 5.27.

Table 5.4: Sample of parameter estimation results in the axial direction

Frequency Band Used:	18 to 28 Hz
The Goodness of Fit:	0.9842
Stiffness $(kN/m)^{-1}$:	2.471
Damping $(N \cdot s/m)^{-1}$:	3.108

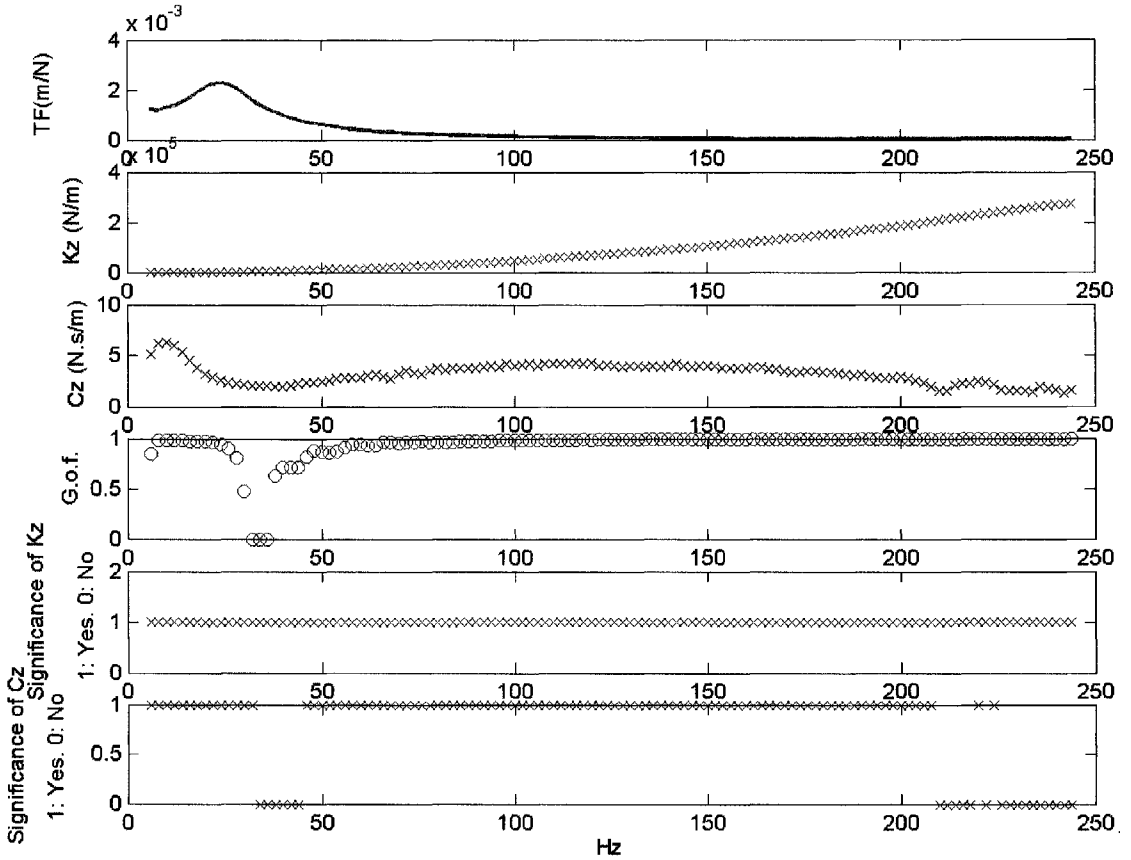

Figure 5.27: The parameter estimation results of HMBs system in the axial direction

A comparison study is also made between the stiffness coefficients in the radial and axial directions as shown in Figure 5.28. It is observed that the maximum stiffness coefficient attained in the radial direction is five times larger than its axial counterpart. This is because the axial direction is only passively controlled, while the radial direction is actively controlled. In addition, the damping coefficients in the axial direction are very much smaller than those in the radial directions. However, it is observed during the experiment that even when a pen is thrust at the rotor in the axial direction, the passive control force can still assist in maintaining the rotor position in the pump housing. Lastly, the largest displacement in the axial direction, corresponding to 10,000 rpm during levitation, is about 70 μm .

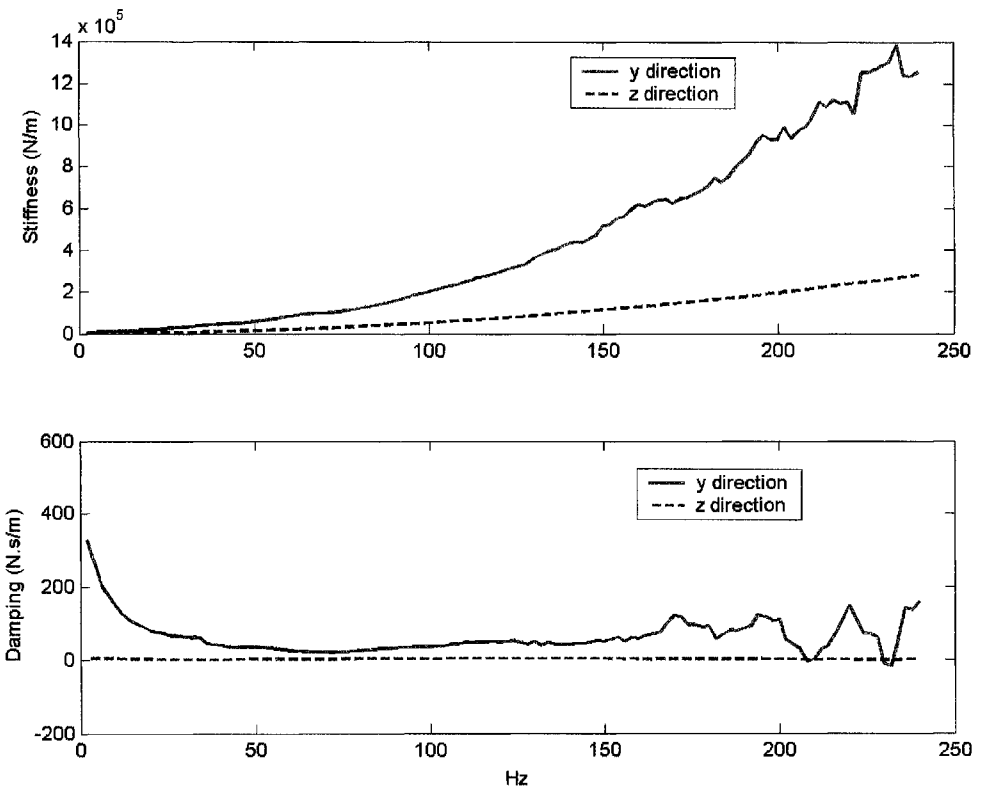

Figure 5.28: Comparisons of estimation results between the axial and radial directions

Chapter 6 Self-sensing AMB

This chapter comprises two parts: the first part is the digital simulation of two self-sensing approaches, namely switching noise demodulation and parameter estimation and the second part is the analog circuit implementation of the self-sensing parameter estimator.

Firstly, the inductor model of magnetic bearings is deduced based on some fundamental electromagnetic equations. The coil current waveform contains the position information of the suspended object because the switching waveform of coil currents is modulated by the air gap of the magnetic bearings. The procedures for switching noise demodulation are presented, and the principles of self-sensing parameter estimation are then introduced. The digital simulation processes of switching noise demodulation and parameter estimation are presented and their simulation results are compared.

An analog circuit implementing the self-sensing parameter estimator is introduced. The self-sensing circuits and the backplane circuit are described accordingly. The static and dynamic tests on the circuit of self-sensing parameter estimator are introduced, and the experimental results are reported.

6.1 Coil inductor model

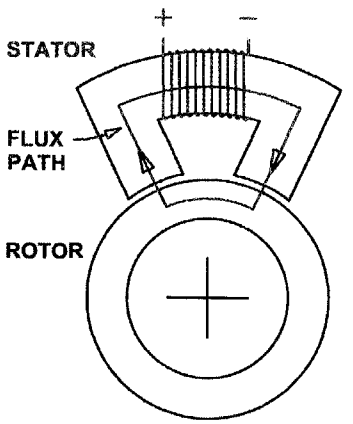

Figure 6.1: Schematics of flux path of AMB

Electromagnetism is the phenomenon in which magnetic flux is generated by electric current. Multiple turns of wires are wrapped around a magnetic core as shown in Figure 6.1. According to Ampère's Loop Law, the relationship between the coil currents and corresponding flux created is expressed as in equation (6.1):

$$\int Hdl = Ni \tag{6.1}$$

where H is magnetic flux intensity, and l represents flux path length.

If the axial flux path is much shorter than that of the radial flux path, then equation (6.1) can be rewritten as:

$$H_c l_c + 2H_g(g_0 - x) = Ni \tag{6.2}$$

where H_c is the flux intensity of the magnetic core, l_c is the flux path length in magnetic medium, H_g is the flux intensity of the air gap, g_0 is the nominal air gap length, and x is the displacement of the suspended object.

For the medium of air, the relationship between H and B is linear as shown in equation (6.3):

$$H_g \mu_0 = B_g \tag{6.3}$$

where μ_0 is the permeability of free air: $4\pi \times 10^{-7}$ (T.m/A).

As for the magnetic core, this relationship is nonlinear because of eddy current loss, hysteresis and saturation. For simplicity, this relationship is generally approximated as linear in the following equation:

$$H_c \mu_0 \mu_r = B_c \tag{6.4}$$

where μ_r is called relative permeability of the material.

Assuming that there is no flux loss in the flux path and the flux cross-section area remains constant through the flux path, then the law of flux conservation can be used as shown below:

$$\Phi = A_c B_c = A_g B_g \tag{6.5}$$

Here $B_g = B_c$. Substituting (6.4) and (6.3) into (6.2), the flux density B can be expressed by the following:

$$B = \mu_0 \frac{Ni}{\left\{\frac{l_c}{\mu_r} + 2(g_0 - x)\right\}} \tag{6.6}$$

Therefore, the flux Φ can be written as:

$$\Phi = A_c B_c = A_g B_g = \frac{\mu_0 N i A_g}{\left\{\frac{l_c}{\mu_r} + 2(g_0 - x)\right\}} \tag{6.7}$$

According to Faraday's law of inductance,

$$V = N\frac{d\Phi}{dt} + Ri \tag{6.8}$$

where V is the voltage applied across the coils having a resistance of R ,and flux Φ is the function of the coil current i, and the air gap g. A perturbation in the air gap, $g = g_0 + x$, gives:

$$\Phi = \Phi(g, i) \tag{6.9}$$

The partial derivative equation of Φ can be written as:

$$\begin{aligned}\frac{d\Phi}{dt} &= \frac{\partial\Phi}{\partial g}\frac{\partial g}{\partial t} + \frac{\partial\Phi}{\partial i}\frac{\partial i}{\partial t} \\ &= \frac{\partial\Phi}{\partial g}\dot{g} + \frac{\partial\Phi}{\partial i}\frac{\partial i}{\partial t}\end{aligned} \tag{6.10}$$

Differentiating Φ with respect to i in the equation (6.7), we can obtain:

$$N\frac{\partial\Phi}{\partial i} = L = \frac{\mu_0 N^2 A_g}{\left(\frac{l_c}{\mu_r} + 2g\right)} \tag{6.11}$$

Equation (6.8) can be rewritten as:

$$V = L\frac{di}{dt} + Ri + i\frac{dL}{dt} \tag{6.12}$$

Usually the last term of the equation (6.12), which is known as back electro-motive-force (EMF), is small compared to $(V - Ri)$, and therefore the equation (6.12) can be simplified and transformed as:

$$\frac{di}{dt} = \frac{V - Ri}{L} \tag{6.13}$$

Equation (6.13) and equation (6.11) are adopted here as the mathematical model of coil inductor. The block diagram of the inductor model implemented in Simulink is shown in Figure 6.2:

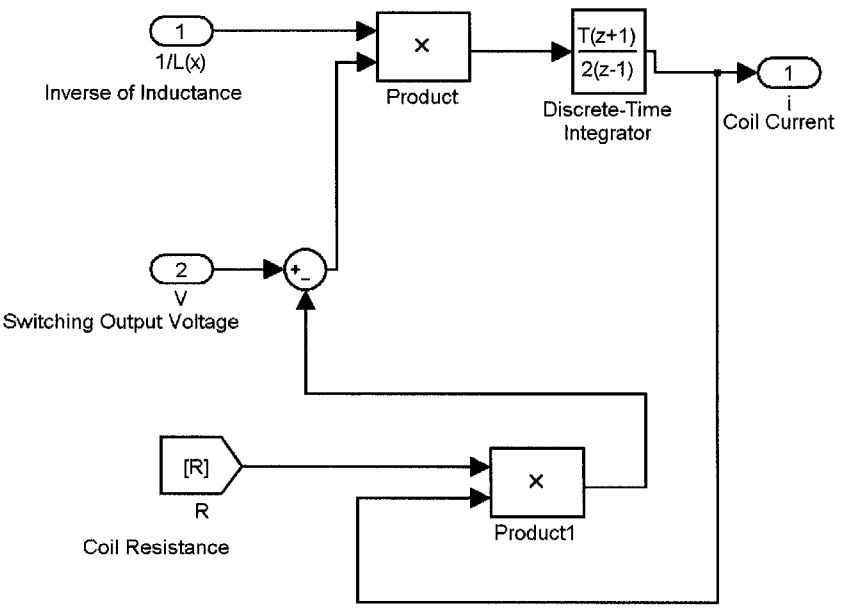

Figure 6.2: Block diagram of the inductor model implemented in Simulink

6.2 Switching noise demodulation

6.2.1 Theoretical analysis

Substituting equation (6.11) into (6.13), we can obtain the equation (6.14):

$$\frac{di}{dt} = \frac{\left(\frac{l_c}{\mu_r} + 2(g_0 \pm x)\right)}{\mu_0 N^2 A_g}(V - Ri) \tag{6.14}$$

From the equation (6.14), the current waveform can be regarded as a carrier waveform (V) modulated by the air gap distance $(g_0 \pm x)$. The gap information can

be obtained from the current signal by demodulation. The high-pass filter, rectifier, and low-pass filter can be used to realize the current demodulation [22].

Prior to constructing the demodulation filters, it is necessary to understand the current signal at the switching frequency. The voltage waveform is shown in Figure 6.3 for the application of a bi-state PWM amplifier whose switching voltage output is V_s.

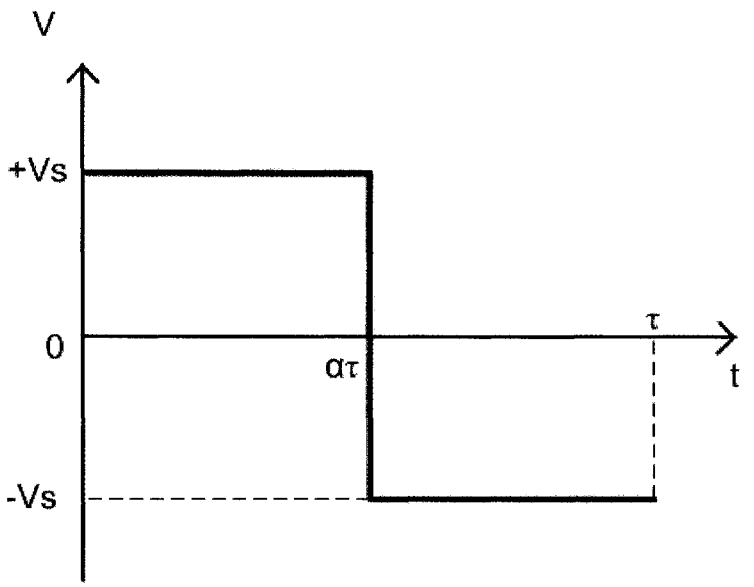

Figure 6.3: The switching voltage waveform in one period

Here, for the sake of simplicity, we start from $t_0 = 0$ to $t = \tau$, where τ is the switching period, and α is the duty cycle of the bi-state amplifier's voltage output. According to the equation (6.14), the current waveform can be obtained by integrating the voltage waveform with the assumption that multiplication of the coil resistance and current is very small compared to the value of voltage. The current waveform can be expressed in equation (6.15).

$$i(t)=\begin{cases} I_0+\dfrac{V_s}{L(x)}t,\ldots\ldots\ldots,0<t<\alpha\tau \\ I_0+\dfrac{2V_s}{L(x)}\alpha\tau-\dfrac{V_s}{L(x)}t,\ldots\ldots,\alpha\tau<t<\tau \end{cases} \tag{6.15}$$

The first part of our demodulation filters is a high-pass filter that removes low-frequency components of the current signal. If the switching frequency is much higher than the displacement frequency of the suspended object, then the low-frequency components of the current signal can be considered to vary linearly with time during one switching cycle. Therefore, the expression for low frequency component of current signal in one period can be approximated as:

$$i_{low}(t)=I_0+\frac{\dfrac{V_s}{L(x)}(2\alpha-1)\tau}{\tau-0}t=I_0+\frac{V_s}{L(x)}(2\alpha-1)t \tag{6.16}$$

Hence, after the high pass filter, the current waveform can be expressed as:

$$i_{hp}(t)=i(t)-i_{low}(t)=i(t)-I_0-\frac{V_s}{L(x)}(2\alpha-1)t \tag{6.17}$$

The second stage of demodulation process is to rectify the output signal of the high-pass filter. The output of the rectifier is an absolute value and expressed in equation (6.18):

$$i_{rectified}(t)=|i_{hp}(t)|=\begin{cases} \dfrac{2V_s}{L(x)}(1-\alpha)t,\ldots\ldots\ldots,0<t<\alpha t \\ \dfrac{2V_s}{L(x)}\alpha(\tau-t),\ldots\ldots\ldots,\alpha t<t<\tau \end{cases} \tag{6.18}$$

The last stage of demodulation is to subject the signal of the rectifier to a low-pass filter that acts as an average calculator over one switching interval of the signal, and its function is expressed as:

$$u = \frac{1}{\tau}\int_0^{\tau} \left| i_{hp}(t) \right| dt \tag{6.19}$$

The output of the low-pass filter is expressed as follows:

$$u = \alpha(1-\alpha)\left(\frac{V_s \tau}{\mu_0 N^2 A_g}\right)\left(\frac{l_c}{\mu_r} + 2(g_0 \pm x)\right) \tag{6.20}$$

It can be seen from equation (6.20) that the output of demodulation is dependent not only on the air gap, but also on the duty cycle of the amplifier.

6.2.2 Digital implementation of the forward path filter

The above-mentioned three-stage circuitries, high-pass filter, rectifier, and low-pass filter can be implemented digitally in Simulink. The switching frequency of the PWM amplifier employed here is 25 kHz, and its voltage supply is 24V. The sampling frequency of Simulink DSP is 250 kHz, i.e. 10 times faster than the PWM switching frequency to avoid signal aliasing and acquire enough signal information.

6.2.2.1 High-pass filter

A second order Butterworth's high-pass filter is used to remove the low-frequency components of the coil current signal. The transfer function of the second order Butterworth's high-pass filter is as follows:

$$H_{high-pass}(s) = \frac{ks^2}{s^2 + \frac{a\omega_c}{b}s + \frac{\omega_c^2}{b}} \tag{6.21}$$

where $a = 1.414$ and $b = 1$ for the second order Butterworth's high-pass filter. k is the gain of the filter, and is defined as 1. The cutoff frequency of the filter, f_c is 15 kHz, which is much higher than the bandwidth of the AMB system (usually less than 2.5 kHz), but much lower than the switching frequency (25 kHz). The cutoff frequency is expressed as $\omega_c = 2\pi \times 15000$ rad/s.

The MATLAB program for implementing the high pass filter is attached in Appendix D. In the program, the continuous-time model is converted to the discrete-time model for the purpose of digital simulation with bilinear transformation:

$$s = \frac{2}{T}\left(\frac{z-1}{z+1}\right) \tag{6.22}$$

The bode diagram of the discrete-time second order high-pass filter is shown in Figure 6.4.

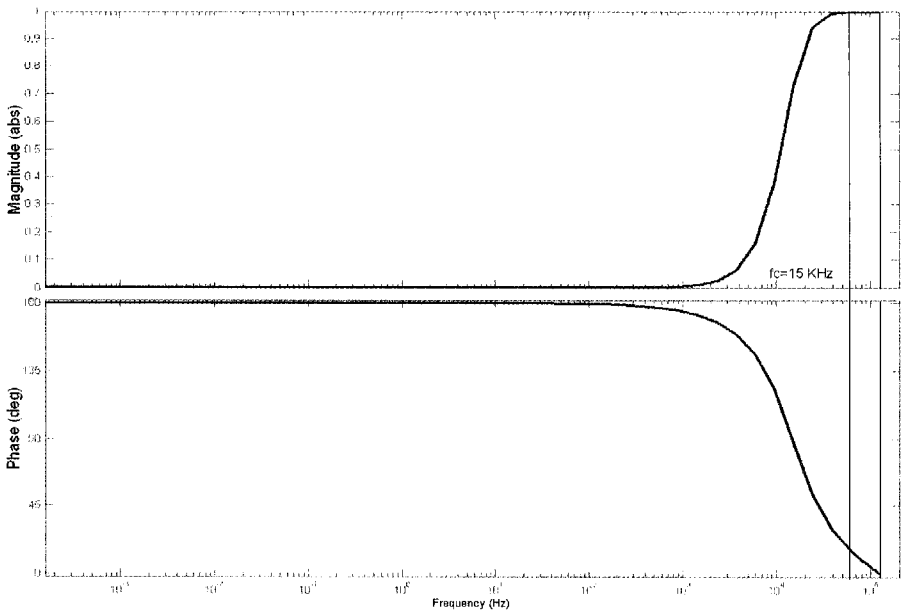

Figure 6.4: Bode diagram of the digital second order high-pass filter

6.2.2.2 Rectifier circuit

It is much easier to implement the rectifier digitally than with analog circuits. In Simulink, there is an "Abs" block that has the function of obtaining the absolute value (abs) of the input signal. The "Abs" block is shown in Figure 6.5:

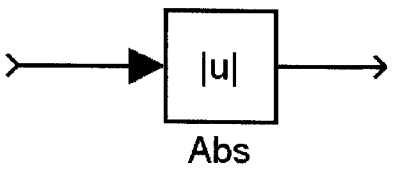

Figure 6.5: The rectifier realized by Abs block in Simulink

6.2.2.3 Low-pass filter

The low-pass filter of the demodulation circuit is also implemented digitally in Simulink. We use a second order low-pass Butterworth filter whose transfer function is as follows:

$$H_{low-pass}(s) = \frac{kb\omega_c^{\,2}}{s^2 + a\omega_c s + b\omega_c^{\,2}} \tag{6.23}$$

where $a = 1.414$ and $b = 1$ for the second order Butterworth filter. We set the gain, k=1, and the cutoff frequency of the filter f_c is 5 kHz. The MATLAB program for implementing the low-pass filter is attached in Appendix D. Figure 6.6 shows the bode diagram of the discrete second order low-pass filter.

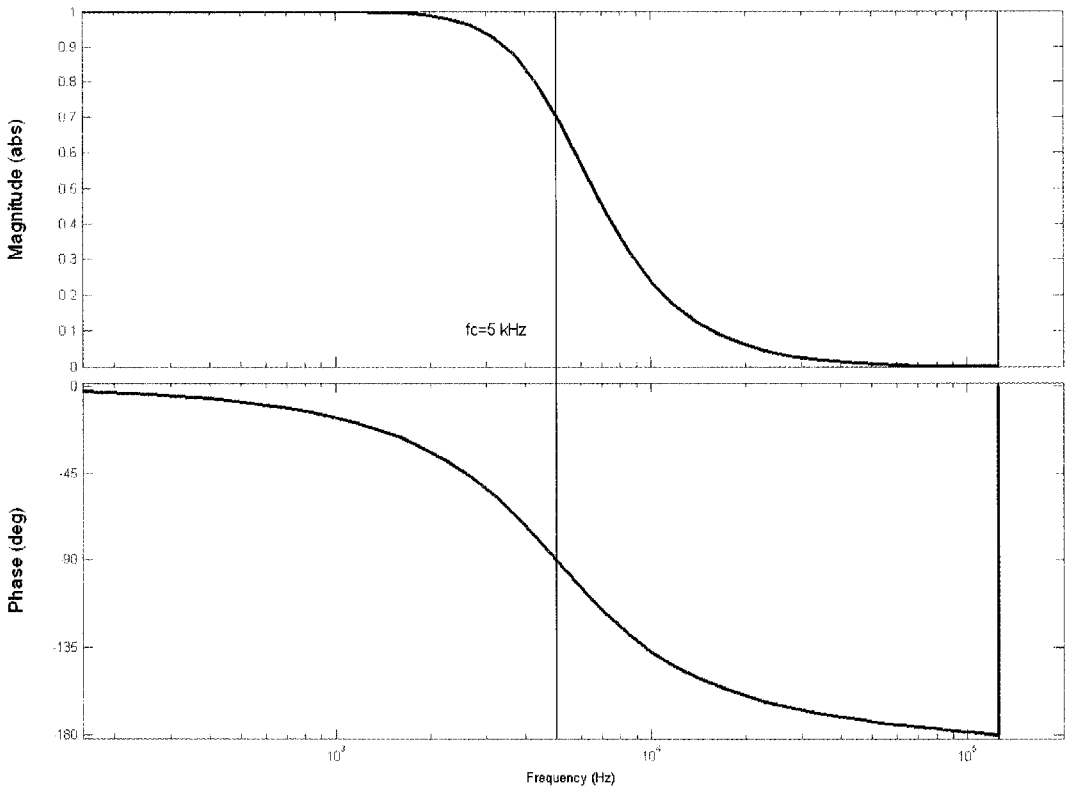

Figure 6.6: Bode diagram of the digital second order low-pass filter

6.2.3 Simulation of switching noise demodulation

The simulation model of switching noise demodulation is designed and implemented in Simulink. The flowchart of the simulation model is shown in Figure 6.7. In the Simulink model as shown in Figure 6.8, the displacement of the suspended object and the switching voltage are generated as the input of the inductor model that is based on the equation (6.13), and the output of the inductor model is the modulated current that contains the position information of the suspended object. Then, the modulated current goes through the forward path filter from which the actual displacement is estimated.

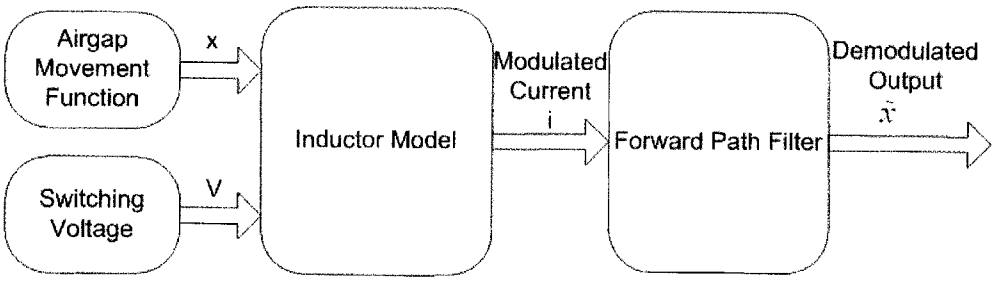

Figure 6.7: Flowchart of simulation model for switching noise demodulation

The block model realized in Simulink is as follows:

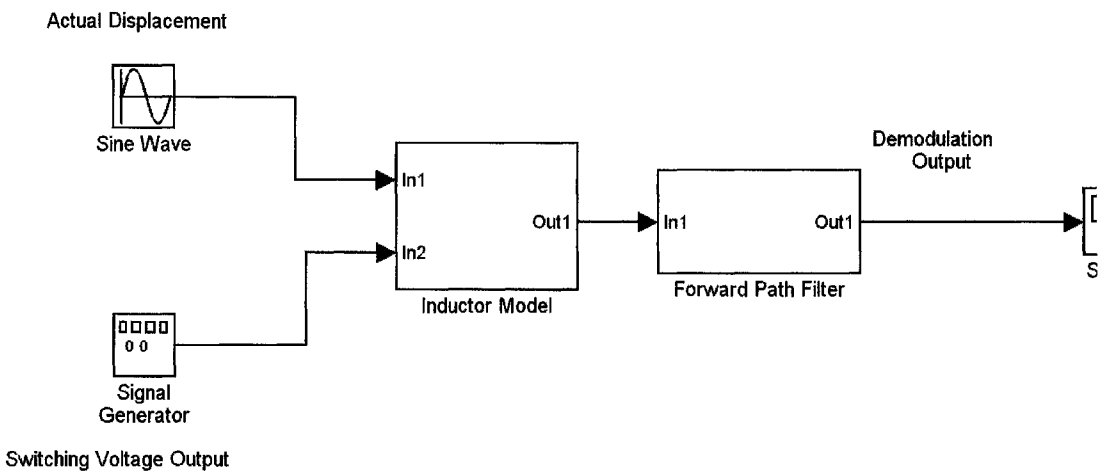

Figure 6.8: Simulink block model of switching noise demodulation

In Figure 6.9, the digital simulation result of the switching noise demodulation is compared with the actual displacement, a discrete sine wave with the frequency of 100 Hz. It can be seen that the output of the forward path filter is in reasonable agreement with the actual displacement, although some delay is observed between the two.

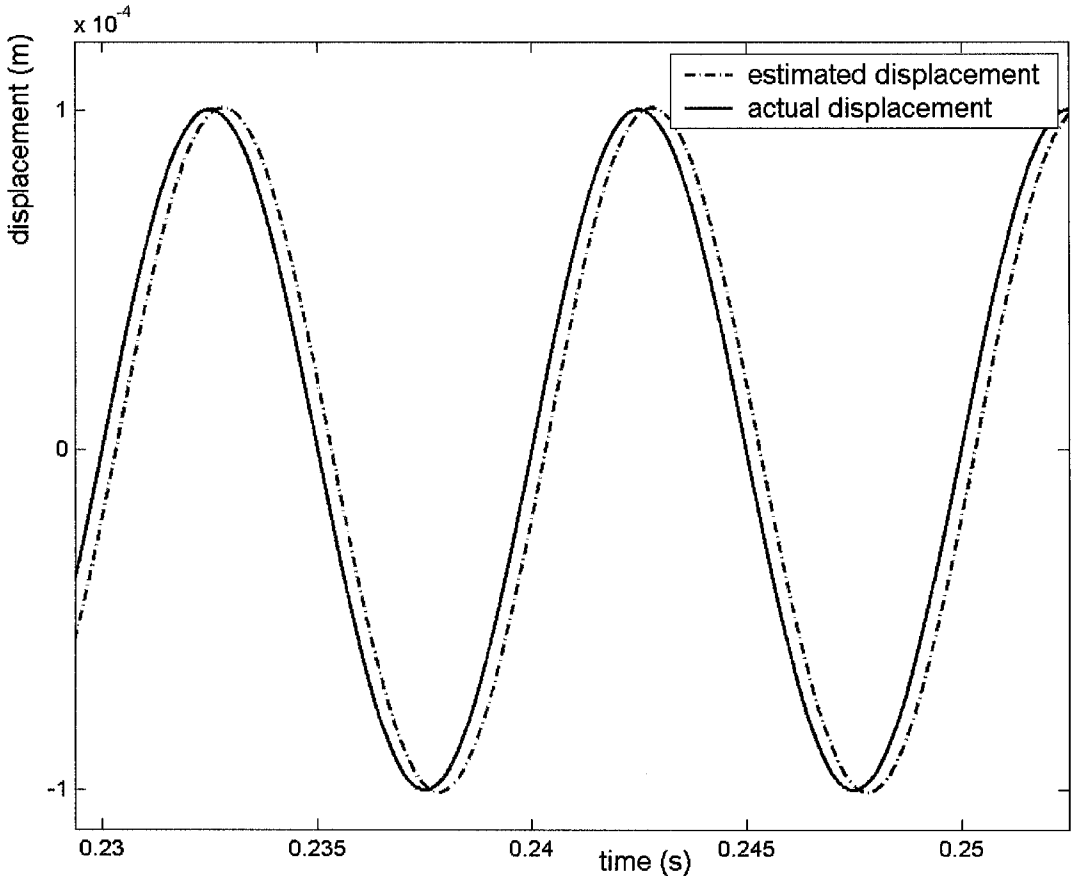

Figure 6.9: Forward path filter output compared with the actual displacement when the duty cycle is constant

The result shown in Figure 6.9 is based on the assumption of the constant duty cycle (50%), however, in practice, the duty cycle changes with the air gap or actual displacement. In order to show the influence of the varying duty cycle on the demodulation results, the duty cycle can be expressed as:

$$\alpha = 0.5 + \alpha_m \cos \omega t \tag{6.24}$$

Then, the variation of the duty cycle from 50% [22] is:

$$\alpha_m = \frac{\omega L I_a}{2V_s} \tag{6.25}$$

where ω is the current frequency, L is the nominal coil inductance, I_a is the current amplitude, and V_s is the switching voltage. In Simulink, a PWM model is added in to generate the variable α that follows equations (6.24) and (6.25), and the following Figure 6.10 shows the forward path filter output when the duty cycle changes with the actual displacement.

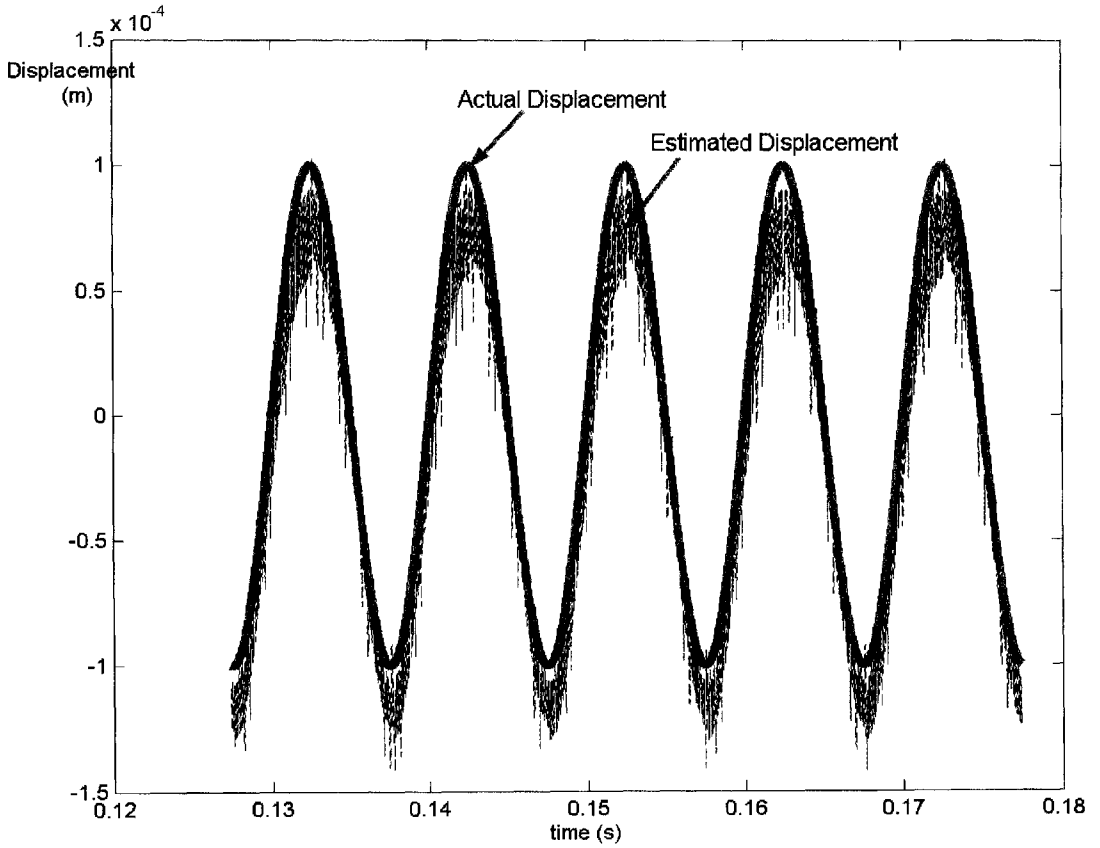

Figure 6.10: Comparison of simulated forward path filter output with the actual displacement with varying duty cycle

It can also be seen from the figure above that the forward path filter output (estimated displacement) is very noisy, lags the actual displacement signal and is contaminated with parasitic noise caused by the changing duty cycle. The enlarged part of Figure 6.10 is shown in Figure 6.11.

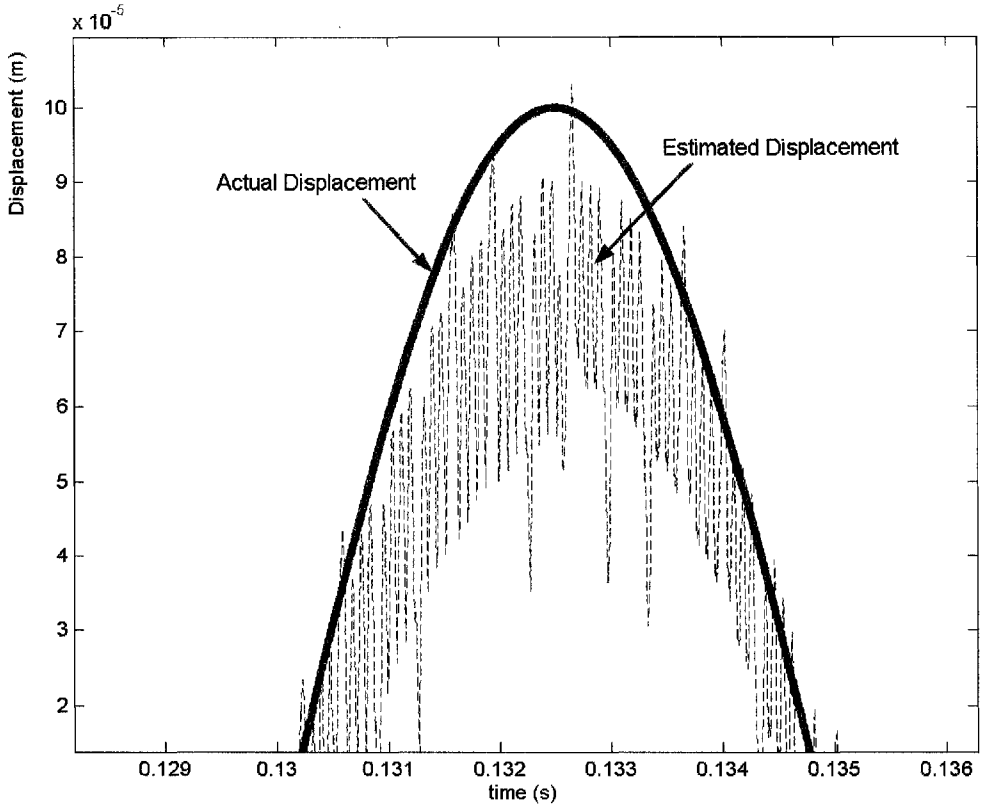

Figure 6.11: Enlarged part of Figure 6.10, showing the corruption caused by the changing duty cycle

It was proposed that by calculating the duty cycle online from the switching voltage information, the influence of the changing duty cycle on the forward path filter output could be removed. However, this proposal is not practical as it only incurs additional computational time penalty and may introduce additional phase lag in the estimated displacement. Consequently, the result would only be as good as the result of the forward pass filter. Maslen and Noh [22] propose the method of parameter estimation that greatly reduces the influence of PWM amplifier's duty cycle and at the same time improves the system measuring bandwidth. The following part presents the digital simulation of the parameter estimation method for the self-sensing AMB system.

6.3 Digital simulation of self-sensing parameter estimation

6.3.1 Introduction

To reduce the error in the estimated displacement output, another forward path filter is introduced in the parameter estimation procedure as shown in the schematics of Figure 6.12. The error between the outputs of two forward path filters will be fed into a convergence controller that updates the estimated air gap, which is then directed back to the simulated inductor model to close the loop. The overall simulation scheme of the parameter estimation procedure implemented in Simulink is shown below:

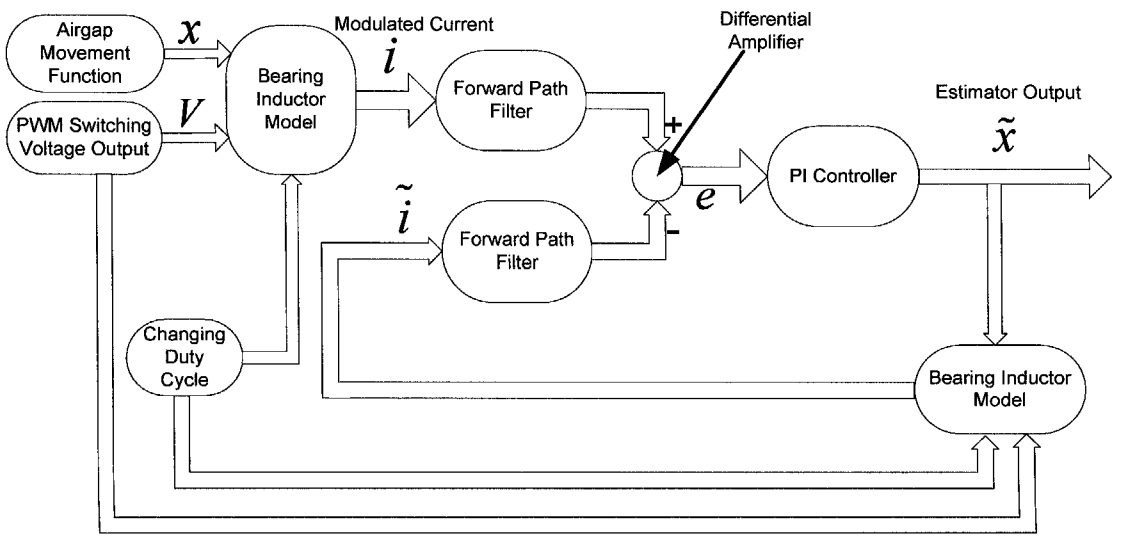

Figure 6.12: Self-sensing parameter estimation scheme for determining air gap displacement

Similar to the Simulink model for switching noise demodulation in Figure 6.7, in the scheme of parameter estimation, the same modulated current $\tilde{i}$ is generated

from the bearing inductor model which is supplied with the air gap movement function (actual displacement) and PWM switching voltage output with a changing duty cycle. Then, the modulated current $\tilde{i}$ goes through the same forward path filter described above, whose output will be compared with the output of the same loop containing the same bearing inductor model and forward path filter, then the error between the outputs of the two forward path filters is processed by the PI controller to update the estimated displacement, which is also at the same time fed back to the simulated bearing inductor model to close the loop.

6.3.2 Simulation results

The digital simulation result of the parameter estimator is shown in Figure 6.13, where it is compared with the actual displacement and the forward path filter output. In the graph, the parameter estimator output matches the actual displacement perfectly, and it is obvious that the parameter estimator is in excellent agreement with the actual displacement with little phase lag and that its performance is much better than the forward path filter alone, thus benefiting from the close loop property of the parameter estimator employing the PI controller.

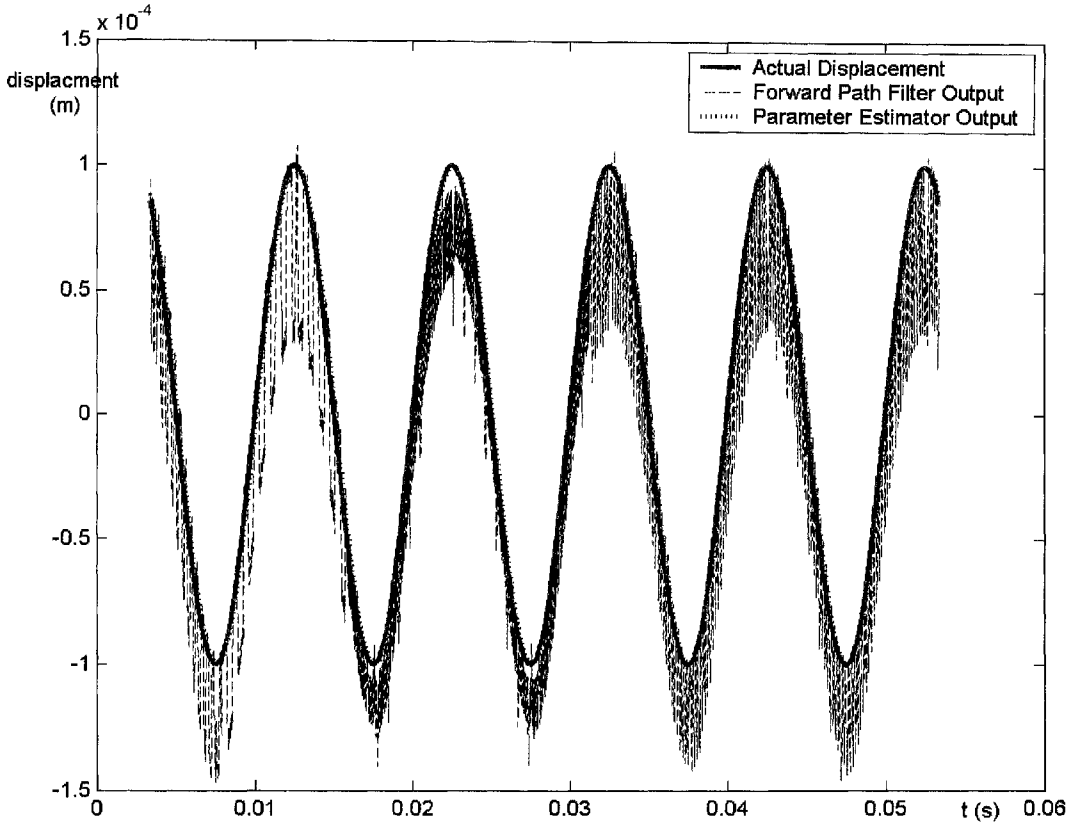

Figure 6.13: Parameter estimator output compared with the actual displacement and the forward path filter output

In order to obtain the amplitude and phase transfer functions of the parameter estimator, the actual displacement x is supplied with a multi-frequency SPHS test signal whose frequency range is set as from 1 to 4000 Hz with a fundamental frequency of 1 Hz. Following that, the output of the parameter estimator is stored along with the input, and then, the frequency response of the parameter estimator can be obtained in MATLAB from the transfer function of the output/input in the frequency domain. The simulation result of the transfer function of the parameter estimator is shown in Figure 6.14 where 'Transfer Function' is shortened to 'TF'.

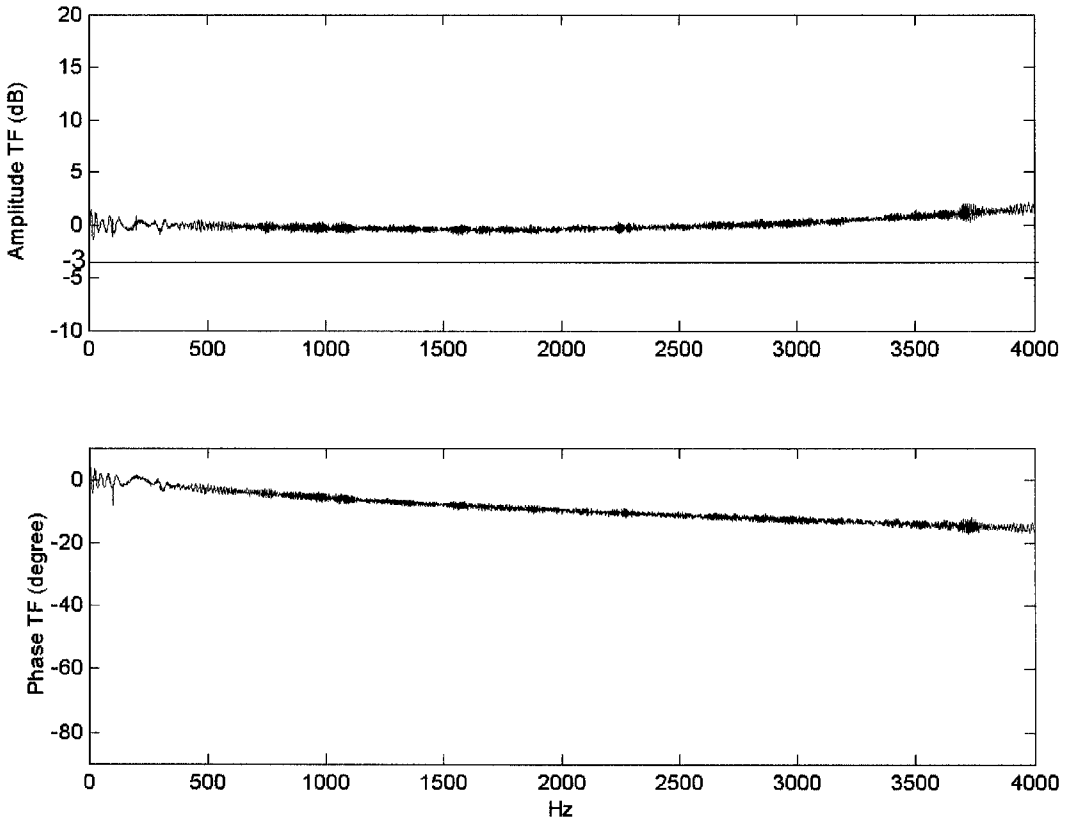

Figure 6.14: Frequency response of self-sensing parameter estimator in simulation

In Figure 6.14, the slight noise on the graph is due to the step effect of the signal digitization. The system bandwidth is observed to be very high, being above 4000 Hz, and the phase lag indicated is small, to be about 18 degrees lag from the frequency of 0 to 4000 Hz.

6.4 Analog circuits of self-sensing parameter estimator

Printed circuit boards (PCBs) have been developed to facilitate the implementation of the self-sensing parameter estimator for the AMB system. OrCAD® software [99] has been used as the design tool for the PCBs. The PCBs are composed of two

types of boards: the self-sensing boards for implementing the self-sensing parameter estimator and the backplane boards for connecting the signals between the power supplies, magnetic bearings, PWM amplifiers and the self-sensing boards. The design, components and function of the PCBs will be introduced. Static and dynamic calibrations of these PCBs will be presented to show the linearity and transfer function of the self-sensing parameter estimator.

6.4.1 Circuit implementations

The first circuit being analyzed is the self-sensing circuit, which adopts the self-sensing approach of the parameter estimation procedure to estimate the position information modulated in the switching current. It is then plugged into the backplane board and integrated as a complete system.

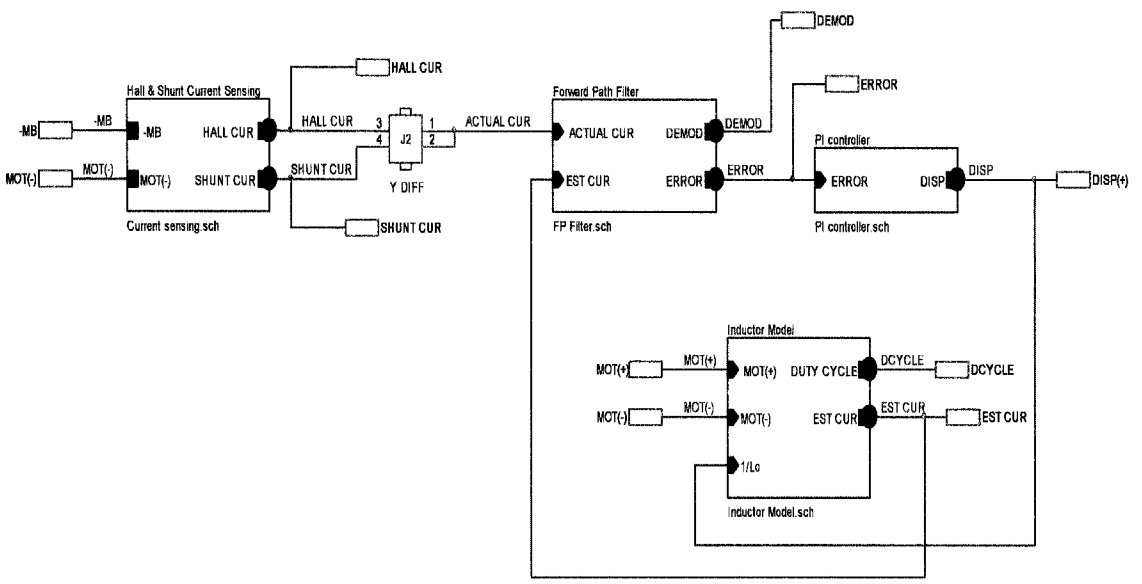

Figure 6.15: The main structure of self-sensing circuit implemented in OrCAD

The followings are the four hierarchical blocks implemented in the self-sensing circuits:

(1) Current sensing

(2) FP (Forward Path) filter

(3) PI controller

(4) Inductor Model

6.4.1.1 Current sensing

In the current sensing circuit design, the Honeywell CSNE151 current sensor is used to sense the current of the magnetic bearings. The output of the current sensor is then fed to the input of the self-sensing circuitries.

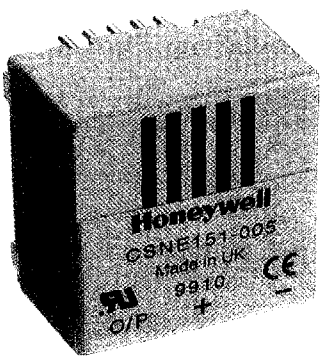

Figure 6.16: Honeywell current sensor CSNE151

During the research work, a few current sensors/transducers were compared and finally, the Honeywell current sensor CSNE151 was selected as the current sensor for the self-sensing parameter estimator, due to its good dynamic performances such as good linearity (0.1%), fast response time (<1 μs) and wide bandwidth (DC to 150 kHz), which is compatible with the outputs of the PWM amplifier employed in this experiment. The graph in Figure 6.17 shows the typical experimentally obtained switching coil current waveform sensed by the current sensor CSNE151.

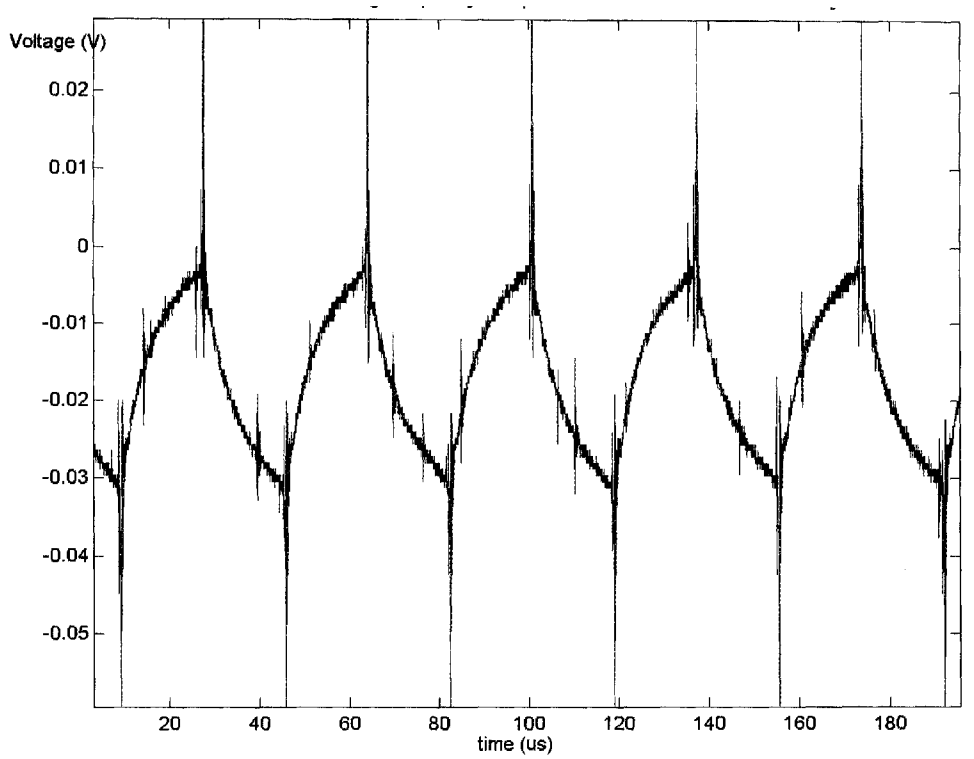

Figure 6.17:The switching coil current represented by voltage waveform as sensed by CSNE151

As can be seen from Figure 6.17, the waveform is not a perfect triangular waveform, but is a little distorted. The vertical discontinuity at the peak of the waveform is caused by the eddy current effect when the amplifier switches on and off.

6.4.1.2 Forward path filter

In this circuit, the actual current and estimated current are both processed by the same type of forward path filters. Firstly, the actual sensed current goes through a band pass filter, and then the ac-to-dc converter chip, AD637, computes the root-mean-square of the switching waveform and gives an equivalent dc output voltage.

Next, the value of both outputs is compared in a differential amplifier, INA105KP, and the difference is delivered to a PI controller for further signal processing.

The band-pass filter used in this design is a multiple feedback band-pass filter. The band-pass filters are called into action to pass a range of frequencies only. In the circuit, a band-pass filter with a frequency bandwidth of 30 kHz and a central frequency of 25 kHz is designed, passing frequencies ranged from 10 kHz to 40 kHz. The gain per stage is 1.15 and the quality factor is 0.83. Based on calculations, the following two-stage band-pass filters are designed with their respective components.

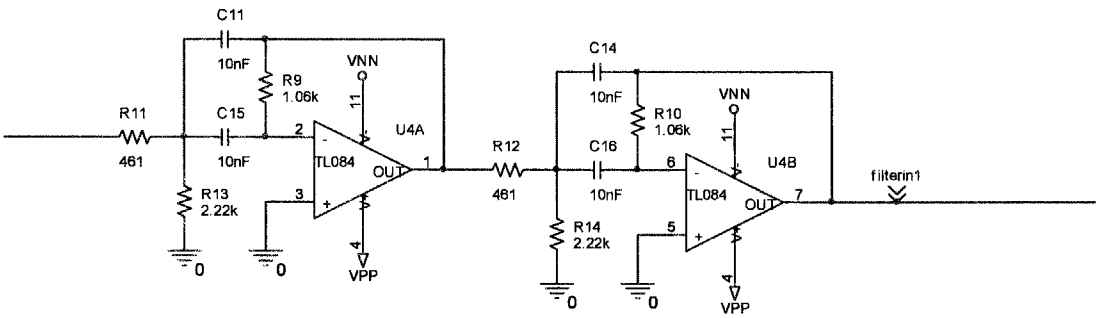

Figure 6.18: The band pass filter used in forward path filter

Figure 6.19 shows the waveform of the coil current after the band pass filter that removes the low frequency component of the sensed current, and only retains and amplifies its switching frequency component.

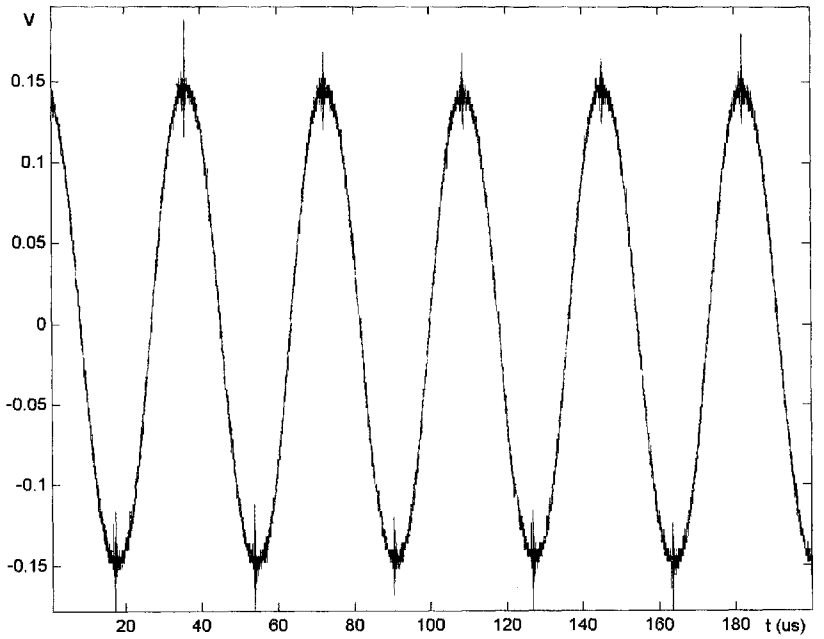

Figure 6.19: Waveform of measured coil current after the band pass filter

The AD637 is a highly accurate, monolithic ac-to-dc converter that computes the true rms value of any complex waveform. In order to reduce the ac ripple component of averaging error inherent in processing ac signals, a 2-Pole Sallen-Key Filter is adopted and its connection with corresponding part values is shown in Figure 6.20.

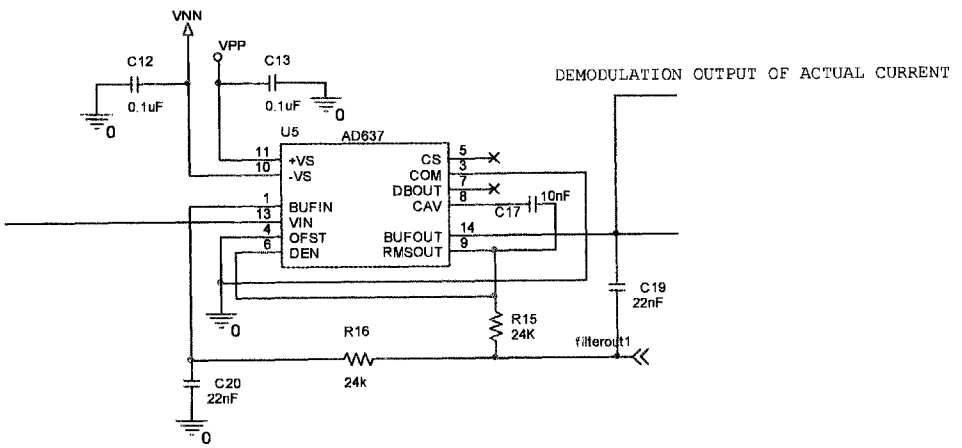

Figure 6.20: AD637 with 2-Pole Sallen-Key Filter acts as a rms-to-dc converter

6.4.1.3 PI controller

The controller used in this project is a Proportional-Integral type. Three potentiometers are used in this circuit design to adjust the Proportional, Integral and Bias terms. The PI's output signal is then amplified to produce the estimated displacement signal. The PI circuit is shown in Figure 6.21.

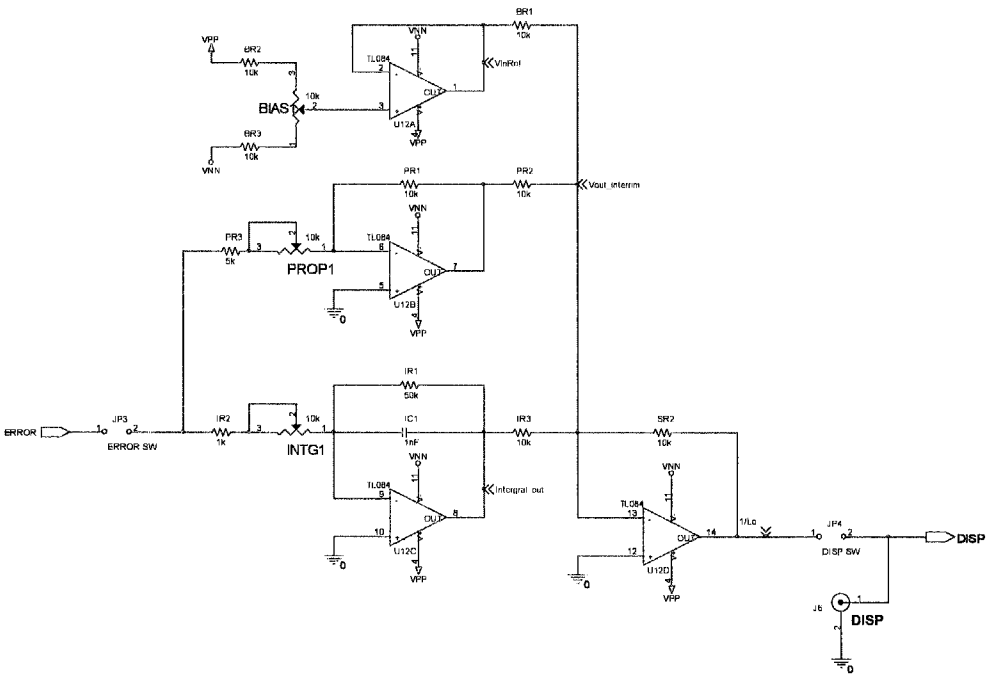

Figure 6.21: The circuit of PI controller

6.4.1.4 Inductor model

The amplifiers' switching output voltages (+) and (-), as well as the estimated displacement, are fed to the inductor model to produce the estimated switching current. The positive voltages and negative voltage outputs from the 2-state PWM amplifier (Copley 4122Z DC Brush Servo Amplifier) are fed to a differential amplifier, INA105KP, to produce the two-state switching voltage carrying the duty cycle information, which is measured and shown in Figure 6.22. The port connection scheme of Copley 2-state PWM amplifiers is attached in Appendix E.

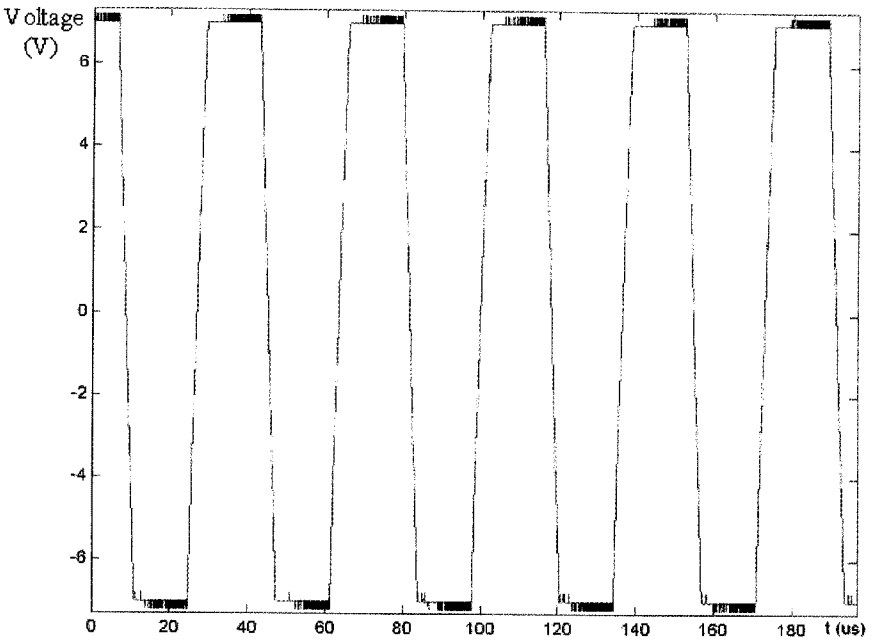

Figure 6.22: Switching voltage obtained by INA105KP

The MPY634KP is used as a balance modulator, with the input of the estimated displacement and the switching voltages. The modulated output will go though an integrator to produce the estimated current that will be fed to another forward path filter, thus forming a closed loop system.

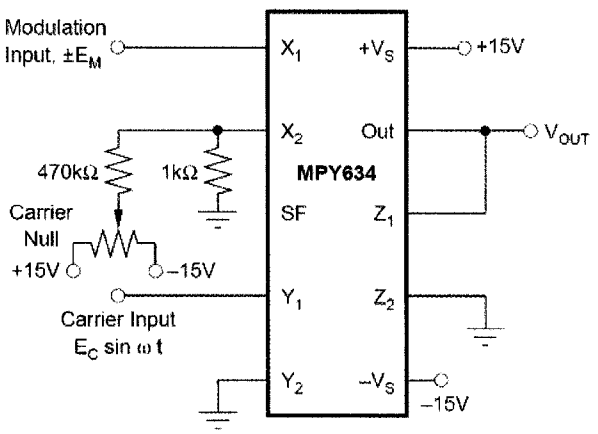

The basic muliplier connection performs balanced modulation. Carrier rejection can be improved by trimming the offset voltage of the modulation input. Better carrier rejection above 2MHz is typically achieved by interchanging the X and Y inputs (carrier applied to the X input).

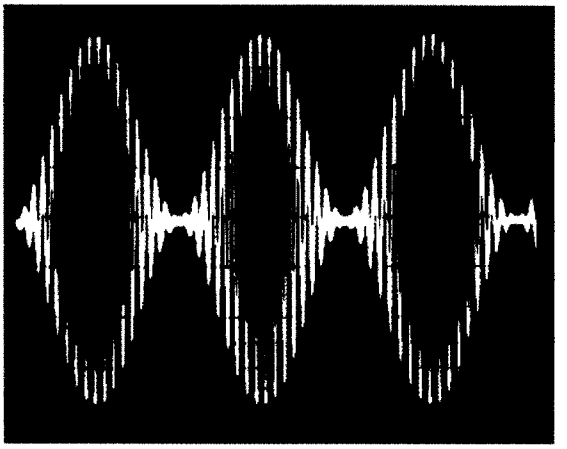

Carrier: f_c = 2MHz, Amplitude = 1Vrms
Signal: f_s = 120kHz, Amplitude = 10V peak

Figure 6.23: MPY634KP functions as a balance modulator with typical modulated output

6.4.1.5 Backplane for self-sensing PCBs

Another circuit that is developed into a printed circuit board is the backplane. In the backplane circuit, four connectors are used and each connector is connected to one self-sensing board. The backplane facilitates power and some other signal connections to the self-sensing circuit boards. The PWM amplifiers, which have power supplies of +25V and -25V, and the self-sensing circuits with power supplies of +14V and -14V, are all connected to the backplane. To facilitate data collection, signals such as the estimated displacement, duty cycle, or error signal from PI controllers are also accessible on the backplane.

It is in this manner, that the backplane makes the overall self-sensing circuit system neater, and can make signal probing and troubleshooting easier. The connection between the self-sensing board and backplane is as shown in Figure 6.24.

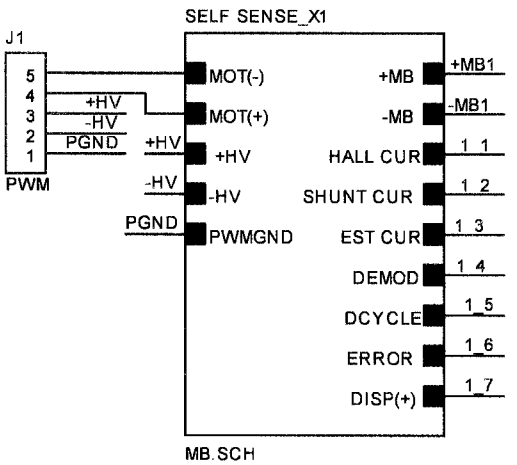

Figure 6.24: Connection between self-sensing board and backplane

Figure 6.25 below shows a photograph of four self-sensing boards mounted on one backplane. It can be imagined that without the connection of the backplane, there would be many cables running between the self-sensing circuit boards, PWM

amplifiers, magnetic bearings and power supplies, and it will be near impossible to probe signals in the self-sensing circuits except for those with the BNC connectors.

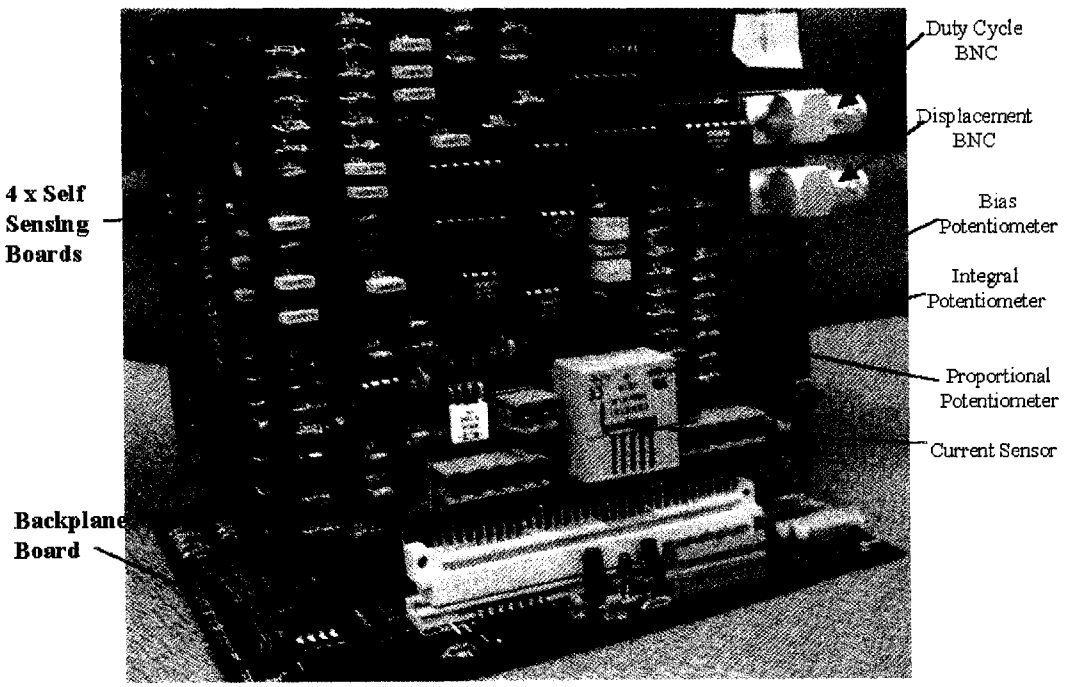

Figure 6.25: Four self-sensing boards mounted on one backplane board

6.4.2 Static and dynamic calibrations of self-sensing scheme

6.4.2.1 Description of the test rig

The photograph of the test rig is shown in Figure 6.26. The middle platform is supported by eight springs in such a manner that only one DOF movable movement is allowed. The upper and lower E-frames are made of silicon steel laminations, and between the two, there is a lamination target that is embedded in the middle platform. The thickness of the laminations is 0.23 mm. The coils of the

E-frames are also connected with the self-sensing PCBs from which the air gap information will be estimated.

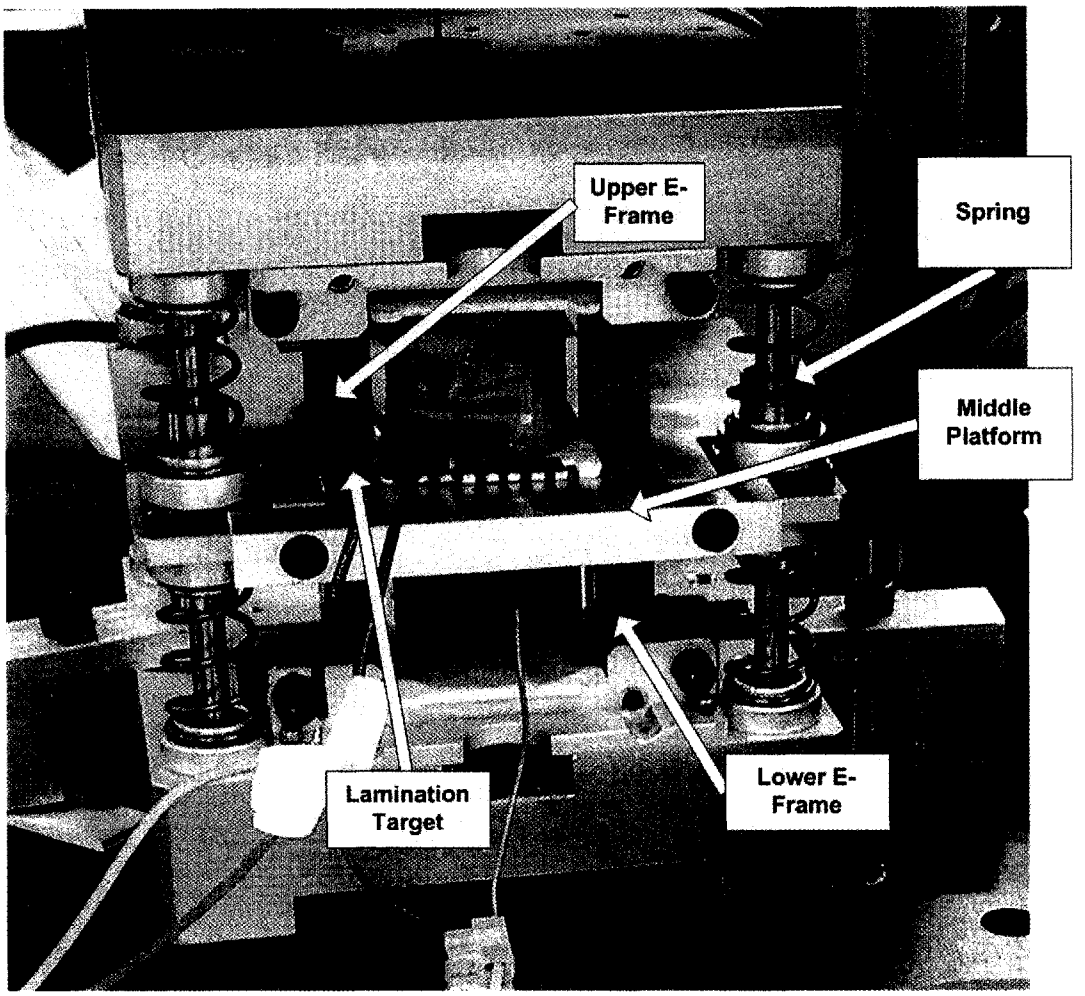

Figure 6.26: Photograph of the self-sensing test rig.

6.4.2.2 Static calibration

A static calibration is performed to examine the linearity of the self-sensing estimated outputs. The photograph in Figure 6.27 shows how the test rig is set up. A M20 screw is used to adjust the position of the middle platform, which is measured by a dial gauge.

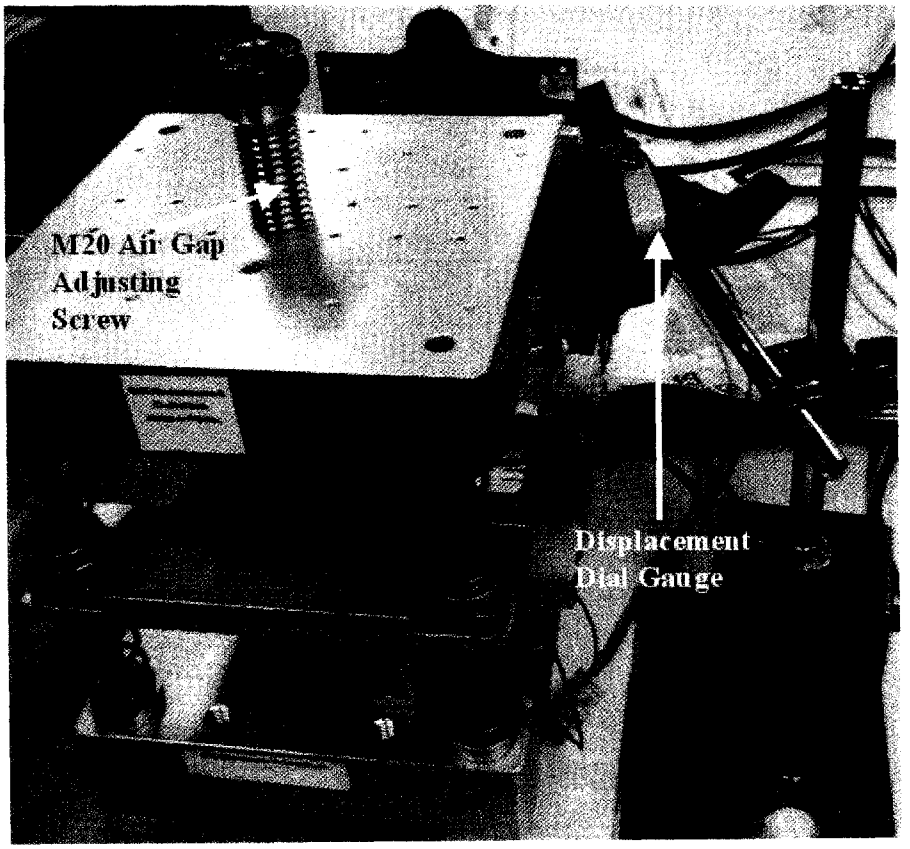

Figure 6.27: Photograph of the self-sensing static calibration test

By adjusting the air gap between the lower E-frame electromagnet (or upper E-frame) and the middle platform by means of an air gap adjusting screw, a range of platform displacements with respect to self-sensing estimated displacement output are recorded and the data is later plotted in a graph. The static calibration result is listed in Table 6.1, where it can be seen that the self-sensing output voltage reaches saturation when the air gap length is larger than 0.5 mm.

Table 6.1: Static calibration result of self-sensing parameter estimator

Displacement (mm)	Self-Sensing Output (mV)
0	0
0.05	22
0.10	46
0.15	68
0.20	90
0.25	113
0.30	136
0.35	158
0.40	180
0.45	202
0.49	220
0.55	222
0.60	223

The data is plotted with a linearly fitted straight line as shown in Figure 6.28.

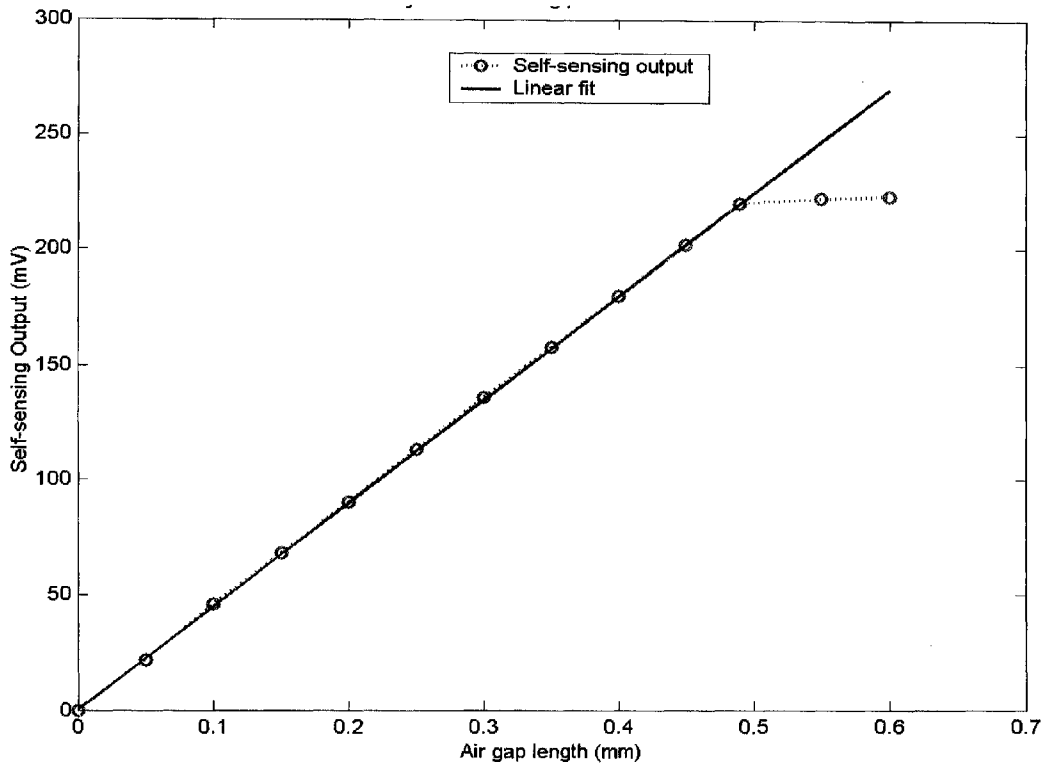

Figure 6.28: Linearity of the self-sensing parameter estimator

As can be seen from Figure 6.28, the self-sensing parameter estimator is very linear, and the gain of the self-sensing output over the platform displacement is about 0.43 V/mm. The maximum linearity error is computed to be around 2.4%.

6.4.2.3 Dynamic calibration

The SPHS is supplied to a shaker to perturb the platform, whose displacement is measured by a commercial eddy current probe (Bently Nevada 7200) and this displacement is simultaneously compared to the self-sensing estimated displacement. In this manner, the two displacements could be compared over the frequency range by examining the self-sensing estimated output over the eddy current probe output. The dynamic calibration is performed by exciting the one DOF test rig with a multi-frequency SPHS test signal. The instrumentation arrangement for the dynamic calibration is shown in Figure 6.29.

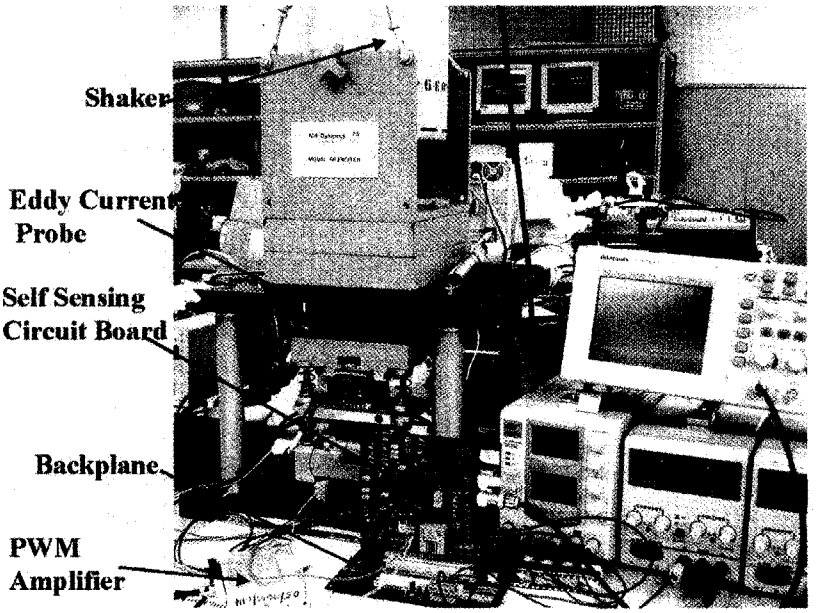

Figure 6.29: Instrumentation arrangement for self-sensing dynamic calibration

Due to the dynamic magnification factor of a second order system of the test rig, its measured displacements around the neighbourhood of resonance are naturally more responsive and ideal for displacement comparison between the estimated and eddy current probe. However, beyond this range of frequency bandwidth, the voltage output of the estimated displacement was observed to be relatively small. This behaviour is compensated by delivering higher excitation force through the shaker to provide better estimated displacement signal to noise measurement.

In addition, in order to keep the output of the eddy current probe and self-sensing parameter estimator within the sampling resolution range of the dSPACE ds1103 A/D converter, the excitation bandwidth of the SPHS is chosen to be 1 to 150 Hz, with a fundamental frequency of 1 Hz. The following time-domain measurements indicate that excellent agreement can be obtained between the eddy current probe output and the self-sensing parameter estimated output.

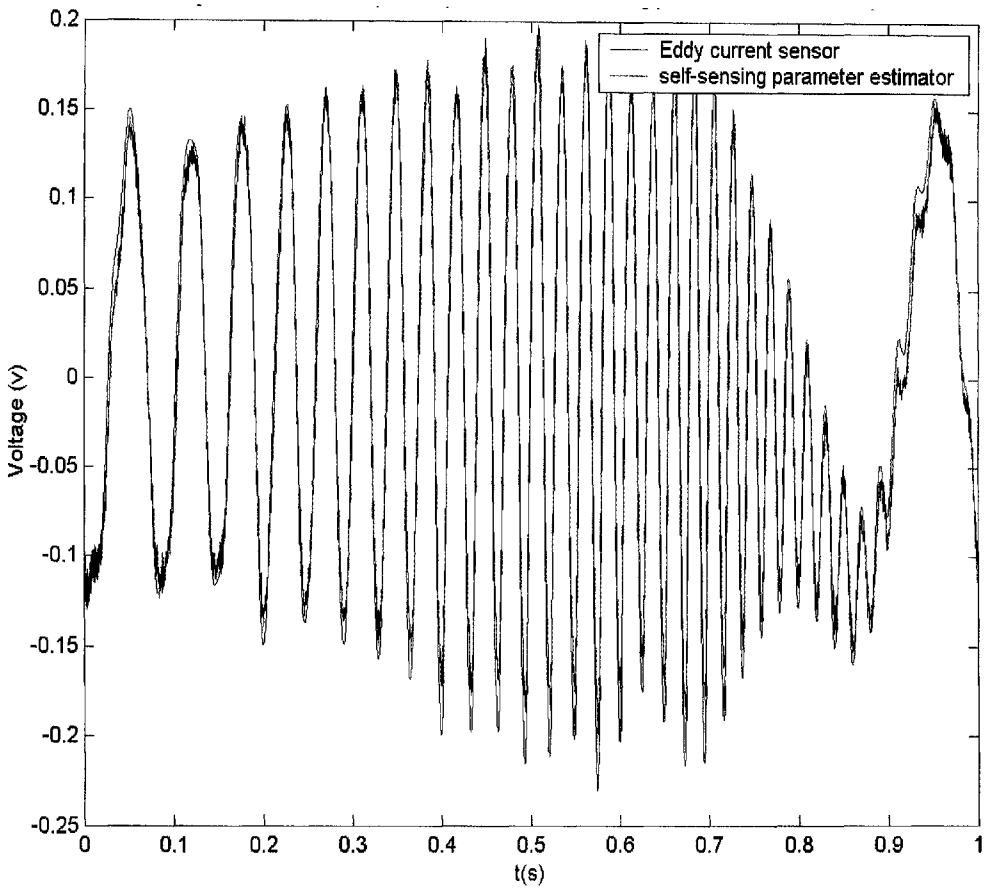

Figure 6.30: Eddy current probe output compared with self-sensing parameter estimated output

From Figure 6.30, it can be observed that the self-sensing parameter estimator output can track the eddy current probe output very well with minimal time delay between the two. The time domain data is transformed into the frequency domain using a FFT algorithm and therefore, the transfer function of the parameter estimator output over the eddy current probe output in frequency domain is obtained, as shown in Figure 6.31.

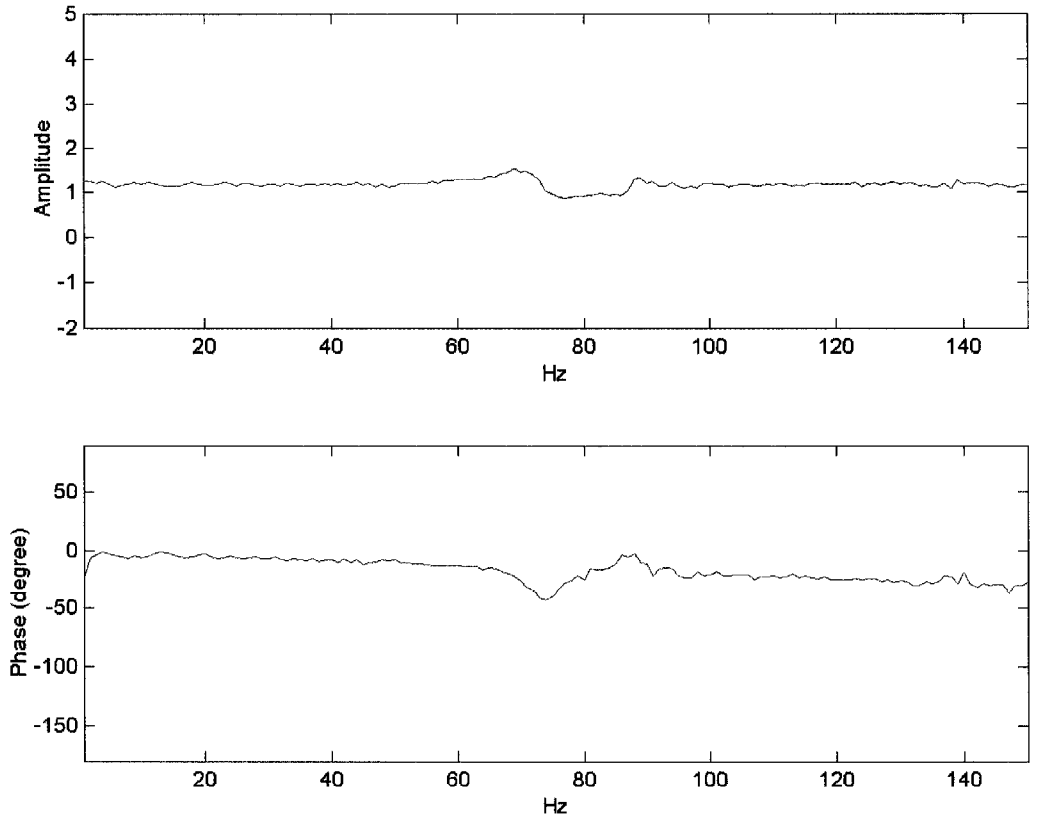

Figure 6.31: Frequency response of self-sensing parameter estimated output over eddy current probe output

The amplitude transfer function is observed to be constant through the whole frequency range, except at 75 Hz where there is a dip in phase angle. This dip is attributed to the resonance of the top plate on which the eddy current probe is mounted, and also the non-collocation of the electromagnets and the eddy current probe. The phase transfer function is observed to decrease marginally throughout the frequency range of 150 Hz. The maximum phase delay is about -30° at the excitation frequency of 150 Hz.

In order to test whether or not the time delay was caused by the data acquisition process, we pumped two absolutely same multi-frequency test signals (bandwidth: 1-150 Hz) simultaneously into a dynamic analyzer and the data acquisition card: dSPACE ds1103 we used. We found from the data acquisition card that there was no any phase difference at all through the whole bandwidth of 1 to 150 Hz between

the two test signals and the their amplitude ratio was perfect 1 in the whole frequency range, which was also confirmed by the same readings of the dynamic analyzer. So we can exclude the possibility of the data acquisition causing the time delay. Through the experiments, we found that the noise to signal ratio of the self-sensing signals was around 1 to 5, which is quite high and the noise frequency varied with movement of the lamination target, which may be the cause of the time delay, but further investigation and confirmation of this is needed in the near future.

In order to make sure that the system can tolerate the added phase lag, based on the self-sensing parameter estimator model shown in Figure 6.12, the simulation was performed to obtain the Bode diagram of the physical implementation of the self-sensing parameter estimator, as shown in Figure 6.32. The corresponding system phase margin is about $-97-(-180)=83$ degree, which is much larger than the added phase lag of 30 degree, and therefore this phase lag should not destabilize the system.

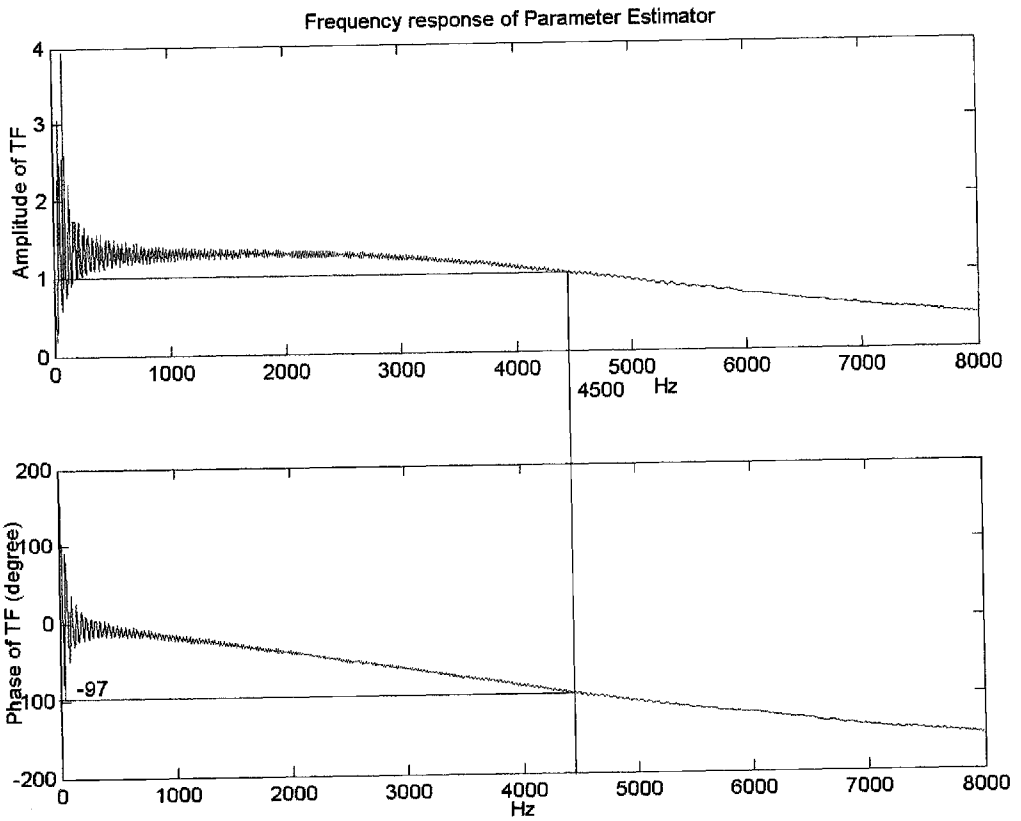

Figure 6.32: Frequency response of the self-sensing parameter estimator when the self-sensing levitated system is at a fixed reference position

Chapter 7 Conclusions & Future work

7.1 Conclusions

In this research, a compact HMBs system has been designed and developed for axial flow blood pump applications with possible self-sensing capability. In Chapter 4, preliminary work on parameter estimation is carried out to obtain the actual stiffness and damping coefficients of the one-DOF magnetically levitated system and also to determine the influences of the PID controllers' variables on its stiffness and damping properties. These experimental investigations help the understanding, implementation and debugging of the estimation algorithm. In Chapter 5, with the assistance of a specially designed test rig, the method of parameter estimation in the frequency domain has been adopted to estimate the stiffness and damping coefficients of the HMBs system of the axial flow blood pump in both the radial and axial directions. The actuators' gain and maximum linear operating range of the HMBs system have also been obtained experimentally with the aid of the same test rig. A self-sensing parameter estimator for AMB system has also been investigated, developed and tested.

The HMBs system of the axial flow blood pump is composed of two identical hybrid magnetic bearings (HMBs) for suspending the rotor, and one brushless and sensorless three-phase PM motor for driving the rotor. In order to decrease the eddy current loss, the stators of the HMBs and the motor are made of 0.23 mm thick silicon steel laminations. PID controllers are used to control the HMBs with active control in the radial axes and passive control in the axial axis. FEA in Maxwell 3D has been performed on the HMBs system to confirm that the active

control forces in radial directions can cause the passive axial control. The STMicroelectronics ST7FMC micro controller is used to control the Lorentz-typed DC brushless motor in the sensorless mode. The HMBs system of the axial flow blood pump can achieve good performance: the rotor can rotate in stable suspension at speeds of up to 14,000 rpm in air, from which it could be foresaw that it also can achieve good performance of the pump system in fluid, since the fluid can provide additional damping to the bearing system. The whole pump design is compact that it is suitable for future intra-ventricular implantation.

The one-DOF magnetically levitated system is realized with a digital PID controller. The parameter estimation method with statistical analysis is utilized to obtain the actual stiffness and damping coefficients of the one-DOF magnetically levitated system online. Experimental results show that there are differences between the actual and effective stiffness and damping coefficients adopted by other researchers. The estimated coefficients are supported by statistical information from a least-square estimation program. It provides a quantitative measure of the model validity by means of goodness of fit and the verification of the estimated coefficients by significance tests. It is also observed that the proportional, integral, and derivative gains of the PID controller have direct influences on both the actual stiffness and damping coefficients of the one-DOF magnetic suspension system.

The HMBs system of the axial flow blood pump is modelled as a typical mass-spring-damper system, and the method of parameter estimation in the frequency domain has been adopted to estimate its stiffness and damping coefficients. A specially designed test rig has made it possible to estimate the system stiffness and damping coefficients in both the radial and axial directions, whether the rotor is

rotating or stationary. From the estimation results of the accurate value of stiffness and damping coefficients in the frequency domain, it can be seen that the stiffness of the magnetic bearing system is dominant in the system dynamic characteristics, and it is frequency dependent: it also increases with the excitation frequency. It is also shown that the proportional gain of the PID controller can change the system stiffness coefficient: with the increase of proportional gain, the system stiffness also increases. In addition, it is found out from the estimation results that in the passively controlled axial axis, the stiffness and damping coefficient are much smaller than those of the radial axes that are actively controlled, but they are significant to the system stability of the axial flow blood pump. All the experimental results are validated by high goodness of fit of the estimation results.

Two current demodulation approaches for self-sensing AMB – switching noise demodulation and parameter estimation – have been introduced and compared. Digital simulation of self-sensing parameter estimation has proven that it can achieve much better system performance and wider system bandwidth. This self-sensing parameter estimator has been developed and tested. Experimental results of static calibration and dynamic calibration of the self-sensing parameter estimator show that it has a good linearity and good dynamic response, and therefore has the potential for future industrial applications. Due to insufficient time, the author has not applied this self-sensing parameter estimator to the HMBs system of the axial flow blood pump developed in this research, which will be further developed by future students.

In summary, in the development of the HMBs system for axial flow blood pump applications with possible self-sensing capability and parameter estimation, the following has been presented in this dissertation:

1. An axial flow blood pump has been designed with the impeller enclosed in the rotor and with a diameter of 40 mm and length of 104 mm. The target pump pressure is 100 mmHg and flow rate is 5 L/min.
2. The magnetically levitated axial flow blood pump has been realized in air with the HMBs system and with a maximum rotational speed of 14,000 rpm and maximum vibration amplitude of 30 μm in the radial directions and 70 μm in the axial direction.
3. The HMBs actuator gain has been obtained experimentally, being around 5.8 N/V and the maximum linear operating range being within 20% neighbourhood of rotor's eccentricity ratio.
4. The radial and axial stiffness of the HMBs system have been obtained experimentally with the method of parameter estimation in the frequency domain: the maximum stiffness is about 1470 kN/m in the radial directions and about 270 kN/m in the axial direction.
5. Self-sensing parameter estimator for the AMB system has been developed and calibrated: its maximum linear displacement range is 0.5 mm, its gain of the self-sensing output over displacement is 0.43 V/mm, and its maximum phase delay is about -30° at the excitation frequency of 150 Hz.

7.2 Future work

There is still some work to be carried out for the accomplishment of the maglev axial flow blood pump with self-sensing HMBs, and they are listed below:

1. Fluid test of the pump. In the near future, the pump performance will be tested in a mock fluid circulation loop. The vibration of the rotating rotor in

fluid, the noise level of the operation, and the pump temperature will all be measured accordingly. Some other data also needs to be obtained, such as the power consumption, pump efficiency, the relationship between the flow rate and differential pressure, etc.

2. Parameter estimation on the pump system in water. Once the pump is water proofed, the same method of parameter estimation in frequency domain introduced in this dissertation will be utilized to investigate system stiffness and damping coefficients in water. It can also be used to find out the fluid influences on the system dynamic properties, with the assistance of the same test rig. Also, with this method, the relationship between the flow rate and the system stiffness will also be investigated, especially in the axial direction.

3. The PWM amplifiers for driving the HMBs system will be changed. The old ones (AMC 25A series) were rated for a peak current of 25A, which exceeds system requirement and causes more power waste. In the future it is needed to change the PWM amplifier to those with low maximum peak and continuous current such as the model of AMC PWM 10A8, which can still satisfy system requirement.

4. The developed self-sensing parameter estimator will be applied to the HMBs system of the axial flow blood pump as an integrated system, in order to replace the eddy current probes. The PI convergence controller will be implemented digitally, in order to ease the tuning procedure.

5. Some additional testing needs to be done to confirm or invalidate the hypothesis in Chapter 6 that the distortion near 75 Hz in the transfer function of the self-sensing parameter estimator is due to the structural

resonance of the plate which supports the eddy current probe, by increasing or decreasing the stiffness of the plate or changing the mass of the plate to see whether or not the resonance moves.

6. By means of simulation, the digital self-sensing parameter estimator has been verified to be able to achieve the same good system performance as analog circuits. The most difficult part of implementing the complete digital self-sensing parameter estimator is the high sampling frequency required. To obtain the minimum required sampling rate for the digital self-sensing parameter estimator, the sampling rate of the simulation is decreased until the system goes unstable; in test when the sampling rate was decreased to 160 kHz, the Simulink simulation error happened, but if it was increased from 160 kHz to 165 kHz, no error happened and the simulation could run well over infinite period of time. So the minimum required sampling rate for the digital self-sensing parameter estimator should be 165 kHz. Unfortunately, it is beyond the capabilities of dSPACE ds1103, the online control board that we are currently using. A good alternative may be the Silicon Lab C8051F060 chip that is programmable throughput of up to 1 MSPS (million samples per second) for each ADC, with high-speed 8051 μC Core up to 25 MIPS (million instructions per second) throughput with 25 MHz system clock. The only difficulty may lie in the programming of the self-sensing parameter estimator in the chip, which is not as easy to program as dSPACE ds1103.

References

[1] Lim T.M, Cheng Shanbao, A compact magnetic bearing system for axial flow blood pump. *Proceedings of International Conference on Control and Automation, IMECS.* Hong Kong, March 2007, pp. 1591-1596.

[2] Saberi A., Chen B. M. and Sannuti P. Loop Transfer Recovery: Analysis and Design. New York: Springer-Verlag, 1993.

[3] Fujita M., Matsumura F., and Shimizu M. H∞ robust control design for a magnetic suspension system. In *Proceedings of the Second International Symposium on Magnetic Bearings*, 1990, Tokyo, Japan.

[4] Tian H. Q. and Nonami K. Robust-control of flexible rotor magnetic bearing systems using discrete-time sliding mode control. *JSME International Journal Series C*, 37(3), pp. 504-512.

[5] Knospe C.R., Fedigan S.J., Hope R.W., and Williams R.D. A multitasking DSP implementation of adaptive magnetic bearing control. *IEEE transactions on control systems technology,* vol.5, No.2, March 1997.

[6] Shi J., Zmood R., and Qin L.J. The direct method for adaptive feed-forward vibration control of magnetic bearing systems. In *Proceedings of Seventh International Conference on Control, Automation, Robotics And Vision*, Dec. 2002, Singapore.

[7] Humphris R.R., Kelm R.D., Lewis D.W., and Allaire P.E. Effect of control algorithms on magnetic journal bearings. *Trans. ASME Journal of Engineering for Gas Turbines and Power*, October 1986.

[8] Sahinkaya M.N., Cole MOT, Burrows C.R. On the use of Schroeder phased harmonic sequences in multi-frequency control of flexible rotor/magnetic bearing systems. In *Proceedings of the 8th International Symposium on Magnetic Bearings*. 2002, Mito, Japan.

[9] Hiroyuki Fujiwara, Koji Ebina, Naohiko Takahashi, Osami Matsushita. Control of flexible rotors supported by active magnetic bearings. In *Proceedings of the 8th International Symposium on Magnetic Bearings*. 2002, Mito, Japan.

[10] Burrows C.R., Sahinkaya M.N. Vibration control of multi-mode rotor-bearing systems. *Proc. R. Soc. Lond.* A 386, 1983, pp. 77-94.

[11] Burrows C. R., Sahinkaya M. N., Clements S. Active vibration control of flexible rotors: an experimental and theoretical study. *Proc. R. Soc. Lond.* A 422, 1989, pp. 123-146.

[12] Tomoaki Takami, Michihiro Kawanishi, Hiroshi Kanki. Advanced control for active magnetic bearing. In *Proceedings of the 8th International Symposium on Magnetic Bearings*. 2002, Mito, Japan.

[13] Hideo Shida, Mitsuhiro Ichihara and Kazuto Seto. Motion and vibration control of flexible rotor using magnetic bearing. In *Proceedings of the 8th International Symposium on Magnetic Bearings*. 2002, Mito, Japan.

[14] Okada Y., Saitoh T., Shinoda. Y. Vibration control of flexible rotor by inclination control magnetic bearings. In *Proceedings of the 1999 IEEE/ASME International Conference on Advanced Intelligent Mechatronics*, September 1999, Atlanta, USA, pp. 788-793.

[15] Kasarda M.E.F., Mendoza H., Kirk R.G., Wicks A. Reduction of subsynchronous vibrations in a single-disk rotor using an active magnetic damper. *Mechanics Research Communications*, 2004, 31 (6), pp. 689-695.

[16] Kim K.J., Lee C.W. Identification of dynamic stiffness of squeeze film damper using active magnetic bearing system as an exciter. *ISCORMA-2*, Poland, 2003.

[17] Aenis M., Knopf E., Nordmann R. Active magnetic bearings for the identification and fault diagnosis in turbomachinery. *Mechatronics*. 2002(12), pp. 1011-1021.

[18] Baun D. Hydrodynamic forces in centrifugal pump and compressor impellers in volute casing: measurements using magnetic bearings and CFD simulations. PhD thesis, University of Virginia, 2002.

[19] Allaire P.E., Hilton E, Baloh M, Maslen E, Barnson G, Noh D, Khanwilkar P, Olsen D. Performance of a continuous flow ventricular assist device: Magnetic bearings design, construction, and testing. *Artif Organs* 1998(22), pp. 475-480.

[20] Hoshi H, Shinshi T, Takatani S. Third-generation blood pumps with mechanical noncontact magnetic bearings. *Artif Organs* 2006; 30(5), pp. 324-338.

[21] Montie D.T. Performance Limitations and Self-Sensing Magnetic Bearings. PhD thesis, University of Virginia, 2003.

[22] Noh M. D. Self-Sensing Magnetic Bearings Driven by a Switching Power Amplifier. PhD thesis, University of Virginia, 1996.

[23] Schweitzer G., Traxler A., and Bleuler H. Active Magnetic Bearings. Verlag der Fachvereine, 1994.

[24] Lu B., Choi H., Buckner G., Tammi K. Linear parameter-varying techniques for control of a magnetic bearing system. *Control Engineering Practice*, 2008, doi:10.1016/j.conengprac.2008.01.002.

[25] Fittro R. A high speed machining spindle with active magnetic bearings: control theory, design and application. PhD thesis, University of Virginia, 1998.

[26] Lim T.M., Zhang Dongsheng. Numerical analysis of blood trauma in an enclosed-impeller axial flow pump. In *Proceedings of the 13th Congress of the International Society for Rotary Blood Pumps* 2005, Tokyo, Japan.

[27] Zmood, R.B., Qin, L.J., Kirk, J.A., Sun, L A. Magnetic bearing system design methodology and its application to a 50 Wh open core composite flywheel. Proceedings of 32nd Energy Conversion Engineering Conference, 1997. vol 4, pp. 2306-2311.

[28] Yong Teng. Magnetic bearing system design using a generic algorithm. PhD thesis, University of Virginia, January 1999.

[29] Malone, C.L. Power to weight optimization for magnetic bearings. In *Proceedings of Magnetic Bearings, Magnetic Drives and Dry Gas Seals Conference & Exhibition,* Virginia, 1993.

[30] Klesen C., Nordmann R., Schonhoff U. Design of a minimum current magnetic bearing. In *Proceedings of the 5th International Symposium on Magnetic Suspension Technology*. Santa Barbara, CA, 1999.

[31] Bloodgood V. Jr., Groom N., Britcher C. Further development of an optimal design approach applied to axial magnetic bearings. In *Proceedings of the 8th International Symposium on Magnetic Bearings*. 2002, Mito, Japan, pp. 489-494

[32] Steffani D., Hofmann W., Design and comparison of different kinds of radial magnetic bearings. In *Proceedings of the 8th International Symposium on Magnetic Bearings*. 2002, Mito, Japan, pp. 461-466.

[33] J. Boehm, R. Gerber, and N.R. C Kiley. Sensors for magnetic bearings. *IEEE Transactions on Magnetics*, 29(6), Nov. 1993.

[34] H. Bleuler, C. Gahler, R. Herzog, R. Larsonneur, T. Mizuno, R. Siegwart, and S. J. Woo. Application of digital signal processors for industrial magnetic bearings. IEEE transactions on control systems technology. Vol. 2. No. 4, December 1994, pp.280-289.

[35] C. R. Knospe, S. J. Fedigan, R. W. Hope, and R. D. Williams, A multitasking DSP implementation of adaptive magnetic bearing control. IEEE Trans. Control Syst. Techno. 5, 1997, pp. 230–237.

[36] Hartavi A.E., Ustun O., Tuncay R.N., Gurleyen F. The design, simulation and experimental study of active magnetic bearing. Electric Machines and Drives Conference, IEEE International, 2001, pp. 492 - 495

[37] McMullen P.T., Huynh C., Hayes R.J. Combination radial-axial magnetic bearing. In *Proceedings of the 8th International Symposium on Magnetic Bearings*. 2002, Mito, Japan, pp 473-478.

[38] Hendershot J., Miller T. Design of brushless permanent-magnet motors. Magna Physics Publishing and Clarendon Press. Oxford, 1994.

[39] Jang S.M., Cho H.W., Choi J.Y., Park J.H., Choi S.K. Development of high-speed brushless DC motor for turbo-compressor. *Electrical Machines and Systems*, 2005. Vol. 2, (27-29), pp. 877 - 882.

[40] Upadhyay R., Fajagopal K. FE analysis and CAD of radial-flux surface mounted permanent magnet brushless DC motors. *IEEE Transactions on Magnetics*. Vol.41. No.10, 2005, pp. 3952-3954.

[41] Bianchi N., Bolognani S. Brushless DC motor design: an optimisation procedure based on genetic algorithms. In *Proceedings of the 8th International Conference on Electrical Machines and Drives*, September, 1997. pp. 16-20.

[42] Bianchi N., Bolognani S., Luise F. Analysis and design of a brushless motor for high speed operation. *IEEE Transaction on Energy Conversion*, Sept. 2005, Vol. 20, Issue 3, pp. 629 – 637.

[43] Zheng P., Wang J., Liu R., Jiang H., Cui S., Cheng S. Performance calculation of brushless DC motor. In *Proceedings of the Eighth International Conference on Electrical Machines and Systems,* 2005, pp. 426- 428.

[44] Wang J., Zhou L.B., Tao G.L. Design and analysis of a multiphase permanent magnet brushless DC motor drive system for high power applications. In *Proceedings of 2nd IEEE Conference on Industrial Electronics and Applications*, 2007, pp. 1182 – 1187.

[45] Olsen DB. The history of continuous-flow blood pumps. *Artificial Organs*, 2000, 24 (6), pp. 401-404.

[46] Goldowsky M. Magnevad-the world's smallest magnetic-bearing turbo pump. *Artificial Organs*, 2004, 28 (10), pp. 945-952.

[47] Noon G.P. The MicroMed DeBakey VAD United States clinical experience. *Artificial Organs*, 2006, 30:A13.

[48] Westaby S. The Jarvik 2000 axial flow pump. *Artificial Organs,* 2006, 30:A12.

[49] Butler K, Farar D, Heatley J. Continued development of the HeartMate II LVAD. *Artificial Organs*, 2006, 30:A13.

[50] EI-Banayosy A, Arusoglu L, Morshuis M, Kizner L, Sarnowski P., Cobaugh D., Koerfer R. Initial out-of-hospital experience with the DuraHeart. *Artificial Organs*, 2006, 30:A1.

[51] Mueller J, Nuesser P, Graichen H, Heinze V, Buchholz H, Ries D, Goettel P. Three years of experience with the magnetically levitated axial flow pump INCOR. *Artificial Organs*, 2006, 30:A13.

[52] Bearnson GB, Jacobs GB, Kirk J, Khanwilkar PS, Nelson KE, Long JW. HeartQuest ventricular assist device magnetically levitated centrifugal blood pump. *Artificial Organs*, 2006, 30(5), pp. 339-346.

[53] Loree HM, Bourque K, Gernes DB, Richardson JS, Poirier VL, Barletta N, Fleischli A, Foiera G, Gempp TM, Schoeb R, Litwak KN, Akimoto T, Kameneva M, Watach MJ, Litwak Philip. The Heart Mate III: design and in vivo studies of a Maglev centrifugal left ventricular assist device. *Artificial Organs*, 2001, 25(5), pp. 386-391.

[54] Chung M.KH, Zhang N, Tansley GD, Woodard JC. Impeller behaviour and displacement of the VentrAssist implantable rotary blood pump. *Artificial Organs*, 2004, 28(3), pp. 287-297.

[55] Berlin Heart. http://www.berlinheart.de/englisch/medpro/incor/Pumpe/.

[56] Chua LP, Su B, Lim TM, and Zhou T. Numerical simulation of an axial flow blood pump. *Artificial Organs*, 2007, 31(7), pp. 560-570.

[57] Carrier Michel , Trudelle Stéphane, Mongrain Rosaire, Garon André, Girard Alain, Camarero Ricardo, Pelletier Conrad, L. Ventricular assist device comprising an enclosed-impeller axial flow blood pump (Patent No: WO/1998/053864).

[58] J.F. Antaki, B.Paden, M.Piovoso and S.Banda. Award-winning control applications. IEEE Control System Magazine, 2002, 22(6), pp. 8-19.

[59] J.F. Antaki, B.Paden, G. Burgreen, and N. Groom. Blood pump having a magnetically suspended rotor. 2001, U.S. Patent 6244835.

[60] Asama H, Shinshi T, Hoshi H, Takatani S., Shimolohbe A. A compact highly efficient and low hemolytic centrifugal blood pump with a magnetically levitated impeller. *Artificial Organs*, 2006, 30(3), pp. 160-167.

[61] Hoshi H, Asama H, Shinshi T, Ohuchi K., Nakamura M., Mizuno T., Arai H., Shimokohbe A., Takatani S. Disposable magnetically levitated centrifugal blood pump: design and in vitro performance. *Artificial Organs*, 2005, 29(7), pp.520-526.

[62] Burrows C.R., and Stanway R. Identification of squeeze-film bearing characteristics. *Journal of Dynamic System, Measurement and Control, ASME Trans.*, 1977,Vol.99, pp. 167-173.

[63] Morton P.G. The derivation of bearing characteristics by means of transient excitation applied directly to a rotating shaft. G.E.C. *Journal of Science and Technology*, 1975,Vol.42, pp. 37-47.

[64] Roberts J.B., Holmes R and Mason P.J. Estimation of squeeze-film damping and inertial coefficients from experimental free-decay data. *Proc. Ins. Mech. Engrs*. PartC, 200(C2), 1986, pp. 123-133.

[65] Nordmann R, and Schollhorn K. Identification of stiffness and damping coefficients of squeeze-film bearings by means of the impact method. *Vibration In Rotating Machinery. I. Mech.E.* C285/80, 1980, pp. 231-238.

[66] Burrows C.R., Sahinkaya M.N. Frequency-domain estimation of linearised journal coefficients. *Journal of Lubrication Technology, ASME Trans.*, 1982, Vol.104, pp. 210-215.

[67] Burrows C.R., Sahinkaya M.N. Parameter estimation of multi-mode rotor-bearing System. *Proc. R. Soc. Lond.*, A379, 1982, pp. 367-387.

[68] Zhou Y. Parameter Estimation and Vibration Control of Rotor-Bearing system. Master Thesis, Nanyang Technological University, 1996.

[69] Schroeder M.R. Synthesis of low-peak-factor signals and binary sequences with low auto correlation. *IEEE Transactions on Information and Theory.* 1970, pp. 85-89.

[70] Matsumura F., Tanaka Y., Mamoru K. Composition of a magnetic bearing system for horizontal shaft and its experimental results. *Electrical Engineering in Japan*, 1983,Vol.103, No.5, pp. 121-128.

[71] Aoyama Y., Okazaki Y. Active magnetic bearing for spindle. *Proceedings of 4th International Workshop on Rare Earth Cobalt Permanent Magnets and Their Applications*, Japan, 1979, pp. 169-176.

[72] Humphris R.R., Allaire P.E., Lewis D.W., Barrett L.E. Diagnostic and control features with magnetic bearings. In *Proceedings of the 24th Intersociety*, vol.3, 6-11 August 1989, pp. 1491-1498.

[73] Williams, R.D., Keith F. J., Allaire P.E. Digital control of active magnetic bearings. *IEEE transactions industrial electronics*. Vol. 37, No. 1, February 1990, pp. 19-27.

[74] Xie Z.Y., Xu L.X., Li Y. Influence of control parameters on dynamic characteristics of AMB system. *Journal of Aerospace Power*, Vol.119, No.12, April 2004, pp. 174-178.

[75] Lim T.M., Cheng Shanbao. Parameter estimation of one-axis magnetically suspended system with a digital PID controller. In *Proceedings of 1st International Conference on Sensing Technology* 2005; pp. 419-424.

[76] Lim T.M., Cheng Shanbao. Parameter Estimation and statistical analysis on frequency-dependent active control forces. *Mechanical Systems and Signal Processing* 2007; 21, pp. 2112-2124.

[77] Polajzer B., Stumberger G., Ritonja J., Tezak O., Dolina D., Hameyer K. Impact magnetic nonlinearities and cross-coupling effects on properties of radial active magnetic bearings. *IEEE Transactions On Magnetics*. Vol.40, No.2, 2004, pp. 798-801.

[78] Kataoka H., Kimura Y., Fujita H., and Takatani S. Influence of radial clearance and rotor motion to hemolysis in a journal bearing of a centrifugal blood pump. *Artif Organs* 2006; 30(11), pp. 841-854.

[79] Kataoka H., Kimura Y., Fujita H., and Takatani S. Measurement of the rotor motion and corresponding hemolysis of a centrifugal blood pump with a magnetic and hydrodynamic hybrid bearing. *Artif Organs* 2005; 29(7), pp. 547-556.

[80] Baloh M.J., Allaire P.E., Hilton E.F., Wei N., Olsen O.B., Bearnson G.B., Khanwikar P.S. Characterization of a magnetic bearing system and fluid properties for a continuous flow ventricular assist device. *Artif Organs* 1999; 23(8), pp. 792-796.

[81] Asama J, Shinshi T, Hoshi H. Dynamic characteristics of a magnetically levitated impeller in a centrifugal blood pump. *Artif Organs* 2007; 31(4), pp. 301-311.

[82] Chung M.K.H., Zhang N., Tansley G.D. and Qian Y. Experimental determination of dynamic characteristics of the VentrAssist implantable rotary blood pump. *Artif Organs* 2004; 28(12), pp. 1089-1094.

[83] Sivadasan K.K. Analysis of self-sensing active magnetic bearings working on inductance measurement principle. *IEEE Transactions on Magnetics*, 32(2), March 1996, pp. 329-334.

[84] Yim J.S., Kim J.H., Sul S. K., Ahn H. J. and Han D. C. Sensorless position control of active magnetic bearings based on high frequency signal injection method. *IEEE Transactions on Industrial Electronics*, Vol. 50, No. 1, February 2003, pp. 83-88.

[85] Okada Y., Matsuda K., and Nagai B. Sensorless magnetic levitation control by measuring the PWM carrier frequency component. In *Proceedings of the Third International Symposium on Magnetic Bearings*, 1992, pp. 176-183.

[86] Ueno S., Matsuda K., Sato H., Okada Y. Position self-sensing control of an axial self-bearing motor. In *Proceedings of 8th International Symposium on Magnetic Bearing*, 2002, Japan, pp. 299-304.

[87] Gurumoorthy R., Soong W.L., Lyons, J.P. and Storace A.F. Implementation of sensorless control of radial magnetic bearings. In *Proceedings of MAG' 95 Magnetic Bearings, Magnetic Drives and Dry Gas Seals,* Washington, D.C., August 1995, pp. 239-248.

[88] Schammass A. and Bleuler H. Experimental results on self-sensing AMB using a three-state PWM amplifier. In *Proceedings of the Eighth International Symposium on Magnetic Bearings*, 2002, Japan, pp. 289-292.

[89] Yim J.S., Sul S.K., Ahn H.J., Han D.C. Sensorless position control of active magnetic bearings based on high frequency signal injection with digital signal processing. *Applied Power Electronics Conference and Exposition*, 2004. APEC '04. Nineteenth Annual IEEE Volume 2, 2004, pp. 1351-1354.

[90] Vischer D. and Bleuler H. Self-sensing active magnetic levitation. *IEEE Transactions on Magnetics*, 29(2), March 1993, pp. 1276-1281.

[91] Vischer D. and Bleuler H. A new approach to sensorless and voltage controlled AMBs based on network theory concepts. In *Proceedings of the Second International Symposium on Magnetic Bearings*, Tokyo, Japan, 1990, pp. 301-306.

[92] Mizuno T., Bleuler H., Gahler C., and Vischer D. Towards practical application of self-sensing magnetic bearings. In *Proceedings of the Third International Symposium on Magnetic Bearings*, Tokyo, Japan, 1992, pp. 169-175.

[93] Kucera L. Robustness of self-sensing magnetic bearings. In *Proceedings of the Magnetic Bearings Industrial Conference*, 1997, pp. 261-270.

[94] Mizuno T., Kitahara E., and Ueyama H. Linear carrier system with self-sensing magnetic suspension tracks. In *Proceedings of the Sixth International Symposium on Magnetic Bearings*, August 1998, pp. 631-640.

[95] Mueller R., Bedenig F., Bleuler H., Mizuno T., Tanaka H., Ueyama H., Kubo A. Position sensorless AMB in four degrees of freedom. In *Proceedings of the Fifth International Symposium on Magnetic Bearings*, August 1996, pp. 101-106.

[96] Morse N., Smith R., Paden B., Antaki J. Position sensed and self-sensing magnetic bearing configurations and associated robustness limitations. In *Proceedings of the 37th IEEE conference on Decision and Control*, Tampa, FL, USA, December, 1998, pp. 2599-2604.

[97] Maslen E.H. Magnetic Bearings. University of Virginia, 2000.

[98] Gujarati D. Essential of Econometrics. McGraw-Hill International Editions, 1992.

[99] OrCAD. http://www.orcad.com/.

[100] Burrows C. R., Kucuk N. C., Sahinkaya M. N., Stanway R. Linearised squeeze film dynamics: model structure and the interpretation of experimentally derived parameters. *Proc. Instn Mech. Engrs,* Part C, 1990, 204(C4), pp. 263-272.

Appendix A

Schroeder Phased Harmonic Sequences (SPHS)

The Schroeder Phased Harmonic Sequences (SPHS) is a signal that contains different frequency components with lowest possible peak value. This low-peak periodic signal $s(t)$ has any given power spectrum P_i, i=1,…,N where P_i is the ratio of the power at $\omega = i\omega_0$ to the total power. i.e.

$$\sum_{i}^{N} P_i = 1 \tag{A.1}$$

SPHS is constructed as:

$$s(t) = \sum_{i=1}^{N} \sqrt{\frac{P_i}{2}} Cos(i\omega_0 t + \phi_i) \tag{A.2}$$

where the phase of each frequency component is

$$\phi_i = \phi_{i-1} - 2\pi \sum_{m=1}^{i-1} P_m, i = 1..N \tag{A.3}$$

Appendix B

Pro/E drawings of the straightener, impeller and diffuser

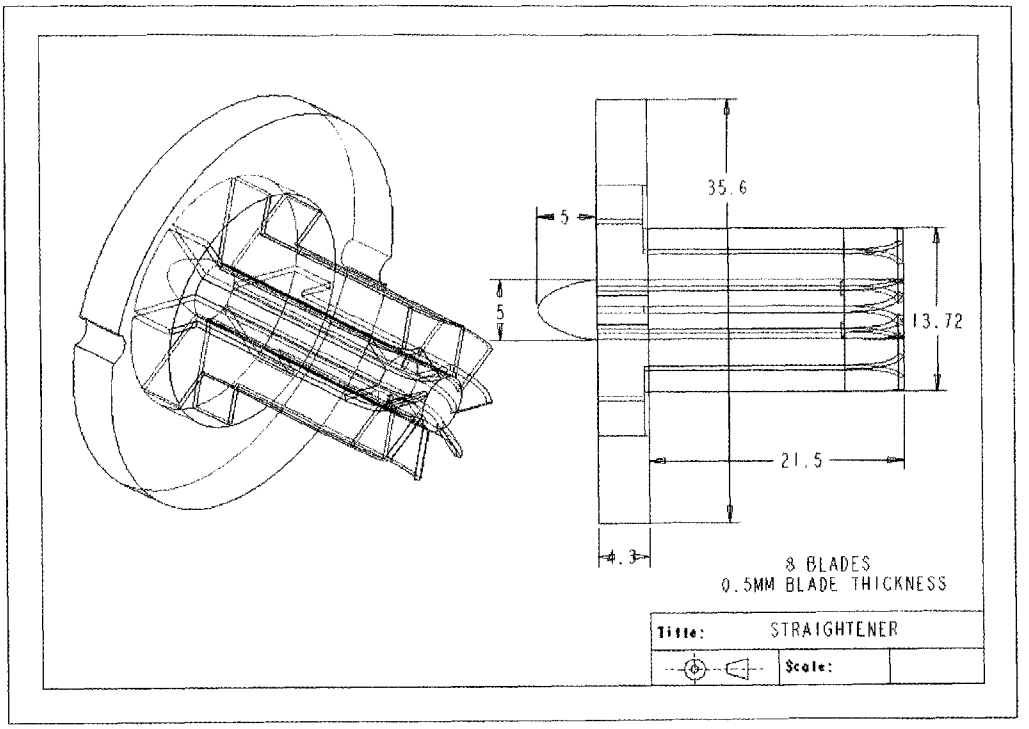

SCALE : 3.500 TYPE : ASSEM NAME : STRAIGHTNER SIZE : A4

Figure B.1 Drawing of the straightener

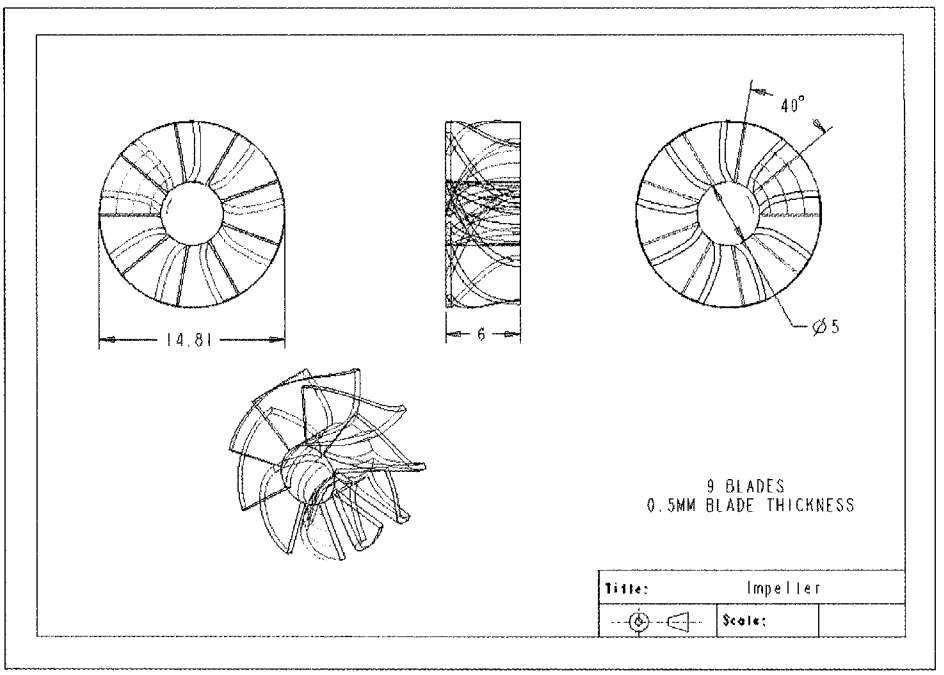

SCALE : 4.000 TYPE : PART NAME : ROTOR_PLS SIZE : A4

Figure B.2 Drawing of the impeller

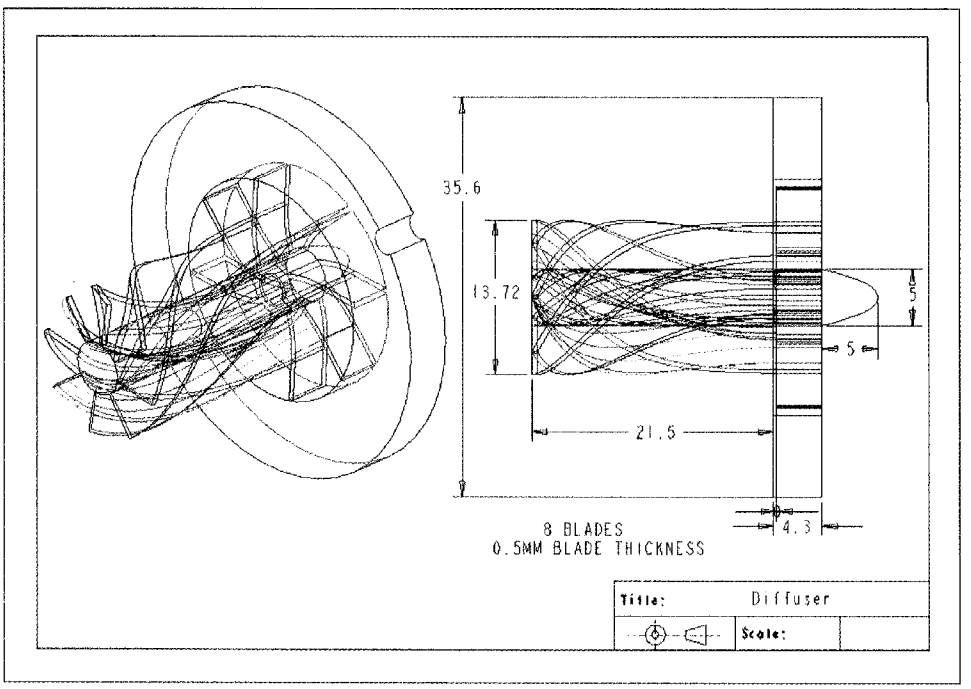

SCALE : 3.500 TYPE : ASSEM NAME : STATOR SIZE : A4

Figure B.3 Drawing of the diffuser

Appendix C

MATLAB program of parameter estimation of magnetic bearings system with statistics

```
clear all;

M = 0.7907; %%% Mass of the plate

Tvalue = 2.0; % 95% confidence interval for 5 degree of freedom

%SCALE of Force and X,Y
sclf=10;   %force scale
sclxy=10/8000;   %eddy current probe scale

kspring = 134e3*0.707;   % spring coefficient

data = load('data/pc/mb10.mat');   % loading datat
     fout2 = (data.mb10.Y(1).Data)*sclf;  %Y(1) is force

     youtlf =(data.mb10.Y(3).Data)*sclxy;   %Y(2) is y probe output  displacement
     xoutlf =(data.mb10.Y(2).Data)*sclxy;  %Y(2) is x probe output   displacement

     youtrg =(data.mb10.Y(5).Data)*sclxy;  %Y(2) is y probe output  displacement
     xoutrg =(data.mb10.Y(4).Data)*sclxy; %Y(2) is x probe output   displacement
%To get the mean of two X probe outputs, and two Y probe outputs
```

```
yout2 = 2*(youtlf+youtrg)/2;  % the y displacement at the rotor centre

xout2 = (xoutlf+xoutrg)/2;   % the x displacement at the rotor centre


fundal = 1;startup = 1;cutoff =250; Fs = 20e3;  Blksize = Fs/fundal;


%Averaging 5 periods

fout2                                                                 =
fft(   (  fout2(1:Blksize)+fout2(1+Blksize:2*Blksize)+fout2(2*Blksize+1:3*Blksiz
e)+fout2(1+Blksize*3:4*Blksize)+fout2(4*Blksize+1:5*Blksize) )/5   );

yout2                                                                 =
fft(   (  yout2(1:Blksize)+yout2(1+Blksize:2*Blksize)+yout2(2*Blksize+1:3*Blksi
ze)+yout2(1+Blksize*3:4*Blksize)+yout2(4*Blksize+1:5*Blksize) )/5   );

xout2                                                                 =
fft(   (  xout2(1:Blksize)+xout2(1+Blksize:2*Blksize)+xout2(2*Blksize+1:3*Blksi
ze)+xout2(1+Blksize*3:4*Blksize)+xout2(4*Blksize+1:5*Blksize) )/5   );


fout = fout2(2:Blksize);

yout = yout2(2:Blksize);

xout = xout2(2:Blksize);


%%%%%%%%%%%%%%%%%%%%%%%%%%%%%%%%%%%%%%%%%%%%%%%%%%%%%%%%%%%%%%%%%%%%%%%%%%%%%%%%%%%%%%%%%%%%%%%%%%%%
%%%%%%     Parameter Estimation In Frequency Domain    %%%%%%%%%%
%%%%%%%%%%%%%%%%%%%%%%%%%%%%%%%%%%%%%%%%%%%%%%%%%%%%%%%%%%%%%%%%%%%%%%%%%%%%%%%%%%%%%%%%%%%%%%%%%


bandwid = 15; overlapping = 12;
```

```
for i=1:2000
  if i==1
    W1 = startup;
    W2 = startup + bandwid;
  else
    W1 = W2 - overlapping;
    W2 = W1 + bandwid;

  end

  if W2 <= cutoff

    N = 0;F = 0; Fo = 0; Yd = 0;

    for j=W1:fundal:W2
      kkk = W1/fundal+N;
      N = N+1;
      W = W1+fundal*(N-1);

      F(N) = 2*pi*W;

      Fo(N)  =  fout(kkk);
      Xd(N)  =  xout(kkk);
      Yd(N)  =  yout(kkk);
```

```
end

GXR =  linspace(0,1,N);   GXI =  linspace(0,1,N);
GYR =  linspace(0,1,N);   GYI =  linspace(0,1,N);

for j=1:N

   GX(j)  =  Xd(j)/Fo(j);
   GY(j)  =  Yd(j)/Fo(j);

   GXR(j)  =  real(GX(j));
   GXI(j)  =  imag(GX(j));

   GYR(j)  =  real(GY(j));
   GYI(j)  =  imag(GY(j));
end

TFX(i) = mean(abs(GX));
TFY(i) = mean(abs(GY));
xxx(i) = (W1+(W2-W1)/2);  % Hz


Wf = zeros(2*N,5); Phif = zeros(5,2); Cf = zeros(2*N,2);
```

```
for j = 1:N
   j2 = 2*j;
   j1 = j2-1;

   WMass  =  M*F(j)*F(j);

   Cf(j1,1)  =  WMass*GXR(j);
   Cf(j1,2)  =  WMass*GYR(j);

   Cf(j2,1)  =  WMass*GXI(j);
   Cf(j2,2)  =  WMass*GYI(j);


   Wf(j1,1) = GXR(j);
   Wf(j1,2) = GYR(j);
   Wf(j1,3) = -F(j)*GXI(j);
   Wf(j1,4) = -F(j)*GYI(j);
   Wf(j1,5) = -1.00;

   Wf(j2,1) = GXI(j);
   Wf(j2,2) = GYI(j);
   Wf(j2,3) = F(j)*GXR(j);
   Wf(j2,4) = F(j)*GYR(j);
   Wf(j2,5) = 0.00;
```

```
end

B = inv(Wf'*Wf);
Phif = B*(Wf')*Cf;

kxx(i) = Phif(1,1)-kspring;
kyx(i) = Phif(1,2);

kxy(i) = Phif(2,1);
kyy(i) = Phif(2,2)-kspring;

cxx(i) = Phif(3,1);
cyx(i) = Phif(3,2);

cxy(i) = Phif(4,1);
cyy(i) = Phif(4,2);

Bx(i)   =   Phif(5,1);
By(i)   =   Phif(5,2);
alpha(i)   =   atan(By(i)/Bx(i))*180/pi;

%%%%%%%%%%%%%%%%%%%%%%%%%%%%%%%%%%%%%%%%
%%%%%%%   Statistics Calculation   %%%%%%%%%%%%%%%%%%%
%%%%%%%%%%%%%%%%%%%%%%%%%%%%%%%%%%%%%%%%
```

```
%Calculate RSS residual sum of squares
% p(i) residual vector

p = Cf - Wf*Phif;
ppp = p'*p;

e(1,i) = ppp(1,1);
e(2,i) = ppp(2,2);

AAA = eye(2*N)-(ones(2*N))/(2*N);

dvvv = Cf'*AAA*Cf;              %total sum of deviation
tss(1,i) = dvvv(1,1);
tss(2,i) = dvvv(2,2);

%Calculate goodness of fit in x, y directions
gof(1,i) = sqrt(1-((2*N-1)*e(1,i))/((2*N-5)*tss(1,i)));  % x direction

gof(2,i) = sqrt(1-((2*N-1)*e(2,i))/((2*N-5)*tss(2,i)));  % y direction

e(1,i) = e(1,i)/(2*N-5);
e(2,i) = e(2,i)/(2*N-5);

%se = zeros(2,i);
for j=1:5
```

```
            se(j,1,i) = sqrt(e(1,i)*B(j,j));
            se(j,2,i) = sqrt(e(2,i)*B(j,j));
        end

        for j=1:2
            for jj=1:5
                tt(jj,j,i)=Phif(jj,j)/se(jj,j,i);

                if abs(tt(jj,j,i)) >= Tvalue
                    sig(jj,j,i) = 1;
                else
                    sig(jj,j,i) = 0;
                end
            end
        end

    end
end

%TFX = 20*log10(TFX);
%TFY = 20*log10(TFY);

%%%%%%%%%%%%%%%%%%%%%%%%%%%%%%%%%%%%%%%%%%%
%%%% %%          Plot Parameter Estimation Results      %%%%%%%%%%%%
%%%%%%%%%%%%%%%%%%%%%%%%%%%%%%%%%%%%%%%%%%%
```

```
subplot(8,1,1);plot(xxx,TFX);ylabel('TFX (m/N)');title('Parameter estimation on
MB in radial directions');
subplot(8,1,2);plot(xxx,TFY);ylabel('TFY (m/N)');
subplot(8,1,3);plot(xxx,kxx);ylabel('KXX (N/m)');
subplot(8,1,4);plot(xxx,kyy);ylabel('KYY (N/m)');
subplot(8,1,5);plot(xxx,cxx);ylabel('CXX (N.s/m)');
subplot(8,1,6);plot(xxx,cyy);ylabel('CYY (N.s/m)');
subplot(8,1,7);plot(xxx,gof(1,:));ylabel('GoF in X');
subplot(8,1,8);plot(xxx,gof(2,:));ylabel('GoF in Y');xlabel('Hz');
%subplot(9,1,9);plot(xxx,alpha);ylabel('Alpha');

for i=1:20

disp([' ']);
disp([' ']);
disp(['**********************************************************']);
disp(['Significance For the ', num2str(xxx(i)),' first set (1:Yes, 0:No)']);
disp([' KXX = ',num2str(kxx(i),'%.6e'),' Significance:---
',num2str(sig(1,1,i),'%.6e')]);
disp([' KYX = ',num2str(kyx(i),'%.6e'),' Significance:---
',num2str(sig(1,2,i),'%.6e')]);
disp([' KXY = ',num2str(kxy(i),'%.6e'),' Significance:---
',num2str(sig(1,2,i),'%.6e')]);
```

```
disp([' KYY = ',num2str(kyy(i),'%.6e'),' Significance:---
',num2str(sig(2,2,i),'%.6e')]);

disp([' CXX = ',num2str(cxx(i),'%.6e'),' Significance:---
',num2str(sig(3,1,i),'%.6e')]);
disp([' CYX = ',num2str(cyx(i),'%.6e'),' Significance:---
',num2str(sig(3,2,i),'%.6e')]);
disp([' CXY = ',num2str(cxy(i),'%.6e'),' Significance:---
',num2str(sig(4,1,i),'%.6e')]);
disp([' CYY = ',num2str(cyy(i),'%.6e'),' Significance:---
',num2str(sig(4,2,i),'%.6e')]);

disp([' Force Angle Alphla = ',num2str(alpha(i),'%.6e')]);
disp([' Goodness of fit in X direction = ',num2str(gof(1,i),'%.6e')]);
disp([' Goodness of fit in Y direction = ',num2str(gof(2,i),'%.6e')]);
disp(['**********************************************************']);
disp([' ']);
disp([' ']);
end
```

Appendix D

MATLAB program of implementing forward path filter for self-sensing AMB

```
%%%%%%%%  ButterWorth Second Order High Pass Filter  %%%%%%%%
wc = 2*pi*15e3;
K = 1;
hpnum = [K 0 0];
hpden = [1 1.414*wc wc*wc];
[dhpnum,dhpden] = c2dm(hpnum,hpden,Ts,'tustin');
%%%%%%%%%%%%%%%%%%%%%%%%%%%%%%%%%%%%%%%%%%%%%%%%%%%%%%%%%%%%%%%%


%%%%%%%%  Second Order ButterWorth Low Pass Filter  %%%%%%%%%
wc = 2*pi*5e3;
K = 1;
lpnum = [K*wc*wc];
lpden = [1 1.414*wc wc*wc];
[dlpnum,dlpden] = c2dm(lpnum,lpden,Ts,'tustin');
%%%%%%%%%%%%%%%%%%%%%%%%%%%%%%%%%%%%%%%%%%%%%%%%%%%%%%%%%%%%%%%%
```

Appendix E

2-State and 3-State PWM amplifiers' connection schemes

The connection scheme of the 2-State PWM Amplifiers (Copley 4122Z) is shown below:

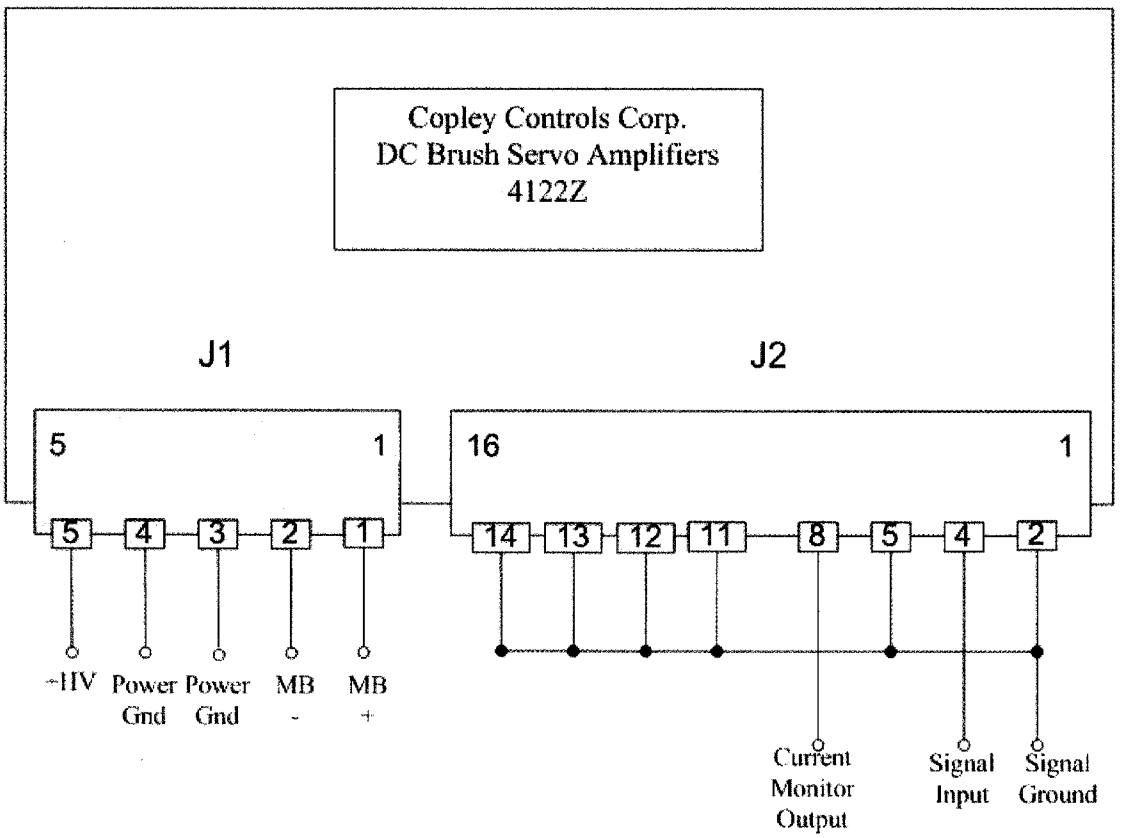

Figure E.1: 2-State PWM amplifier (Copley 4122Z) connection scheme

The connection scheme of the 3-State PWM Amplifiers (AMC 25A) is shown below:

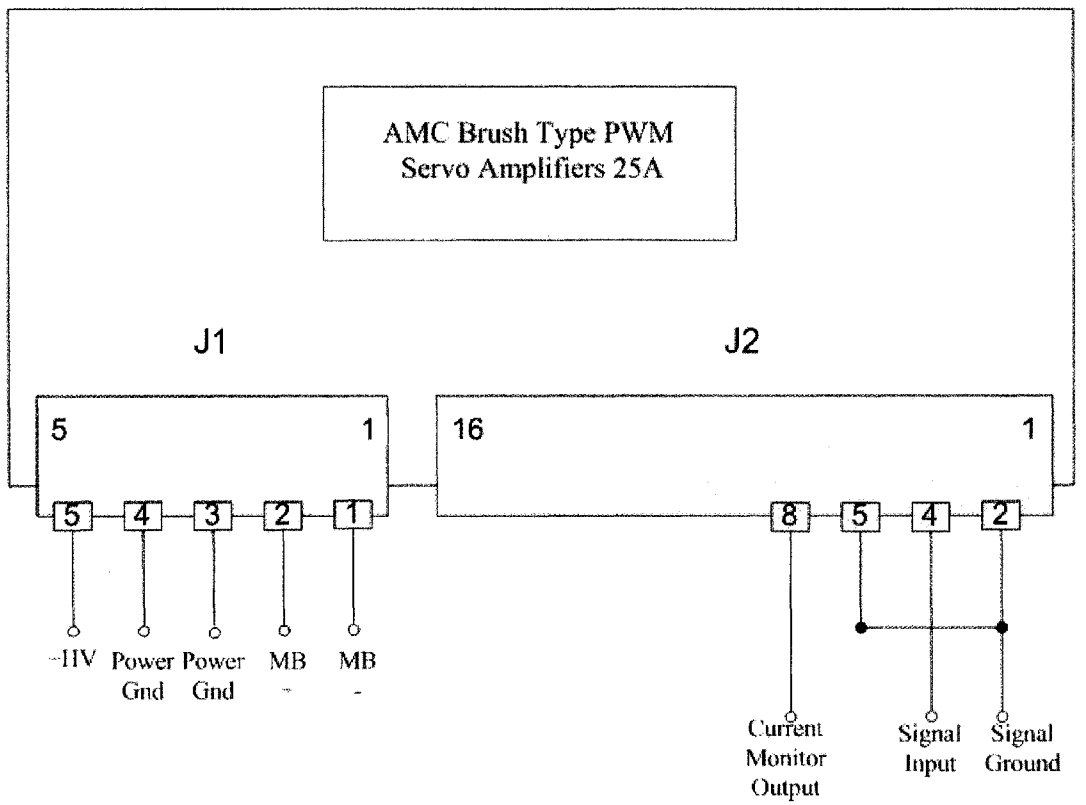

Figure E.2: 3-State PWM amplifiers (AMC 25A) connection scheme